

vol. 1 X71-73535
2 X71-73554
3 X71-73584

N72-146722 N1/144n
CR-114398
February
KSS-10

R-678

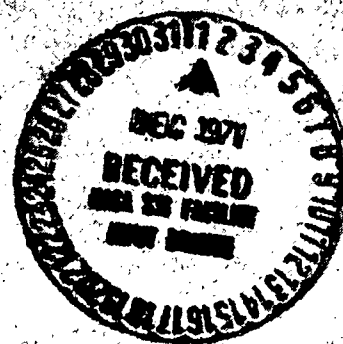
Volume IV

GUIDANCE AND NAVIGATION REQUIREMENTS
FOR UNMANNED FLYBY AND SWINGBY MISSIONS
TO THE OUTER PLANETS

October 1971

DRA

CASE FILE
COPY



CHARLES STARK DRAPER
LABORATORY

MASSACHUSETTS INSTITUTE OF TECHNOLOGY

CAMBRIDGE, MASSACHUSETTS, 02139

GUIDANCE AND NAVIGATION REQUIREMENTS

FOR UNMANNED FLYBY AND SWINGBY

MISSIONS TO THE OUTER PLANETS

(Final Technical Report on Phase C of Contract NAS-2-5043)

VOLUME IV HIGH THRUST MISSIONS - Part 2

OCTOBER 1971

CHARLES STARK DRAPER LABORATORY
MASSACHUSETTS INSTITUTE OF TECHNOLOGY
CAMBRIDGE, MASSACHUSETTS

Approved: Donald C Fraser Date: 12 October 1971
Dr. Donald C. Fraser, Program Manager

Approved: David G Hoag Date: 13 Oct 71
David G. Hoag, Associate Director
Charles Stark Draper Laboratory

Approved: R. R. Ragan for Date: 13 Oct 71
Ralph R. Ragan, Deputy Director
Charles Stark Draper Laboratory

ACKNOWLEDGEMENT

This report was prepared under DSR Project 55-32700, sponsored by the Ames Research Center, National Aeronautics and Space Administration through Contract NAS 2-5043.

The following are the contributors to this Phase C technical report:

Donald C. Fraser
Harvey L. Malchow
Patricia Farrington
Lester L. Sackett

The publication of this report does not constitute approval by the National Aeronautics and Space Administration of the findings or the conclusions contained therein. It is published only for the exchange and stimulation of ideas.

ABSTRACT

The studies reported in this volume are concerned with guidance and navigation requirements for a set of impulsive thrust missions involving one or more outer planets or comets. Specific missions considered include two Jupiter entry missions of 800 and 1200 day duration, two multiple swingby missions with the sequences Jupiter-Uranus-Neptune and Jupiter-Saturn-Pluto, and two comet rendezvous missions involving the short period comets P/Tempel 2 and P/Tuttle-Giacobini-Kresak.

Results show the relative utility of onboard and Earth-based DSN navigation. The effects of parametric variations in navigation accuracy, measurement rate, and miscellaneous constraints are determined. The utility of a TV type onboard navigation sensor - sighting on planetary satellites and comets - is examined. Velocity corrections required for the nominal and parametrically varied cases are tabulated.

TABLE OF CONTENTS

ABSTRACT	PAGE
CHAPTER 1. INTRODUCTION	1
1.1 PROBLEM STATEMENT AND OBJECTIVES	1
1.2 MISSION DESCRIPTION	3
1.2.1 Comet Rendezvous Missions	3
1.2.2 Jupiter Entry Missions	4
1.2.3 Three Planet Grand Tours	7
CHAPTER 2. MODELING AND SIMULATION	13
2.1 FILTERING	13
2.2 THE DEEP SPACE NETWORK MODEL	14
2.3 ONBOARD NAVIGATION - TELEVISION	15
2.4 ONBOARD NAVIGATION - SCANNING PHOTOMETER	16
2.5 PHENOMENA ERRORS	17
2.5.1 Planet Ephemerides	17
2.5.2 Planet Radius Uncertainty	17
2.5.3 Satellite Ephemerides	17
2.5.4 Mass Uncertainties	19
2.5.5 Planetary Horizon Uncertainties	19
2.5.6 Comet Ephemerides	19
2.5.7 Comet Radius Uncertainty	22
2.6 GUIDANCE ERROR MODEL	22
2.7 ORGANIZATION OF THE TRADE-OFF COMPUTATION PROCEDURE	22
CHAPTER 3. SIMULATION RESULTS	29
3.1 COMET MISSION RESULTS	30
3.1.1 Tempel 2 Mission	35
3.1.2 Tuttle- Giacobini-Kresak Mission	45

CHAPTER 3.	SIMULATION RESULTS (Continued)	
3.2	JUPITER ENTRY MISSIONS	52
3.2.1	800 Day Entry Mission Results	54
3.2.2	1200 Day Entry Mission Results	68
3.3	MULTIPLE PLANET SWINGBY MISSIONS	75
3.3.1	Jupiter-Uranus-Neptune Swingby Mission	75
3.3.2	Jupiter-Saturn-Pluto Swingby Mission	79
3.3.3	Onboard Navigation Using a TV Type Sensor	101
CHAPTER 4.	SUMMARY AND RECOMMENDATIONS	105
4.1	SUMMARY	105
4.2	RECOMMENDATIONS	108
REFERENCES		111
APPENDIX A	EXPLANATION OF GEOMETRY PLOTS	115
A.1	INTERPLANETARY TRAJECTORY GEOMETRIES	115
A.2	PLANETARY PASSAGE TRAJECTORY GEOMETRIES	116
APPENDIX B	TEMPEL 2 MISSION PLOTS	121
APPENDIX C	TUTTLE-GIACOBINI-KRESAK MISSION PLOTS	131
APPENDIX D	800 DAY JUPITER ENTRY MISSION PLOTS	141
APPENDIX E	1200 DAY JUPITER ENTRY MISSION PLOTS	153
APPENDIX F	NEPTUNE GRAND TOUR MISSION PLOTS	163
APPENDIX G	PLUTO GRAND TOUR MISSION PLOTS	187
APPENDIX H	ONBOARD SENSOR CONSIDERATIONS	213
H.1	SIGNAL LEVELS	214
1.1	Planetary Satellite Magnitudes	214
1.2	Comet Brightness Levels	219

H. 2	PROBLEMS WITH IMAGE TUBES AND SATELLITE SIGHTINGS	228
2. 1	Limiting Stellar Magnitudes	228
2. 2	Star Availability	229
2. 3	Dynamic Range Problems-Image Spreading	229
2. 4	Scattered Light Noise Problems	230
2. 5	Image Tube Choices for Satellite Navigation	234
H. 3	COMET NAVIGATION SENSORS	235
3. 1	Scanning Photometer Problems	235
3. 2	Image Tube Problems	237
APPENDIX I	ON PLANET CENTER FINDING	239
I. 1	DSN BY ITSELF COMPARED TO DSN WITH A LIMB SENSOR	240
I. 2	BISECTING A TWO-LIMB SCAN	242
I. 3	SIGHTINGS ON THE PLANETARY SATELLITES	242
I. 4	DIRECT PLANETARY IMAGE ANALYSIS	242
APPENDIX J	SIMULATION EQUATIONS	245
J. 1	FILTER EQUATIONS	245
J. 2	GRAM-SCHMIDT SQUARE ROOT UPDATE	252
J. 3	STATE DEFINITION	253
J. 4	COORDINATE TRANSFORMATIONS	254
J. 5	ENTRY ANGLE EQUATIONS	256
J. 6	STAR ELEVATION MEASUREMENT WITH PLANET RADIUS	258
J. 7	TELEVISION MEASUREMENT EQUATIONS	259

CHAPTER 1

INTRODUCTION

1.1 PROBLEM STATEMENT AND OBJECTIVES

Recent interest in the exploration of the outer planets by means of unmanned space probes has stimulated the definition of a number of potential missions. These missions include direct flights to a specific planet, and swingby flights, which, by passing close to more than one astronomical object, can maximize the useful life of a probe while minimizing fuel requirements.

The studies reported in this volume have been concerned with guidance and navigation requirements for a set of missions involving one or more outer planets or comets. Specific missions considered include two Jupiter entry missions of 800 and 1200 day duration, two multiple swingby missions with the sequences Jupiter-Uranus-Neptune and Jupiter-Saturn-Pluto, and two comet rendezvous missions involving the short period comets P/Tempel 2 and P/Tuttle-Giacobini-Kresak. The comet missions utilize a Jupiter swingby.

This report is the fourth and final volume of a series which presents the study results obtained under NASA contract NAS-2-5043. The work was performed under the direction of the Advanced Concepts and Missions Division, Office of Advanced Research and Technology. Volume I of the series is a summary report which summarizes the contents of the other volumes. Volume II examines three impulsive-thrust missions which include a Jupiter flyby, a Jupiter swingby to Saturn, and a four planet Grand Tour with the sequence Jupiter-Saturn-Uranus-Neptune. Volume III analyzes low-thrust, ion-propulsion flights to Jupiter and to Saturn.

This volume follows closely the work reported in Volume II of the series. In that volume the guidance and navigation requirements for unmanned, impulsive-thrust swingby and Grand Tour missions were analyzed

with the general aim of determining the relative utility of Earth-based, spacecraft-based, and combined Earth- and spacecraft-based navigation systems. Both navigation modes were analyzed under near optimal operating conditions. For example, the onboard system was allowed to choose a minimal error measurement by combining choices from lists of available solar system bodies, measurement types, and sufficiently bright stars. The deep space tracking network was assumed to be operating at full capacity.

The present studies examine the guidance and navigation requirements for a set of six missions different from those studied earlier, and assess the degradation in performance caused by onboard and Earth-based navigation systems that operate under suboptimal conditions. In this context the following problem areas are addressed:

1. The relative utility of onboard navigation is examined in relation to restricted Earth-based tracking.
2. Unestimated bias noise is considered as part of the onboard navigation noise model. The earlier studies modeled white noise only.
3. The importance of measurement frequency for onboard systems is evaluated.
4. The periods of operation of the onboard navigation system are restricted to intervals near pericenter and intervals outside of the expected science package activity zones.
5. An image tube sensor is considered as a navigation instrument.
6. Ephemeris uncertainties of planetary satellites and the two comets are examined as parameters.
7. The utility of a scanning type navigation sensor is analyzed under restrictive conditions. Measurements are limited to determining the angle between a star and the target planet limb, with limited sets of available stars.
8. The coupling between guidance errors and navigation accuracy is assessed.

While the missions considered here are high thrust or impulsive, and involve one or more of the outer planets, they have certain characteristics that are distinctly different from those considered in Volume II. The Jupiter entry missions have well defined terminal conditions that provide an increased need for the study of navigation guidance coupling. One of the multiple planet swingby missions includes the planet Pluto which has the largest planetary mass and ephemeris uncertainties. Finally, the comet rendezvous missions involve a final target whose mass is negligible in terms of perturbing the spacecraft trajectory. Earth-based telescope observations reduce the comet ephemeris uncertainties. This information, together with Earth-based radio measurements of the spacecraft position give an initial spacecraft position relative to the comet. The remainder of the burden of accurately locating the spacecraft position with respect to the comet falls solely on the onboard navigation sensor.

The organizational format of this volume is as follows. Chapter 1 is introductory material. Chapter 2 details the simulation formulation and presents the error models. Chapter 3 lists the navigation and guidance results on a mission by mission basis, and discusses their interpretation. Chapter 4 summarizes the results and recommends appropriate further study. The Appendices contain mission geometry plots, discussions of onboard sensor problems, and detailed derivations of the simulation equations.

1.2 MISSION DESCRIPTION

Basic data for the six considered missions is presented below. Appendices A through G, in addition, contain a number of useful geometry plots for each of the missions.

1.2.1 Comet Rendezvous Missions

There are approximately thirty astronomical objects designated as "short period" comets. These comets are characterized by aphelion distances in the vicinity of Jupiter, perihelion distances of one to two A.U., and periods of roughly five years. Because these objects orbit near Jupiter's

orbit, it is possible, on occasion, to use a Jupiter swingby to construct a rendezvous mission. Such trajectories have been identified by the Advanced Concepts and Mission Division NASA/OART which supplied spacecraft trajectories for rendezvous with the comets P/Tempel 2 and P/Tuttle-Giacobini-Kresak. From a scientific standpoint these rendezvous missions have several advantages over a pure flyby. For example they allow direct sampling of the material of the tail and coma without the encumbrance of high relative velocities between spacecraft and comet.

On these missions the spacecraft leaves Earth relatively close to the comet, and after Jupiter swingby spends the second half of the mission within less than 1 A.U. of the comet. At large solar distances however, these comets are extremely dim objects since the coma has not formed and one is left with a nucleus of a magnitude in the range 20 to 30. Therefore not only can these objects not be observed at these ranges by onboard navigation sensors, they also cannot be observed by Earth telescope until they are within 1 to 2 A.U. of the sun. Since these objects are strongly affected by both nongravitational forces their ephemeris uncertainties are large until they can be observed by Earth telescope. The comet P/Tuttle-Giacobini-Kresak has a much larger ephemeris uncertainty ascribed to it than P/Tempel 2 because its orbit is strongly perturbed by Jupiter on the 1987 passage.

Basic data for the comet missions is listed in Tables 1-I and 1-II. The trajectories are illustrated in Figures 1-1 and 1-2. Time intervals in the figures are marked in 60 day increments. The sphere of influence is defined here as that surface within which the near planet is assumed to be the sole gravitation source.

1.2.2 Jupiter Entry Missions.

These two missions are designed for direct atmospheric probing, therefore the entry conditions are of primary interest. These include radius from the mass centroid, entry angle, velocity, and the geographical location at entry. The two missions differ mainly in the location of the entry point and the associated time of flight. The 800 day mission enters near the

TABLE 1-I

Basic Trajectory Data for the Tempel 2
Comet Rendezvous Mission

Launch Date	September 10, 1989
Hyperbolic Excess Speed	9.5 km/sec
Jupiter Arrival Date	November 22, 1991
Jupiter Passage Distance	24.9 Jupiter Radii
Time Within Jupiter Sphere of Influence	152.8 Days
Rendezvous Date	January 17, 1994
Time from Comet Perhelion	58 Days
Comet Relative Approach Velocity	3.7 km/sec

TABLE 1-II

Basic Trajectory Data for the Tuttle-Giacobini-Kresak
Comet Rendezvous Mission

Launch Date	May 4, 1985
Hyperbolic Excess Speed	9.7 km/sec
Jupiter Arrival Date	October 27, 1987
Jupiter Passage Distance	204.8 Jupiter Radii
Time Within Jupiter Sphere of Influence	163.2 Days
Rendezvous Date	December 19, 1989
Time from Comet Perhelion	50 Days
Comet Relative Approach Velocity	5.6 km/sec

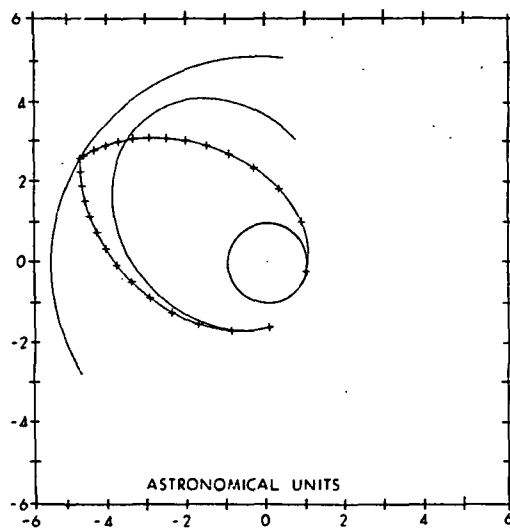


Fig. 1-1 P/Tempel II Mission, Interplanetary Geometry

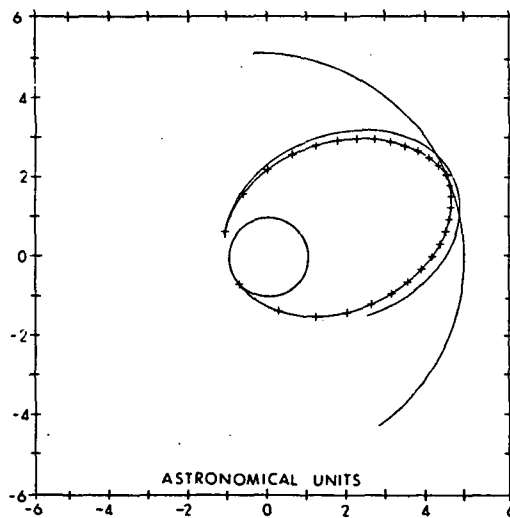


Fig. 1-2 P/Tuttle-Giacobini-Kresak Mission, Interplanetary Geometry

terminator while the 1200 day mission entry point is slightly displaced from the brightest point of the apparition. Tables 1-III and 1-IV list the pertinent trajectory information and Figures 1-3 and 1-4 show the terminal geometry.

1.2.3 Three Planet Grand Tours

The positions of the planets Uranus, Neptune and Pluto are such that for the next several decades an assortment of three-body Grand Tours are possible using Jupiter as the first of the sequence. The two missions considered here are the sequence Jupiter-Uranus-Neptune, to be launched in 1979, and Jupiter-Saturn-Pluto to be launched in 1977. Tables 1-V and 1-VI list the important trajectory data, and Figures 1-5 and 1-6 depict the interplanetary geometry.

TABLE 1-III

Basic Trajectory Data for the 800 Day
Jupiter Entry Mission

Launch Date	October 8, 1978
Hyperbolic Excess Speed	9.6 km/sec
Arrival Date	December 16, 1980
Inclination	10 Deg.
Entry Angle	-15 Deg.
Entry Radial Distance	71640 km
Relative Entry Velocity at Equator	47.2 km/sec
Time from Sphere of Influence to Entry	72.3 Days

TABLE 1-IV

Basic Trajectory Data for the 1200 Day
Jupiter Entry Mission

Launch Date	October 8, 1978
Hyperbolic Excess Speed	9.6 km/sec
Arrival Date	January 20, 1982
Inclination	10 Deg.
Entry Angle	-15 Deg.
Entry Radial Distance	71640 km
Relative Entry Velocity at Equator	47.1 km/sec
Time from Sphere of Influence to Entry	80.6 Days

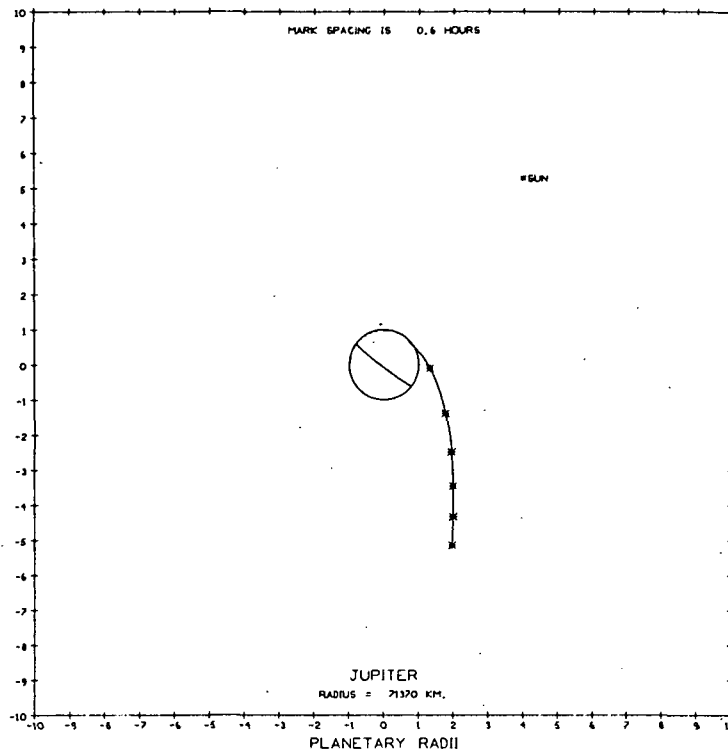


Fig. 1-3 Jupiter 800 Day Entry Geometry

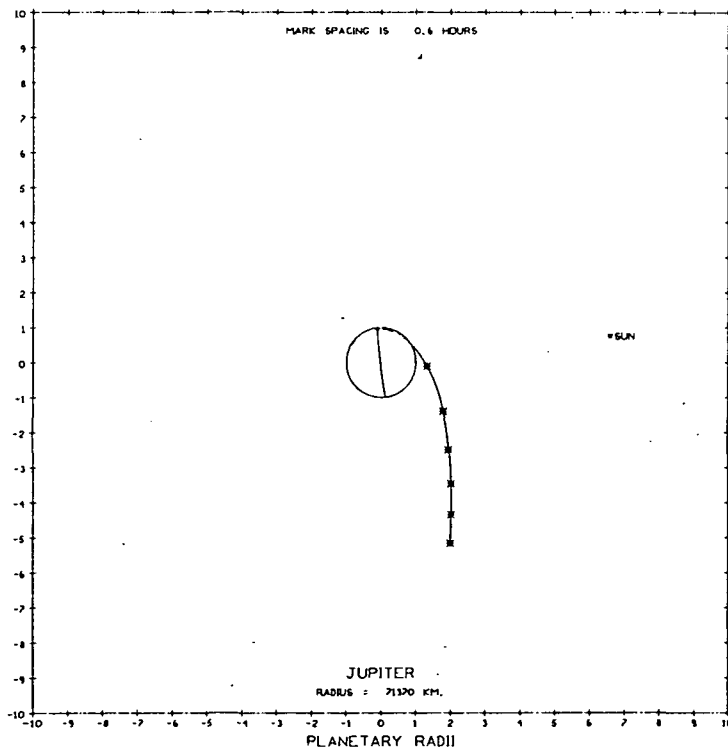


Fig. 1-4 Jupiter 1200 Day Entry Geometry

TABLE 1-V

Basic Data for the Jupiter-Uranus-Neptune
Multiple Planet Swingby

Launch Date	November 4, 1979
Hyperbolic Excess Speed	10.3 km/sec
Jupiter Arrival Date	May 30, 1981
Jupiter Passage Distance	8.4 Jupiter Radii
Time Within Jupiter Sphere of Influence	93.6 Days
Uranus Arrival Date	January 17, 1986
Uranus Passage Distance	2.2 Uranus Radii
Time Within Uranus Sphere of Influence	81.2 Days
Neptune Arrival Date	August 22, 1989
Neptune Passage Distance	2.0 Neptune Radii
Time from Sphere of Influence to Perigee	60.1 Days

TABLE 1-VI

Basic Data for the Jupiter-Saturn-Pluto
Multiple Planet Swingby

Launch Date	September 4, 1977
Hyperbolic Excess Speed	10.3 km/sec
Jupiter Arrival Date	March 1, 1979
Jupiter Passage Distance	4.4 Jupiter Radii
Time Within Jupiter Sphere of Influence	93.8 Days
Saturn Arrival Date	November 11, 1980
Saturn Passage Distance	10.2 Saturn Radii
Time Within Saturn Sphere of Influence	81.0 Days
Pluto Arrival Date	September 22, 1986
Pluto Passage Distance	2.0 Pluto Radii
Time From Pluto Sphere of Influence to Perigee	9.5 Days

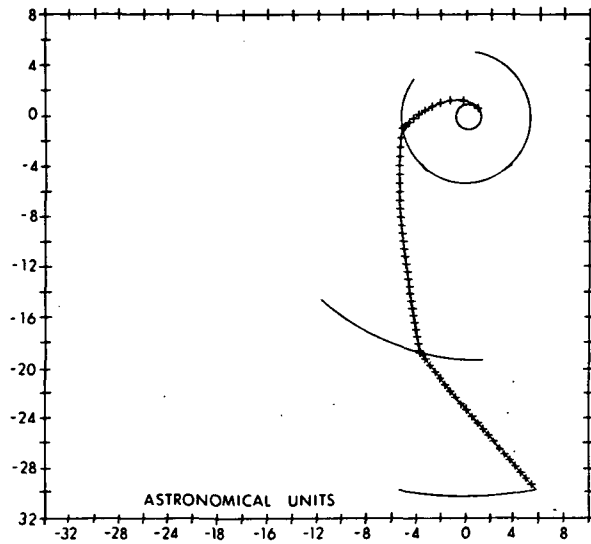


Fig. 1-5 Interplanetary Geometry for the Jupiter-Uranus-Neptune Multiple Planet Swingby

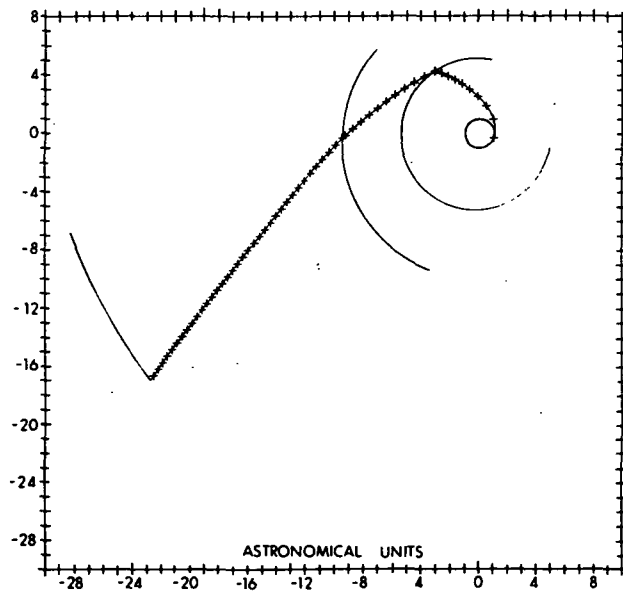


Fig. 1-6 Interplanetary Geometry for the Jupiter-Saturn-Pluto Multiple Planet Swingby

CHAPTER 2

MODELING AND SIMULATION

In this chapter, the models and methods used to perform statistical simulations of deep space missions are summarized. More detail may be found in Appendices H, I, and J. Much of what might be included here has already been thoroughly discussed in Vol. 2, Ch. II of this report, and the reader is referred to that chapter for additional background on the nature of this study. In this chapter, we mention some of the important areas of concern to the present results and also discuss important differences from the earlier work or additions made in this phase of the study.

A detailed statistical analysis of the outer planet and comet missions described in the previous chapter was performed to determine the tradeoff between navigation via the use of a ground tracking system and a supplemental onboard navigation system. Two different types of onboard navigation instruments were considered, one being a scanning photometer instrument of the nature considered in earlier phases of this contract and the other a science television camera. Many different uncertainties affect the accuracy of guidance and navigation on these missions. These quantities are discussed in this chapter and their nominal values are presented. The general organization of the computer simulation is also discussed.

2.1 FILTERING

In the simulation, the statistics of first order deviations from a reference trajectory are considered. Given the additional assumption of Gauss-Markov processes, only second order statistics are necessary. Recursive linear filtering with unestimated but considered biases is used. Unestimated biases include dynamic biases (planet or sun mass uncertainty) and measurement biases (station location errors for the Earth-based radio measurements and instrument biases for the onboard navigation).

The statistics are affected by four main steps: extrapolation from one time to another, velocity corrections, DSN measurement incorporation, and onboard measurement incorporations. In order to increase numerical

accuracy, and decrease the possibility of numerical difficulties, a square root formulation of the filter equations was utilized. The necessary equations are outlined in detail in Appendix J.

2.2 THE DEEP SPACE NETWORK MODEL

The Earth-based radio measurements from the Deep Space Network (DSN) were modelled in the same way as in the earlier phases of this study. The equations used to process an Earth-based doppler radar measurement are based upon a simple model of the information content of a DSN measurement which is due to Hamilton and Melbourne¹. The required measurement partial derivatives are derived directly from these equations and then an approximate method of compressing each pass of data is developed by assuming constant measurement geometry over the pass. The complete set of equations which result from this analysis is given in Appendix E of Vol. II.

In this study DSN pass frequency was reduced for many cases since in an actual mission, continuous tracking over the entire trajectory would not be either practical or necessary. For the multiple-planet swingbys and the comet missions it was assumed that there would be 100% tracking for about one week prior to a velocity correction, in order to more accurately determine the spacecraft state prior to this important maneuver. It was also assumed that there was 100% tracking for about one month prior and following pericenter passage of a planet, since during this period the trajectory can be altered significantly by the gravitational field of the planet and since data transmission is during this phase. DSN tracking was set, somewhat arbitrarily, at one eight-hour pass per 28 days up to one astronomical unit from the approaching planet and then one eight-hour pass per 14 days up to the time for 100% tracking. Tracking frequencies greater than this seemed to be unnecessary since the 100% tracking near the planet reduced the estimation errors to similar levels regardless of interplanetary tracking frequencies. For the comet missions, 100% tracking began nominally at 20 days prior to rendezvous time.

The nominal value for Doppler noise was 1 mm/sec and the station location biases were 1 meter off the spin axis and 2 meters in equivalent longitude.

2.3 ONBOARD NAVIGATION-TELEVISION

It is quite likely that a science television camera (TV) will be included on flights to the outer planets or comets. The information obtained using this camera could also be used for navigational purposes, supplementing Earth-based radio measurements (DSN). Extensive analysis of the use of such an instrument has been performed by Duxbury and others at JPL and much of what follows in this section is based upon their work.

When in the vicinity of a planet, the TV is used to measure the direction to one or more of the planetary satellites. By imaging the satellite in the TV coordinate system, one gains information about the position of the spacecraft relative to the satellite, and by considering the position of the satellite relative to its primary, one obtains information on the spacecraft's position relative to the primary planet. Inertial position data is obtained through the background stars and possibly through an onboard attitude reference.

In this study, simplified instrument measurement errors, and satellite ephemeris errors were included. Only one satellite per planet was used because of the limit on the number of variables which could be estimated in the simulation program. Simulations performed with this simple model give an approximate estimate of the value of using an onboard TV to supplement DSN versus using DSN only. They also provide a rough comparison with the use of a scanning photometer instrument.

For the two comet approaches studied, TV could be used only within a few days of rendezvous because of the dimness of these objects. In the given cases the comet, and in particular the comet nucleus, would be observed. After coma formation, the TV measurement would be degraded since fewer stars which could be used for calibration could be seen in the picture. Stars near the nucleus would be masked by the coma radiation.

A series of TV pictures would be taken, transmitted to Earth and processed. One measures the two components of position perpendicular to the line of sight to the object being viewed. This series of TV pictures is approximated in the simulation by a single measurement incorporation at preset time intervals. Each measurement is corrupted by instrument measurement noise which is approximated by white noise and an unestimated bias. Noise sources include electromagnetic and optical distortion. The instrument errors from all noise sources are combined into an equivalent white noise and bias, and these values have been parameterized. The nominal values used were suggested by Duxbury^{2,3,4,5} of JPL, and consist of a $5''$ unestimated bias and a $2''$ white noise.

Limitations were placed on the use of TV by the brightness of satellites (or comets) and nearness of the line of sight to a bright object like the parent planet or the sun. No measurements were taken during an interval prior to a comet mission terminal point to allow time for data processing.

2.4 ONBOARD NAVIGATION-SCANNING PHOTOMETER

The scanning photometer can be used to make angular measurements. The angle observed can be planet angular diameter, planet center to star, planet limb to star, etc. Only planet (or comet) limb to star measurements were made in this phase of the study. The measurement error is a combination of 1) the inherent instrument error and 2) the uncertainty involved in defining the planet limb. Since instrument and phenomena error were assumed independent, their variances were simply added to give the total white noise variance. The scanning photometer is assumed to be a visible light instrument, hence it is required that the planet limb be sunlit. The simulation requires a 30° minimum sun-spacecraft-planet angle before scanning photometer measurements are allowed. Planet (comet) radius uncertainty was estimated and included, in the measurement partials (see Appendix J).

In order to improve the scanning photometer measurement mode, a bias component of instrument error was included in the simulation used in this phase of the study. The bias was unestimated, but "considered" in

the same sense as the DSN bias. If the bias had been estimated, it would have been practically eliminated after several measurements. In an actual instrument, due for example to temperature fluxuations, there are slowly varying bias components and also phenomena which cause bias components to develop. Thus biases cannot be completely calibrated out. This situation was approximated by assuming that the bias component was unestimated but considered.

The same 37 Apollo navigational stars were used as in earlier phases of the study. In Vol. II, Ch. II, there is a discussion of the measurement schedule optimization used to select the star needed for the measurment to be incorporated.

2.5 PHENOMENA ERRORS

2.5.1 Planet Ephemerides

As in previous phases of this study, the planet (or comet) ephemeris error was included as an estimated quantity. Values used are given in Table 2-I. The Pluto values are taken from Ref. 6, all others are from Ref. 7.

2.5.2 Planet Radius Uncertainty

Planet radius uncertainties are included as an estimated parameter in this study phase. A discussion of the planetary radius uncertainties is included in Vol. II, Section II.C. Values used in this study phase are listed in Table 2-II, and have been taken directly from the recent survey by Dollfus.⁸ The Pluto radius uncertainty was taken from Ref. 9.

2.5.3 Satellite Ephemerides

In the simulation, when a television instrument is used for onboard navigation during the multiple planet swingby missions, sighting of a planet's satellites is assumed. As is discussed in Vol. II, Section II.C, the ephemeris errors for the satellites are approximately the same as for the parent planet.

Table 2-I Planetary Ephemeris Errors

	1 σ values		
	tangent (km)	normal (km)	radial (km)
Jupiter	± 383	± 383	± 100
Saturn	± 800	± 800	± 200
Uranus	± 1400	± 1400	± 400
Neptune	± 2200	± 2200	± 600
Pluto	± 9000	± 9000	± 9000

Table 2-II Planetary Radius and Radius Uncertainty

	1 σ radius	
	radius (km)	uncert. (km)
Jupiter	71,370	33
Saturn	60,500	80
Uranus	24,850	93
Neptune	22,700	150
Pluto	3,000	200

Since the uncertainty in the radial direction can be reduced significantly by using the analysis in Vol. II, Section II.C.5, and because of limitations on the number of variables which could be estimated, only two components of satellite ephemeris error were considered. The nominal values of these uncertainties are listed in Table 2-III.

2.5.4 Mass Uncertainties

The error in the estimated mass of the sun and the planets was included in the simulation as an unestimated but considered parameter. The comets were assumed massless. The inverse masses (with respect to the sun) and their estimated uncertainties are listed in Table 2-IV. The Jupiter, Pluto and sun values are taken from Ref. 10, and the others from Ref. 7.

2.5.5 Planetary Horizon Uncertainties

An uncertainty in the location of the horizon is introduced from two primary sources: an uncertainty in the atmospheric model derived from Earth-based measurements, and from the statistical fluctuation in the atmospheric meteorology. An analysis was done in the earlier phase of the study to obtain typical values for this error (see Vol. II, Sec. II.C). They are reproduced here in Table 2-V with the addition of a value for the planet Pluto.

2.5.6 Comet Ephemerides

The orbital elements for P/Tempel 2 and P/Tuttle-Giacobini-Kresak for the epoch at rendezvous were supplied by B. Marsden of the Smithsonian Astrophysical Observatory.¹¹ The orbital elements for both comets are given in Table 2-VI.

The apriori expected uncertainties in the comets ephemerides were derived from information which was also supplied by Marsden.¹¹ His error values were based on previous sightings of the comets and on the predicted effect of gravitational and nongravitational forces acting prior to the rendezvous time. A close passage to Jupiter previous to the rendezvous causes particularly large uncertainties in the case of P/Tuttle-Giacobini-Kresak.

Table 2-III Satellite Ephemeris Uncertainties

Planet	Satellite	1 σ Eph. Uncert. (km)	
		Tan	Norm
Jupiter	Io		
	Europa	400	400
	Ganymede		
	Callisto		
Saturn	Titan	900	900
Uranus	Ariel	1500	1500
	Umbriel		
	Titania		
	Oberon		
Neptune	Triton	2500	2500

Table 2-IV Mass Uncertainties

	mass ⁻¹	1 σ mass uncert.
Jupiter	1047.39	$\pm .00247$
Saturn	3497.6	± 0.1
Uranus	22,934	± 2
Neptune	18,889	± 20.7
Pluto	1,812,000	$\pm 40,000$

Table 2-V Planetary Horizon Altitude Uncertainty

	1 σ visible (km)
Jupiter	10
Saturn	10
Uranus	10
Neptune	10
Pluto	10

Table 2-VI Comet Orbital Elements

Element	Tempel 2	Tuttle-Giacobini- Kresak
semi major axis	3.106 a.u.	3.101 a.u.
eccentricity	0.522	0.656
inclination	11.98 degs.	9.24 degs.
longitude of ascending node	117.58 degs.	141.02 degs.
argument of perihelion	194.88 degs.	61.46 degs.
perihelion date	2449428.31	2447929.67

The values of ephemeris uncertainty prior to Earth sightings and after Earth sighting, assuming a 0.3 arc second telescope accuracy are given in Table 2-VII.

The nuclei of the two comets have been observed on previous revolutions, and it is assumed that they will be observable at the time of rendezvous or at least within a few weeks of the time of rendezvous. Observation of the nucleus would reduce the ephemeris uncertainty from that associated with the optical centroid of the entire comet. The effects of Earth sightings are incorporated as a single reduction in the estimation error covariance occurring nominally at 20 days before rendezvous. Earth sightings over this short period essentially reduce the two components of ephemeris uncertainty normal to the Earth-comet line of sight.

2.5.7 Comet Radius Uncertainty

The estimated radii of the comet nuclei are taken from Ref. 12. The coma, after formation, would have a radius of about 1500 cm. The nucleus was assumed to be spherical but with a relatively large radius bias set at a 3σ value of 25%. It also has a large phenomena error, modelled as a white noise, to account for the nonspherical and irregular shape of the nucleus. These values are given in Table 2-VIII.

2.6 GUIDANCE ERROR MODEL

FTA guidance is assumed for all missions. The main error contributions are from accelerometer bias, accelerometer scale factor error, and engine cutoff uncertainty. These have nominal values of .3 cm/sec, 50 $\mu g / g$ and .05 sec respectively. A more thorough discussion of the implementation is given in Vol. II, Section II.C.

2.7 ORGANIZATION OF THE TRADE-OFF COMPUTATION PROCEDURE

The previous sections of this chapter have discussed error models for the various physical phenomena, instrument and system characteristics which are germane to this study. The purpose of this section is to describe the computational procedure in which all these ingredients are combined to perform the tradeoff studies.

Table 2-VII Ephemeris Uncertainties Before and After
Earth Sighting

Tempel 2		
	unsighted	0.3
	values (km)	sighted
LOS to Earth	400	400
Component		
Tangential	4000	600
Component		
Normal	1000	600
Component		

Tuttle-Giacobini-Kresak

nominal		
	unsighted	0.3
	values(km)	sighted
LOS to Earth	10,000	10,000
Component		
Tangential	500,000	260
Component		
Normal	10,000	260
Component		

Table 2-VIII Comet Radii and Uncertainties

	radius (km)	1 σ radius uncertainty (km)	1 σ horizon uncertainty (km)
P/Tempel 2	2	.05	.16
P/Tuttle- Giacobini-Kresak	.5	.1	.04

Figure 2-1 gives a flow chart of the major elements of the computer program which performs the error analysis. This procedure begins with initial values for all the covariance matrices defined in the first section of this chapter and in Appendix J. These could be the end result of a transplanetary injection or the terminal conditions from a previous leg of the same mission. The usual operating mode is to begin with the transplanetary injection errors and proceed through the mission, running successively each interplanetary and near planet leg. Each new leg is started from the terminal conditions of the previous leg.

As can be seen from Fig. 2-1 there is a main computation loop in the program. There are as many cycles through this main computation loop as there are predetermined "decision points" in the leg of the mission under study. The frequency, spacing, and total number of these points is completely flexible but must be specified prior to run time. The times for velocity corrections were prespecified for this phase of the study. The nominal times were at one week after injection, immediately after passing the sphere of influence, and at about two days prior to pericenter passage. The first velocity correction is performed to eliminate injection errors. The one at the sphere of influence corrects for error built up over the long interplanetary leg of the trajectory and aims the spacecraft for the correct swingby or terminal geometry. The velocity correction near pericenter utilizes increased knowledge of the state gained in-close approach, and makes a final correction if this is a terminal leg or aims the spacecraft for the swingby. Upon leaving the sphere of influence another velocity correction is made, utilizing all the state estimation data from the previous passage and aiming the spacecraft for the next encounter. For the comet approach, there were velocity corrections shortly after incorporating Earth-based telescope information, and after a few measurements were taken with the onboard instrument.

The first step within the main computation loop is to extrapolate the initial conditions to the time of the first decision point under a two-body approximation to the free-fall situation. The reference state is extrapolated by solving Kepler's problem along the reference trajectory between the initial time and the time of first decision point. Simultaneously, a set of

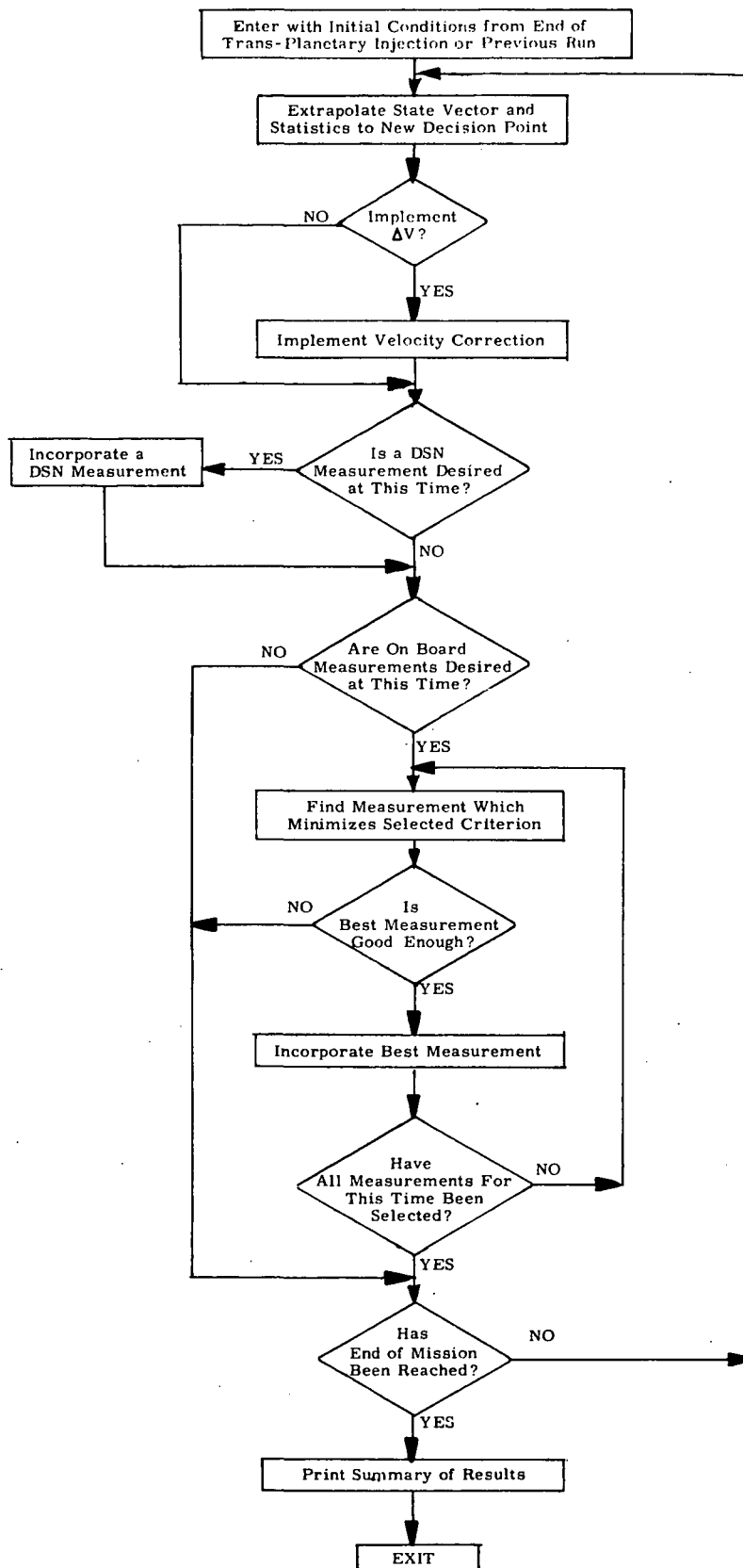


Figure 2-1 Simulation Logic Diagram

partial derivatives is computed which can be used to generate the state transition matrix associated with the solution to the linear perturbation equations between these two times. After the statistics have been extrapolated and if the prespecified time has been reached, a velocity correction is made.

Once the velocity correction decision has been made the program continues to the question of whether or not to process a DSN measurement at this time. If it is determined that this is one of the predetermined times that such a ground tracking measurement is to be incorporated this is done.

After the DSN measurement choice has been made the program continues to the questions of whether to make an onboard measurement at this time and what measurement to take. One of two options may be exercised at this point. The first is not to make a measurement at all. In this case the state and statistics are extrapolated to the next decision point and the entire process repeated. The second option is to either make a TV measurement or to select a star with which to make a scanning photometer measurement. If the scanning photometer is used, the star is chosen such that the measurement would minimize the mean squared position estimation error at a preselected target point (usually the destination point).

For entry and multiple planet swingby missions only one type of scanning photometer measurement was made, namely star elevation (planet limb to star angle) measurements. One of 37 stars given in Table II-7 of Vol. II was used.

A number of constraints are used to eliminate measurements which should be rejected for physical reasons. These include:

1. Two lines of sight farther apart than the optical instrument can permit.
2. Line of sight to a star too close to the line of sight to the sun.
3. Star behind the planet/moon.
4. Line of sight to a star too close to the line of sight to the planet limb.

5. Line of sight to a planet edge too close to the line of sight to the sun. (not made of the spacecraft is in the planet shadow.)
6. Planet or star behind the sun.
7. Lines of sight to dark edges of planets are rejected.

For TV measurements no selection process was necessary; the measurement times and satellites used were prespecified. For the comet missions, TV measurement frequencies of 2 meas./day and 4 meas./day were assumed for the Tempel 2 and P/Tuttle-Giacobini-Kresak missions respectively. On the flyby missions TV sightings were made at a rate of 1 meas./2days for approximately 20 days, 2 meas./day for 10 days and finally 4 meas./day for the last day. Plots (displayed in Appendix H) were made of the satellite or comet brightness to determine turn-on and turn-off time. In addition, a TV measurement was not made if a satellite was obscured by the parent planet or if the spacecraft-satellite/comet LOS was too close to the spacecraft-sun LOS.

Further details of the computational procedure are given in Vol. II, Section II-E. A discussion of measurement schedule optimization is given in Vol. II, Section II-F.

CHAPTER 3

SIMULATION RESULTS

In this chapter the results of extensive mission simulations are presented in the form of tables, graphs, and discussions. The two comet missions are paired in Section 3.1 followed by the Jupiter entry missions in Section 3.2 and the multiple-planet swingby missions in Section 3.3. Key computer results are tabulated at the beginning of the sections and are to be interpreted as described in this introductory section.

Estimation and guidance errors are listed in separate tables. The estimation , or equivalently, navigation errors, represent the uncertainty in knowlege of a dynamical quantity, while the guidance errors are the expected actual deviations (one sigma) from a nominal trajectory. The simulations are performed in a sequence of interplanetary (sphere of influence to sphere of influence) and planetary passage (inside sphere of influence) legs. The results generally correspond to errors at the end of each leg of a given mission. However, for the multiple-planet swingby missions, periapsis error values are also listed for each planet passage. For the Jupiter entry and comet missions terminal errors are listed.

Position and velocity magnitudes are given at the sphere of influence. For the planetary passage leg, position uncertainties are tabulated in three components, and the total magnitudes of position and velocity errors are given. The down range component is taken along the velocity vector, cross range is perpendicular to the velocity and in the plane containing the velocity vector and the direction to the planet centroid. The out of plane error is taken parallel to the orbital angular momentum vector. During the planet passage the position and velocity vectors are defined in a planet-centered coordinate system. Position errors are taken with respect to the local planet or comet. Errors for a number of "cases" or variations in navigation and guidance characteristics are listed in the tables. Specific parameters for the "nominal" cases in each mission are described at the beginning of each different mission section. The descriptions of the listed cases are as follows:

nominal	- This case has the expected operational input characteristics such as best estimates of onboard navigation instrument noise characteristics and Deep Space Tracking Network operational procedure.
DSN ONLY	- Navigation for this case is done only by the Earth-based Deep Space Network.
8 hr/2 wk	- Deep Space Network is assumed to be used only for one 8 hour pass in each two week interval except for continuous tracking for two weeks prior to a velocity correction and for 4 weeks on either side of pericenter.
OB	- Stands for onboard navigation using a scanning photometer. Onboard navigation is always combined with nominal DSN tracking. The first number following OB is the sensor one-sigma white noise, the second is the one-sigma bias error.
TV	- Stands for onboard navigation using a television sensor.
ephemeris x n	- Ephemeris errors are scaled up or down from their nominal values by the factor n.
Off at E-n	- No navigation measurements are made after n days from periapsis or terminal time (whichever applies). [*] If only hours are involved the designation is E-n hr.
On at E-n	- Similar to the above except that navigation measurements are limited to the interval from E-n to periapsis or terminal time.
ΔV	- Velocity correction.

3.1 COMET MISSION RESULTS

Two missions to short period comets have been examined. The missions have a number of characteristics that are quite similar, for example the periods of the comets are both about 5.5 years, both rendezvous points

^{*} On egress from periapsis the designation changes sign. Thus navigation limited to a period after periapsis would be designated by E+n. Symmetric limitation about periapsis is designated E±n.

are placed at about 2 months before comet periapsis, both spacecraft trajectories include a Jupiter swingby, and the total flight times are only 8% different. However there are also a number of significantly different characteristics associated with each mission. The terminal closing speeds are quite different. On the Tempel 2 mission the closing speed at mission termination is 3.6 km/sec compared to 5.2 km/sec on the Tuttle-Giacobini-Kresak mission. The comet T-G-K is a considerably fainter object than Tempel 2. Thus if the onboard navigation sensor had the same detection threshold for both missions, onboard sensing could commence further out on the Tempel 2 mission. Initial ephemeris uncertainties are considerably different for the two comets, with T-G-K having much larger initial values. Finally the contribution to guidance and navigation made by Earth based telescope sightings on the comets are different. At twenty days before rendezvous, the nominal point at which Earth sightings are incorporated, the Earth-spacecraft distance on the Tempel 2 mission is two and one half times larger than on the T-G-K mission, thus Earth-based sighting at a given angular accuracy will produce a larger error reduction for the T-G-K mission.

The terminal point on each mission is taken to be one hour before collision with the comet nucleus. At the high indicated closing speeds only 5-10 minutes would be required to traverse a 1500 km radius coma to strike the nucleus. At one hour out, the spacecraft is about 12000 km from Tempel 2 and about 19000 km from Tuttle-Giacobini-Kresak. The one hour final time limit on navigation information accumulation is an arbitrary choice which would seem to allow sufficient time for the Earth communications, attitude changes, and thrusting associated with the large terminal velocity correction that causes rendezvous instead of collision. Results shown in this section do not consider the final large velocity correction but only the small corrections needed to minimize position error and to put the spacecraft back on its nominal course.

No attempt was made to minimize spacecraft position errors with respect to Jupiter by adding onboard navigation because these errors were already small, using Deep Space Network navigation, compared to uncertainties in the comet ephemeris.

The Earth-based contribution to navigation error reduction is treated as a single measurement input. Thus the rms telescope angular errors is multiplied by the comet-Earth distance to reduce the initial comet ephemeris uncertainty. The telescope accuracy is a parameter of the study. If the Earth-based measurement does not reduce the ephemeris uncertainty, the smaller a priori value is used. The Earth-based telescope only reduces two components of the ephemeris leaving the line of sight (i.e., unsighted) component unchanged. The unsighted component is also a parameter of the study which reflects the potential range of the initial ephemeris uncertainty. Values of the ephemeris uncertainty before and after Earth sightings of various accuracy are listed in Table 3-I. These values are used in the simulations. Nominal Earth-based measurement accuracy is taken as 0.3 arcseconds. For a discussion of the unsighted values see Chapter 2.

The first column of Table 3-I gives the nominal (apriori) ephemeris error components if no Earth-based telescope sighting is made. The next three columns give the components for various accuracy Earth telescopes. The presence of an asterisk by an entry indicates that for that accuracy telescope no improvement is possible using Earth-based observations. The final two columns give the ephemeris error components for the case where the unsighted (radial) values are ten times bigger or smaller and a three arcsecond Earth-based sighting of the comet is made.

A summary of the key comet mission nominal input parameters is provided in Table 3-II.

As a final observation on the ephemeris error components, it should be noted that spacecraft based observations are highly effective in reducing the error in the Earth-comet direction. The reason for this is that in both comet missions the approach to the comet is made approximately from below the comets' orbital plane. This makes it possible to obtain information in the direction which cannot be determined from Earth. Thus the Earth and spacecraft based measurements augment each other in the best way possible on these missions.

TABLE 3 - I
Parametric Ephemeris Uncertainties
Before and After Earth Sighting

	Before Earth Sighting	Tempel II			Unsighted Radial Component x 10	Unsighted Radial Component x 1/10
		3 π sighted	0.3 π sighted	0.03 π sighted		
Radial Component	400	400	400	400	4000	40
Tangential Component	4000	4000*	600	60	600	600*
Normal Component	1000	1000*	600	60	600	600*

Tuttle - Giacobini - Kresak

	Before Earth Sighting	3 π sighted	0.3 π sighted	0.03 π sighted	Unsighted Radial Component x 10	Unsighted Radial Component x 1/10
Radial Component	10,000	10,000	10,000	10,000	100,000	1000
Tangential Component	500,000	2600	260	26	260	260
Normal Component	10,000	2600	260	26	260	260

* These values are initially smaller than the 3 π projection.

TABLE 3 - II
Nominal Comet Mission Parameters

<u>Parameter</u>	<u>Tempel II</u>	<u>P/Tuttle-Giacobini-Kresak</u>
Earth Telescope Accuracy	0.3" (600km)	0.3" (260km)
Ephemeris Uncert. (radial value)	400 km	10,000 km
Image Tube Noise (white noise, bias)	2", 5"	2", 5"
Onboard Nav. Turn-on Time	E-10 days	E-2 days
Earth Sighting Input Time	E-20 days	E-20 days
Time of Velocity Corrections	E-19, 8 days	E-19, 1.5 days
DSN Tracking	a) 8hr/2 weeks interplanetary b) Continuous During Jupiter Passage, E ₊ 30 days c) Continuous - Last 28 days and First 10 days	same
TV Meas. Freq.	2 meas. /day	4 meas. /day

3.1.1 Tempel 2 Mission

The key numerical results for this mission are listed in Tables 3-III and 3-IV. The nominal case uses a T.V. navigation sensor which has a white noise error of 2 arcseconds and a bias error of 5 arcseconds. The T.V. is assumed to be turned on 10 days before mission termination. Earth-based measurement information is incorporated at 20 days before rendezvous, and velocity corrections are at 19 and 8 days before rendezvous. Initial ephemeris uncertainties for the nominal case are listed in Table 3-I in the 0.3 arcsecond column.

The position errors listed in Tables 3-III and 3-IV are with respect to the comet. The dominant error in position estimation and guidance position is in the component along the line of sight from the spacecraft to the comet which is also the direction of relative velocity. The TV instrument drastically reduces the two components which it observes in just a few measurements. Each TV measurement is equivalent to one or more frames, which, when processed, would yield the equivalent white noise and bias assumed here.

The position estimation uncertainty of the spacecraft with respect to the comet is seen to be insensitive to a doubling of the TV noise levels (both the bias and white noise). This is because the onboard sighting can observe only two components of the spacecraft position uncertainty with respect to the comet. This leaves the error dominated by the third component, which is along the spacecraft-comet line of sight. It is not until onboard instrument accuracy is degraded to the point that errors are of the order of those obtained with an Earth-based telescope that the effect of decreasing onboard instrument accuracy is noticeable.

At the time of the last TV measurement, at approximately 12 hours from rendezvous, the comet-spacecraft distance is 1.6×10^5 km. At this distance, the angular subtense of a 10 arcsecond uncertainty (like the double TV noise bias) is roughly 80 km which is much smaller than the 600 km residual position uncertainty in the down range direction about which the onboard sensor gathers no information. Thus, when a residual unsighted uncertainty component remains, and is of the order of 600 km, the onboard TV system accuracy requirements can be relaxed considerably without

TABLE 3 -III
Tempel II Mission
Navigation Results

Case	Position Estimation Error (km)				Velocity Error Est. (M/sec)	Ephem. Error Est. (km)
	Down Range	CR	OP	MAG		
Nominal	608	3.5	3.5	608	.021	607
TV noise x 2	608	7.0	7.0	608	.021	607
ΔV at E-8, 1	608	3.5	3.5	608	.023	608
ΔV at E-19, 1	608	3.5	3.5	608	.024	608
ΔV at E-19, 5	608	3.5	3.5	608	.021	608
0.03" Earth Meas.	156	3.5	3.5	156	.020	153
Unsignt. Comp. x 1/10	186	3.5	3.5	186	.020	161
Unsignt. Comp. x 10	658	3.5	3.5	658	.031	659
TV Noise x 10	608	70.6	70.8	616	.021	615
TV on at E-18.5	608	3.5	3.5	608	.021	608
3" Earth Meas.	1078	3.5	3.5	1078	.022	1077
TV on at E-14.5	608	3.5	3.5	608	.021	607
Telescope Sight at E-46 days	606	3.5	3.5	606	.020	606
Telescope Sight at E-86 days	607	3.5	3.5	607	.020	607
No nucleus .3" teles, scanplot	608	97.7	65.9	619	.021	618
No nucleus 3" telesc, scanplot	1077	69.5	73.9	1082	.022	1082

TABLE 3 - IV
Tempel II Mission
Guidance Results

Case	Guid. Pos. Error (km)				Time of ΔV_1		Time of ΔV_2		Total ΔV
	DR	CR	OP	MAG	(days)	(M/sec)	(days)	(M/sec)	(M/sec)
Nominal	609	68.3	67.5	616	E-19	3.88	E-8	1.25	5.14
TV noise x 2	609	13.0	12.9	636	E-19	3.88	E-8	1.26	5.14
ΔV at E-8,1	608	11.6	11.6	608	E-8	9.63	E-1	1.07	10.70
ΔV at E-19,1	608	11.6	11.6	608	E-19	3.88	E-1	10.50	14.40
ΔV at E-19,5	608	44.2	43.9	608	E-19	3.88	E-5	2.02	5.90
0.03" Earth Meas.	159	67.4	65.8	185	E-19	3.92	E-8	0.888	4.81
Unsight. comp. x 1/10	190	68.7	66.7	213	E-19	3.00	E-8	0.880	3.88
Unsight. comp. x 10	659	68.3	67.6	666	E-19	25.40	E-8	5.92	31.32
TV noise x 10	611	500	485	927	E-19	3.88	E-8	0.78	4.66
TV on at E-18.5	609	68.0	67.6	616	E-19	3.88	E-8	1.25	5.14
3" Earth Meas.	1078	68.3	67.7	1083	E-19	3.00	E-8	5.87	8.87
TV on at E-14.5	609	68.2	67.6	616	E-19	3.88	E-8	1.26	5.14
Telescope Sighting at E-46	606	68.2	67.5	614	E-46	1.49	E-8	1.17	2.66
Telescope Sighting at E-86	608	68.5	67.5	615	E-86	0.90	E-8	1.35	2.25
No nucleus .3" telesc, SP	610	323	335	767	E-19	3.88	E-8	1.06	4.94
No nucleus 3" telesc, SP	1087	419	428	1241	E-19	3.00	E-8	5.80	8.80

significantly degrading the magnitude of the position uncertainty. This conclusion is substantiated by Figure 3-1 which shows that the TV noise level does not increase position uncertainty until it is scaled upward by a factor of 10. At these noise levels the concomitant angular subtense is of the order of the residual position component along the line of sight.

It is interesting to examine the effect on position uncertainty of removing the comet nucleus and sighting on the coma. This leads to larger measurement errors because the effective instrument error is increased and the coma has an associated radius uncertainty. The two no-nucleus cases are listed in Tables 3-III and 3-IV. The onboard instrument used is a scanning photometer rather than a TV sensor and the instrument noise values are 60 and 10 arcseconds for white noise and bias respectively. The coma radius uncertainty is set at 250 km (1σ). The tables show that under these conditions the unsighted (by spacecraft observation) component uncertainty, dictated by Earth-based optical sightings still dominates the position uncertainty. However the components perpendicular to the spacecraft-comet line of sight are seen to be considerably larger.

The effect of increased TV noise levels on guidance position errors is somewhat more pronounced as can be seen in Figure 3-2. This is because the final course correction was made at E-8 days and was based on the information gathered in only 4 TV measurements. The terminal navigation position uncertainty is smaller because it is based on 18 TV measurements.

Because of the existence of an unsighted position uncertainty component that can be partially reduced by Earth-based sightings, such sightings, if they are sufficiently accurate, can reduce position uncertainties in nearly direct proportion to their accuracy. For the Tempel 2 mission, both initial ephemeris uncertainties and Earth-based sighting accuracy have a strong effect on the guidance and navigation accuracies. The effects are displayed in Figures 3-3 and 3-4. Figure 3-3 shows that for the less than nominal cases the Earth sighting and initial ephemeris uncertainty have a nearly equal effect, but for the larger than nominal cases the initial ephemeris becomes less important. This means that if the initial ephemeris uncertainty is large compared to the Earth sighting accuracy, the sighting will drop

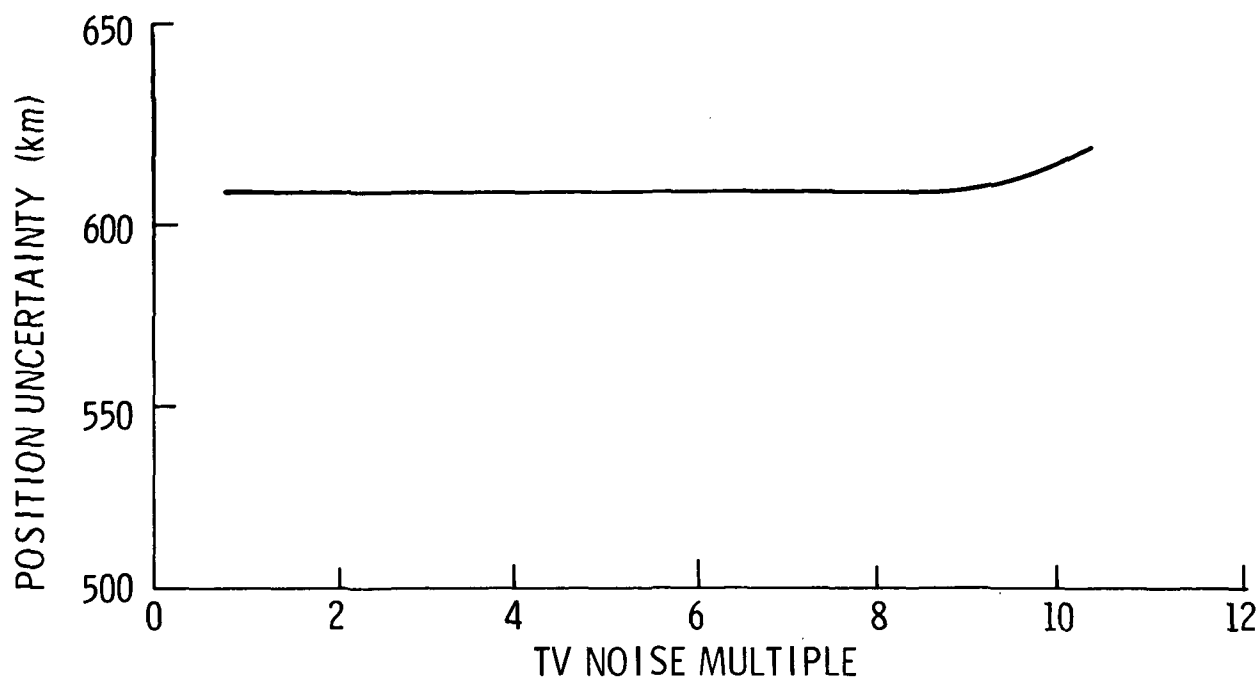


Figure 3-1. Effect of Scaling TV Noise Levels on Position Uncertainty.

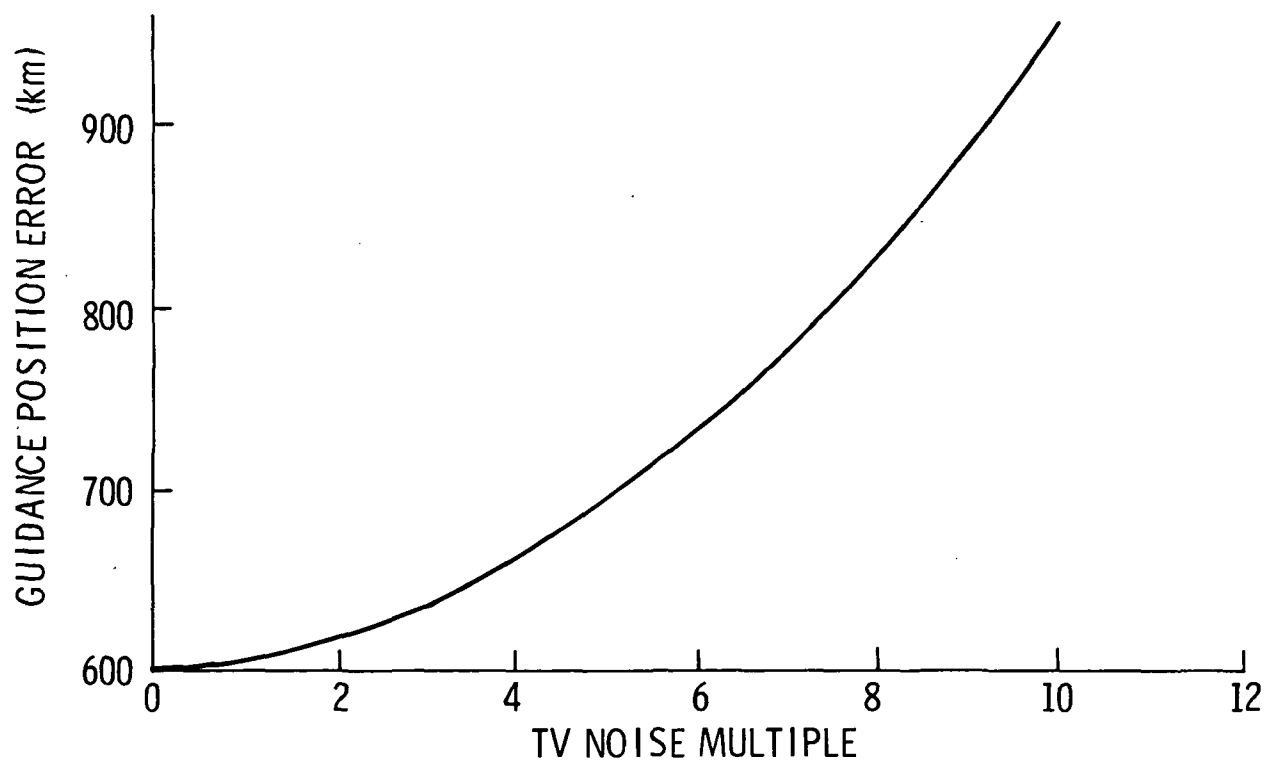


Figure 3-2. Effect of Scaling TV Noise Levels on Guidance Position Error.

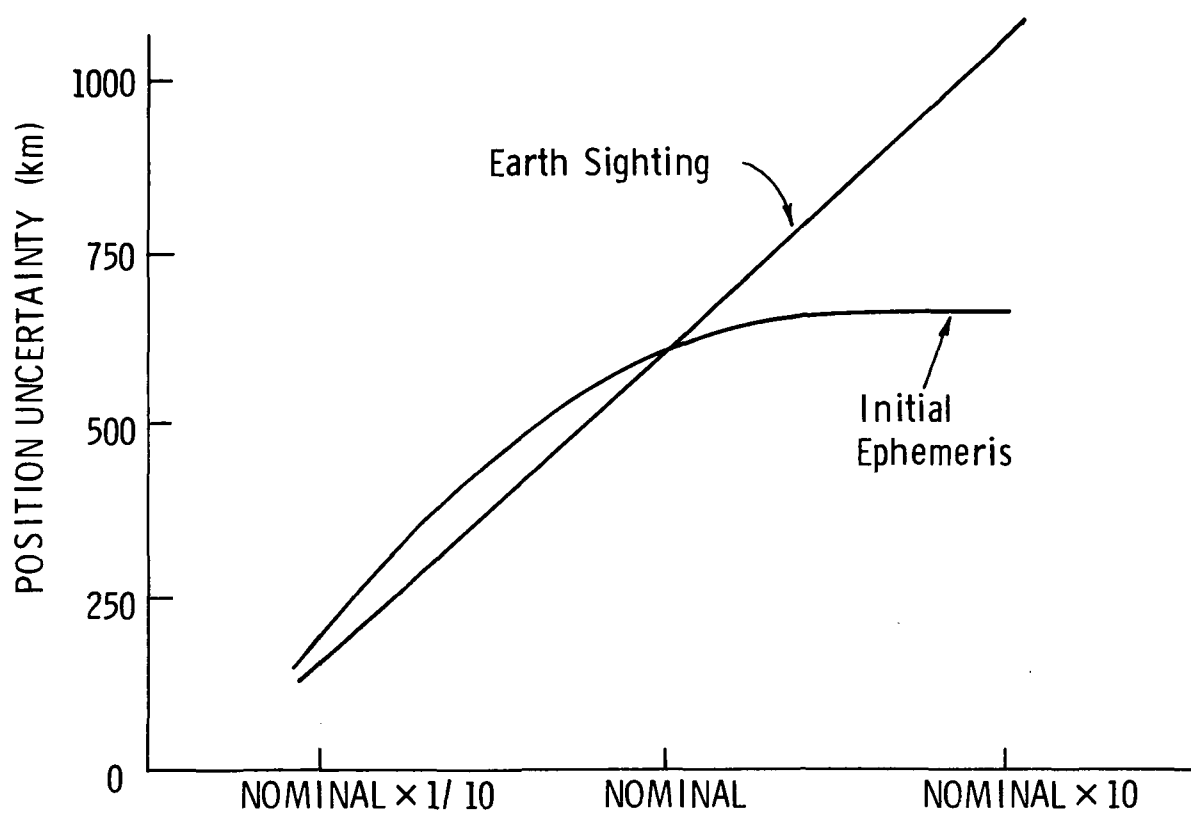


Figure 3-3. Effects of Earth Sighting and Initial Ephemeris Uncertainty on the Position Estimates.

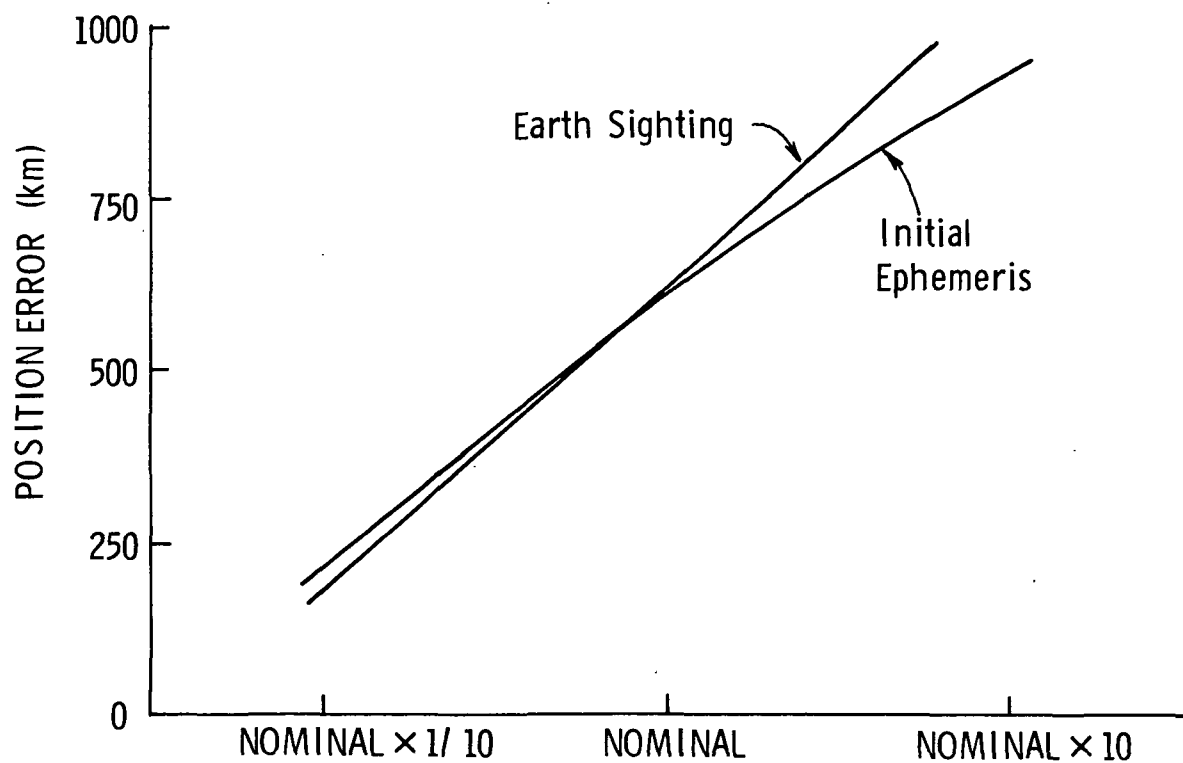


Figure 3-4. Effects of Earth Sighting and Initial Ephemeris Uncertainty on Guidance Position Error.

the ephemeris uncertainty down to the sighting accuracy level, and onboard navigation will reduce to some degree the other component thus lessening the importance of the initial ephemeris values. In the absence of Earth-based sightings, of course, the position uncertainty would be proportional to the ephemeris uncertainty, and would not level out when the Earth-based sighting accuracy becomes close to the ephemeris uncertainty. Figure 3-4 shows similar curves for the guidance position error. The initial ephemeris curve does not drop away from the Earth sighting curve as rapidly as in the position estimation case (Figure 3-3) because the guidance position error is determined by less onboard navigation information than the position estimation error, i.e., the final ΔV occurs before the final navigation measurements. Thus the Earth sighting reduces two components of the ephemeris leaving a third for onboard navigation to operate on, but if the guidance position error is determined by only a few onboard sightings, this third component will be little reduced, and the resulting guidance error will be proportionally larger.

The ephemeris estimation uncertainty is generally quite nearly equal to the position estimation with respect to the comet for these missions and may be slightly smaller or larger depending on the relative accuracy of the position estimation, and the Earth-based telescope and DSN measurement accuracy. Each measurement source (onboard, Earth optical, Earth Radio) measures a different quantity, and the details of the interaction of these measurements determine the exact relationship between position and ephemeris uncertainties. The position of the spacecraft with respect to Earth is known to within 181 km at E-19 days, and this value diminishes to 95 km by the time of mission termination. Since the position error with respect to the comet in many of the cases is close to 600 km, the lack of knowledge of spacecraft position relative to the comet limits reduction of comet ephemeris uncertainties. Position uncertainty with respect to the comet would have to be reduced to near the 95 km level before spacecraft position uncertainty with respect to Earth (determined by the DSN) would strongly influence the ephemeris uncertainty.

The first course correction for most of the listed cases took place at E-19 days, or 1 day after inclusion of the Earth-based sighting information. As can be seen from the results, Table 3-IV, the initial ΔV value is strongly dependent upon the initial ephemeris uncertainty and the time of application. Larger TV noise levels and variations in the TV turn-on time do not alter the first ΔV because they do not alter the initial position deviation. However, the initial position error is directly proportional to the assumed unsighted (from Earth) component value, and the ΔV is therefore proportional to this value.

The second ΔV is affected by both its timing and the Earth sighting and ephemeris values. Figure 3-5 shows the relationship between the time of the second ΔV and its magnitude. The magnitude is essentially hyperbolic because of the constant guidance position error that must be corrected in less time as the mission termination approaches.

This figure also displays the reduction in cross range or out of plane guidance error which can be expected in return for making the second midcourse correction later. The total guidance error, however, is still dominated by the along track component.

Figure 3-6 shows the effects of variations in Earth-based sighting and initial ephemeris uncertainty on the second ΔV . Both uncertainty sources are seen to have nearly the same effect. The ΔV is relatively constant between the nominal and 1/10 nominal cases because the residual position deviations, after the first ΔV , and after navigation measurements have been included, are not greatly different.

Total final ΔV 's for the cases examined range from 3.89 to 31.32 m/sec as is illustrated in Figure 3-7. The large initial ephemeris or unsighted component case requires the largest value. The next two values in order of decreasing ΔV are 14.4 and 9.70 m/sec which correspond to a "late" ΔV_2 in the first case and a "late" ΔV_1 in the second case. The 3 arcsecond Earth sighting case requires a total ΔV nearly equal to the late second ΔV case, and this case is followed by a cluster of values near the nominal value of 5.14 m/sec. A less than nominal ΔV is required in the 0.03 arcsecond Earth sighting case because the position uncertainty is

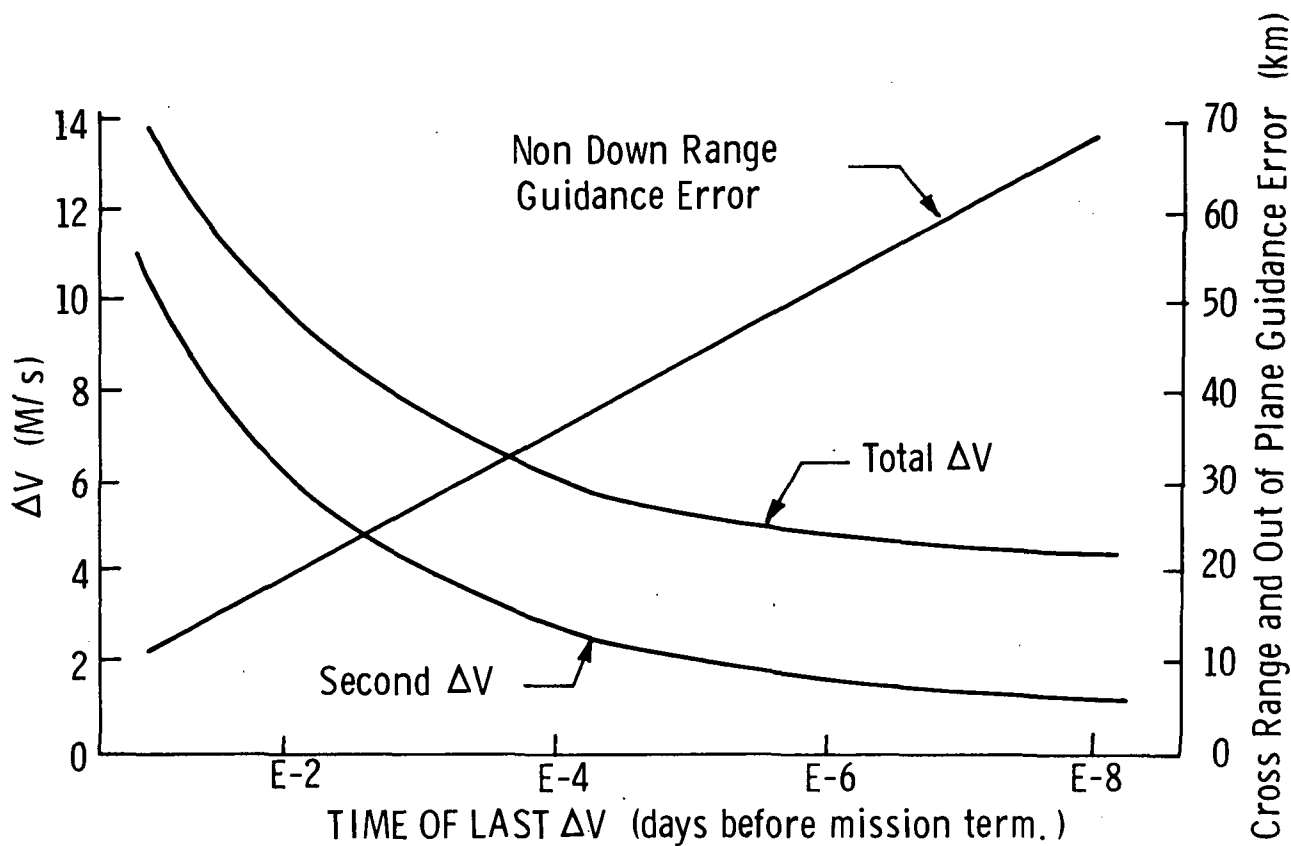


Figure 3-5. Relationship of Second ΔV to Time of Burn.

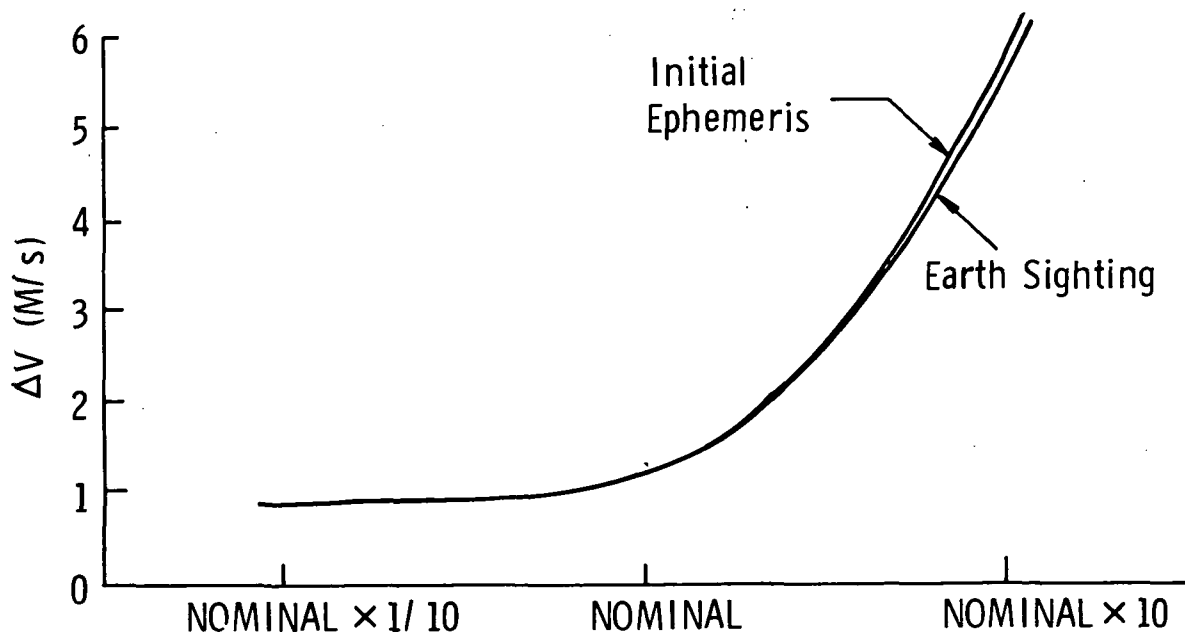


Figure 3-6. Effects of Earth Sighting Accuracy and Initial Ephemeris Uncertainty on the Second ΔV .

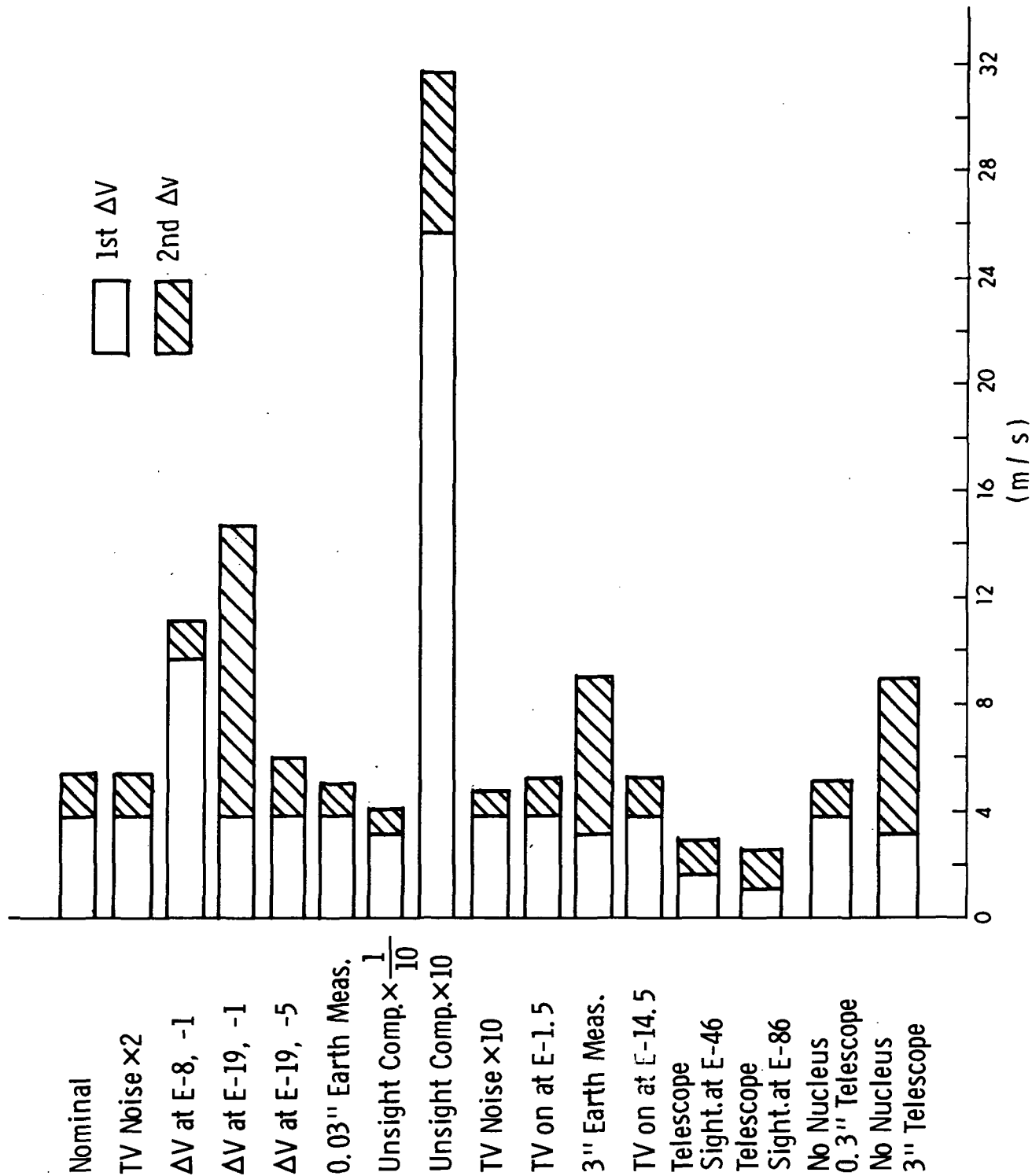


Fig. 3-7 Tempel II Midcourse Velocity Corrections

decreased before the first ΔV occurs. In this case the first ΔV is slightly larger, but the more accurate burn yields a much smaller position deviation at the time of the second ΔV , thus the second ΔV is reduced by an amount that is greater than the ΔV increase seen at ΔV_1 . Reduction of the unsighted component by a factor of ten directly reduces the initial position deviation which in turn drops the ΔV requirement to its lowest value of 3.89 m/sec.

Further reduction of the ΔV can be obtained by including the Earth-based optical sighting data at an earlier time. It can be seen from the ΔV list in Figure 3-7 that the total ΔV 's for earlier Earth-sighting input are lower than the nominal case, ranging down to 2.25 m/sec when the Earth sighting input occurs at E-100 days. For this mission, the earlier Earth-sighting date may be more realistic because of more unfavorable sun-Earth-comet angles near rendezvous (see Appendix H.1.2).

Table 3-V summarizes the nominal ΔV requirements for the Tempel 2 mission.

3.1.2 Tuttle-Giacobini-Kresak Mission

A summary of the guidance and navigation results is given in Tables 3-VI and 3-VII. Essentially the same set of parametric variations has been applied to this mission as to the Tempel 2 mission so that comparisons can be made. The nominal case for this mission has two significant differences from the Tempel 2 nominal case. First the turn-on time for the onboard TV sensor is at E-2 days as opposed to E-10 days for the Tempel 2 mission. Secondly, the initial ephemeris uncertainties are much larger (see Table 3-I and Chapter 2). These differences, plus a much smaller Earth-comet distance at the T-G-K encounter combine to make the results for the Tuttle-Giacobini-Kresak mission considerably different from those of the Tempel 2 mission.

At E-20 days the Earth-comet distance on the T-G-K mission is 1.2 A.U. as opposed to 2.7 A.U. at the same time in the Tempel 2 mission. Thus Earth-based sighting at a given accuracy level is twice as effective on the T-G-K mission. The position and ephemeris uncertainties are reduced accordingly with a nominal value of position uncertainty of 285 km compared to 608 km for the Tempel 2 mission.

TABLE 3-V

Tempel II ΔV Summary^{*, +}

Terminal ΔV s										
Time of ΔV_a (days)	ΔV_a Mag. (M/S)	Time of ΔV_b (days)	ΔV_b Mag. (M/S)	Time of ΔV_c (days)	ΔV_c Mag. (M/S)	Time of ΔV_1 (days)	ΔV_1 Mag. (M/S)	Time of ΔV_2 (days)	ΔV_2 Mag. (M/S)	
E-880.4 ¹	1.39	E-804.6 ²	5.93	E-727.6 ³	0.94	E-19	3.88	E-8	1.25	Nominal

*does not include injection error correction of 25.2 M/sec.

+see Table 3-IV for values of ΔV_1 and ΔV_2 related to other parametric variations¹Sphere of Influence entry²Jupiter Periplanet³Sphere of Influence egress

TABLE 3 - VI

Tuttle - Giacobini - Kresak Mission

Navigation Results

Case	Position Estimation Error (km)				Velocity Error	Ephem. Error
	DR	CR	OP	MAG	Est. (M/sec)	Est. (km)
Nominal	285	2.6	2.6	285	.164	287
0.03" Earth Measurement	61.8	2.6	2.6	61.9	.163	58.6
3" Earth Measurement	2751	2.6	2.6	2750	.166	2752
Unsignt. Comp. x 1/10	283	2.7	2.7	283	.033	286
Unsignt. Comp. x 10	288	2.9	2.9	288	.366	288
TV Noise x 2	285	5.3	5.3	285	.166	287
TV on at E-8	285	5.4	5.4	285	.164	287
TV Noise x 10	285	60.0	53.6	296	.166	298

TABLE 3 - VII

Tuttle - Giacobini - Kresak Mission

Guidance Results

Case	Guidance Position Error (km)			Time of		Time of		Total ΔV (M/sec)
	DR	CR	OP	MAG	ΔV_1 (days)	ΔV_1 (M/sec)	ΔV_2 (days)	ΔV_2 (M/sec)
Nominal	285	21.6	21.6	286	E-19.5	298	E-1.5	79.5
0.03" Earth Measurement	63.9	21.0	21.6	70.7	E-19.5	298	E-1.5	79.4
3" Earth Measurement	2751	21.7	21.7	2752	E-19.5	298	E-1.5	81.7
Unsignt. Comp. x 1/10	283	20.8	20.8	285	E-19.5	30.0	E-1.5	8.28
Unsignt. Comp. x 10	291	22.5	62.5	304	E-19.5	2979	E-1.5	77.8
TV Noise x 2	285	41.2	41.6	291	E-19.5	298	E-1.5	79.4
TV on at E-8	286	24.3	24.3	287	E-19.5	298	E-1.5	79.4
TV Noise x 10	321	230	406	566	E-19.5	298	E-1.5	79.4

Because of the much larger initial ephemeris uncertainty associated with T-G-K, the 3 arcsecond Earth-based sighting error leaves unreduced, a much larger uncertainty component along the onboard sensor line of sight, thus increasing the position uncertainty proportionately. The 3 arcsecond related position uncertainty is 2750 km on the T-G-K mission compared to 285 km on the Tempel 2 mission for the nominal cases. The 0.03 arcsecond Earth sighting case reduces position uncertainty to its lowest value of 61.9 km.

A plot of the temporal variations of position uncertainties for the nominal cases of the two comet missions is presented in Fig. 3-8. The plots, which give the extrapolated terminal position estimation error versus time to encounter, illustrate an essential feature of the onboard navigation, namely, that the instrument measurement uncertainty is much smaller than the uncertainties associated with the ephemeris and Earth-based measurements. Thus in a single measurement it effectively reduces the error down to the residual level dictated by Earth-based optical sighting accuracy. The Tempel 2 curve starts lower because the initial ephemeris uncertainty values are smaller, and gets its main reduction when the onboard system is turned on at 10 days. The Tuttle-Giacobini-Kresak curve shows a drop to a lower final uncertainty because of the more effective Earth-based sighting at the 0.3 arcsecond accuracy level. Note that the first onboard sighting is made later on the T-G-K mission.

Guidance position error is affected somewhat by the TV noise level and more strongly by the Earth sighting accuracy. Figure 3-9 shows the effect of increasing TV noise level. At lower TV noise levels the line of sight, uncorrectable position error dominates, and the noise has little effect. When the noise level reaches several times the nominal level the ΔV 's are less able to reduce the position error normal to the line of sight, and these components begin to make a significant contribution to the position error magnitude. Figure 3-10 shows the extreme importance of Earth-based optical sightings to the reduction of guidance position error. The position error is dominated by the spacecraft-comet line of sight component, and this component cannot be reduced by a ΔV unless there is an Earth sighting

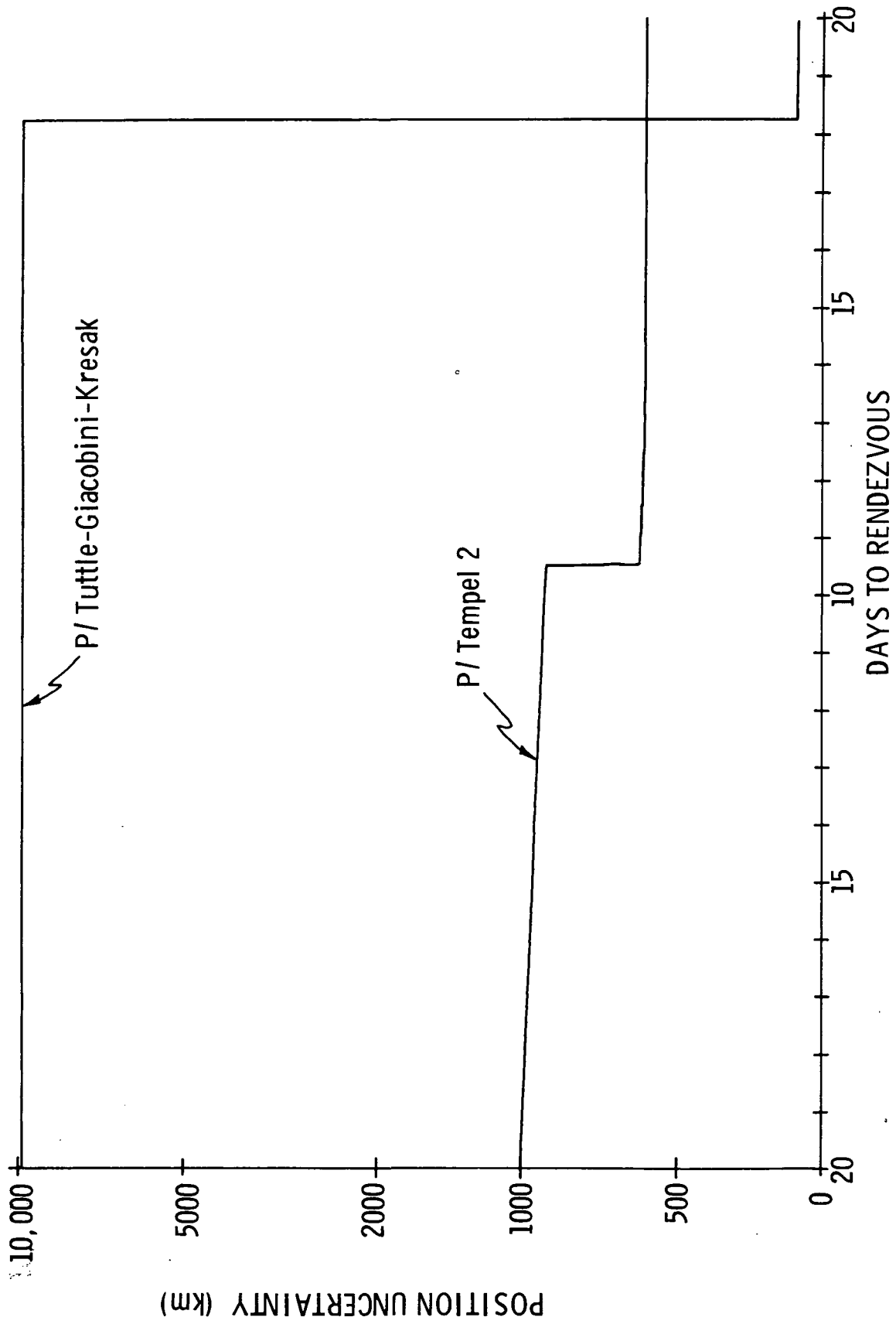


Figure 3-8 Temporal Behavior of Position Uncertainty with Respect to Comet.

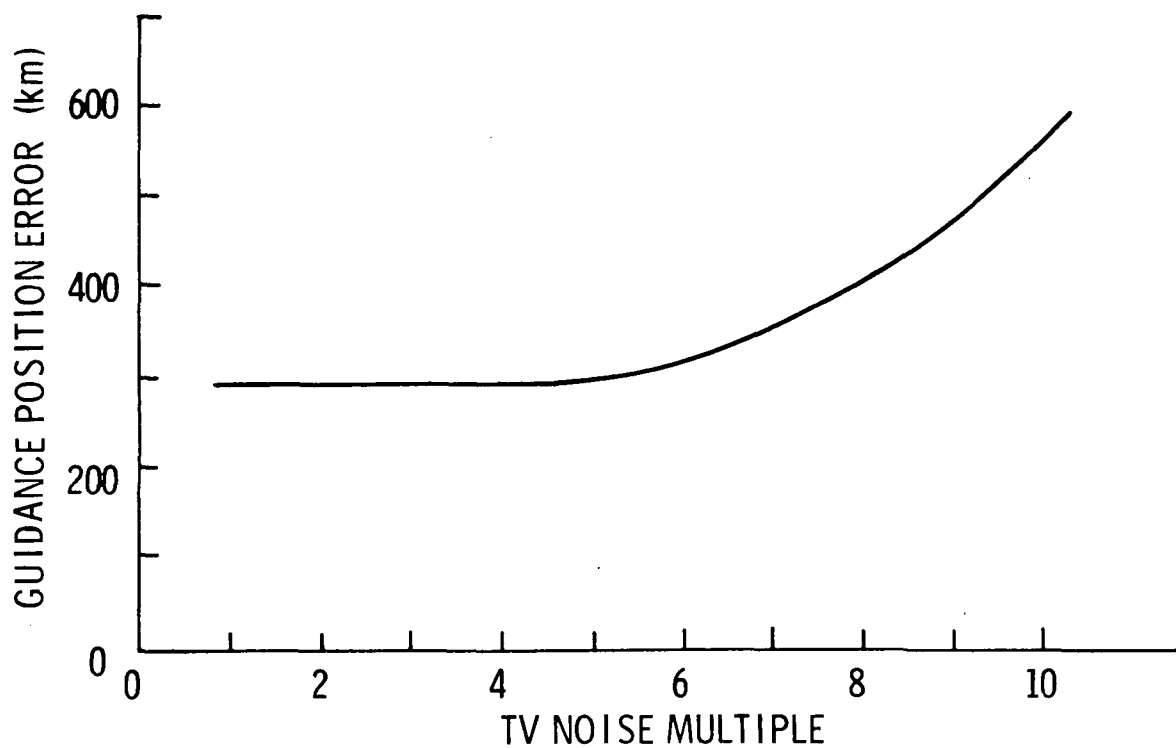


Figure 3-9. Effects of TV Noise on Guidance Position Error.

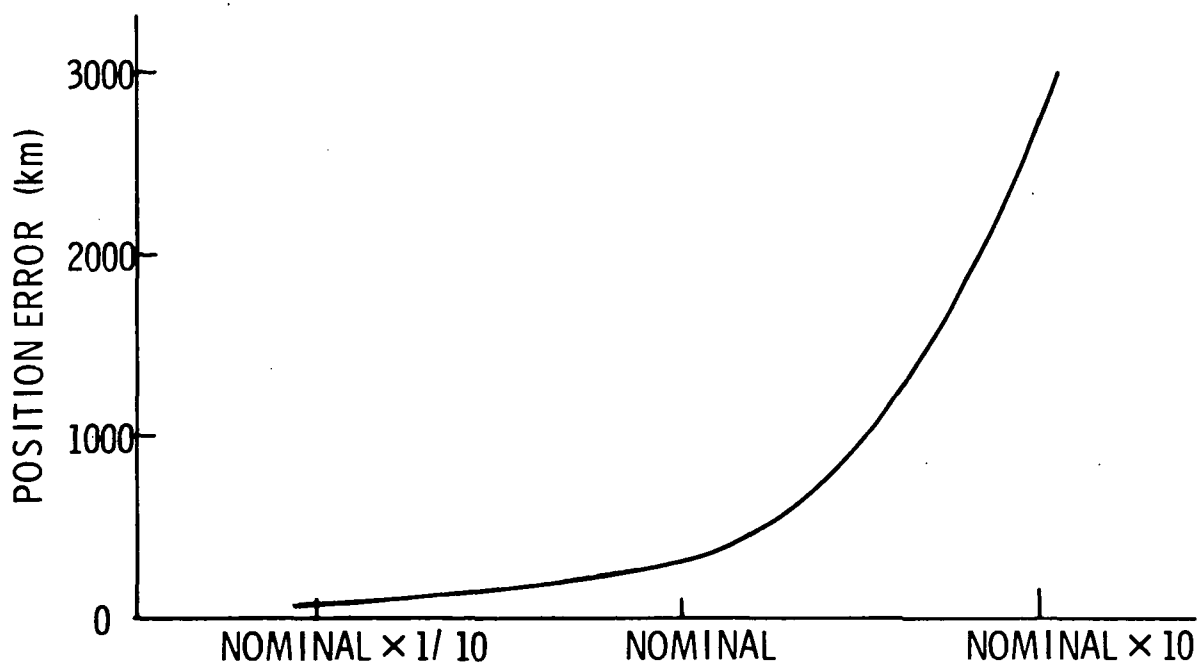


Figure 3-10. Effects of Earth-Based Optical Sightings on Guidance Position Error.

that specifies the correction. For this mission the line of sight position error component could grow, in the absence of Earth-based sightings, as large as the initial ephemeris uncertainty which is 500,000 km.

Velocity corrections on the T-G-K mission are much larger than the Tempel 2 mission values because of the larger initial ephemeris uncertainty. It is therefore important for these missions to perform a priori ephemeris studies using Earth-based sightings during earlier orbits of the comet. The first ΔV for the T-G-K mission is approximately 300 m/sec which is nearly two orders of magnitude larger than the Tempel 2 mission value. A ΔV of this size becomes appreciable in comparison to the large terminal ΔV of 5.7 km/sec needed to effect rendezvous.

The second ΔV on the T-G-K mission is also considerably larger than that incurred on the Tempel 2 mission, but this is partly attributable to the later second ΔV on the T-G-K mission. The nominal T-G-K second burn is at E-1.5 days compared to E-8 for the Tempel 2 mission. Nominal ΔV requirements for the T-G-K mission are listed in Table 3-VIII.

3.2 JUPITER ENTRY MISSIONS

Most of the nominal input conditions of these missions are defined in Chapter 2. In addition there are some nominal conditions that are specific to the entry missions, for example, the entry angle, velocity and altitude are listed in Chapter 1. Onboard navigation measurements for the 800 day mission are taken starting at the range of 1 A.U. from Jupiter and continuing at the following frequencies: one measurement every 10 days for the first 180 days; one measurement every 2 days for the next 68 days; one measurement every $1/2$ day for the next day; one measurement every $1/4$ day for the next two days; one measurement every $1/8$ day for the next half day, and finally a measurement each hour for the final half day. The total number of measurements is 75. Measurements on the 1200 day mission also start at 1 A.U. from Jupiter. The frequency begins at one measurement per 10 days for 240 days, then increases to one per 2 days for 76 days. The next day has three measurements, and then the rate increases to 4/day for two days. The first half of the last day has a 2/hour measurement rate which increases to 1/hour for the last half day. The total measurement number is 86.

TABLE 3- VIII

T-G-K ΔV Summary^{*, +}

Nominal Case

Time of ΔV_a (days)	ΔV_a Mag. (M/S)	Time of ΔV_b (days)	ΔV_b Mag. (M/S)	Time of ΔV_c (days)	ΔV_c Mag. (M/S)	Time of ΔV_1 (days)	ΔV_1 Mag. (M/S)	Time of ΔV_2 (days)	ΔV_2 Mag. (M/S)
E-864.1 ¹	1.29	E-782.5 ²	0.12	E-700.9 ³	0.54	E-19.5	298	E-1.5	79.5

Nominal

* does not include injection error correction of 25.8 M/sec,

+ see Table 3- VII for values of ΔV_1 and ΔV_2 related to other parametric variations¹Sphere of Influence entry²Jupiter Periplanet³Sphere of Influence egress

Nominal course corrections are scheduled at E-70.3 days, and E-3 days on the 800 day mission, and E-78.6, and E-2 on the 1200 day mission. Each mission also has a post injection correction at 10 days after launch. Nominal guidance and navigation parameters for the entry missions are summarized in Table IX.

Most of the interesting simulation results relate to the entry conditions and the projected guidance errors. However, the error values at the sphere of influence of Jupiter are also of interest because they can propagate to entry.

3.2.1 800 Day Entry Mission Results

Since no course corrections are made between the initial correction at 10 days into the mission, and arrival at the Jupiter sphere of influence, the guidance errors are dominated by the conditions that exist at the initial correction. Lack of knowledge of the spacecraft state relative to Jupiter at this early stage, and accelerometer and thrust cut-off uncertainties, are the main contributors to these errors. Therefore, variations in the onboard navigation measurements and the DSN characteristics have little effect on the results. Only the ephemeris uncertainties noticeably affect the guidance errors since they directly influence knowledge of the vehicle state relative to Jupiter. Thus the results for all the various cases, excluding those with initial ephemeris variation, are the same. The guidance position error with nominal ephemeris uncertainty at the Jupiter sphere of influence is 7150 km. The guidance velocity error is 1.29 m/sec at this point. The effects of ephemeris variations are small. When the nominal ephemeris uncertainty is reduced by a factor of 3 the guidance error magnitude drops by only 0.3%. Increasing the initial ephemeris error by a factor of 3 increases the guidance error magnitude by only 2.4% to 7320 km. The magnitude of the initial velocity correction is 25.2 m/sec.

Estimation errors at the Jupiter sphere of influence taken with respect to Jupiter, show moderate variations among the navigation cases. Table 3-X lists the simulated estimation error results.

TABLE 3 - IX
Nominal Jupiter Entry
Mission Parameters

Quantity	800 Day Mission Value	1200 Day Mission Value
Course Corrections	E-790, 70.3, 3	E-1190, 78.6, 2
OB Turn On	1 A. U.	1 A. U.
OB Inst. Acc.	Bias = 5", WN = 1"	Bias = 5", WN = 1"
Entry Angle	15°	15°
Entry Velocity	47.1 km/sec	47.2 km/sec
Entry Altitude	71,640 km	71,640 km
DSN Tracking	Full Time	Full Time

TABLE 3 - X
Jupiter 800 Day Entry Mission
Estimation Errors
(At Jupiter Sphere of Influence)

Case	Position Uncertainty (km)	Velocity Uncertainty (M/sec)	Ephemeris Uncertainty (km)			
			X	Y	Z	Mag.
Nominal DSN Only	582.0	0.000976	119.0	400.0	404.0	581.0
DSN Only 8Hr/2Wk	584.0	0.00152	122.0	400.0	404.0	581.0
Nominal	439.0	0.000976	112.0	331.0	263.0	437.0
OB 1-.5	269.0	0.000976	104.0	212.0	122.0	266.0
OB 5-.5	515.0	0.000976	118.0	392.0	310.0	514.0
OB 10-.5	558.0	0.000976	119.0	400.0	369.0	557.0
OB 1-1	278.0	0.000976	104.0	214.0	138.0	275.0
OB 1-1 $\mu_{\text{sun}} = 0$	278.0	0.000897	104.0	214.0	138.0	275.0
OB 5-5	521.0	0.000976	119.0	398.0	311.0	519.0
OB 10-5	558.0	0.000976	119.0	400.0	369.0	557.0
Nominal, Ephemeris x 1/3	188.0	0.000976	40.0	133.0	121.0	184.0
Nominal Ephemeris x 3	749.0	0.000976	308.0	581.0	356.0	748.0

Two cases are exhibited in the table which show the effect of a variation in the solar mass uncertainty. The zero uncertainty case ($\mu_{\text{sun}} = 0$) differs from the nominal case by about 9% in the magnitude of the velocity uncertainty.

Velocity uncertainty is also affected by a reduction of DSN tracking from full time to one 8 hr. pass each two weeks, and increases by 56% to 1.52×10^{-3} m/sec.

Altering the initial ephemeris uncertainty has a strong effect on the position uncertainty with respect to Jupiter at the sphere of influence. Figure 3-11 shows this effect. Since position error has ephemeris error added to it at the sphere of influence, and because the position uncertainty in heliocentric coordinates is initially smaller than the ephemeris uncertainty, the position uncertainty curve is nearly coincident with that drawn for the ephemeris in Fig. 3-11.

Variations in ephemeris uncertainty with onboard navigation noise characteristics are shown in Fig. 3-12. Ephemeris uncertainty values are seen to be little reduced from the DSN-only case unless both white noise and bias errors are initially small. At a bias level of 0.5 arcseconds and a white noise of 1 arcsecond the ephemeris uncertainty is reduced roughly in half. Fig. 3-12 also shows that at white noise levels above 5 arcseconds a bias reduction has no effect.

Terminal estimation errors for the 800 day entry mission are listed in Table 3-XI. Once again, if the DSN is used only 8 hr/2 wk until the last four weeks when it is employed full time, there is negligible degradation of the estimates from the full time tracking values.

Shutting off DSN on a DSN-only mission at various intervals before entry, strongly affects every estimation error. This early shutdown is related to the type of entry mission considered. For example, on a deflected bus mission, the earlier the bus is deflected, the lower the deflection ΔV and the less navigational information available for the final probe midcourse correction. Figure 3-13 shows the effect of early DSN shutdown on position and ephemeris errors. Even a cutoff at two days out results in a hundred-fold

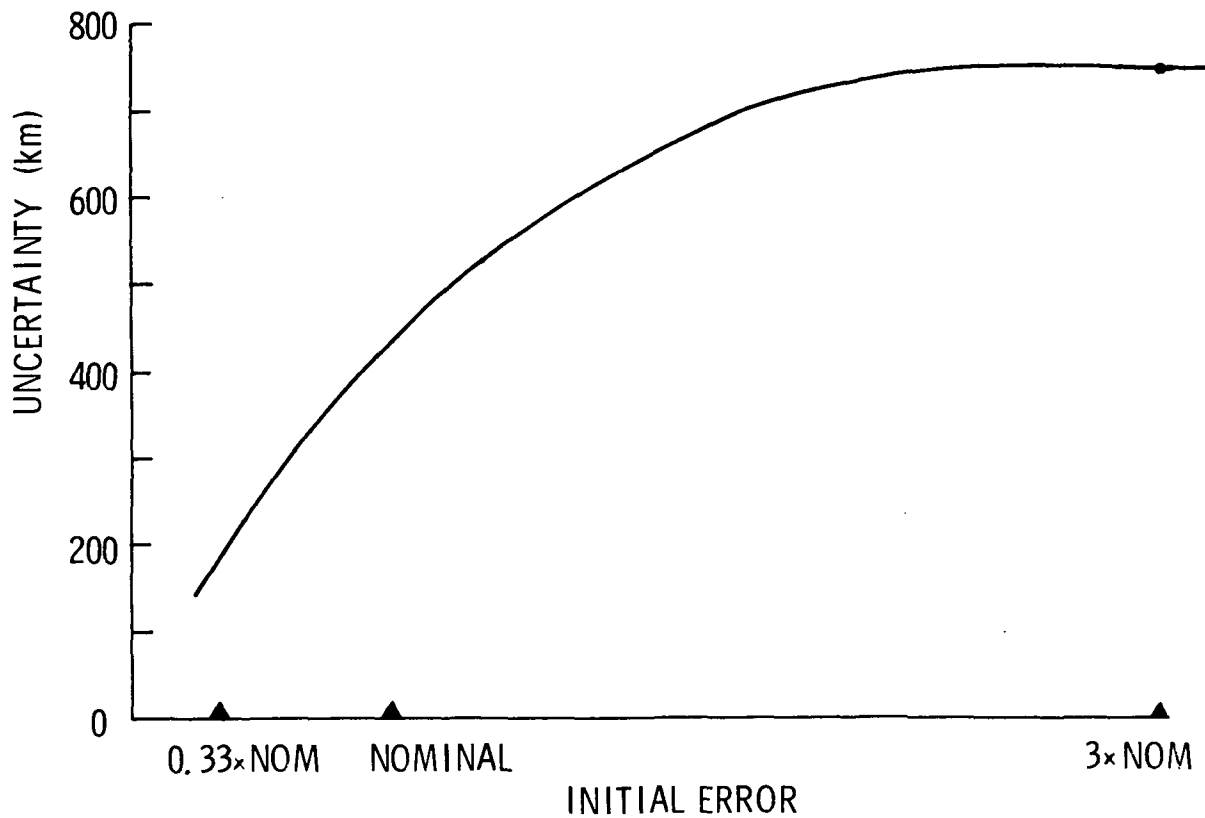


Figure 3-11. Effect of Initial Ephemeris Uncertainty on Sphere of Influence Ephemeris Uncertainty.

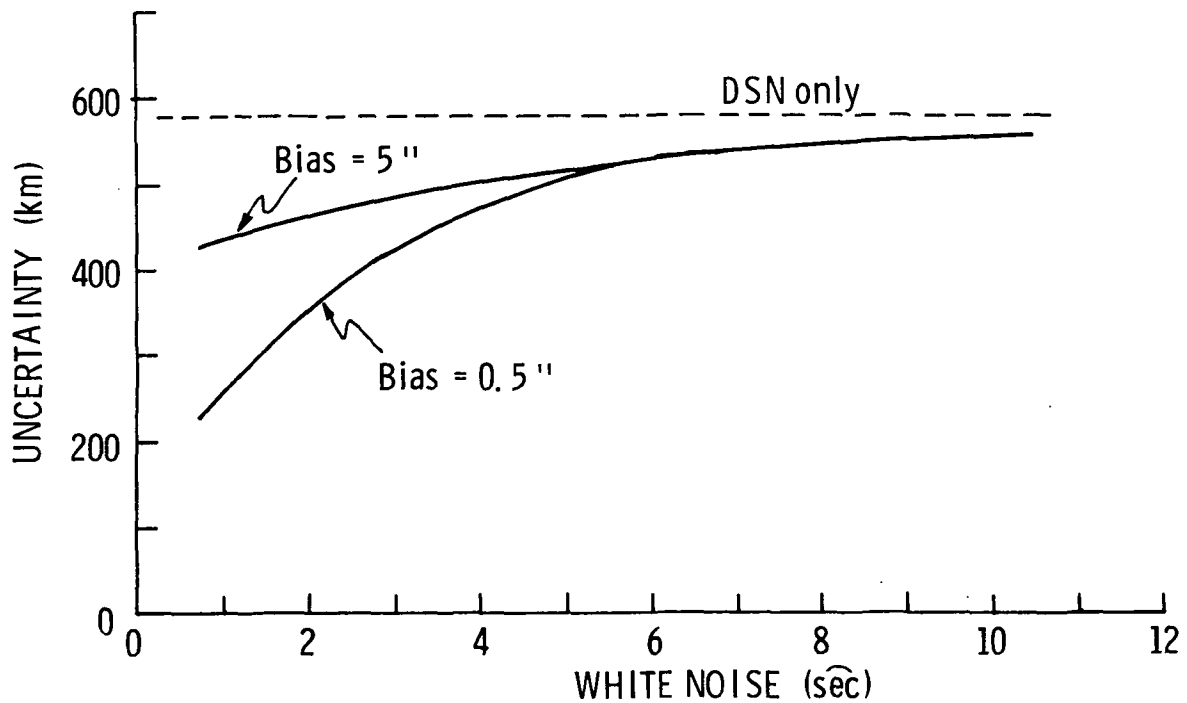


Figure 3-12. Sphere of Influence Ephemeris Uncertainty versus Onboard Navigation White Noise.

TABLE 3 - XI

Jupiter 800 Day Entry Mission.

Terminal Estimation Errors

Case	Down Range	Cross Range	Out of Plane	Mag.	Velocity Mag. (m/sec)	Ephemeris (km)			Mag.	Radius (km)	Entry Angle (deg)
						X	Y	Z			
Nominal DSN Only	0.96	0.14	2.88	3.04	3.26	31.3	24.1	38.8	55.4	33.3	0.000374
DSN Only 8Hr/2wk	0.96	0.14	2.89	3.05	3.27	44.5	33.9	43.9	71.2	33.3	0.000375
DSN Only Off at E-40	2292.0	61.1	32.2	2200.0	906.0	98.8	386.0	387.0	555.0	33.3	0.865
DSN Only Off at E-20	1634.0	42.8	30.7	1630.0	674.0	98.8	281.0	387.0	486.0	33.3	0.642
DSN Only Off at E-2	471.0	19.2	30.7	472.0	198.0	84.1	50.1	385.0	398.0	33.3	0.181
Nominal	0.557	.131	0.862	1.03	0.996	31.2	23.2	18.3	42.9	4.70	0.000218
Ephemeris x 3	0.561	.140	0.842	1.02	0.997	32.3	23.4	18.4	43.9	4.70	0.000219
Ephemeris x 1/3	0.550	0.128	0.773	0.958	0.899	24.8	22.0	17.5	37.5	5.07	0.000217
OB, 1-.5	0.530	0.150	0.542	0.769	0.649	31.1	23.1	16.2	42.0	2.58	0.000209
OB, 5-.5	0.573	0.132	0.956	1.12	1.10	31.2	23.2	19.0	43.2	4.63	0.000225
OB, 10-.5	0.637	0.133	1.39	1.53	1.58	31.2	23.3	22.7	45.0	6.90	0.000250
OB, 1-1	0.532	0.129	0.586	0.802	0.696	31.1	23.1	16.5	42.1	2.59	0.000210
OB, 5-5	0.586	0.132	1.04	1.20	1.20	31.2	23.2	19.7	43.6	6.51	0.000230
OB, 10-5	0.631	0.132	1.35	1.49	1.53	31.2	23.3	22.3	45.0	9.01	0.000248

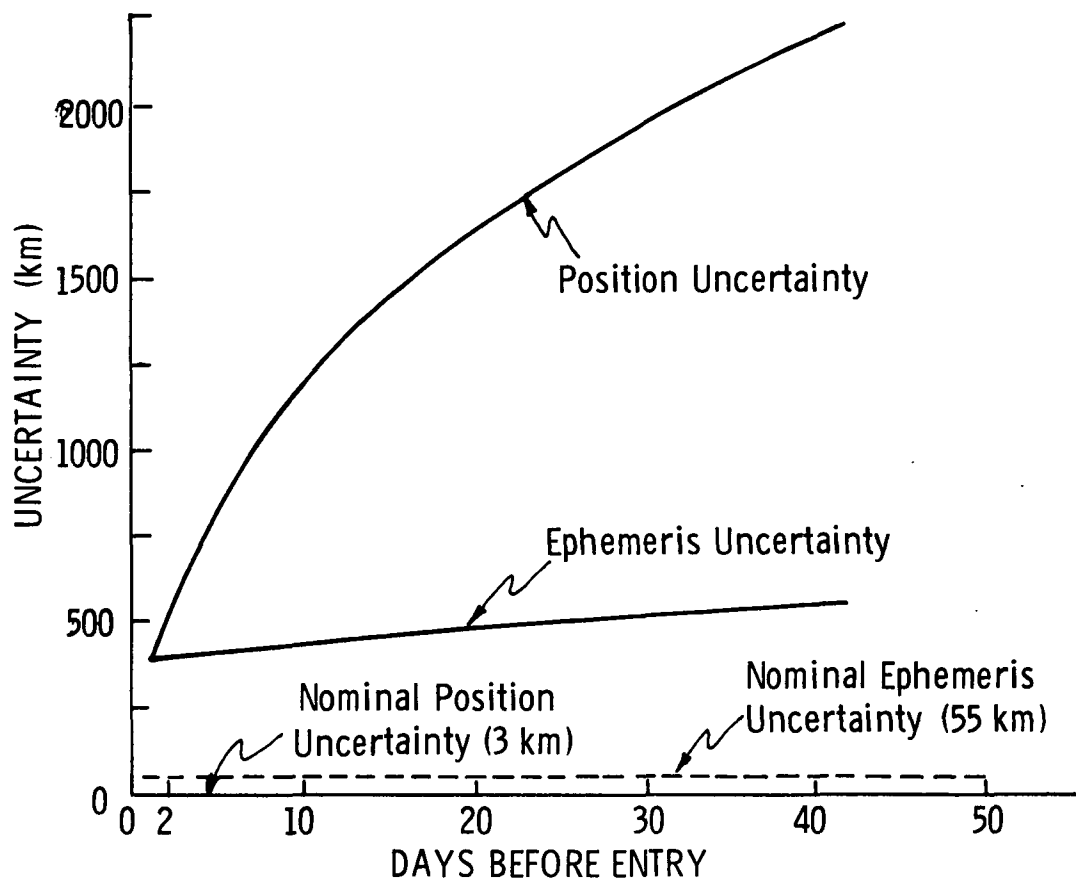


Figure 3-13. Effects of Early DSN Shutdown on Terminal Position and Ephemeris Estimates.

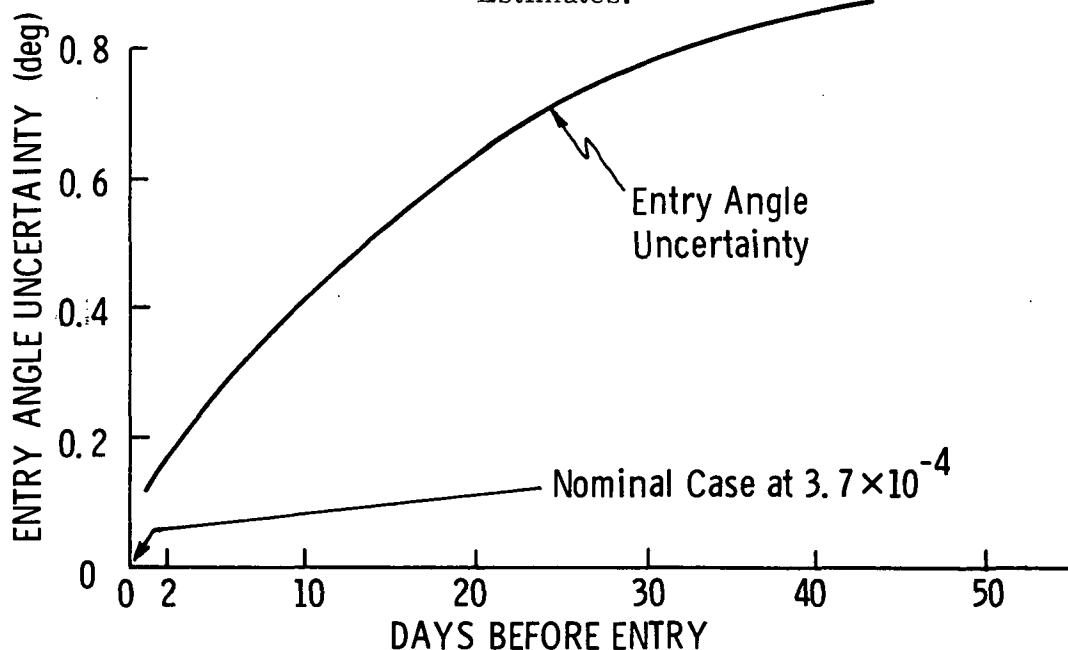


Figure 3-14. Effects of Early DSN Shutdown on Terminal Entry Angle Estimates.

increase in position uncertainty. Ephemeris errors are relatively unaffected over the considered cutoff time range. It is interesting to note that if the DSN-only case is allowed to run to termination, the out-of-plane component of position uncertainty is largest. This is to be contrasted with a down-range dominant error for the early shutdown cases. Figure 3-14 shows the effects of early shutdown on the entry angle estimation error.

Terminal estimation uncertainties associated with the onboard noise characteristics are displayed in Figures 3-15 through 3-18. Figure 3-15 shows that the main navigation contribution made by the onboard system to terminal error reduction is in the out-of-plane component. Figure 3-16 shows that a bias reduction from 5 arcseconds to 0.5 arcseconds is unimportant unless the white noise level is also reduced. Figure 3-17 shows that onboard navigation makes little contribution to terminal ephemeris uncertainty reduction. Figure 3-18 shows the contribution the onboard system can make to radius estimation error reduction. This could be of primary importance only if entry angles shallower than 15° were contemplated.

Guidance errors are of particular interest on these missions because they bound the entry condition errors which are important for entry vehicle design. Table 3-XII summarizes the guidance error results for the 800 day mission. Reduced DSN tracking frequency in the earlier part of the mission is again seen to be unimportant. Early DSN turn-off in the DSN only case has a strong effect on terminal guidance. The position error is increased significantly along the path, for example the E-40 turn-off case has an along-the-path error of 2198 km compared to the nominal value of 679 km. The along-the-path error is not particularly important by itself, but it is important in the sense that it contributes to the entry attitude error. In fact, the entry attitude error is seen to be directly proportional to the along-the-path position error. Note that the guidance errors are smaller in the E-2 case than in the nominal case.

It is instructive to look at the various navigation combinations to see how they relatively affect the guidance errors. This is done in Fig. 3-19 where the cases are ordered in terms of their associated entry angle error.

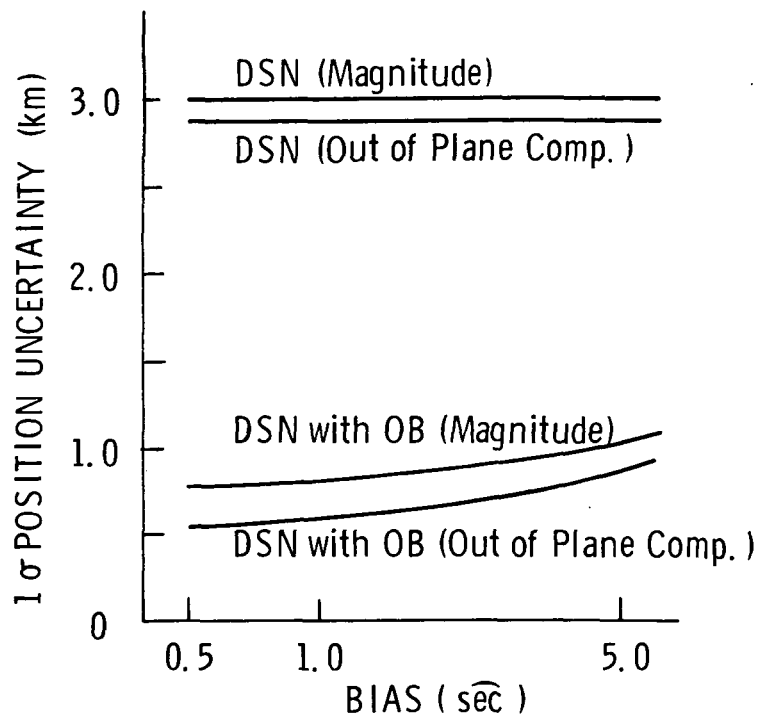


Fig. 3-15 Terminal Position Uncertainty vs. Onboard Photometer Bias Error

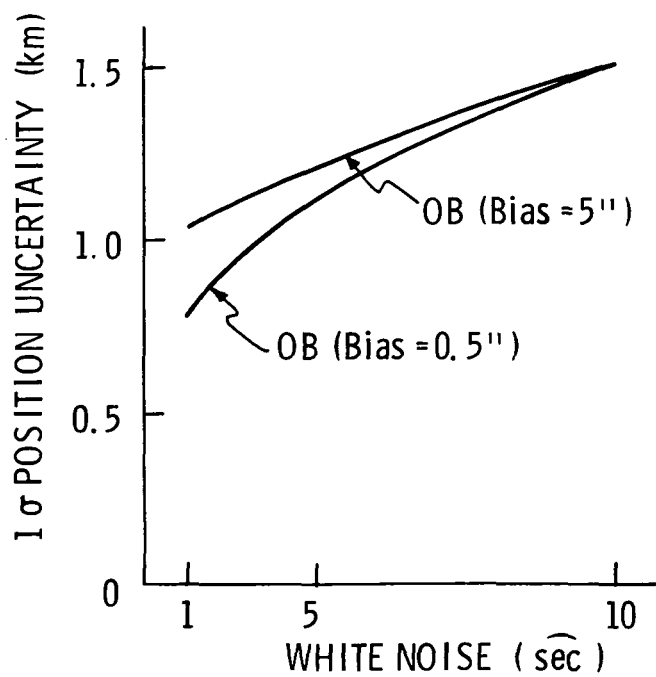


Fig. 3-16 Terminal Position Uncertainty vs. Onboard Inst. White Noise

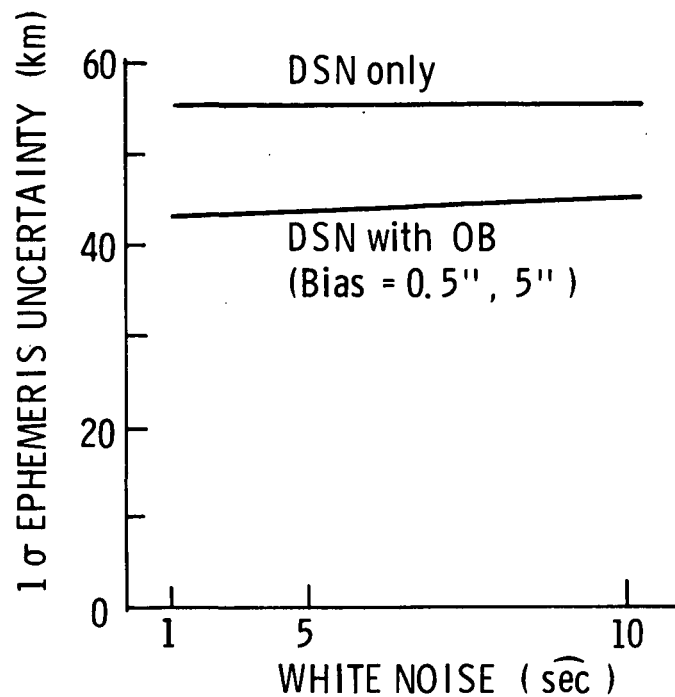


Fig. 3-17 Terminal Ephemeris Uncertainty vs. Onboard Photometer White Noise

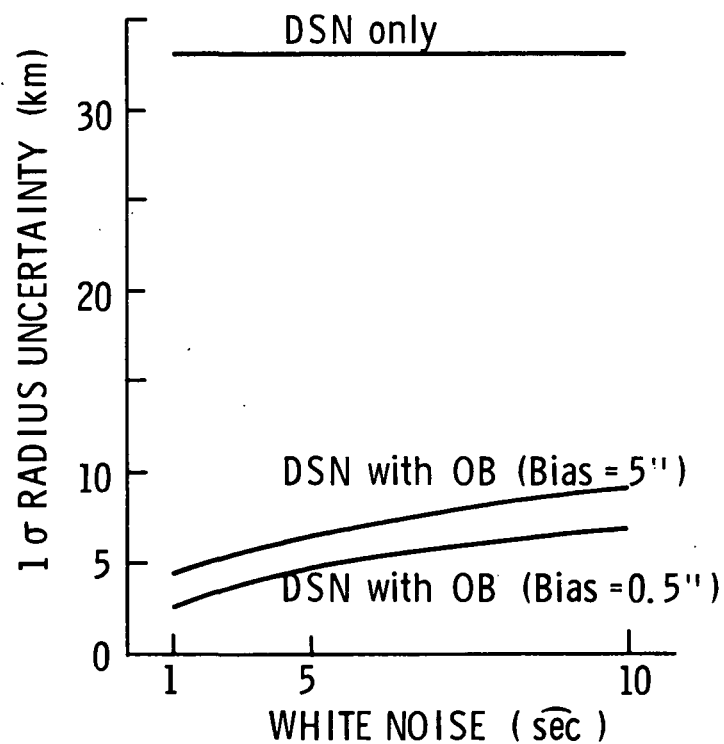


Fig. 3-18 Terminal Radius Uncertainty vs. Onboard Photometer White Noise

TABLE 3 - XII

Jupiter 800 Day Entry Mission
Terminal Guidance Errors + ΔV s

	Position Error (km)				Entry Angle Error (deg)	Entry Altitude Error (km)	Velocity Error Mag. (m/sec)	Time of ΔV_1 days from entry	ΔV_1 Mag. (m/sec)	Time of ΔV_2 days from entry	ΔV_2 Mag. (m/sec)
	Down Range	Cross Range	Out of Plane	Mag.							
Nominal DSN Only	679.0	23.5	31.9	681.0	0.263	232.0	284.0	70.3	1.72	3.0	2.94
DSN Only 8Hr/2Wk	692.0	25.1	32.1	693.0	0.267	232.0	289.0	70.3	1.72	2.8	3.28
DSN Only Off at E-40	2198.0	55.8	31.0	2293.0	0.902	556.0	945.0	70.3	1.73	38.3	0.090
DSN Only Off at E-20	1056.0	44.9	31.2	1657.0	0.651	405.0	684.0	70.3	1.73	18.0	0.277
DSN Only Off at E-2	540.0	20.5	30.7	541.0	0.208	158.0	227.0	70.3	1.73	2.3	4.02
Nominal	357.0	10.7	10.0	357.0	0.139	89.2	148.0	70.3	1.72	3.0	2.71
ΔV at E-36 Hr	188.0	7.26	4.20	188.0	0.075	53.7	77.3	70.3	1.72	1.5	6.47
ΔV at E-6 Hr	27.5	1.80	2.84	27.7	0.040	32.8	451.0	70.3	1.73	0.4	44.9
Ephemeris $\times 3$	353.0	11.3	6.79	353.0	0.153	93.8	145.0	70.3	1.74	3.0	5.61
Ephemeris $\times 1/3$	240.0	8.01	6.89	241.0	0.0934	69.7	99.8	70.3	1.73	2.8	1.84
OB, 1-.5	262.0	6.54	2.12	262.0	0.102	73.5	108.0	70.3	1.73	3.0	2.23
OB, 5-.5	424.0	13.6	16.4	424.0	0.164	112.0	177.0	70.3	1.73	3.0	2.97
OB, 10-.5	541.0	18.4	24.2	542.0	0.209	153.0	226.0	70.3	1.73	3.0	2.99
OB, 10-5	543.0	18.4	24.5	544.0	0.210	154.0	227.0	70.3	1.73	3.0	2.99
OB, 5-5	435.0	14.1	17.6	436.0	0.169	117.0	181.0	70.3	1.73	3.0	3.00
OB, 1-1	266.0	6.76	2.70	266.0	0.104	74.3	110.0	70.3	1.73	3.0	2.24

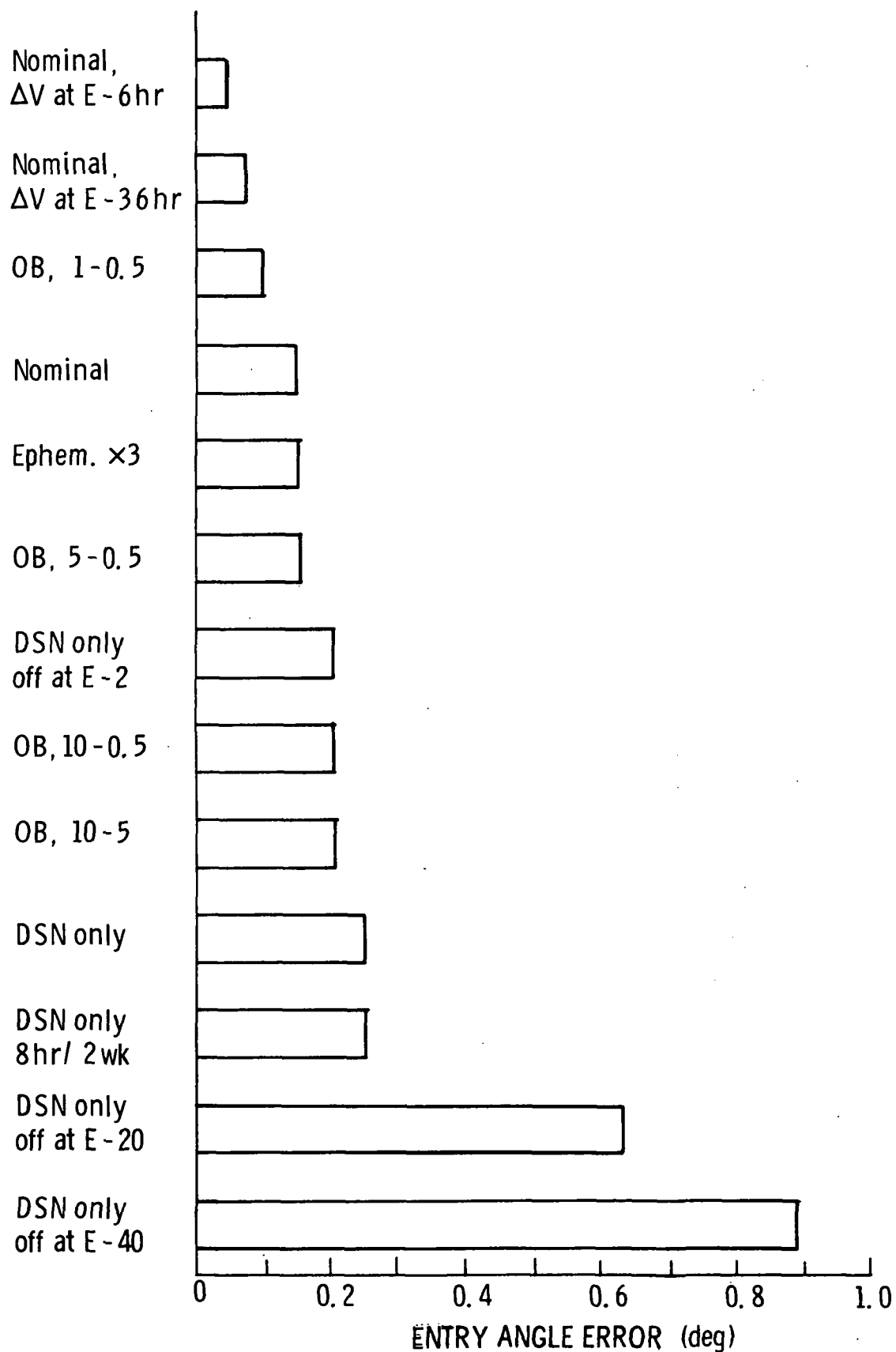


Fig. 3-19 Listing of Cases in Order of Increasing Entry Angle Error.

It is clear from the figure that the best way to reduce entry angle error is to make the last course correction as late as possible. However, Table 3-XII shows a ΔV for the E-6 hr. case of 44.9 m/sec which is a factor of 16 larger than the nominal final ΔV . This factor of 15 increase in ΔV buys a six-fold decrease in the entry angle error. For a final ΔV at E-36 hr a doubling of the nominal ΔV reduces the entry angle error by a factor of 3. The large, early DSN turn-off cases are seen to result in proportionately large angle errors although the ΔV 's are reduced. The E-2 DSN turn-off case is not strictly comparable to the nominal because an extra day's information is included in the final ΔV determination. The final nominal ΔV is at E-3 days. Figure 3-20 shows the relationship between the time of the last ΔV and the entry angle error. The error can be seen to decrease steadily until the burn is made at the third day before encountered, and then to decrease rapidly. The figure also shows the ΔV magnitude relationship to the time of implementation. If entry angle error reduction and ΔV minimization were weighted by relative importance, Figure 3-20 would show the optimal burn time.

Figure 3-21 shows the relationship between the entry attitude error and the onboard navigation sensor noise characteristics. The onboard system is capable of reducing the attitude error considerably although this reduction is probably not significant unless shallower entry angles are used. The DSN reduction of altitude errors is limited by the initial assumptions concerning the radius uncertainty because DSN gains no additional radius information by measurement. Therefore the relative utility of onboard navigation for reducing entry guidance errors is proportional to the initial assumptions about planet radii, and onboard navigation becomes more important as the entry angles grow smaller.

Table 3-XII lists guidance velocity error magnitudes only. It is interesting to note that this error is mainly along the cross range direction which is related to the larger nonlinear acceleration associated with this component.

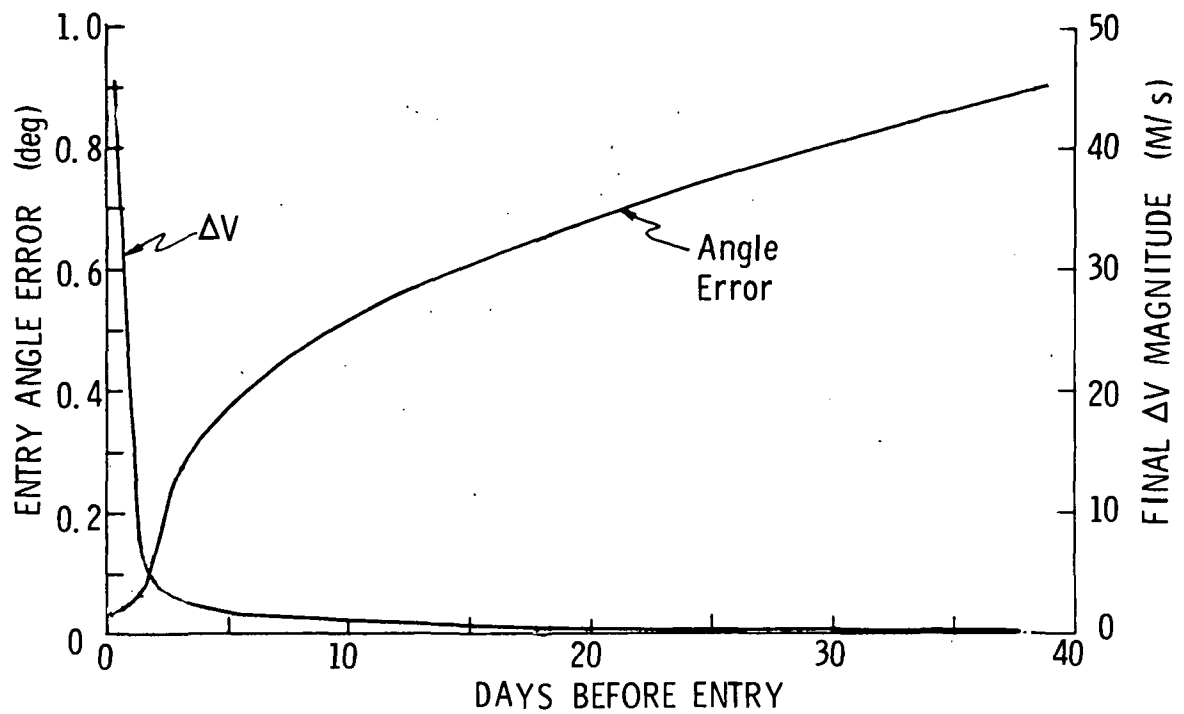


Figure 3-20. Dependence of Entry Angle Error and ΔV Magnitude on Time of Last ΔV .

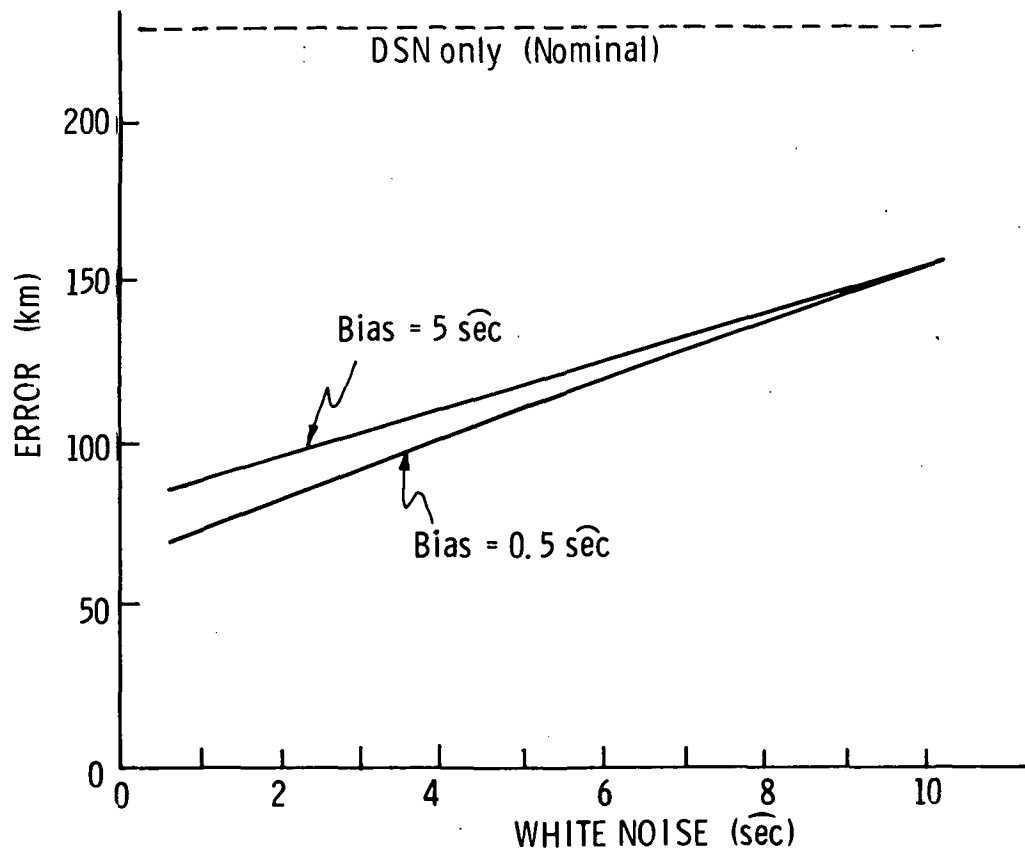


Figure 3-21. Entry Altitude Error Dependence on Onboard Sensor Noise.

On the near planet leg of this mission the stars Tauri and Virginis were chosen as optimal about 60% of the time, and a total of 9 stars were selected from a list of 37 for 57 measurements. Thus a restricted star field is not expected to degrade onboard navigation capability significantly.

One final interesting feature of this mission is the coupling between navigation and guidance. Figures 3-22 and 3-23 show this coupling for DSN only and DSN plus OB cases. Since we are using linear guidance it is expected that these curves would be roughly linear. However, neither curve would pass through the point (0,0) because of the limits of thrust accuracy (Chapter 2).

Nominal ΔV schedule and magnitudes are summarized in Table 3-XIII.

3.2.2 1200 Day Entry Mission Results

Guidance and navigation results for the 1200 day mission bear a close resemblance to the 800 day results, therefore a smaller number of cases were examined. However, the approach geometry is somewhat different than in the 800 day case, and the spacecraft spends a portion of its time outside of Jupiter's orbit which lowers DSN effectiveness. The longer flight time between the first course correction and arrival at Jupiter's sphere of influence produces larger guidance errors.

Table 3-XIV lists the values of the estimation errors at the Jupiter sphere of influence. The magnitude of the 800 day minimum guidance position error at this point is 7150 km compared to the much larger 34,000 km for the 1200 day mission. This is caused by the longer flight time from the first course correction at 10 days out to the sphere of influence. The errors have 1110 days to propagate as opposed to 720 days on the 800 day mission.

Estimation errors at the sphere of influence for the two missions are relatively close with the 1200 day uncertainty magnitudes uniformly and slightly larger. The onboard navigation instrument is, as usual, most effective in reducing the out of plane component of position error. In particular, the small onboard noise case (OB, 1-.5) reduces the out-of-plane

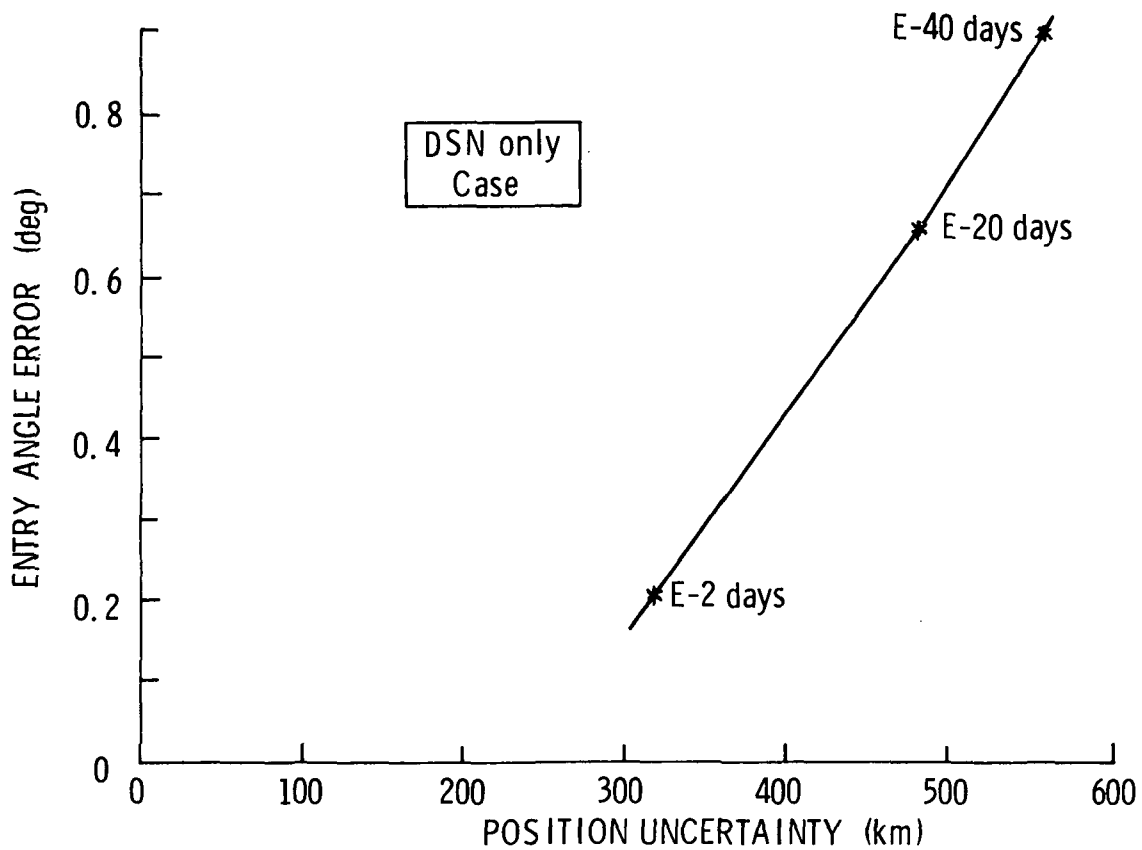


Fig. 3-22 Coupling Between Position Uncertainty and Entry Angle Guidance, DSN Case

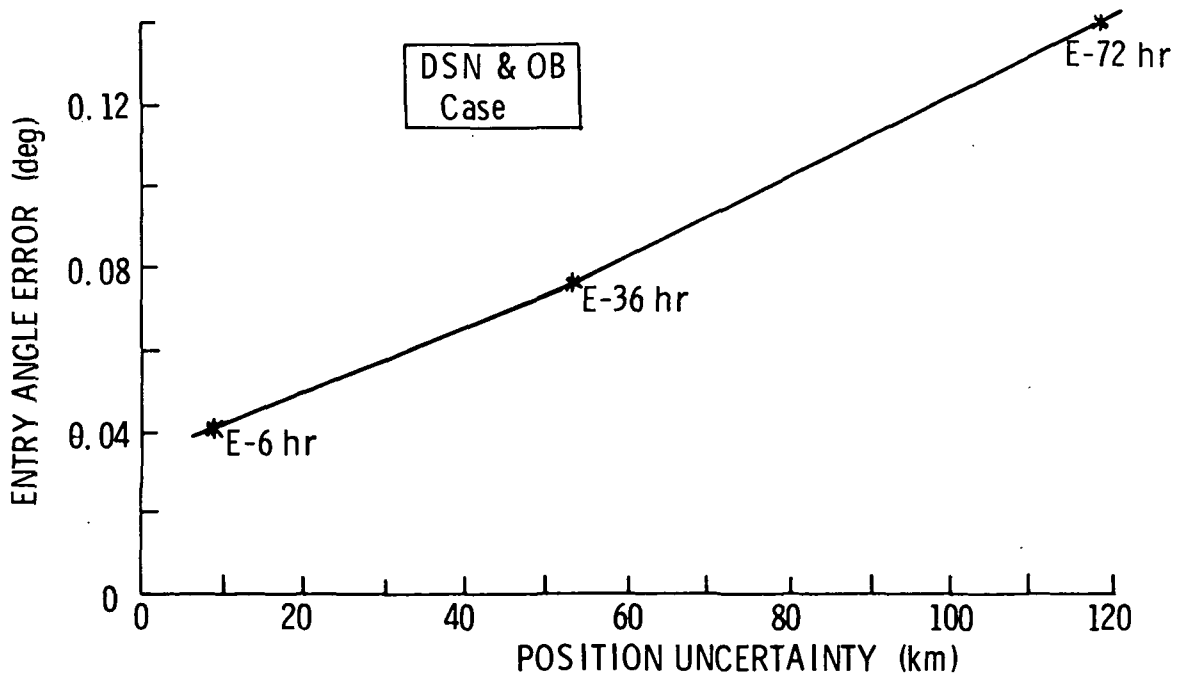


Fig. 3-23 Coupling Between Position Uncertainty and Entry Angle Guidance Error, Onboard Case

TABLE 3-XIII
Jupiter 800 Day Nominal
 ΔV Schedule *+

Time of ΔV_1 (days)	ΔV_1 mag. (M/sec)	Time of ΔV_2 (days)	ΔV_2 mag.
E - 70.3	1.72	E - 3.0	2.94

*table does not include injection error
correction of 25.2 M/sec.

+parametric variations are listed in Table 3-XII.

TABLE 3- XIV

Jupiter 1200 Day Entry Mission
Sphere of Influence Estimation Errors

Case	Position (km)	Velocity (M/sec)	X	Ephemeris (km)		Mag.
				Y	Z	
DSN Only	584.0	0.000620	201.0	366.0	404.0	581.0
Nominal	465.0	0.000606	196.0	366.0	201.0	461.0
OB, 1-.5	406.0	0.000604	151.0	345.0	137.0	401.0
OB, 1-1	406.0	0.000604	155.0	342.0	141.0	401.0
OB, 5-5	515.0	0.000606	196.0	367.0	297.0	511.0
OB, 10-5	556.0	0.000606	201.0	365.0	362.0	552.0

component of position uncertainty from 407 to 135 km which is essentially identical to the out-of-plane component reduction to 121 km effected in the 800 day mission case (not shown in the table).

Terminal estimation errors for the 1200 day mission are listed in Table 3-XV. The DSN-only case can be seen to have larger position and ephemeris uncertainties than in the 800 day mission due to the different flight geometry. Terminal position uncertainty magnitude for the 1200 day mission is 14 km as contrasted with 3 km for the 800 day mission. When onboard navigation is added, the position errors become quite similar and are uniformly 1 to 2% larger in the 1200 day mission cases. Ephemeris errors for the DSN-only cases are considerably larger on the 1200 day mission. For example the 1200 day mission has an ephemeris uncertainty of 221 km compared to 55 km for the 800 day mission. In both cases the out-of-plane component dominates this uncertainty, but DSN is less effective in reducing the out-of-plane component under the terminal geometry conditions of the 1200 day mission.

To examine the effects on terminal navigation errors due to early termination of DSN measurements, one case with DSN turning off at 2 hours from entry has been run. Results show nearly a doubling of position, velocity and ephemeris uncertainties.

Terminal guidance errors for the 1200 day mission are listed in Table 3-XVI. The DSN-only and DSN-off at E-2 hr. cases are identical as expected since the last ΔV is at E-2 days. The nominal terminal errors for the 1200 day mission are uniformly smaller than for the 800 day mission because the last ΔV on the 800 day mission was at E-3 rather than E-2. The best onboard system reduces the entry angle error by a factor of 3 from 0.3 deg. to 0.09 deg. Entry altitude and entry velocity are reduced similarly.

On the near planet leg of the 1200 day mission, with a scanning photometer onboard sensor, 17 stars are used from the list of 37. 6 stars are selected by the computer in roughly 75% of the measurements. It is estimated that the a priori restriction of the star field to 6 or 7 stars would result in negligible error increases.

TABLE 3-XV

Jupiter 1200 Day Entry Mission
Terminal Estimation Errors

Case	Position (km)			Velocity (M/sec)	Entry Angle (deg)	Entry Altitude (km)	Ephemeris Mag. (km)
	Down Range	Cross Range	Out of Plane				
DSN Only	2.04	1.00	13.9	14.0	16.2	0.000913	33.8
Nominal	0.58	0.41	0.94	1.17	1.12	0.000259	4.05
DSN Only Off at E-2 Hr	9.45	2.50	25.9	27.7	30.6	0.00348	37.6
OB, 1-.5	0.56	0.39	0.56	0.89	0.67	0.000252	2.52
OB, 1-1	0.57	0.40	0.54	0.89	0.67	0.000253	2.90
OB, 5-5	0.58	0.41	1.07	1.28	1.27	0.000262	6.96
OB, 10-5	0.64	0.52	1.44	1.66	1.77	0.000271	9.55
							221.0
							88.7
							384.0
							83.8
							84.5
							90.1
							91.7

TABLE 3-XVI

Jupiter 1200 Day Entry Mission
Terminal Guidance Errors

Case	Position Error (km)				Entry Angle Error (deg)	Entry Altitude Error (km)	Velocity Error Mag. (M/sec)
	Down Range	Cross Range	Out of Plane	Mag.			
DSN Only	769.0	17.8	26.6	810.0	0.32	226.0	323.0
Nominal	306.0	6.14	3.28	306.0	0.12	92.0	137.0
DSN Only Off at E-2 Hr	809.0	18.1	27.6	810.0	0.32	226.0	340.0
OB, 1-.5	219.0	4.15	1.36	219.0	0.09	68.2	105.0
OB, 1-1	223.0	4.23	1.54	223.0	0.09	70.6	107.0
OB, 5-5	433.0	9.59	18.5	434.0	0.17	125.0	188.0
OB, 10-5	547.0	11.8	20.7	548.0	0.22	146.0	233.0

A summary of the nominal ΔV requirements for the 1200 day mission is given in Table 3-XVII.

3.3 MULTIPLE PLANET SWINGBY MISSIONS

Two three planet swingby missions were simulated; i.e., the 1979 Jupiter-Uranus-Neptune mission and the 1977 Jupiter-Saturn-Pluto mission (see Chapter 1 for trajectory details). Results related to these missions are a natural sequel to the two planet swingby and the Grand Tour simulation results presented in Vol. II of this series. As in Vol. II, the chief aim here is to parametrically establish the relative importance of Earth-based and spacecraft-based navigation for two different impulsive high-thrust missions. However, the present studies broaden the framework for this evaluation by adding an unestimated bias to the onboard sensor noise model, and by reducing the DSN on-to-off ratio since the previous volume assumed continuous tracking.

A number of runs were made to parameterize several quantities that were held constant in the earlier studies. These quantities include the bias error levels of the onboard navigation sensor, the ephemeris uncertainties of the planets, turn-on time, the near planet turn-off time of the DSN, and the measurement frequency. In addition, an evaluation of a TV type onboard sensor was made. The sensor was assumed to sight on planetary satellites against a star background. Finally, a single mission leg was simulated with a considerable reduction in the list of available stars to assess the related error increases.

Table XVIII lists the more important nominal case inputs except for onboard measurement frequency which is listed in Table XIX. In Table XIX the outbound frequencies are not shown because they are symmetric in time about pericenter. These frequencies are for the scanning photometer instrument only.

3.3.1 Jupiter-Uranus-Neptune Swingby Mission

The relative effectiveness of DSN only, and DSN with onboard navigation systems is indicated by the position uncertainties for the nominal cases

TABLE 3-XVII
Jupiter 1200 Day
 ΔV Summary

Case	Time of ΔV_1 days from entry	ΔV_1 Mag. (M/sec)	Time of ΔV_2 days from entry	ΔV_2 Mag. (M/sec)
DSN Only	78.6	11.3	2.0	6.65
Nominal	78.6	11.3	2.0	7.03
DSN Only Off at E-2 Hr	78.6	11.3	2.0	7.03
OB, 1-.5	78.6	11.3	2.0	6.57
OB, 1-1	78.6	11.3	2.0	6.57
OB, 5-5	78.6	11.3	2.0	7.00
OB, 10-5	78.6	11.3	2.0	7.00

TABLE 3-XVIII

Nominal Case Inputs for the Multiple Planet Swingby Missions

<u>Parameter</u>	<u>Nominal Value</u>
Onboard Sensor White noise and bias	1", 5"
Onboard Sensor turn-on distance	1 A. U.
Onboard Sensor turn-off distance	Exit S. O. I.
DSN Tracking Period	1. 8hr/4 weeks from S. O. I. to 1 A. U. 2. 8 hr/2 weeks from S.O.I to E+30d 3. Full track 10d before ΔV , and within E+30d
DSN Doppler Noise and Station Location Bias	1 mm/sec, 1 meter off spin axis, 2 meters of longitude

TABLE 3-XIX

Nominal Onboard Measurement Frequency
- Multiple Planet Swingby Missions

Scanning Photometer
(1 A. U. to Pericenter)

Mission - Leg	$\frac{1}{\text{Freq. (Meas./day)}}$ Period (days)	2	3	4	5	Total Inbound	Total Outbound	Passage Total
Neptune Mission	$\frac{1}{7}$	$\frac{1}{2}$	$\frac{2}{\text{E-4}}$	$\frac{6}{\text{E-2}}$	$\frac{12}{\text{E-1}}$	60	36	96
Jupiter Passage	E-152 to E-47	to E-4	to E-2	to E-1	to E-0			
Neptune Mission	$\frac{1}{7}$	$\frac{1}{2}$	$\frac{4}{\text{E-2}}$	$\frac{8}{\text{E-.73}}$	$\frac{24}{\text{E-.62}}$	56	30	86
Uranus Passage	E-168 to E-41	to E-2	to E-.73	to E-.62	to E-0			
Neptune Mission	$\frac{1}{2}$	$\frac{2}{\text{E-10}}$	$\frac{6}{\text{E-1}}$	$\frac{25}{\text{E-.12}}$		58	—	58
Neptune Passage	E-74 to E-40	to E-1	to E-.12	to E-0				
Pluto Mission	$\frac{1}{7}$	$\frac{1}{4}$	$\frac{1}{2}$	$\frac{24}{\text{E-3}}$		49	33	82
Jupiter Passage	E-153 to E-59	to E-47	to E-3	to E-0				
Pluto Mission	$\frac{1}{7}$	$\frac{1}{2}$	$\frac{1}{3}$	$\frac{3}{\text{E-4}}$		37	23	60
Saturn Passage	E-103 to E-51	to E-41	to E-4	to E-0				
Pluto Mission	$\frac{1}{7}$	$\frac{1}{2}$	$\frac{2}{\text{E-31}}$	$\frac{24}{\text{E-1}}$		55	—	55
Pluto Passage	E-101 to E-31	to E-9.5	to E-1	to E-0				

listed in Tables 3-XX, XXI and XXII. On the Jupiter leg, at the inbound sphere of influence, there is little difference between values associated with the two systems, but at pericenter the addition of an onboard sensor reduces the position uncertainty from 65.7 to 3.45 km. At the outbound sphere of influence the uncertainties have increased from the pericenter values, but the onboard related value remains considerably smaller than the associated inbound sphere of influence value while the DSN related value increases slightly. This is because the near rectilinear motion along the outbound hyperbolic asymptote reduces the amount of information which can be obtained with the DSN alone while the uncertainties are being driven upward by the planetary mass uncertainty. A pattern similar to this propagates through the remaining swingbys, but the relative value of onboard navigation increases in each successive leg. This is illustrated in Fig. 3-24, where uncertainties for the inbound sphere of influence, pericenter and outbound sphere of influence positions are displayed at each planet.

The effects of onboard sensor noise levels are illustrated in Figs. 3-25 and 3-26. The white noise variations are seen to have a moderate effect from Fig. 3-25. A factor of 10 increase in the white noise standard deviation causes only a factor of 1.7 increase in position uncertainty. The bias error is seen to have little effect (except for the Neptune terminal leg) in Fig. 3-26. This is because the bias is effectively reduced by making measurements between stars on opposite sides of the planet and the planet limbs. Since the star separations are assumed to be accurately known this type of constant bias reduction is possible. An example would be the bias associated with the scanning photometer angle encoder. However the Neptune curve is based upon data generated with a restricted star field which does not permit the filter to make selections which minimize the bias, hence the larger uncertainties are produced.

Ephemeris uncertainties at the outbound sphere of influence on the Jupiter passage are all roughly 95 km except for the raised and lowered ephemeris cases. This is because the ephemeris limit is being imposed by the ability of the DSN to locate the spacecraft with respect to Earth, and therefore onboard capability can make only small reductions.

TABLE 3-XX

Jupiter Leg, Neptune Mission
Estimation Uncertainties

Case	Position Uncertainty (km)			Ephemeris Uncertainty (km)		Sphere of Influence Velocity Uncert. (M/sec)	Peri Planet Radius Uncert. (km)
	Sphere of Influence (Inbound)	Peri Planet	Sphere of Influence (Outbound)	Sphere of Influence (Inbound)	Sphere of Influence (Outbound)		
DSN only							
Nominal	563	65.70	659	551	95.6	0.156	33.30
DSN + OB							
Nominal	427	3.45	122	411	94.6	0.030	4.63
OB, 5-5	510	4.62	204	497	94.7	0.049	10.20
OB, 5-10	531	4.93	238	518	94.7	0.057	11.00
OB, 10-5	546	7.34	335	533	94.8	0.080	12.80
OB, 5-1	503	4.57	196	490	94.7	0.047	4.46
Ephemeris x 1/3	211	3.28	118	176	71.1	0.029	8.45
Ephemeris x 3	641	3.38	120	630	104	0.029	4.34

TABLE 3-XXI

Uranus Leg. Neptune Mission
Estimation Uncertainties

Case	Position Uncertainty (km)			Ephemeris Uncertainty (km)		Velocity Uncertainty (M/sec)	Radius Uncertainty (km)
	Sphere of Influence (Inbound)	Peri Planet (Outbound)	Sphere of Influence (Outbound)	Sphere of Influence (Inbound)	Sphere of Influence (Outbound)	Sphere of Influence (Outbound)	
DSN only Nominal	1806	958	1607	1150	714	0.458	94.00
DSN + OB Nominal	650	7.53	297	888	708	0.085	4.50
OB, 5-5	1220	8.47	531	1420	1000	0.151	5.32
OB, 5-10	1760	8.56	641	1700	1000	0.183	6.80
OB, 10-5	1720	9.63	841	1680	1010	0.240	5.69
OB, 5-1	1170	8.28	502	1400	1010	0.143	3.41
Ephemeris x 1/3	579	7.49	298	603	476	0.085	4.29
Ephemeris x 3	1470	7.46	297	1940	1290	0.085	4.03

TABLE 3-XXII

Neptune Leg, Neptune Mission
Guidance and Navigation Errors

Case	Position Uncertainty(km)		Ephem. Uncert. (km)	Velocity Uncert. (M/sec)	Radius Uncert. (km)	Guidance Pos. Error (km)		Guidance Vel. Error (M/sec)	Total ΔV (M/sec)	Ephem. Uncert. (km)
	Sphere of Influence (Inbound)	Peri Planet	Sphere of Influence (Inbound)	Sphere of Influence (Inbound)	Peri Planet	Sphere of Influence (Inbound)	Sphere of Influence (Inbound)	Sphere of Influence (Inbound)		Peri Planet
DSN only Nominal	3780	1905	3170	.0160	150	50,000	.810	17.60	2230	
DSN + OB Nominal	1102	13.3	1766	.0140	10.70	11,250	.432	7.62	1489	
OB, 5-5	1820	19.7	2080	.0130	14.00	17,800	1.020	13.28	1520	
OB, 5-10	2700	43.3	2610	.0140	29.40	21,000	1.360	19.10	1530	
OB, 10-5	2620	23.0	2560	.0140	19.90	26,800	1.780	19.79	1530	
OB, 5-1	1730	13.8	2080	.0130	9.66	17,000	0.958	12.56	1530	
Ephemeris x 1/3	793	12.7	897	.0090	10.00	10,900	0.592	7.00	714	
Ephemeris x 3	2006	21.0	2660	.0110	19.70	14,400	0.591	10.00	1810	

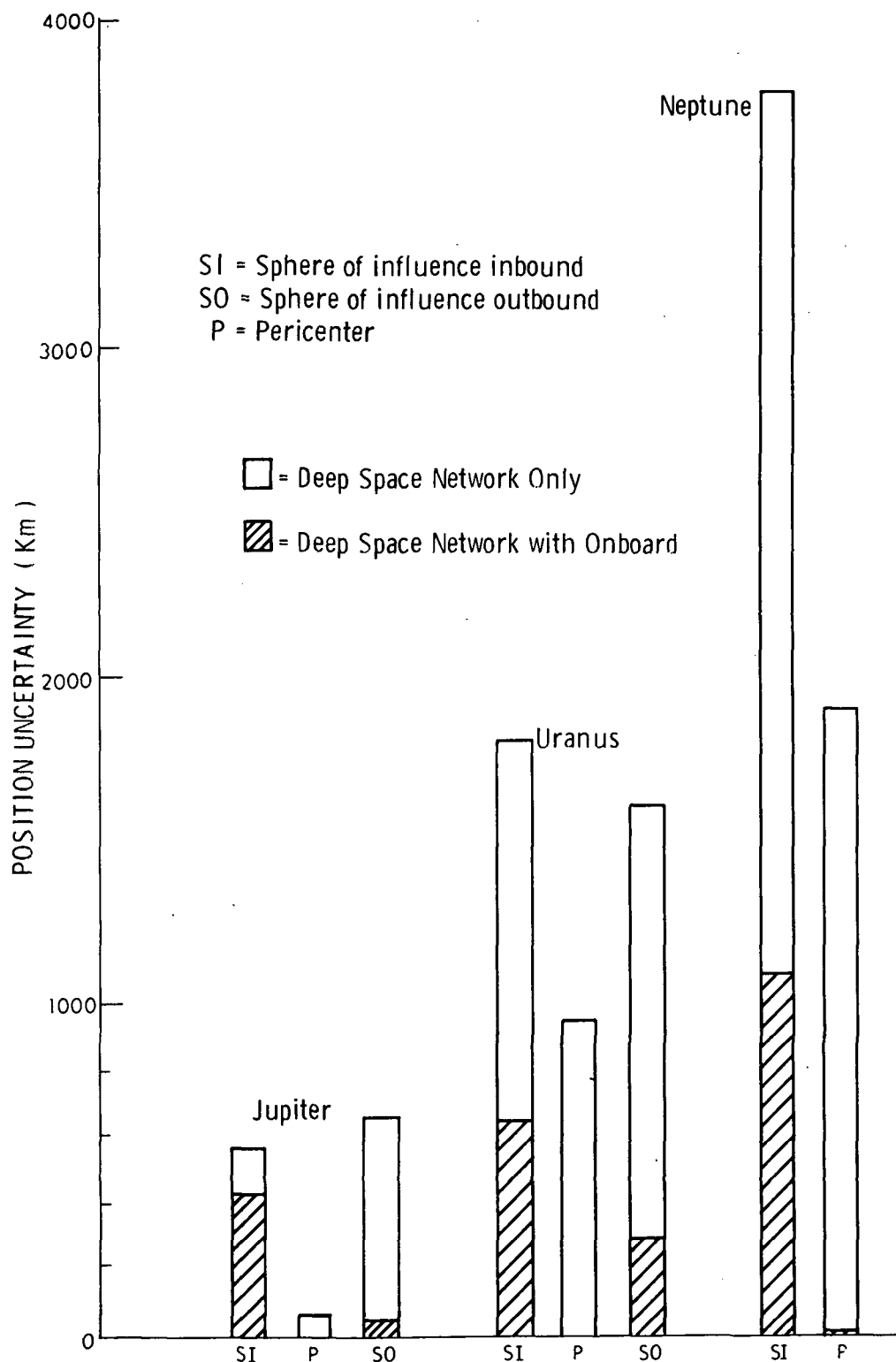


Fig. 3-24 Neptune 3 Planet Swingby Position Uncertainty

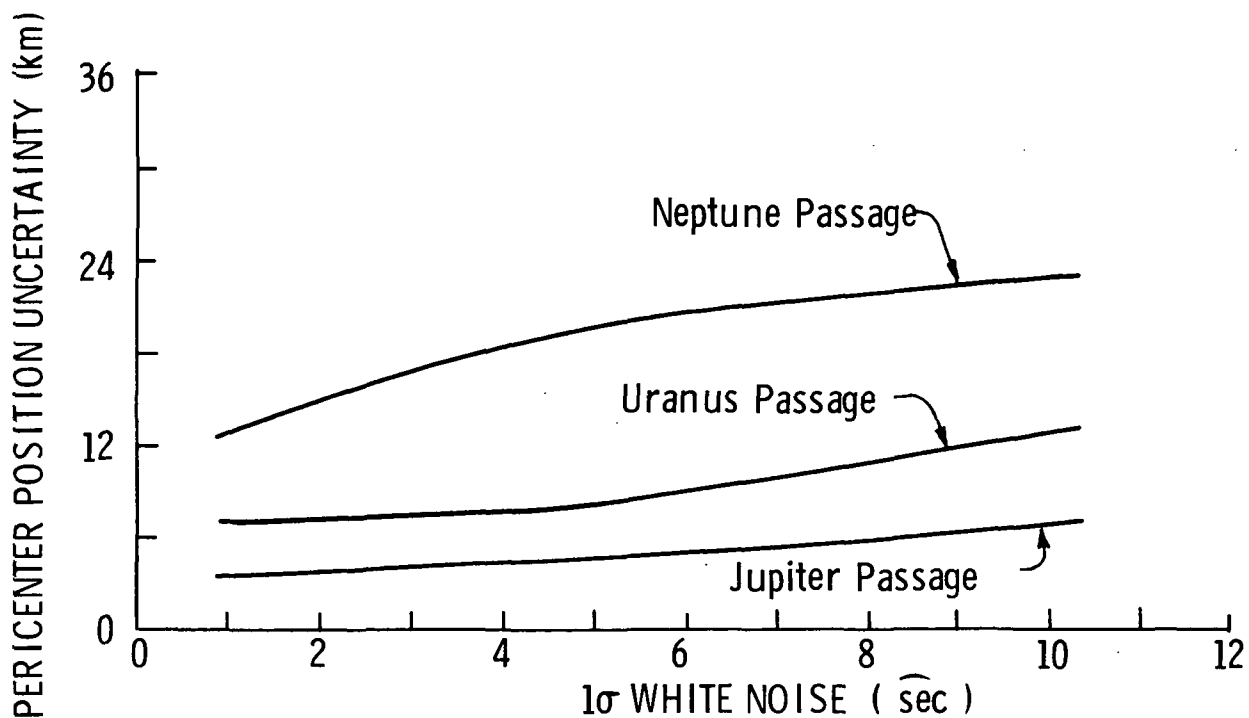


Fig. 3-25 Onboard Sensor White Noise Effects on Position Uncertainty (5 arcsec bias)

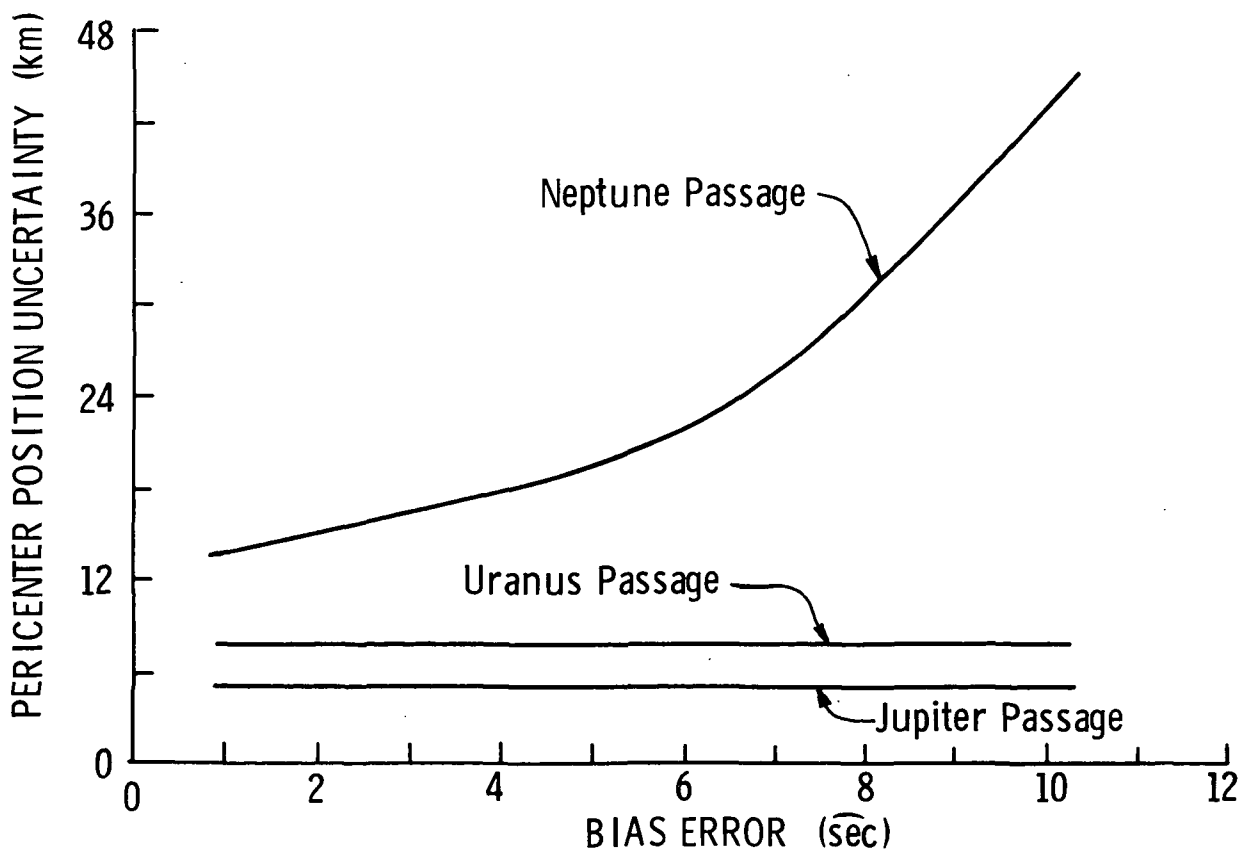


Fig. 3-26 Onboard Sensor Bias Effects on Position Uncertainty (5 arcsec white noise)

Tables 3-XX, 3-XXI and 3-XXII list the results for scaled initial ephemeris values. At the larger spacecraft-planet ranges the scaled up or down ephemeris significantly effect the position uncertainty, but near pericenter the effect is found to be negligible for the Jupiter and Neptune passages. This is illustrated in Figs. 3-27 and 3-28.

One of the more interesting onboard effects is related to the time (or equivalently range) of turn-on or turn-off of the onboard sensor. Table 3-XXIII contains the guidance and navigation results for variations in the on and off time of the sensor on the Uranus leg of the Neptune mission. In the two types of cases, the sensor is turned either on or off at a given number of planetary radii. If the sensor is turned off at a certain point it is assumed that it has been on from 1 A.U out to the turn-off point. Symmetry is assumed about pericenter so that, for example, if the sensor is turned off at $E - 10$ it is turned on again at $E + 10$. Since these effects are noticed only from the turn-off point inward, the errors and uncertainties are listed for pericenter and the outbound sphere of influence. The position uncertainty related effects are illustrated in Figs. 3-29 and 3-30. Figure 3-29 shows the effects at pericenter. It can be seen that at pericenter there is little effect over the range of 5 to 50 radii. However, the curves get steeper at either end indicating a drastic increase in position uncertainty as turn-on becomes later or turn-off earlier. The crossing point of the two curves in Fig. 3-29 is the equal error reduction point, i.e., if the sensor is either turned on or off at approximately 22.5 radii, the same pericenter error results. However, at the outbound sphere of influence, the crossing point is much further out as Fig. 3-30 shows. This is because of the assumption of symmetry in the on and off times about pericenter. The early off case gets turned back on again on the outbound side of pericenter and takes measurements up to the sphere of influence, thus producing a greater reduction in the uncertainty at the outbound sphere of influence point. The ephemeris uncertainty in each case (from Table XXIII) is essentially constant due to the Earth related measurement limitations of DSN. Velocity uncertainties are seen from the table to be affected in roughly the same way as the position uncertainty. Radius uncertainty is strongly

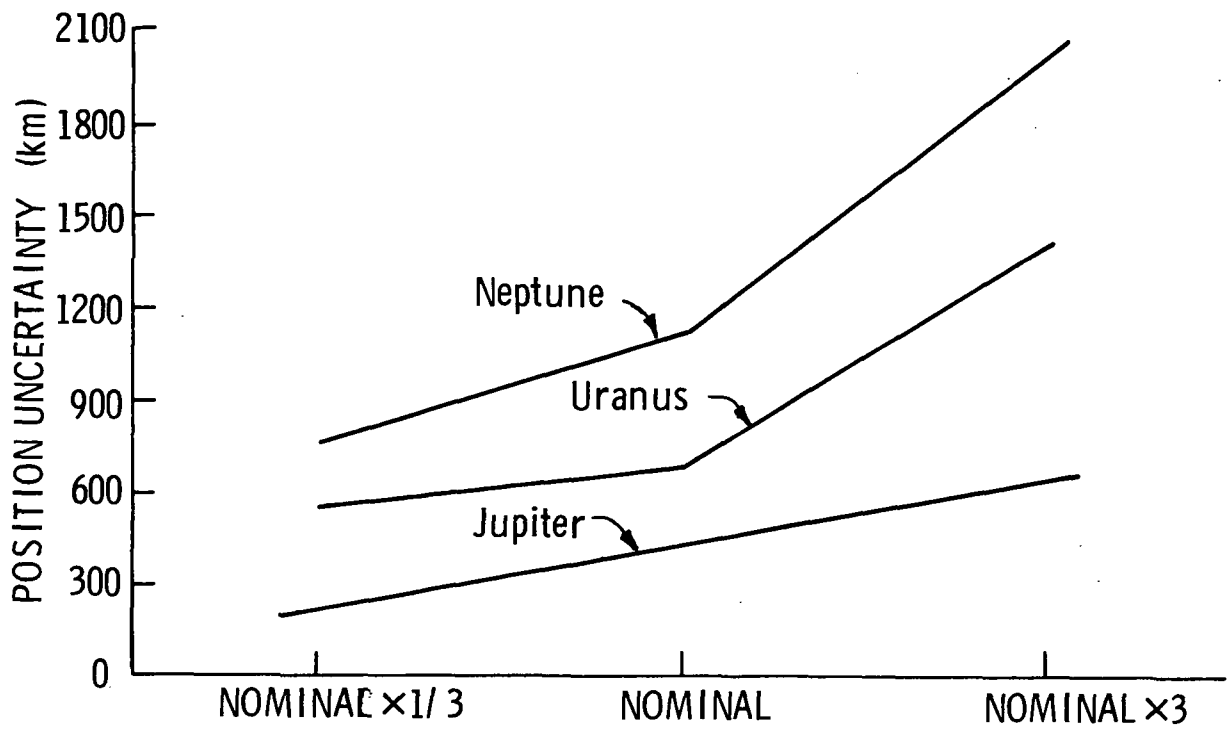


Fig. 3-27 Ephemeris Effects on Sphere of Influence Position Uncertainty

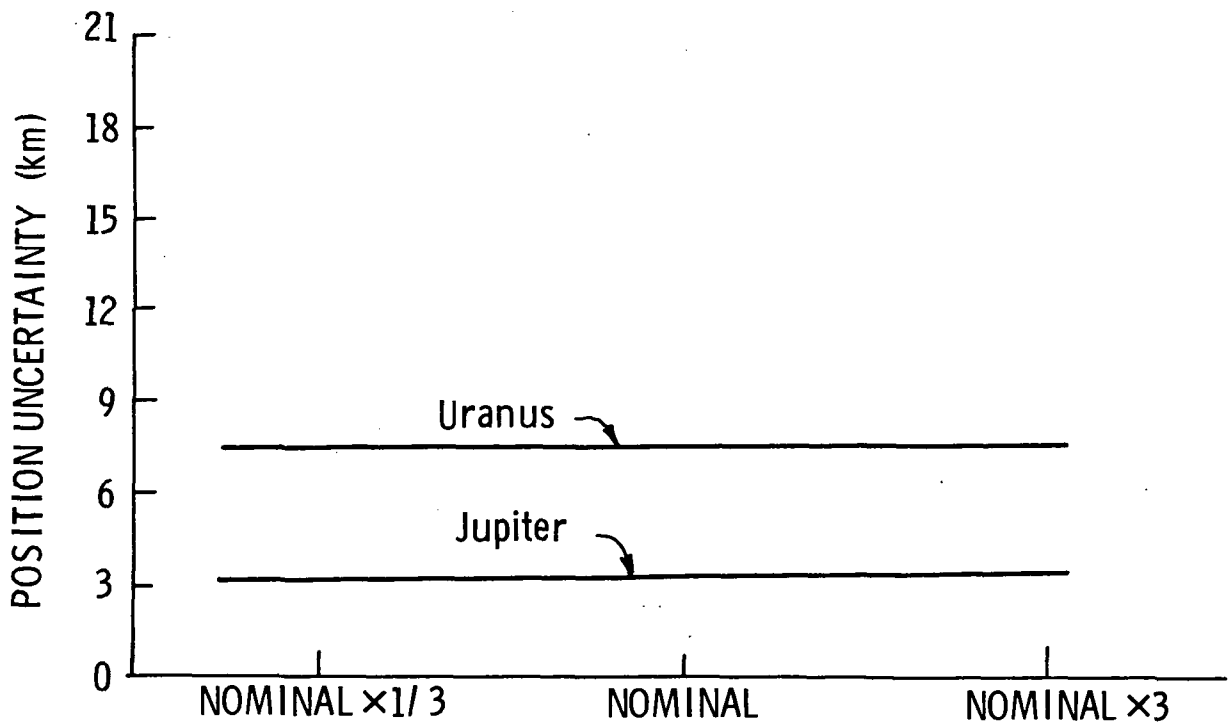


Fig. 3-28 Ephemeris Effects on Pericenter Position Uncertainty

TABLE 3-XXIII

Uranus Passage, Neptune Mission
Guidance and Navigation Errors

Case	Position Uncertainty (km)	Sphere of Influence (Outbound)	Ephemeris Uncertainty (km)	Velocity Uncert. (M/sec)	Radius Uncert. (km)	Guidance Position Error (km)	Guidance Velocity Error (M/sec)	Sphere of Influence (Outbound)	Total ΔV (M/sec)
OB, on at 5 radii	10.70	1540	710	.4390	7.00	219,000	62.20		2.78
OB, on at 22.5 radii	9.06	1470	710	.4180	6.12	219,000	62.20		2.78
OB, on at 50 radii	7.98	785	710	.2230	4.85	219,000	62.20		2.78
OB, off at 5 radii	8.57	298	708	.0848	6.03	50,100	14.20		4.71
OB, off at 22.5 radii	9.00	304	708	.0866	8.21	50,100	14.20		4.71
OB, off at 50 radii	10.70	308	708	.0876	21.30	50,100	14.20		4.71
Extra ΔV at E+2, DSN	957.00	1670	714	.4770	94.00	49,100	17.70		220.00
DSN only on at E-7	964.00	1580	721	.4500	94.00	723,000	206.00		5.81
DSN only on at E-14	961.00	1640	718	.4700	94.00	42,300	25.80		232.80
Extra ΔV at E+2, DSN + OB	7.60	295	708	.0840	94.00	659	1.18		19.79

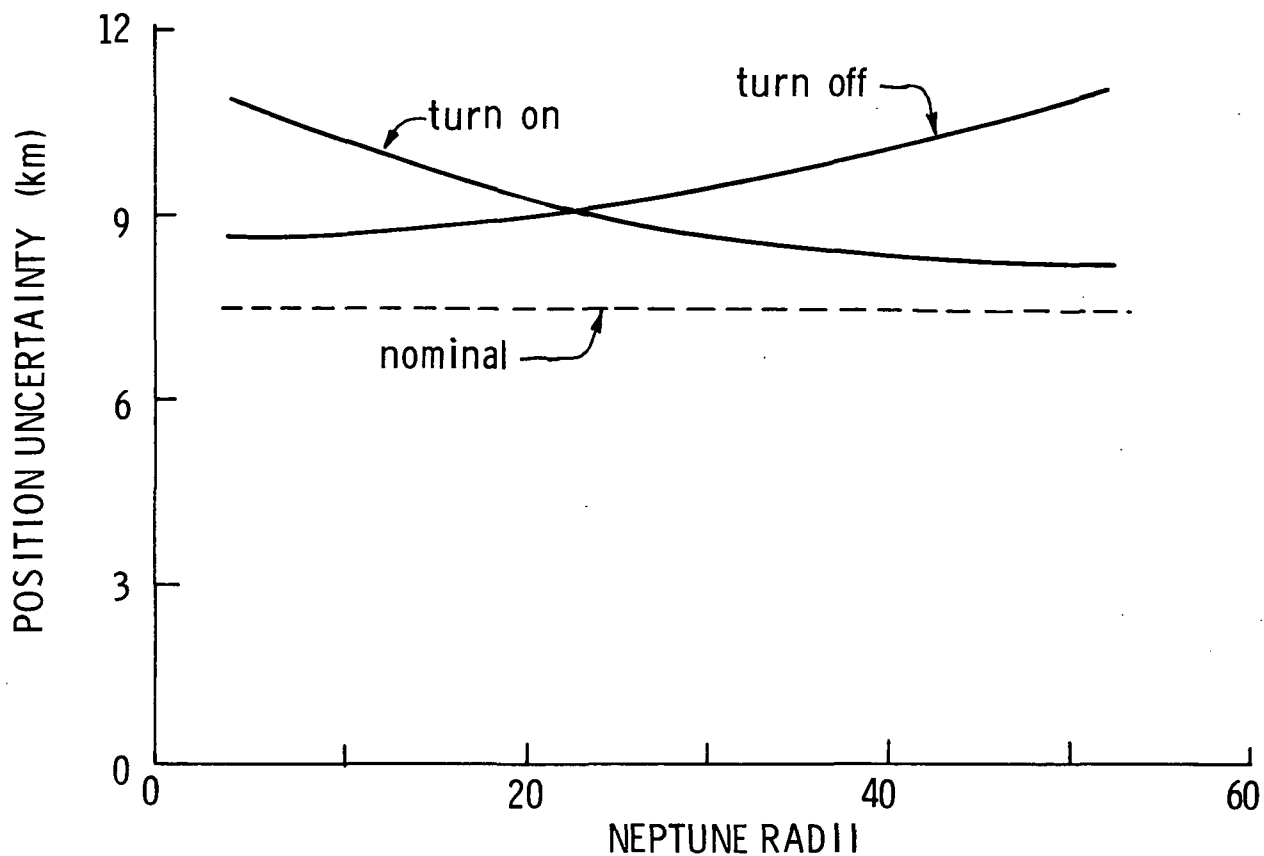


Fig. 3-29 Effects of Late Turn-on, or Early Turn-off of Onboard Navigation., Pericenter Position Uncertainty.

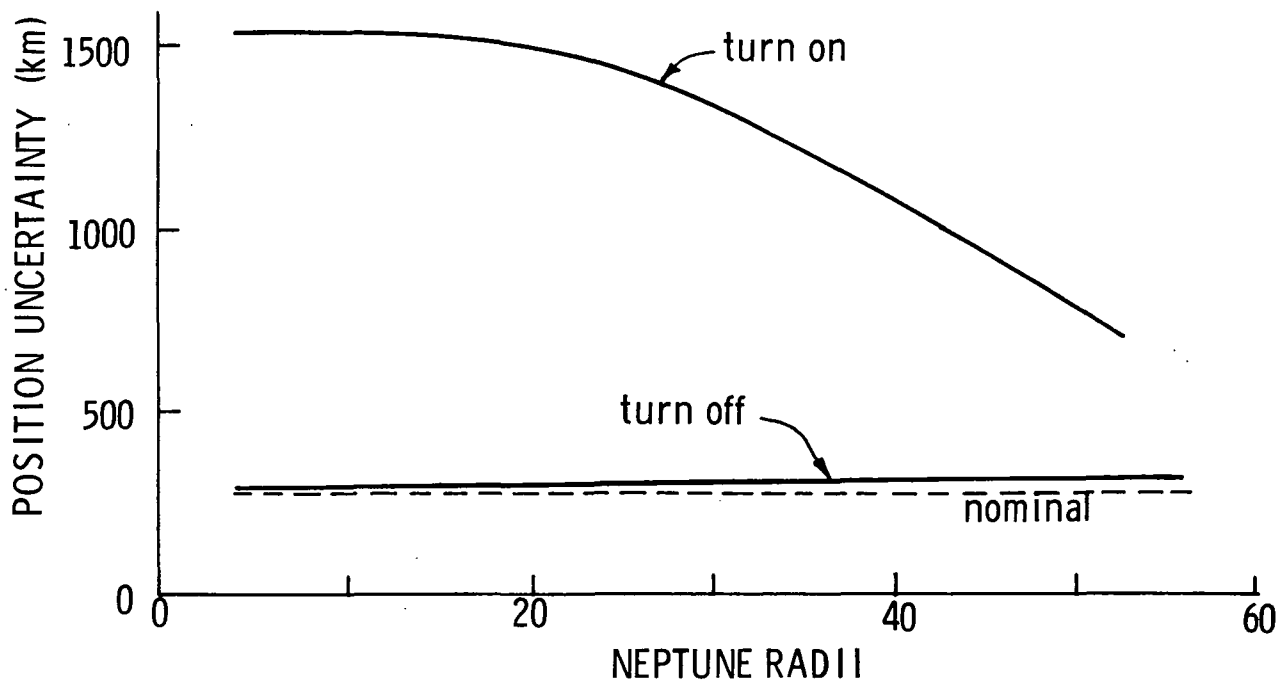


Fig. 3-30 Effects of Late Turn-on or Turn-off of Onboard Navigation., Sphere of Influence Outbound Values.

affected as the early turn-off point moves out near 50 radii. Guidance errors are seen to depend primarily on the turn-on time in relation to the latest velocity correction. In the late turn-on cases a velocity correction is made shortly after onboard turn-on at 50 radii, and insufficient measurements are made to significantly alter the resulting guidance error. Conversely, in the early-off cases essentially all the measurements have been made by the time of the ΔV so these resultant guidance errors are very closely the same as the nominal, but different from the late-on cases. Since the early-off cases feed more navigation information into the near pericenter ΔV , the associated guidance errors are considerably smaller, while the near pericenter ΔV is correspondingly larger.

A summary of the nominal ΔV 's required for the Jupiter-Uranus-Neptune mission is presented in Table XXVI. Timing of the ΔV 's is noted with respect to pericenter or encounter (E).

Guidance errors for the nominal DSN-only and DSN with onboard cases are listed in Tables 3-XXIII, XXIV, and XXV along with results for varied onboard sensor noise levels and ephemeris uncertainties. The inbound sphere of influence values of guidance position and velocity error are relatively constant for both the Jupiter and Uranus passages. However, the outbound sphere of influence values show a wide range of variation. On the Jupiter leg, the DSN-only related position error is several times larger than the DSN with onboard value, and on the Uranus leg the DSN-only error is approximately twenty times larger. Velocity errors are related in nearly the same ratios. The varied onboard noise cases show considerable variation with the largest noise case having a 4 to 1 ratio of guidance position error over nominal on the Uranus passage, and a 2 to 1 ratio on the Jupiter passage.

3.3.2 Jupiter-Saturn-Pluto Swingby Mission

Three full pass simulations through all three legs of the Pluto mission were run. These were a nominal DSN only case, a nominal DSN with onboard case, and a DSN only case with DSN Doppler white noise increased by a factor of 10. The position estimation uncertainties for these cases are

TABLE 3-XXIV

Jupiter Leg, Neptune Mission
Guidance Errors & ΔV

Case	Position Error (km)		Velocity Error (M/sec)		Total ΔV (M/sec) (Excluding Post Earth)
	Sphere of Influence (Inbound)	Sphere of Influence (Outbound)	Sphere of Influence (Inbound)	Sphere of Influence (Outbound)	
DSN only Nominal	3614	15,070	1.09	3.60	2.52
DSN + OB Nominal	3950	2088	1.09	0.66	2.97
OB, 5-5	3950	3230	1.09	0.88	3.26
OB, 5-10	3950	3790	1.09	0.99	3.29
OB, 10-5	3950	4590	1.09	1.17	3.37
OB, 5-1	3950	3060	1.09	0.85	3.22
Ephemeris x 1/3	3910	1980	1.09	0.65	2.22
Ephemeris x 3	4250	2070	1.09	0.66	3.53

TABLE 3-XXV

Uranus Leg, Neptune Mission
Guidance Errors and ΔV

Case	Position Error (km)		Velocity Error (M/sec)		Total ΔV (M/sec)
	Sphere of Influence (Inbound)	Sphere of Influence (Outbound)	Sphere of Influence (Inbound)	Sphere of Influence (Outbound)	
DSN only Nominal	17,740	691,000	8.100	197.00	8.06
DSN + OB Nominal	8220	36,000	0.043	10.26	5.14
OB, 5-5	9600	86,400	0.071	24.60	8.44
OB, 5-10	10,200	117,000	0.072	33.20	11.20
OB, 10-5	12,000	151,000	0.089	42.90	11.90
OB, 5-1	9470	81,100	0.071	23.00	7.95
Ephemeris x 1/3	8120	50,100	0.060	14.20	5.24
Ephemeris x 3	10,100	49,900	0.060	14.20	6.94

TABLE 3-XXVI

Nominal ΔV Summary for J-U-N Multiple Planet Swingby*

	Time of ΔV_1	ΔV_1 Mag. (M/sec)	Time of ΔV_2	ΔV_2 Mag. (M/sec)	Time of ΔV_3	ΔV_3 Mag. (M/sec)	Time of ΔV_4	ΔV_4 Mag. (M/sec)
Jupiter Passage	E - 44.82	1.24	E - 2	1.74	E + 56.82	0.67	—	
Uranus Passage	E - 38.64	1.96	E - 2	2.75	E + 2	15.1	E + 50.64	10.68
Neptune Passage	E - 50.11	2.52	E - 2	4.45	—		—	

*does not include injection error correction of 25.6 M/sec

listed in Table 3-XXVII and summarized in Fig. 3-31. The relative utility of onboard navigation is much greater at pericenter for reducing position uncertainties in roughly the same proportions as on the Neptune mission. However, the figure also shows that if DSN Doppler noise is larger by a factor of 10, the onboard system also offers substantial reductions of position uncertainty at the inbound and outbound sphere of influence points.

Guidance errors are affected in a fashion similar to the position uncertainties as can be seen from Table 3-XXVIII. On the Jupiter inbound leg the guidance position error at the sphere of influence is nearly the same for all three cases since this value is determined primarily by the conditions at the first ΔV . On the outbound Jupiter leg however, the values separate, with a greater multiple of error for the DSN only case over DSN with onboard, than for the increased Doppler noise DSN only case over the nominal DSN only. This relationship can be seen from the table to continue to build through the remaining legs of the mission.

A number of special runs were made on the Pluto leg of the mission to examine effects such as onboard sensor bias, measurement frequency and star field restrictions. The effects of early DSN turn-off were also examined. These results are listed in Table 3-XXIX. The first two tabulated cases have a parameterized onboard sensor bias error with the nominal case listed in Table 3-XXVII falling in between the two parameterized cases in Table XXIX. The periplanet position uncertainty is roughly doubled when the bias is increased from 5 (nominal) to 10 arcseconds. Also strongly affected is the pericenter radius uncertainty. The 1-1 case yields a particularly small value of 27.6 km.

Scaling of the onboard sensor measurement frequency by factors of 1/2 and 2 times nominal produces effects similar to the bias error variations. Halving or doubling the frequency can be seen, from Table 3-XXIX to cause equal percentages of increase or decrease in the position uncertainty at pericenter. Effects of the measurement frequency scaling are illustrated in Fig. 3-32 for the position and Pluto radius uncertainties.

The nominal ΔV time on the Pluto passage is at E-2 days, which produces a pericenter guidance error in the nominal DSN with onboard

TABLE 3-XXVII
Pluto Mission
Estimation Uncertainties

		Jupiter Leg				
		Position Uncertainty (km)		Ephemeris Uncertainty (km)		Radius Uncert. (km)
Case		Sphere of Influence (Inbound)	Peri Planet	Sphere of Influence (Outbound)	Sphere of Influence (Outbound)	Velocity Uncert. (M/sec)
DSN only						
Nominal		563	27.2	411	551	111
DSN + OB						
Nominal		459	1.30	123	445	111
DSN only						
Doppler Noise x10		614	146	1130	551	218
Saturn Leg						
DSN only						
Nominal		1360	475	1690	1150	530
DSN + OB						
Nominal		893	28	239	694	490
DSN only						
Doppler Noise x10		4070	796	11,200	1150	906
Pluto Leg						
DSN only						
Nominal		16,200	8970	---	15,600	---
DSN + OB						
Nominal		8890	59.4	---	9520	---
DSN only						
Doppler Noise x10		26,600	10,900	---	15,600	---
						200.00
						35.70
						200.00

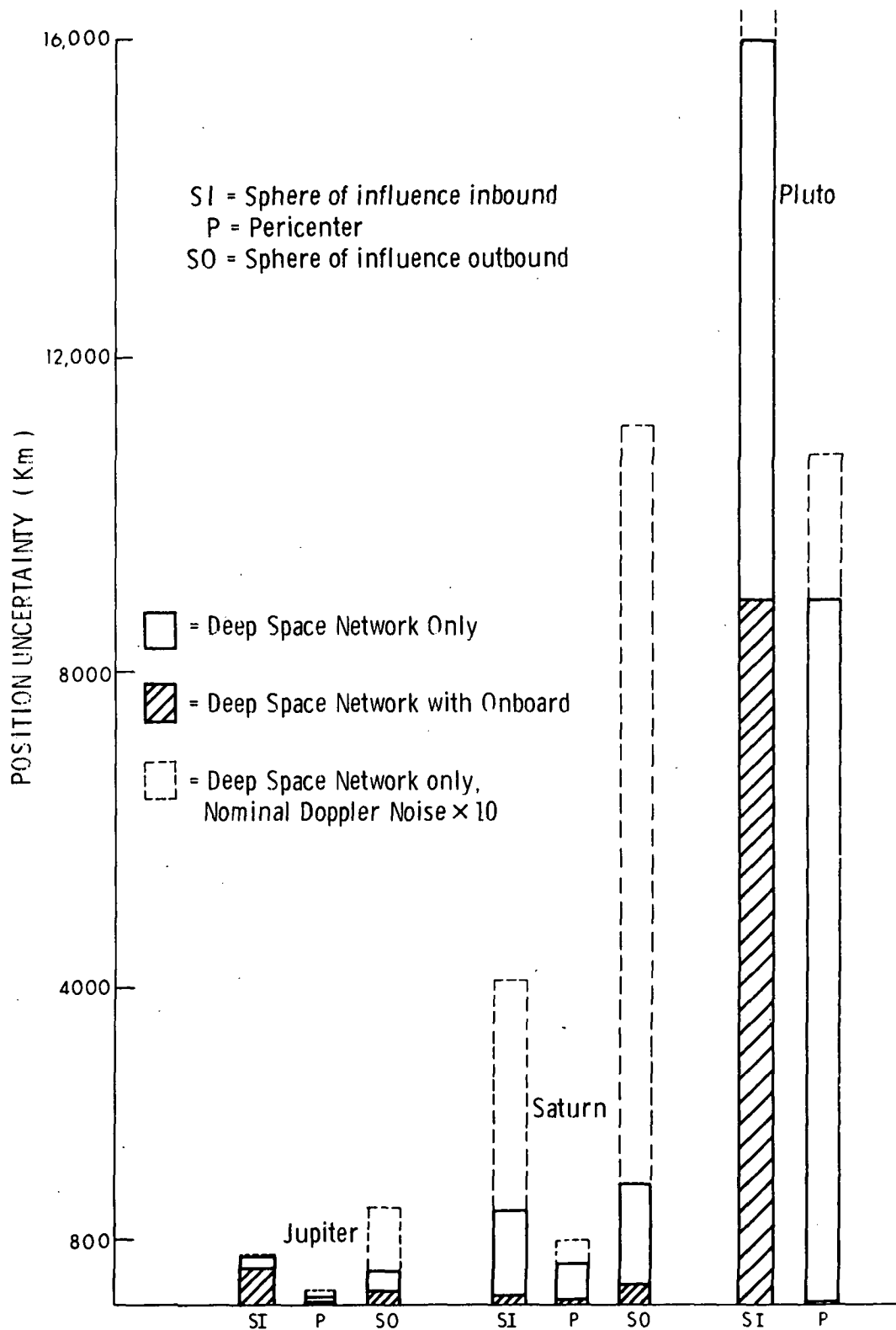


Fig. 3-31 Pluto 3 Planet Swingby Position Uncertainty

TABLE 3-XXVIII
Pluto Mission
Guidance Errors & ΔV

Case	Jupiter Leg				Total ΔV (M/sec)
	Position Error (km)		Velocity Error (M/sec)		
	Sphere of Influence (Inbound)	Sphere of Influence (Outbound)	Sphere of Influence (Inbound)	Sphere of Influence (Outbound)	
DSN only Nominal	3610	15,400	.0023	3.60	2.00
DSN + OB Nominal	3610	6980	.0023	1.67	2.46
DSN only Doppler Noise x10	3690	27,300	.0044	6.35	2.00
Saturn Leg					
DSN only Nominal	4600	35,400	.6130	9.93	12.48
DSN + OB Nominal	3050	4070	.5070	1.12	11.13
DSN only Doppler Noise x10	10,300	119,000	.7270	32.70	16.34
Pluto Leg					
DSN only Nominal	56,600	---	.3760	---	96.59
DSN + OB Nominal	21,800	---	.0840	---	54.30

TABLE 3-XXIX
Pluto Passage, Pluto Mission
Guidance and Navigation Errors

Case	Position Uncertainty(km)	Ephemeris Uncert. (km)	Sphere of Influence (Inbound)	Velocity Uncert. (M/sec)	Radius Uncert. (km)	Guidance Position Error (km)	Guidance Velocity Error (M/sec)	Total ΔV (M/sec)
	Sphere of Influence (Inbound)	Peri Planet		Sphere of Influence (Inbound)	Peri Planet	Peri Planet	Peri Planet	
OB, 1-1	8820	47.5	9420	.019	27.60	6450	148	65.2
OB, 1-10	8920	119	9560	.019	74.80	8850	192	41.6
OB Meas. freq. $\times 1/2$	8890	107	9530	.019	39.20	8540	187	49.5
OB Meas. freq. $\times 2$	8890	36.3	9480	.019	24.80	7900	170	51.2
Nominal ΔV at E-. 5	8890	60.7	9520	.019	35.70	2010	127	145.0
DSN off at E-2.3 ΔV at E-2	16,200	16,200	15,600	.096	200	16,200	422	81.5
DSN only DSN off at E-5 ΔV at E-5	16,200	16,200	15,600	.096	200	16,200	422	79.1
DSN only DSN off at E-. 5 ΔV at E-. 5	16,200	16,100	15,500	.096	200	16,100	421	117.0
Restricted Star Field	8890	105	---	---	65.80	8350	182	49.9
DSN + OB Doppler Noise $\times 10$	9340	64.5	12,700	.051	35.90	9140	617	592.0

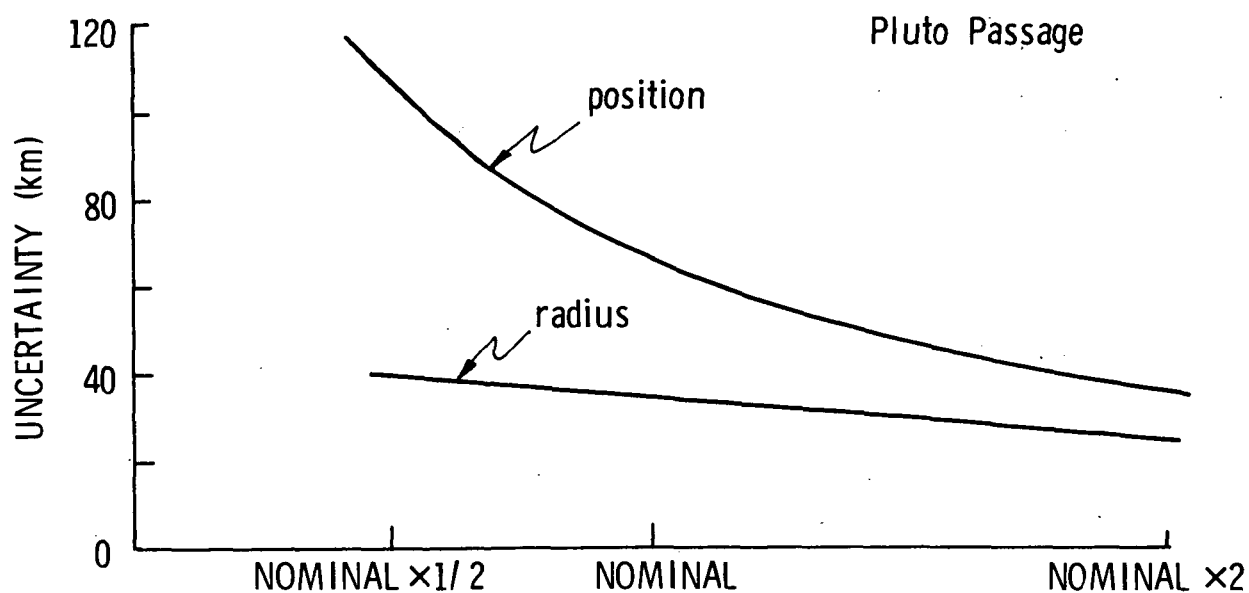


Fig. 3-32 Onboard Measurement Frequency Effects on Pericenter Position and Radius Uncertainty

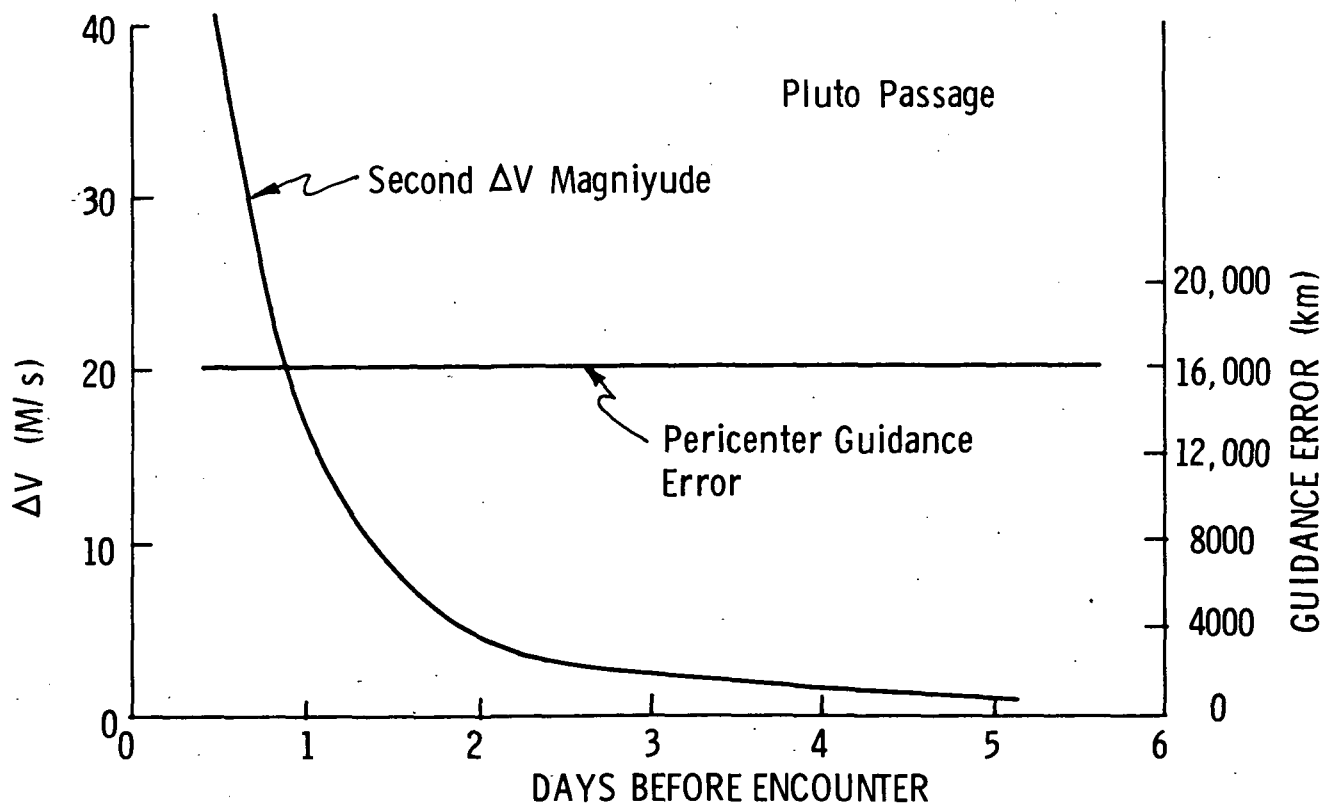


Fig. 3-33 Relationship Between Guidance Error and Timing of Second ΔV (DSM only case)

case of about 8000 km. On a close passage this might be an unacceptably large error, thus to see what improvement might be made by delaying the ΔV , a case was run with the ΔV at E-0.5 days allowing time for position uncertainty reduction. The resultant guidance error was dropped from 8000 to 2000 km. However, the ΔV magnitude penalty for this improvement was about 100 m/sec.

Because of the small mass of Pluto, the DSN does not gather much information about the spacecraft position with respect to the planet until very close to pericenter. This means that the position uncertainty remains essentially unchanged from the sphere of influence crossing to very near pericenter. The nominal DSN case with tracking up to pericenter yields a pericenter position uncertainty of about 9000 km (Table 3-XXVII). Three early turn-off DSN only cases were run with ΔV 's following immediately after turn-off. The results show (Table 3-XXIX) that loss of even the last 1/2 days worth of information causes the sphere of influence position uncertainty to remain unreduced by the time pericenter is reached. At E-0.5 days the spacecraft is still about 250 radii away from Pluto. Given no improvement in position knowledge, the guidance position error cannot be reduced as Fig. 3-33 shows, thus in the DSN only case the final ΔV would have to be made perhaps only a few hours before pericenter to reduce the guidance error significantly, and the reduction would only be as low as the position uncertainty of roughly 9000 km at a tremendous ΔV penalty.

When a nominal onboard system with final ΔV at E-2 days is considered along with an increase in DSN Doppler noise, the final ΔV magnitude is very large. The guidance position error at the inbound sphere of influence is 376,000 km (not tabulated) compared to 26,000 km in the nominal DSN case. The onboard sensor however, fixes the position to within 9,000 km, thus an extremely large ΔV is needed to reduce the guidance error of 376,000 km down to near 9,000 km over a period of only several days. The ΔV is given in Table 3-XXIX as 592 m/sec.

Nominal ΔV requirements for the Jupiter-Saturn Pluto mission are listed in Table XXX.

TABLE 3-XXX

Nominal ΔV Summary for J-S-P Multiple Planet Swingby*

	Time of ΔV_1	ΔV_1 ag. (M/sec)	Time of ΔV_2	ΔV_2 ag. (M/sec)	Time of ΔV_3	ΔV_3 ag. (M/sec)
Jupiter Passage	E - 44.98	1.20	E - 6.98	0.43	E + 47.98	1.05
Saturn Passage	E - 38.54	0.92	E - 2	5.04	E + 50.54	1.15
Pluto Passage	E - 7.50	30.6	E - 2	22.5		

*does not include injection error correction of 25.9 M/sec.

The effects of a restricted star field are also shown in Table 3-XXIX. Normal optimal sighting procedure for these simulations is to allow the sensor to select the star that yields the maximum error reduction from a list of 37. In the case considered the three most frequently selected stars were substituted for the list of 37. The results are listed in Table 3-XXIX. The major effects are the approximate doubling of the pericenter position and radius uncertainty estimates. It may be possible to reduce the effects of star field restriction by selection according to error reduction rather than frequency of choice. This possibility has not been examined.

3.3.3 Onboard Navigation Using a TV Type Sensor

A few cases were analyzed that replaced the scanning photometer sensor with a TV Type device. Thirty-five TV measurements were taken over a planet-spacecraft distance interval of 50 to 1000 planetary radii compared with about 60 measurements for the scanning photometer (see Table XIX). The TV device has nominal noise of 2 arcseconds white noise and 5 seconds bias in two dimensions compared to 1 and 5 arcseconds in one direction for the scanning device. The TV sensor sights on planetary satellites against a star background. Only one satellite is used for each planet and no attempt was made to optimize satellite choice at each measurement point. Constraints on sighting range etc. were established according to the criteria discussed in Appendix H. Thus, for example, Titan was used on the Saturn passage, but the brightness was considered too low for sightings after pericenter. Results for the Saturn passage are listed in Table 3-XXXI. Satellite initial ephemeris uncertainty is displayed as a parameter. The TV system shows little improvement over DSN only at the outbound sphere of influence point primarily because of the trajectory geometry which places Titan near the sun after pericenter passage thus severely lowering the satellite brightness while increasing the scattered sunlight problem. However, at pericenter the TV device is very effective considering that it is turned off at 50 Jupiter radii away from the parent planet. Assumptions about the initial ephemeris uncertainty are seen to be relatively unimportant. Table 3-XXXII shows similar results for the Neptune leg of the Neptune mission. On this table the TV noise values are

TABLE 3-XXXI
TV NAVIGATION
Saturn Passage

Quantity	DSN only	Ephemeris 9000 km	TV Ephemeris 2700 km	Ephemeris 900 km	Scanning Photometer
Position Uncertainty (km)					
Sphere of Influence Outbound	1686	1651	1650	1412	239
Pericenter Position Uncertainty (km)	475	126	126	93.5	30

TABLE 3-XXXII

TV Navigation at Neptune

Quantity	TV with Noise		TV with Noise		Scanning Photometer
	DSN only	2-5	4-10		
Pericenter Position Uncertainty (km)	3780	138	82		10.5
Pericenter Guidance Position Error (km)	3526	1043	985		884.0
Pericenter Ephemeris Uncertainty (km)	2227	1497	1497		1472.0

varied, and the guidance position error and planet ephemeris uncertainties are listed. The initial satellite ephemeris uncertainty for the satellite Triton on this leg was assumed to be 2500 km. The results in Table 3-XXXII show TV navigation very effective at reducing pericenter guidance error and position uncertainty below the DSN only values to about the same levels as the scanning photometer. The scanning photometer is more effective in reducing pericenter position uncertainty mainly because it is allowed to continue sightings to pericenter. TV is turned off earlier here because of the possibility of excessive signal (see Appendix H), and because the TV sensor is expected to be used as a planet imaging device for scientific measurements at short range.

CHAPTER 4

SUMMARY AND RECOMMENDATIONS

Guidance and navigation characteristics for three classes of missions have been computed. Two different missions were included in each class for a total of six mission analyses.

4.1 SUMMARY

Most of the results and conclusions are specific to each considered mission, however there are some conclusions that relate to all the missions. For example, the addition of an unestimated bias error to the onboard navigation sensor was found not to significantly change directly comparable results that were produced in Volume I of this series. The reason for this is that the bias error is effectively reduced by complementary measurements involving stars whose angular separations are much more accurately known than the initial bias estimate (see Section 3.3).

Another additional noise source, namely the solar mass uncertainty, was examined, and it was found that increasing this uncertainty by a factor of 10 over the nominal value did not substantially alter the results.

Onboard navigation was found to be useful, under certain conditions, for each of the three classes of missions. It was found to be essential for the comet missions, very valuable for the multiple planet swingbys, and useful under very shallow entry angle conditions for the Jupiter entry missions.

One of the aims of the comet mission studies was to assess the relative contributions of Earth-based telescope and onboard sensor navigation measurements. Results show that Earth-based telescope sightings ultimately limit the navigational accuracy and scale the ΔV magnitudes. Although the Earth telescopes nominally have better accuracy than the onboard system by an order of magnitude, the onboard system will be making measurements from a much shorter range. The Earth-based measurements also determine the ephemeris uncertainty relative to the a priori ephemeris

prediction before onboard sightings are begun, and thus define the space to be searched by the onboard system. Relative position uncertainty of the comet with respect to the spacecraft is essentially given by the residual Earth-based uncertainty which is unsighted by the onboard sensor. This is due to a large uncertainty in the comet dimensions. Because of this limiting accuracy, the onboard sensor does not have to meet stringent accuracy requirements, and the nominal 0.3 arc second Earth-based sighting requires only arcminute like onboard accuracy for compatibility. Because of the importance of Earth-based telescope sightings it is clear that only certain comets at certain revolutions will be suitable objects for rendezvous missions. For example, the Tempel 2 mission presents a very poor Earth-sighting situation for about 140 days surrounding rendezvous. The Sun-Earth-comet angle is less than 45 degrees in this period. The comet Tuttle-Giacobini-Kresak is dim enough to force a very large telescope to work at its very limits to make pre-rendezvous sightings.

Onboard sensors on these missions are faced with extremely weak signals, and can be expected to pick up the comet signal only after the spacecraft is within a few days of rendezvous. Thus a rather small amount of time is available for onboard measurements and measurement data processing. Because of the dimness of these objects an onboard sensor capable of integrating signal will be an important aid to early detection. Because of the need to detect the comets as early as possible to reduce ΔV 's, and because imaging of the comet against a star background is a highly effective navigation measurement, an image tube appears to be the primary candidate for an onboard sensor for comet missions similar to those examined.

It was assumed throughout the bulk of the comet simulations that the comet nucleus would be visible from acquisition through rendezvous. This assumption was based upon previous telescopic sightings. However the case with a nucleus indistinguishable from the coma was also examined, and although the coma radius was more than 1000 times the nuclear radius, it was found that the terminal position uncertainties were still bounded primarily by the limiting Earth telescope sighting accuracy.

The ΔV 's for the comet missions were generally quite large particularly for the T-G-K mission where under the most severe conditions a ΔV of roughly 3 Km/sec was required. However, this value, as well as the other terminal ΔV 's for less severe conditions, is pessimistic since the large ΔV required to effect rendezvous was not considered. A large part of the computed ΔV 's necessary to maintain nominal terminal kinematics could conceivably subtract from the large rendezvous ΔV . Therefore the computed values have to be considered as upper bounds.

Results for the Jupiter entry missions are focused upon the errors and uncertainties in the terminal conditions at the nominal entry point. Entry velocity, angle and altitude are of interest. The guidance errors in these quantities are determined by the navigation uncertainties at the time of the last course correction, or by the time of the last navigation measurement if that should occur earlier than the last course correction. Both the timing of the last ΔV and the last navigation measurement were examined with regard to their effects on the entry guidance errors. It was found that the timing of the last navigation measurement is of primary importance, and that at about E-2 days the entry condition errors begin to increase rapidly with earlier navigation shutdown. For example the angle error jumps to 0.5 degrees at E-10 days from a value of .075 at two days.

An onboard navigation system could potentially fill two roles on a mission of this type. First of all, if it were autonomous, and if it was necessary to turn off the DSN early for scientific purposes, then the onboard system could continue to gather navigation data closer to Jupiter thus reducing the entry errors. Secondly, if a very shallow entry angle was of interest, a limb sensor would be important for establishing the direction to the limb and thus for controlling the entry angle.

The three planet swingby studies were an extension of work reported in Volume I which examined a two planet swingby and a four planet grand tour. The present studies sought to determine whether or not the relative utility of onboard navigation is altered when onboard sensor process noise is added to the model. Also the effects of increased onboard measurement

frequency, increased DSN doppler noise, and restricted star fields were considered. The use of TV type navigation measurements sighting on the planetary satellite was examined.

The results show that onboard navigation remains extremely useful in spite of the added onboard sensor bias error. The periplanet position uncertainty at Pluto, for example, is about 100 Km with onboard navigation compared to 9000 Km for the unaided DSN system. Navigation measurements made on the angle between a star and the near planet using a scanning device appear to be closely comparable to those made with an image tube measuring planetary satellite - star angles. The scanning device is however dependent upon DSN to some degree in the modeled mode of operation, and the image tube finds an absence of satellites at Pluto. Both devices also can serve as valuable science instruments. Increased DSN doppler noise (by an order of magnitude) was found to have only a moderate effect on DSN performance during planetary passage, but had a large nearly proportional effect on interplanetary position uncertainties. Alteration of the onboard measurement frequency was found to have nearly an inverse effect on periplanet position uncertainty within the examined frequency range.

It was hypothesized early in these studies that a restricted star field would have little effect on the performance of an onboard navigation scanning device, but the results show that star field restrictions have to be carefully made if the device performance is to remain relatively unchanged.

A final general conclusion relating to all the missions is that a recasting of the filter equations in a square root formulation avoids the numerical difficulties that were associated with round-off errors under the old formulation. This procedure is discussed in Appendix J.

4.2 RECOMMENDATIONS

The study results presented here have been parametric and aimed at establishing the limits of guidance errors, navigation uncertainties, and velocity corrections. A logical next step in preparing for outer planet or comet missions is to select specific missions and proceed with their

optimization. From a guidance and navigation standpoint this optimization would involve the design of an optimal guidance law and minimization of trajectory correction fuel requirements. A specific navigation sensor configuration would be selected, constraints defined, and an optimal navigation measurement schedule established.

REFERENCES

1. Hamilton, T.W., Melbourne, W.G., "Information Content of a Single Pass of Doppler Data from a Distant Spacecraft", Jet Propulsion Laboratory Space Programs Summary 37-39, Vol. III, March - April 1966, Pasadena California.
2. Duxbury, T.C., Ohtakay, H., "In Flight Calibration of a Navigation Instrument", AIAA Guidance Control and Flight Mechanics Conference, Santa Barbara California, August 1970.
3. Duxbury, T.C., Breckenridge, "Mariner Mars 1969 Optical Approach Navigation", AIAA 8th Aerospace Sciences Meeting, New York, N. Y., January 1970.
4. Duxbury, T.C., "A Spacecraft-Based Navigation Instrument for Outer Planet Missions", AIAA/AAS Astrodynamics Conference, Princeton, New Jersey, August 1969.
5. Duxbury, T.C., Private Telephone Communication with H. Malchow MIT Charles Stark Draper Laboratory, March 1971.
6. Manning, L.A., "Letter to D. C. Fraser of MIT C. S. Draper Laboratory, "NASA/OART Mission Analysis Division, July 7, 1970.
7. Manning, L.A., "Letter to J. H. Flanders of MIT C. S. Draper Laboratory, "NASA/OART Mission Analysis Division, August 5, 1968.
8. Dollfus, A., "New Optical Measurements of the Diameter of Jupiter, Saturn, Uranus and Neptune", Icarus, Vol. 12, 1970, pp. 101-117.
9. Dollfus, A. (Ed.), Surfaces and Interiors of Planets and Satellites, Academic Press, New York, 1970.

10. Melbourne, W., et. al., "Constants and Related Information for Astrodynamic Calculations, 1968", NASA Technical Report No. 32-1306, July 1968.
11. Marsden, B., Private Report to MIT/DL on Cometary Trajectory Analysis, June 1971.
12. Roemer, E., Memoirs of the Royal Society of Liege, Vol. 12, pg. 23, July 1965.
13. Pace, G., "UBV-Subroutine to Compute Photometric Magnitudes of the Planets and their Satellites," JPL TR/523, February 1971.
14. Quarterly Journal of the Royal Astronomical Association, Vol. 4, No. 3, September 1962.
15. Quarterly Journal of the Royal Astronomical Association, Vol. 9, No. 3, September 1967.
16. Ramsey, R.C., "Spectral Irradiance from Stars and Planets, above the Atmosphere, from 0.1 to 100.0 Microns," Applied Optics, Vol. 1, No. 4, July 1962.
17. Wells, W.C., IIT Research Institute, Personal Communication to C.H. Acton of JPL, November 6, 1973.
18. Burt, R.B. and Jolliffe, S.A.W., Starfield Recognition Using Television Techniques, Institute of Electrical Engineers Paper No. 3990 E, June 1963.
19. Johnson, W.M., "Star Set Selection Routine for a Stellar-Inertial Reference System," MIT/DL Report No. E-2061, November 1968.

20. Stanton, R.H., "Challenger in Developing an Approach Guidance Instrument for the Outer Planets", American Astronautical Society Paper No. AAS-71-119, June 29, 1971.
21. Weimer, P.K., et. al., Photoelectronic Imaging Devices, Vol. II, pg. 453, Plenum Press, New York, 1971. (L.M. Biberman Ed.)
22. Solomon, P.M., "Applications of Slow-Scan Television Systems to Planetary Exploration", Journal of the SMPTE, Vol. 79, July 1970.
23. Jazwinski, A., Stochastic Processes and Filtering Theory, Academic Press, 1970.
24. Fourth Quarterly Progress Report, Contract NAS 9-10386, Chapter 1, C. S. Draper Laboratory, April 30, 1971.
25. R. Battin, Astronautical Guidance, McGraw-Hill, New York, N. Y., 1964.

APPENDIX A

EXPLANATION OF GEOMETRY PLOTS

The purpose of this appendix is to explain the use of the plots given in Appendices B-G to obtain the geometrical properties of the interplanetary and planetary passage legs of the missions used as examples in this study. The plots included herein are invaluable to the scheduling of the onboard navigation system. In addition, they display mission phenomena such as distances to navigational targets and sun angles which are basic to the design and implementation of the onboard navigation system. Section A.1 will describe the interplanetary trajectory plots which give an overall view of the mission. The planetary passage plots described in Section A.2 show the geometry of the mission at the critical hours near pericenter.

A.1 INTERPLANETARY TRAJECTORY GEOMETRIES

The first plot shown in each Appendix displays the overall mission geometry and is used primarily to provide geometrical support for the other plots. The markings on the spacecraft and planet trajectories are at the same equal time intervals to aid in determining the relative positions of the planets and spacecraft. Circles and arcs of circles represent planetary orbits with the innermost representing the orbit of the Earth. The rather elliptical orbits shown in Figs. B-1 and C-1 are those of the comets.

There are four additional plots for each interplanetary leg. The first plot in each group gives the range to the planets of possible interest. This is valuable for deciding which planet to use for navigation sightings as the spacecraft proceeds along its trajectory. In the absence of other constraints which would prohibit the measurement, those measurements which employ the closest near body are potentially the most useful. This plot is also used to decide during what periods the various planets are too far away to detect with an IR instrument and to provide the navigation system design with information about the target ranges his sensors must deal with.

The second plot in each series gives the spacecraft-Earth-sun angle. The purpose of this plot is to identify those phases of the mission where the spacecraft line of sight (from Earth) comes too close to the sun line of sight to permit tracking of the vehicle from Earth. A check of all these plots reveals the fact that there are very few times when the ground based antennas will not be able to track the spacecraft because it is behind the sun. Note that only on the Uranus approach of the Neptune Grand Tour and on the Saturn approach of the Pluto Grand Tour does one of these periods even come close to an encounter time.

The third graph in each group provides the sun-spacecraft-planet angle for each leg. This is of much use in setting up the onboard measurement schedule because it displays those periods in which the line of sight to the planet is too close to the line of sight to the sun to permit use of the planet for navigational purposes. It also informs the sensor designer what range of sun angles his instrument will encounter.

The final plot in each group gives the Earth-spacecraft-planet angle for each leg. This is of interest to the systems designer because he must be aware of the relative location of the planet and Earth so that functions related to each body can be coordinated. As an example of such coordination, consider the problem of orienting the spacecraft, communications antenna, star tracker, and/or planet sensor such that a navigational sighting can be performed without losing communication with the Earth.

An example of using these plots to create a candidate onboard measurement schedule is given in Appendix A of Volume II.

A.2 PLANETARY PASSAGE TRAJECTORY GEOMETRIES

The planetary passage plots present those physical parameters which are indispensable for a preliminary analysis of the use of an onboard navigation system during the period in which the spacecraft is well within the sphere of influence of a planet. These characteristics are illustrated here for the planetary encounters of four of the six missions used as examples in the study. The Jupiter passage plots for the comet missions are omitted because on these missions ground tracking is used exclusively

until the spacecraft is near the comet. The value of the data contained in these plots should not be underestimated - the overall scheduling and measurement selection which can be performed with this information can eliminate the need for a costly computer search through a much larger set of possible measurement combinations.

The format of the presentation of the planetary passage geometries presented in this appendix is a sequence of from five to seven plots for each mission depending upon the existence of moons of this planet.

The first plot in each series is a plan view of the hyperbolic pass of the planet. It provides an overall view of the passage. The direction of the sun is indicated in each case. By using this plot, one determines which is the sunlit side of the terminator line (shown drawn on the planet). In all cases passage is from right to left around the planet, thus in the Saturn case the approach is made from the direction of the sun. This results in an approach to the light side and a retreat from the dark side of the planet. In the case of Saturn, the inner edge of the rings is drawn on the plan view. The dotted edge is below the plane of the paper. The plan view is also useful for determining when star occultations might be available. Star occultations are potentially useful measurements only when the relative motion is such that a dark edge of the planet passes into the star field. Note that until the spacecraft is very close to the planet there is little relative motion of this type. If the planet has an atmosphere, as the outer planets have, the intersection of the star with the edge of the planet must occur far enough from the terminator line so that there is no light leakage. If we assume a central angle value of about 20° for this distance, we see that when the approach is made from out of the sun there isn't much opportunity to find good star occultations. The final use to be mentioned here is that by simply noting whether a light edge is available at any given time one can determine whether or not an IR capability is required to make a measurement at that time.

The second plot in each group gives the range to the planet in planet radii and kilometers. Note that in each case very little time is spent close to periplanet. Use of this plot together with the ranges to the planetary

satellites given in the sixth plot of each group, enables one to determine whether or not a satellite might be a better navigational target than the planet. This could be the case if the distance to the satellite is much less than the distance to the planet.

The third graph gives the angle subtended by the planet versus time. Again the tremendous speed at which the probe passes periplanet is apparent from this plot. This plot and the previous one have much meaning to the instrument designer as they provide information on the size and distance of the near body. In addition, this plot is useful to determine during what period planet diameter measurements will be useful. The geometry is favorable only during the time the subtended angle is large - which isn't very long.

The fourth plot gives the Earth-probe-planet angle. Besides giving information to the systems designer and mission planner, this plot reveals during what period the spacecraft is behind the planet as viewed from Earth. Note that it is never occulted for more than a few hours. Of equal interest is the sun-spacecraft-planet angle. It is extremely useful to onboard system scheduling because it reveals when the lines of sight to the planet and sun are too close to permit using the planet for sightings. For the near planet passages this doesn't occur for any significant length of time. Because this angle is very similar to the Earth-spacecraft-planet angle, becoming more so as one gets farther from Earth, it was decided to print only the first plot.

The sixth plot in each group gives the ranges to the principle satellites of each planet. A use of this plot was discussed above in conjunction with the planetary range figure. The code for the satellites is given in Table A-I. For example, moon 1 at Jupiter is Io. It is interesting to note that on the Jupiter passage of the Neptune Grand Tour the approach to Europa is actually closer than to the planet itself. The mission might be planned either to avoid such a close encounter in order to limit the perturbation on the trajectory, or to capitalize upon it for scientific information. In either case, the orbital period of Jupiter's satellites is so small compared to the trip time to Jupiter that fixed-time-of-arrival guidance would be a necessity for mission success.

TABLE A-I

Code For Planetary Satellites

Planet	Satellite	Code Number
Jupiter	Io	1
	Europa	2
	Ganymede	3
	Callisto	4
Saturn	Titan	1
Uranus	Ariel	1
	Umbriel	2
	Titania	3
	Oberon	4
Neptune	Triton	1

The seventh graph in each group gives the moon-spacecraft-planet angle and thus reveals the location of the satellite relative to the planet. Although satellite-planet measurements have been eliminated due to the large phenomena error that would result, this plot is still useful because it identifies those times when the satellite is not visible from the spacecraft. The sun-satellite-spacecraft angle is used to determine whether or not the satellite is sunlit at a potential navigation sighting time. This information, which is given in the seventh plot of each group, reveals whether or not an IR capability is required to make a measurement.

The final plot in each group gives the sun-probe-satellite angle. This has precisely the same uses as the sun-probe-planet angle. For example, it would be possible for a moon to be close enough to be useful but for the line of sight to the moon to be too close to the line of sight to the sun for useable measurement.

The purpose of this study has been to determine the effects caused by varying a given parameter. Consequently, an effort was made to hold constant as many other factors as possible. For this reason, it was decided to use only star elevation measurements. Although these plots did not effect the measurement choice they were highly instrumental in making up the measurement schedule and were invaluable in understanding the mission geometry.

APPENDIX B

TEMPEL- 2 MISSION PLOTS

This appendix contains the plots for the Tempel II Mission. An explanation of their use is given in Appendix A.

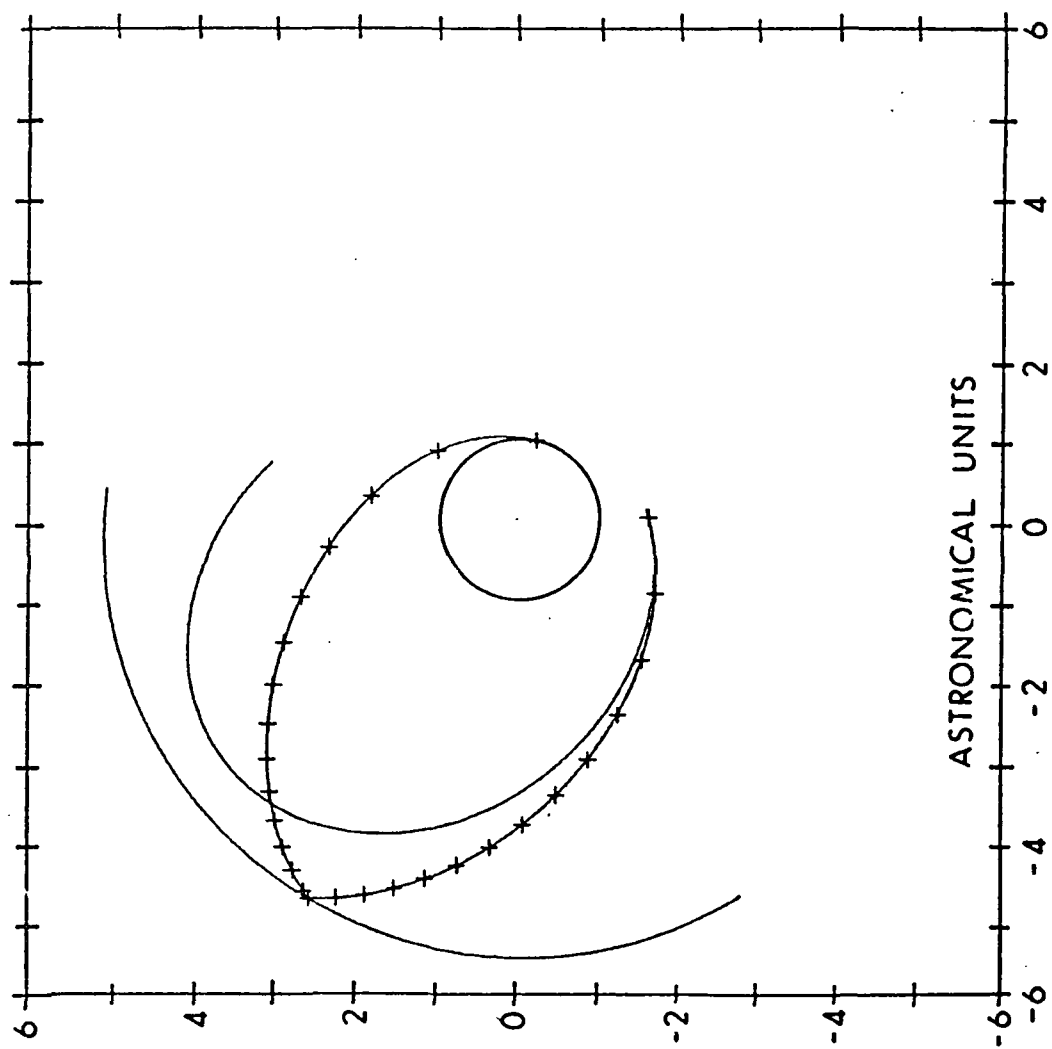


Fig. B-1 Trajectory for Tempel 2 Mission

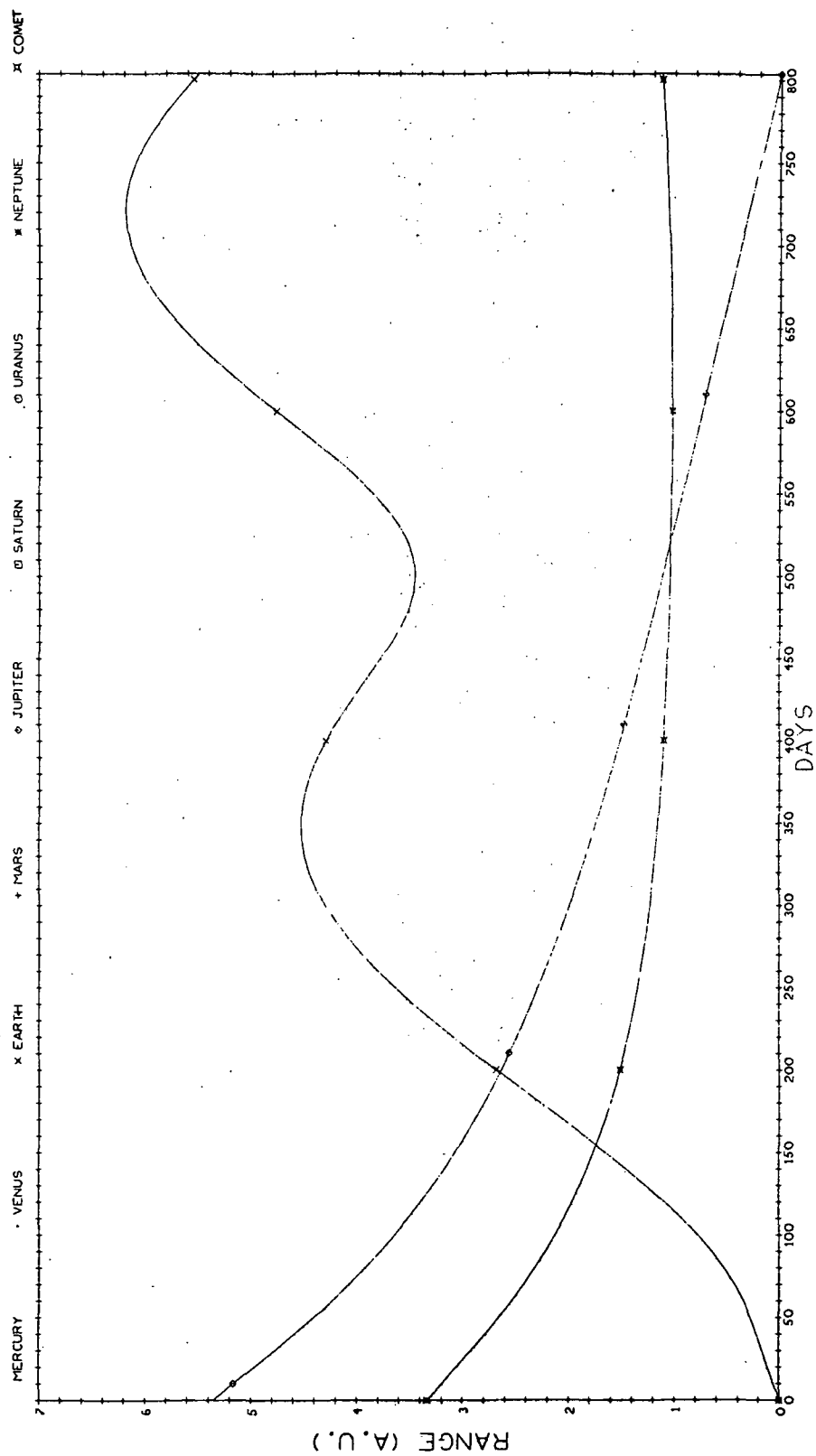


Fig. B-2-1 Ranges to Planets for the Interplanetary (Earth-Jupiter) Leg of the Tempel 2 Mission

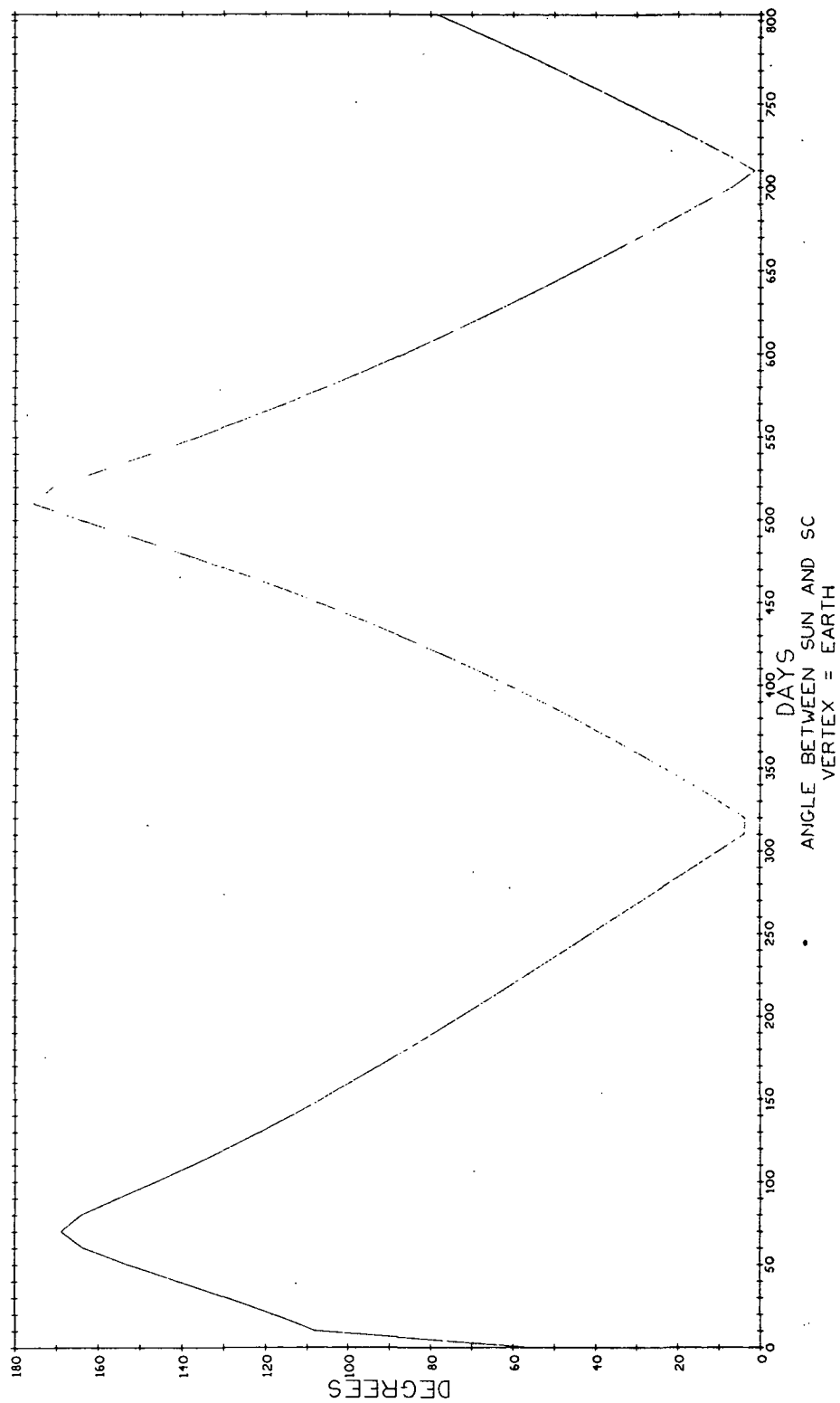


Fig. B-2-2 Spacecraft-Earth-Sun Angles for the Interplanetary (Earth-Jupiter) Leg of the Tempel 2 Mission

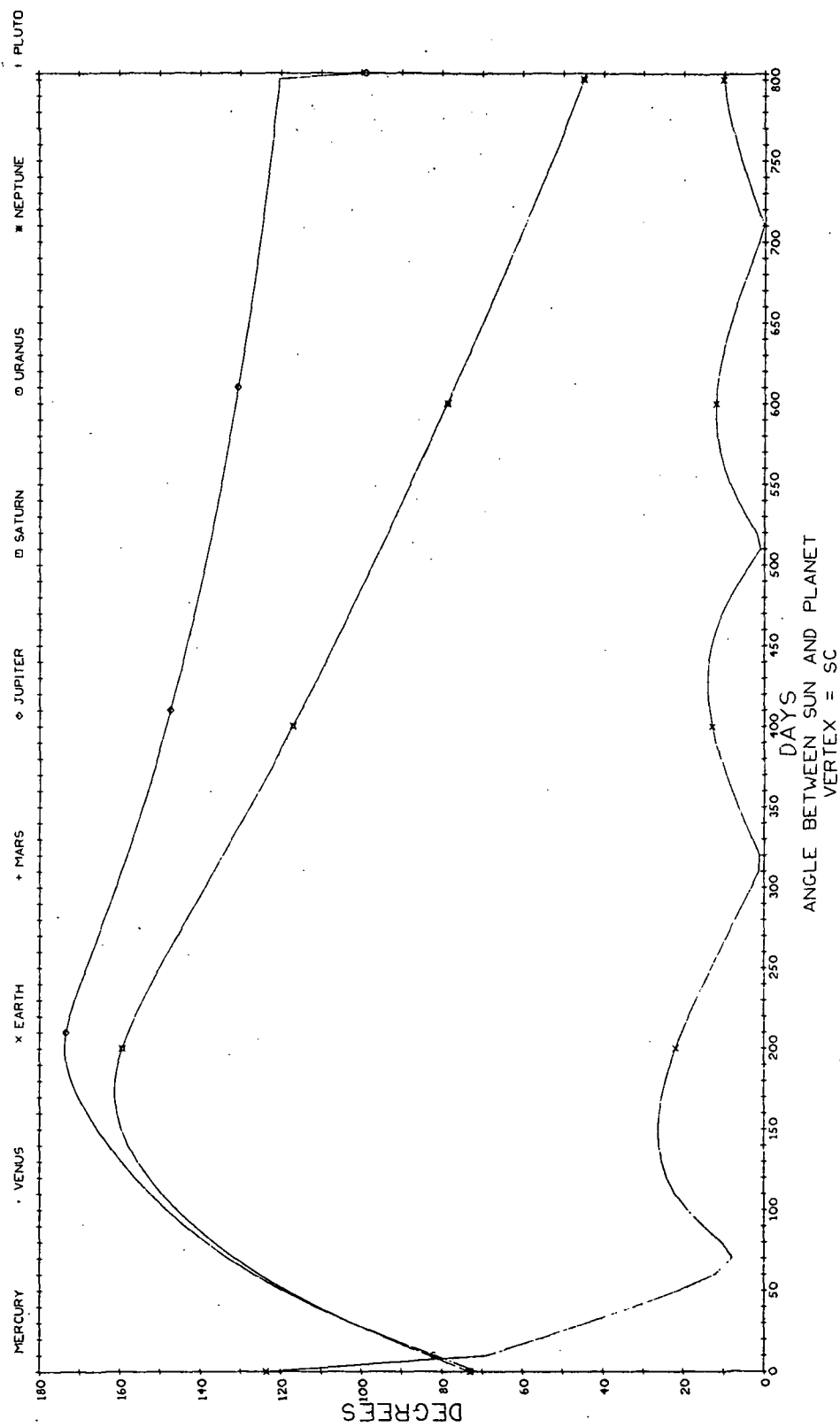


Fig. B-2-3 Sun-Spacecraft-Planet Angles for the Interplanetary (Earth-Jupiter) Leg of the Tempel 2 Mission

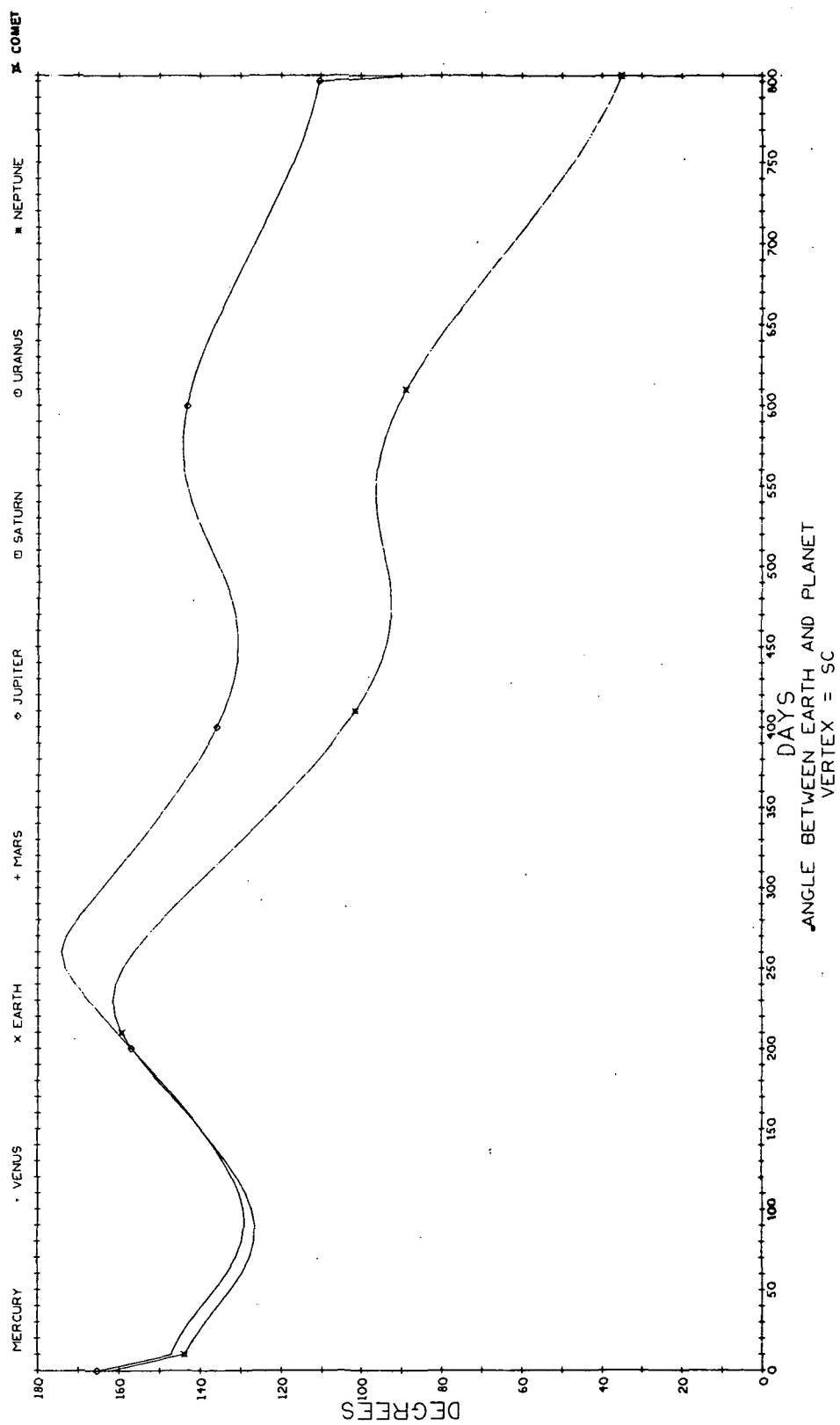


Fig. B-2-4 Earth-Spacecraft-Planet Angles for the Interplanetary (Earth-Jupiter) Leg of the Tempel 2 Mission

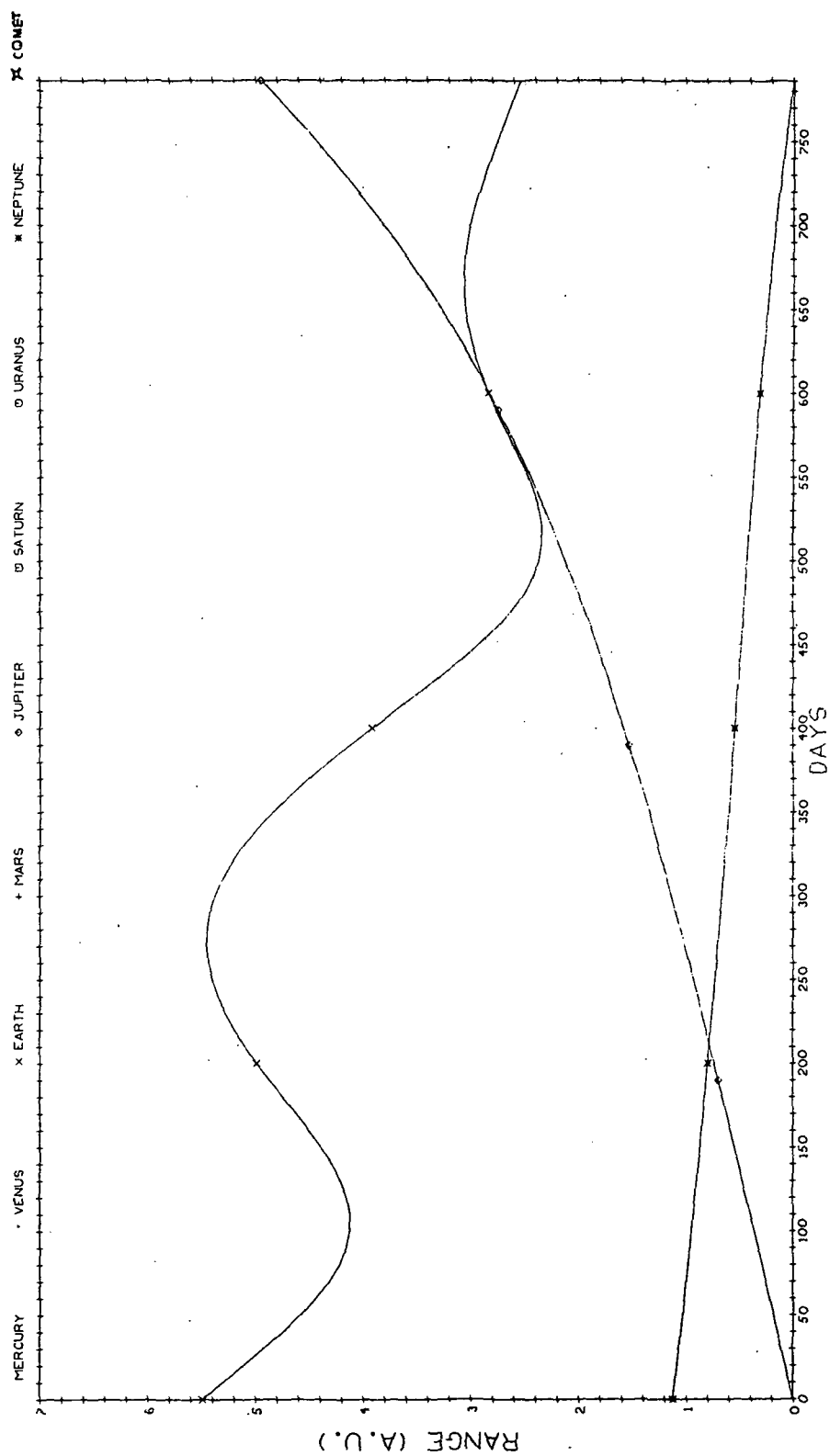


Fig. B-3-1 Ranges to Planets for Interplanetary (Jupiter-Comet) Leg of the Tempel 2 Mission

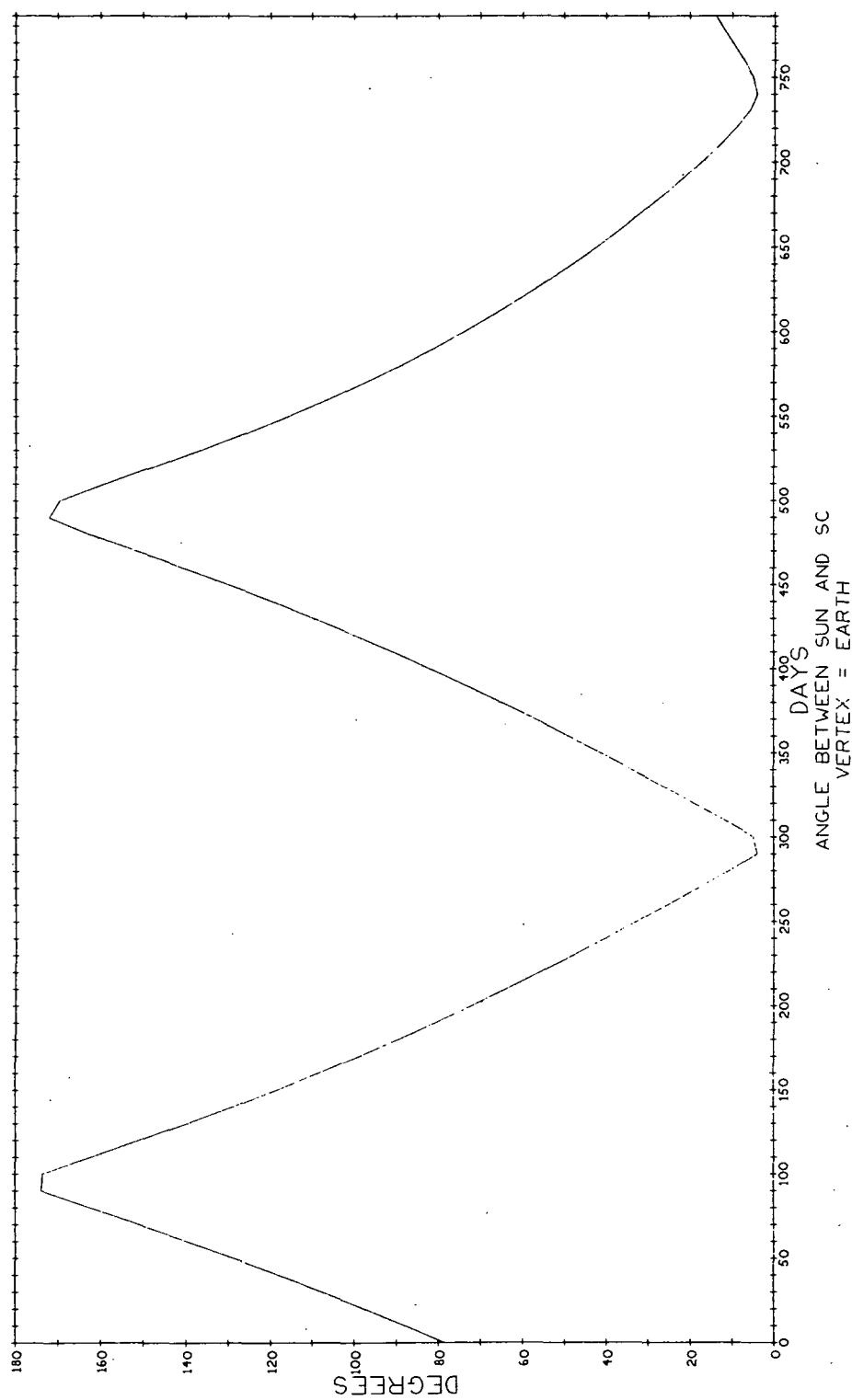


Fig. B-3-2 Spacecraft-Earth-Sun Angle for the Interplanetary (Jupiter-Comet) Leg of the Tempel 2 Mission

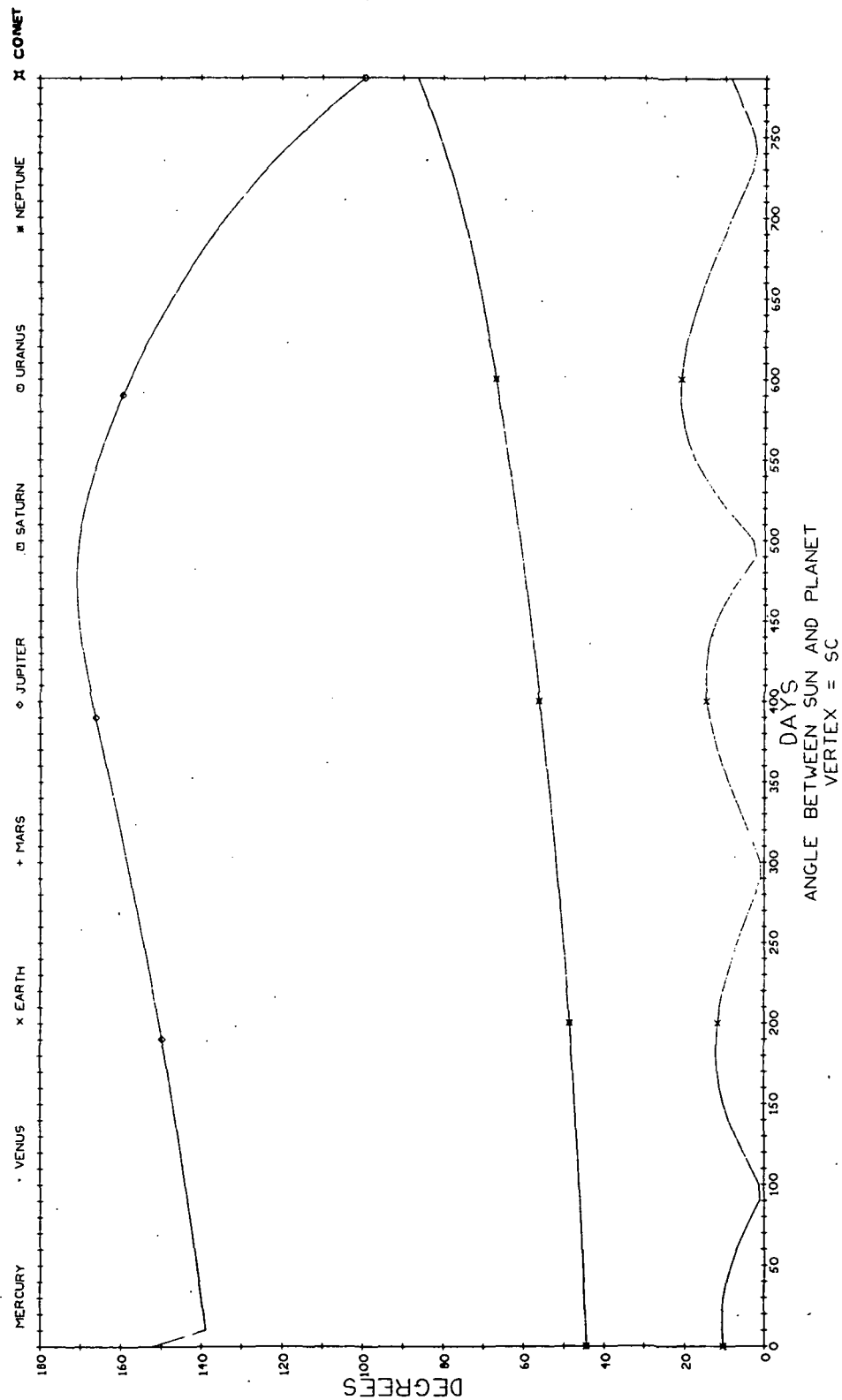


Fig. B-3-3 Sun-Spacecraft-Planet Angles for the Interplanetary (Jupiter-Comet) Leg of the Tempel 2 Mission

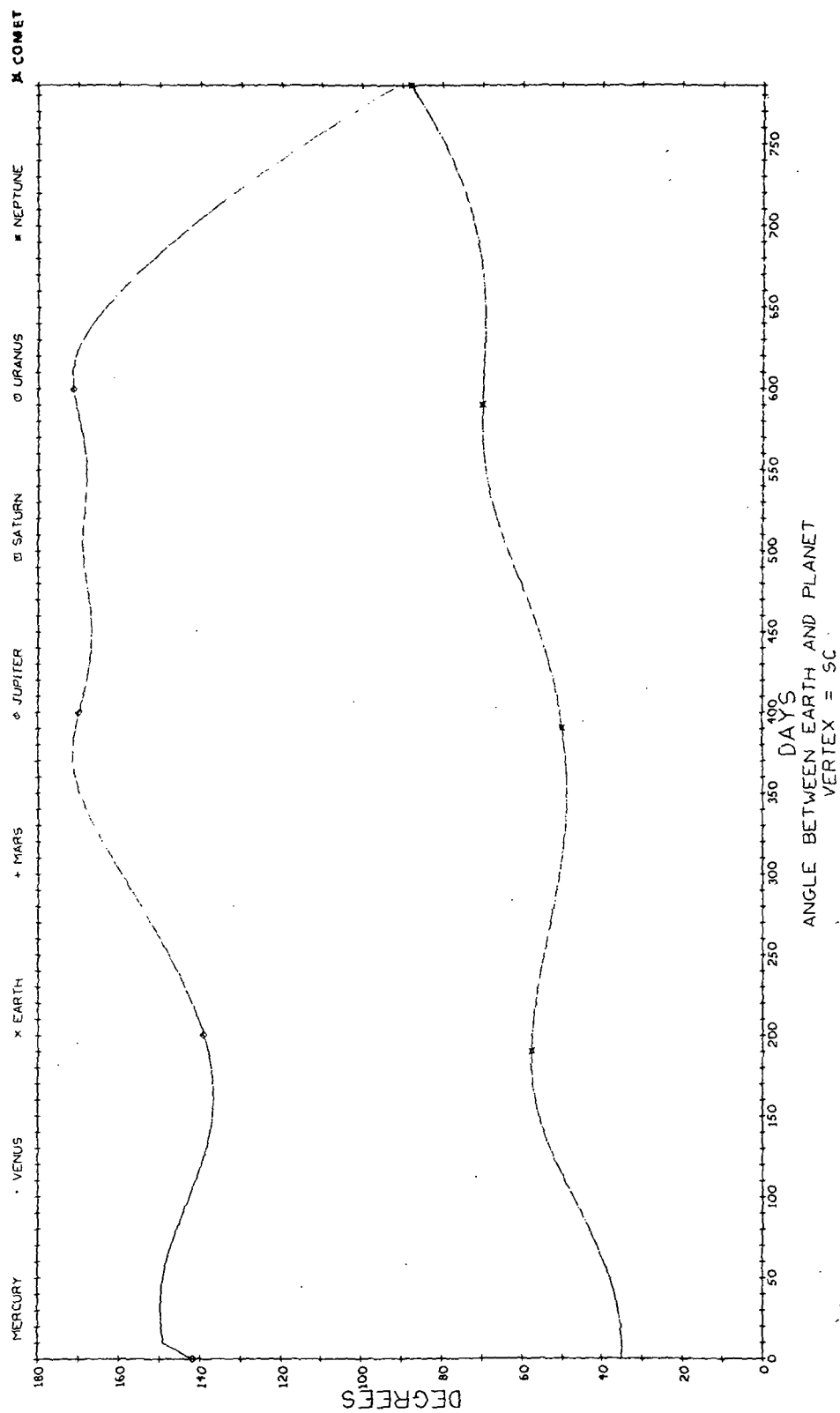


Fig. B-3-4 Earth-Spacecraft-Planet Angles for the Interplanetary Leg (Jupiter-Comet) of the Tempel 2 Mission

APPENDIX C

TUTTLE-GIACOBINI-KRESAK MISSION PLOTS

This appendix contains the plots for the Tuttle-Giacobini-Kresak Mission. An explanation of their use is given in Appendix A.

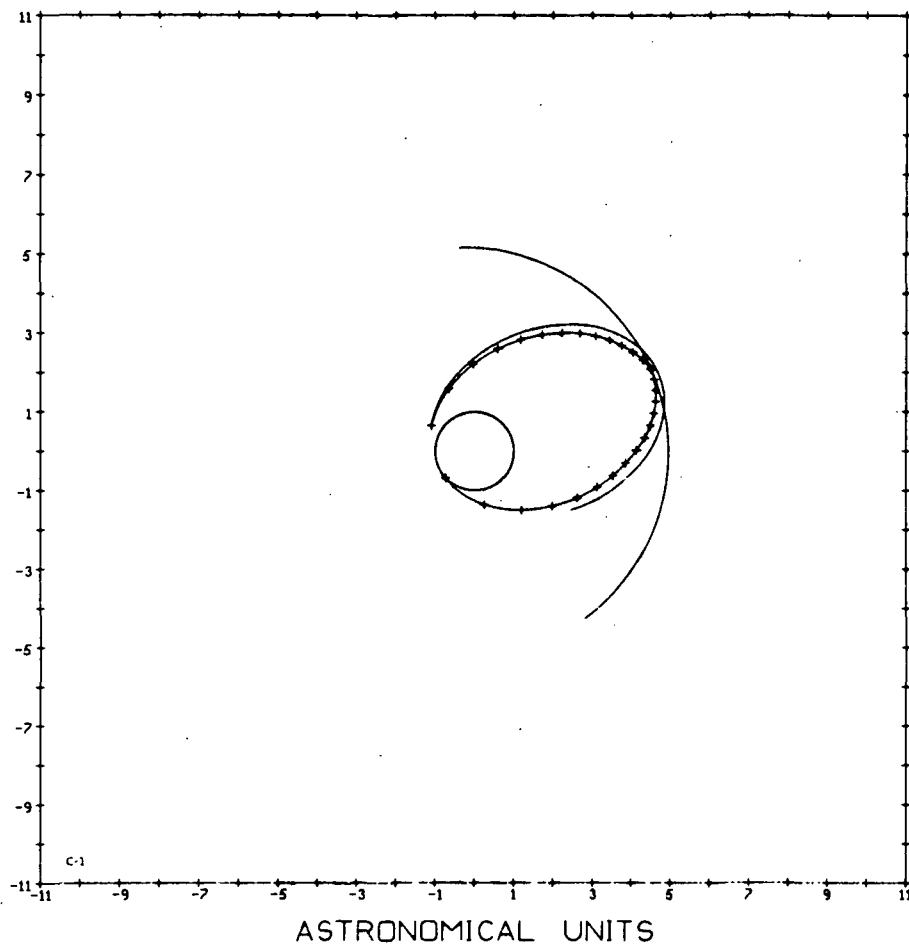


Fig. C-1 Trajectory for Tuttle-Giacobini-Kresak Mission

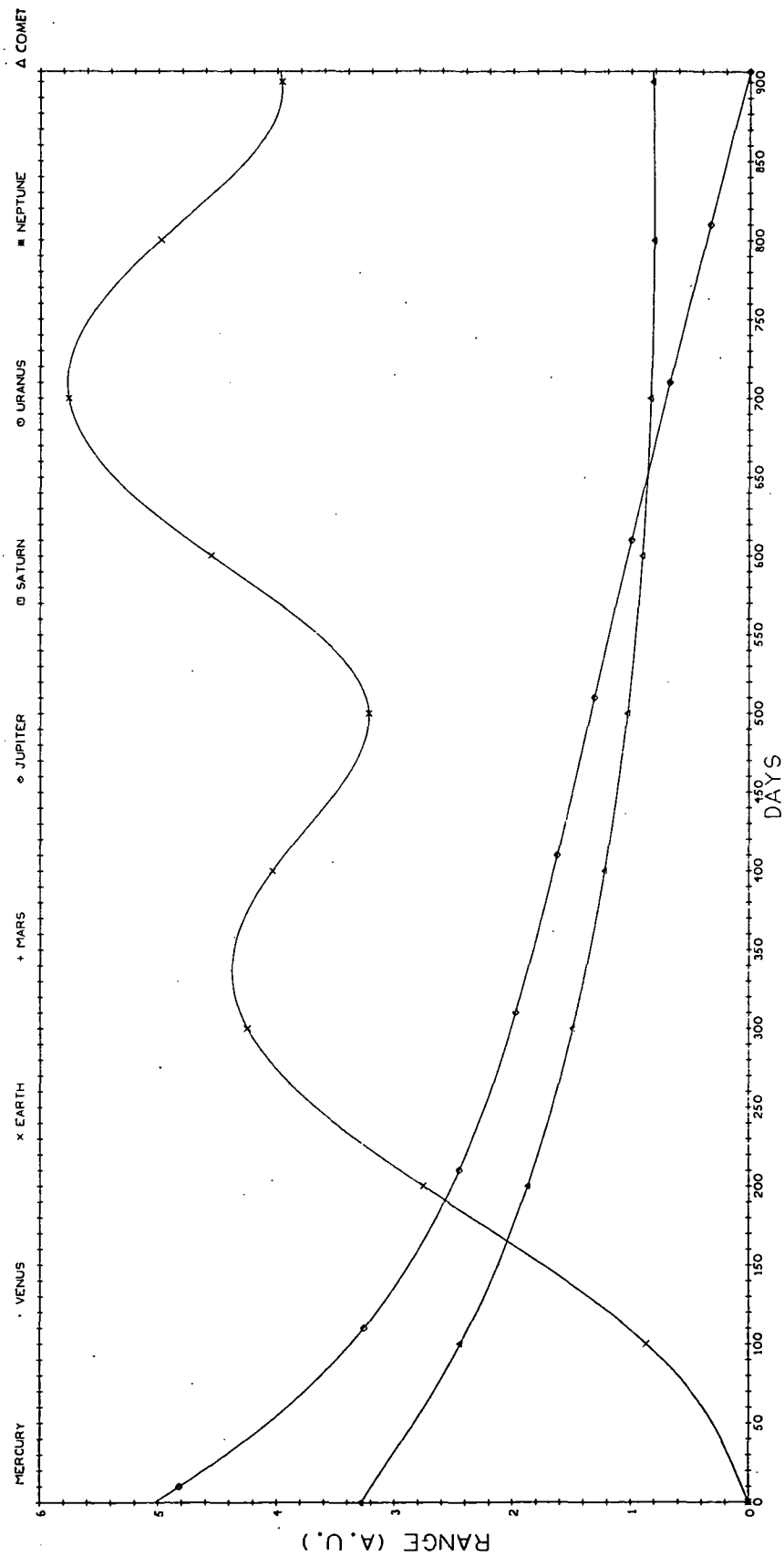


Fig. C-2-1 Ranges to Planets During Earth-Jupiter Interplanetary Leg on the Tuttle-Giocobini-Kresak Mission

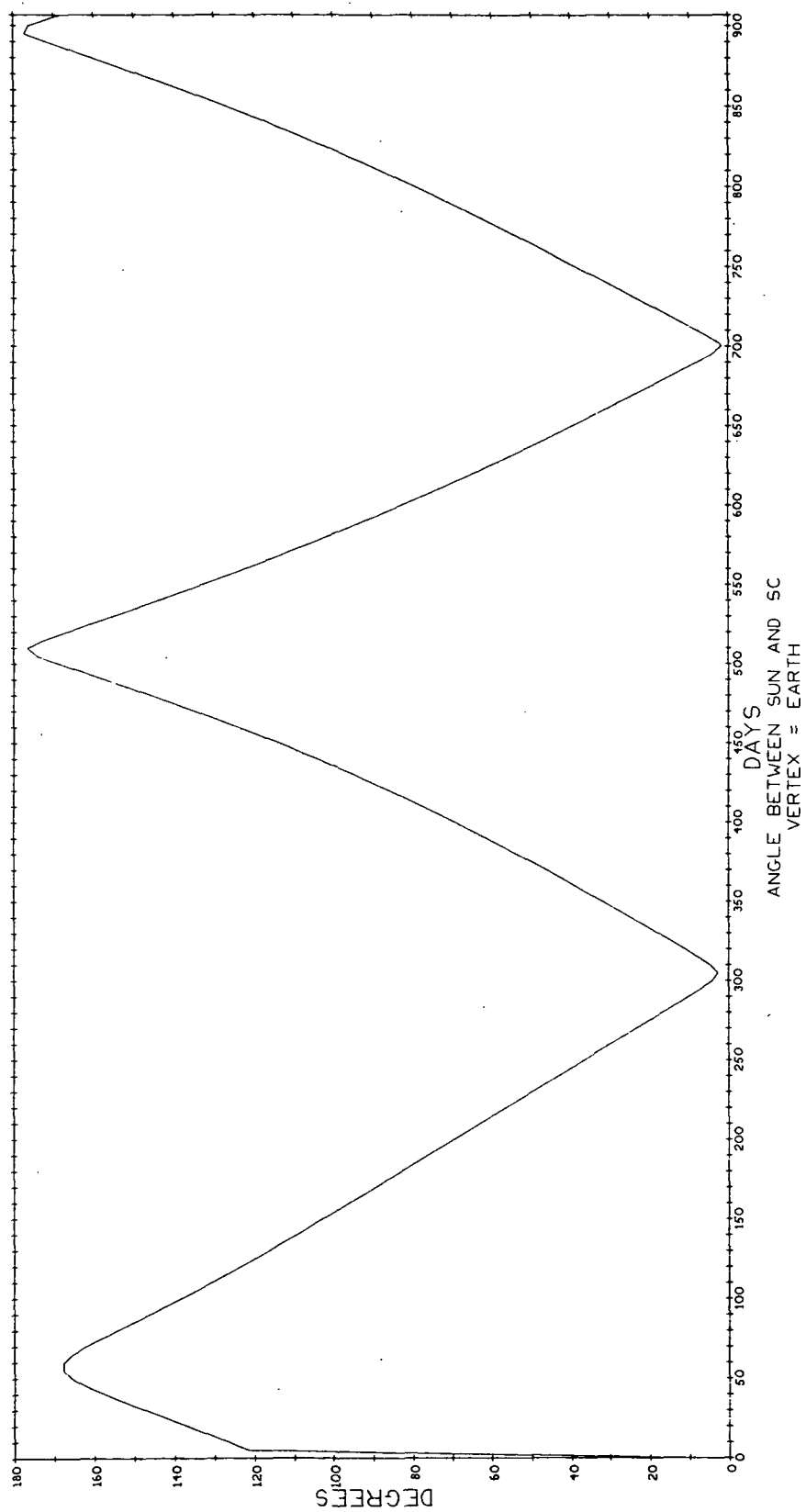


Fig. C-2-2 Spacecraft-Earth-Sun Angle During Earth-Jupiter Interplanetary Leg of the Tuttle-Giobolini-Kresak Mission

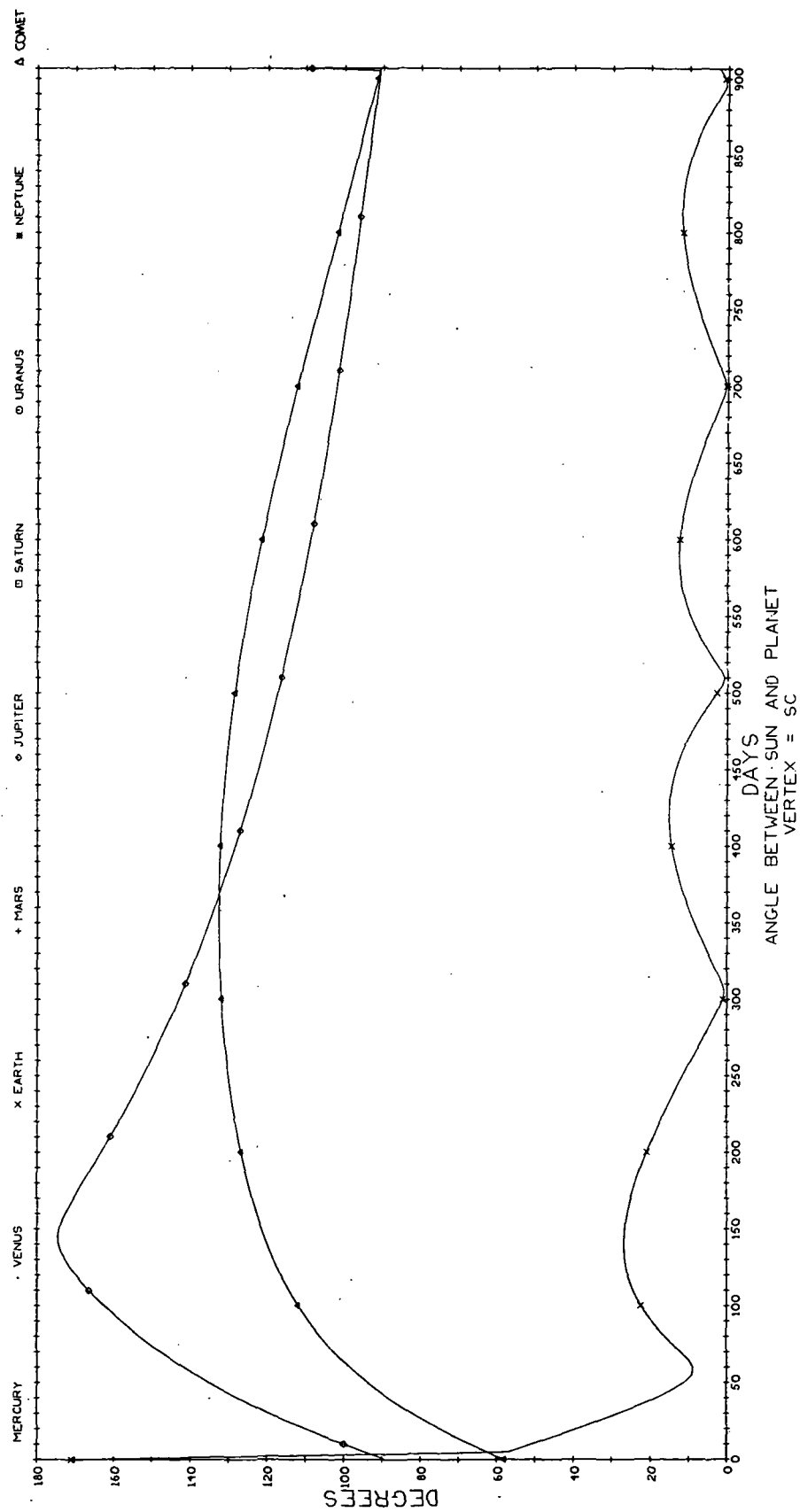


Fig. C-2-3 Sun-Spacecraft-Planet Angles During Earth-Jupiter Interplanetary Leg of the Tuttle-Giobolini-Kresak Mission

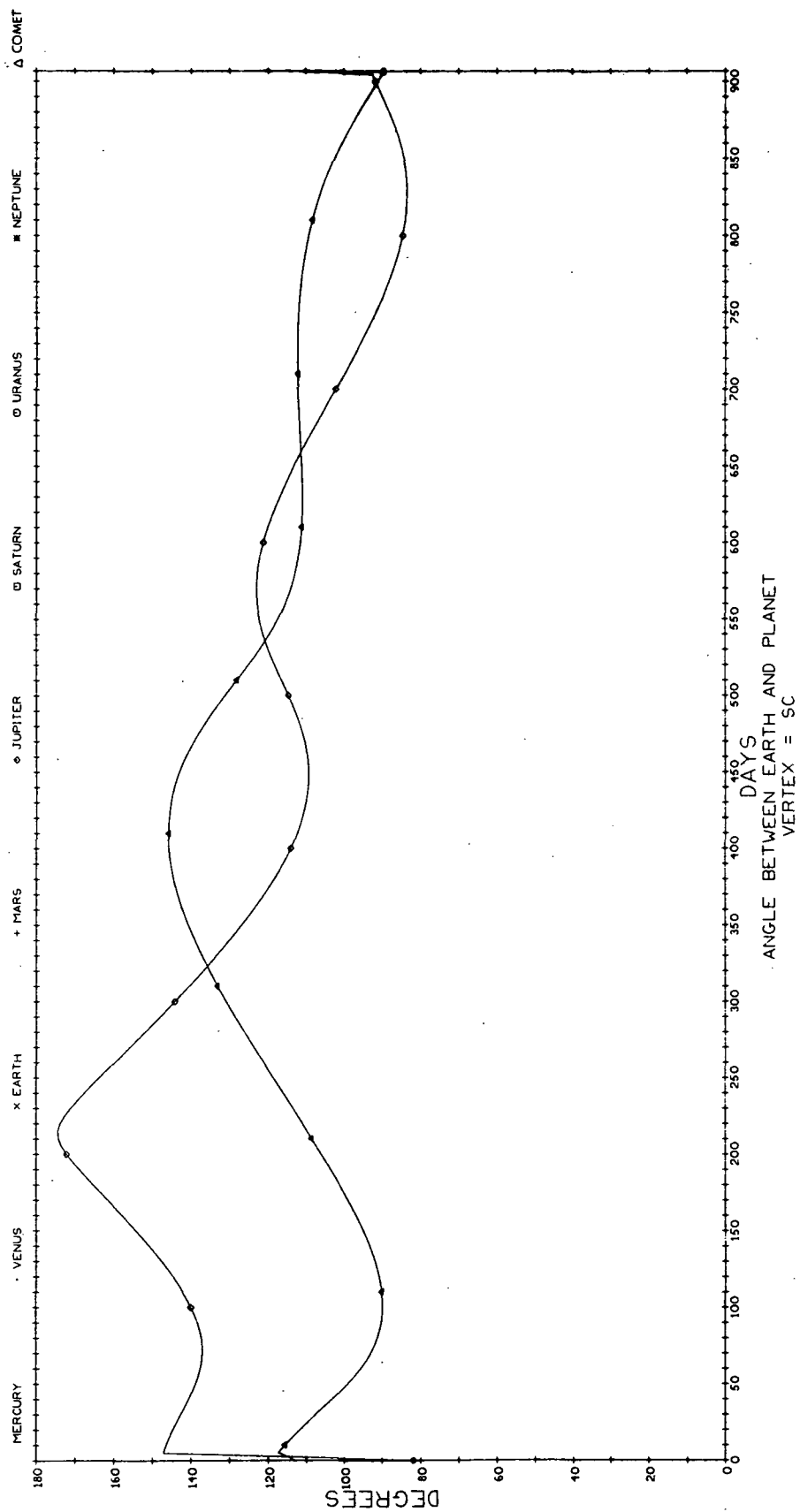


Fig. C-2-4 Earth-Spacecraft-Planet Angles During the Earth-Jupiter Interplanetary Leg of the Tuttle-Giacobini-Kresak Mission

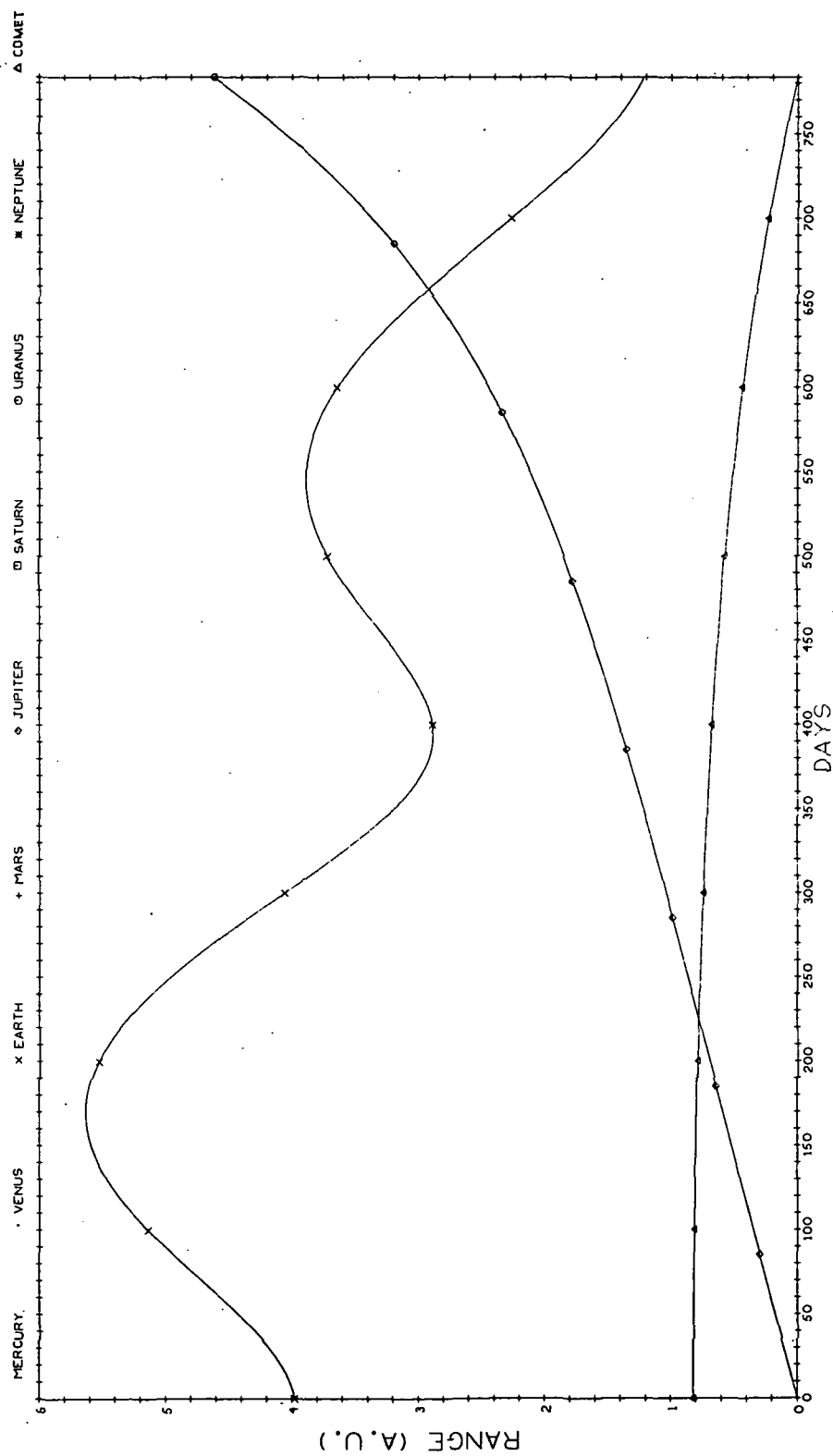


Fig. C-3-1 Ranges to Planets During Jupiter-Comet Interplanetary Leg of the Tuttle-Giacobini-Kresak Mission

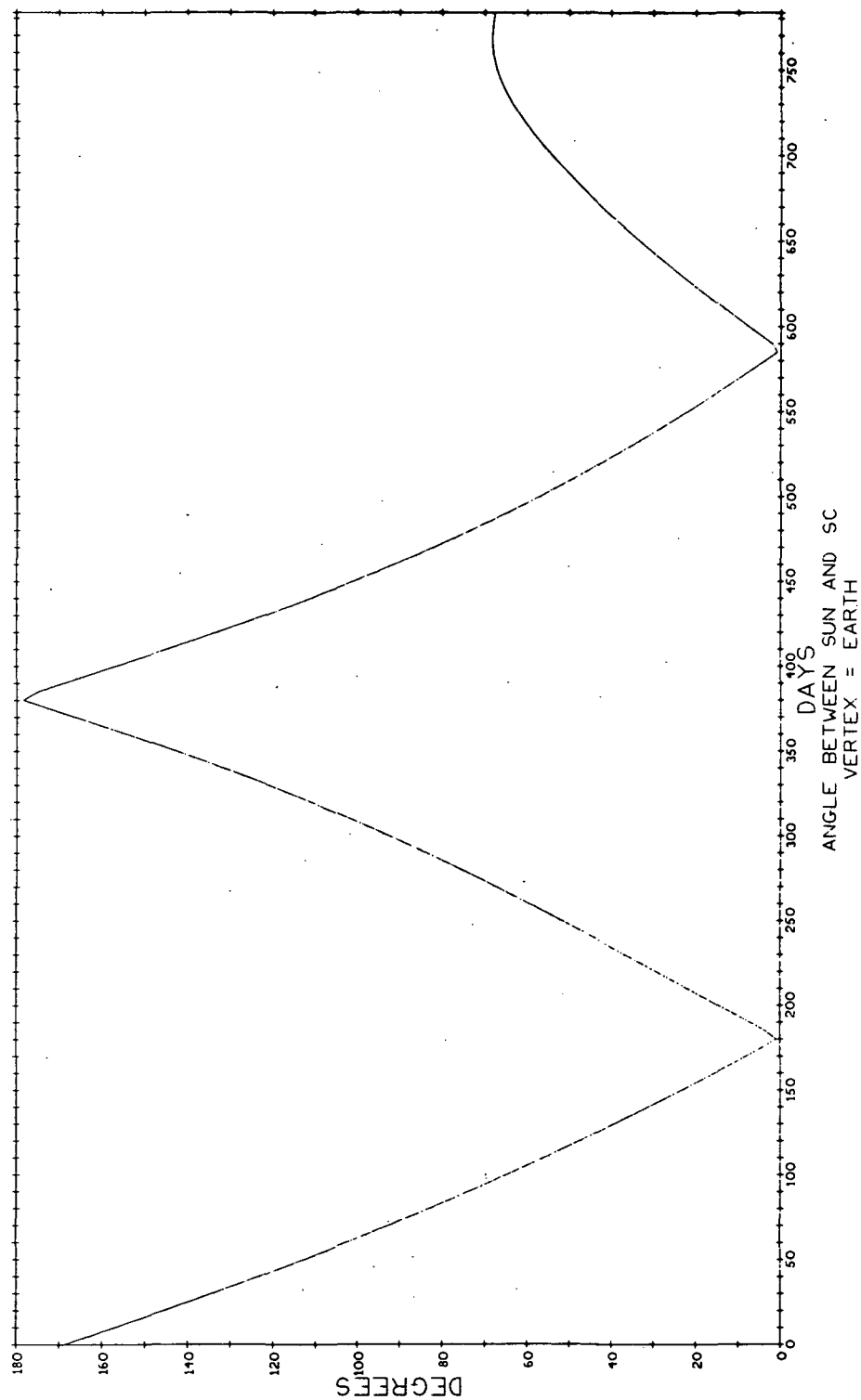


Fig. C-3-2 Spacecraft-Earth-Sun Angle During Jupiter-Comet Interplanetary Leg of the Tuttle-Giacobini-Kresak Mission

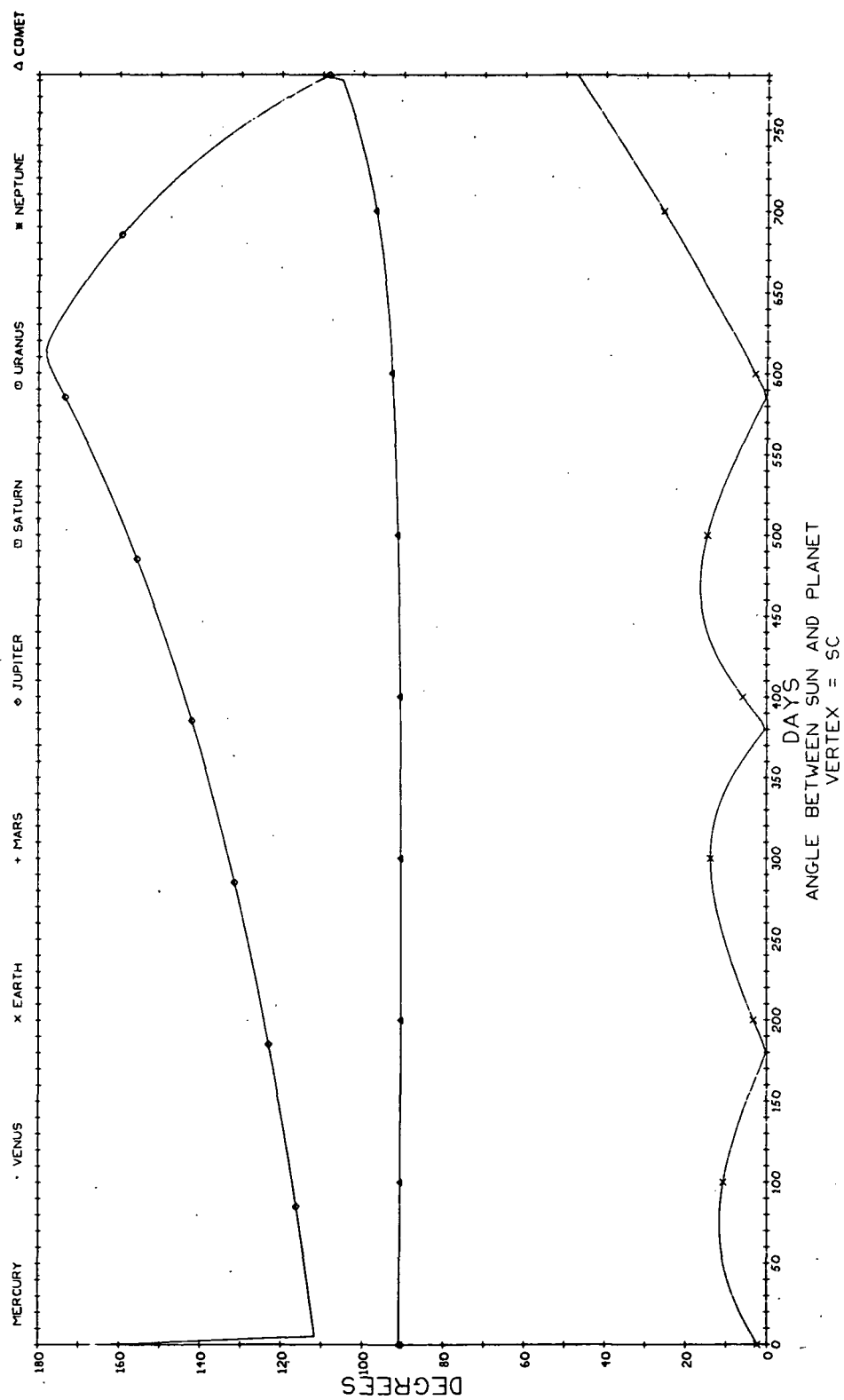


Fig. C-3-3 Sun-Spacecraft-Planet Angle During Jupiter-Comet Interplanetary Leg of the Tuttle-Giacobini-Kresak Mission

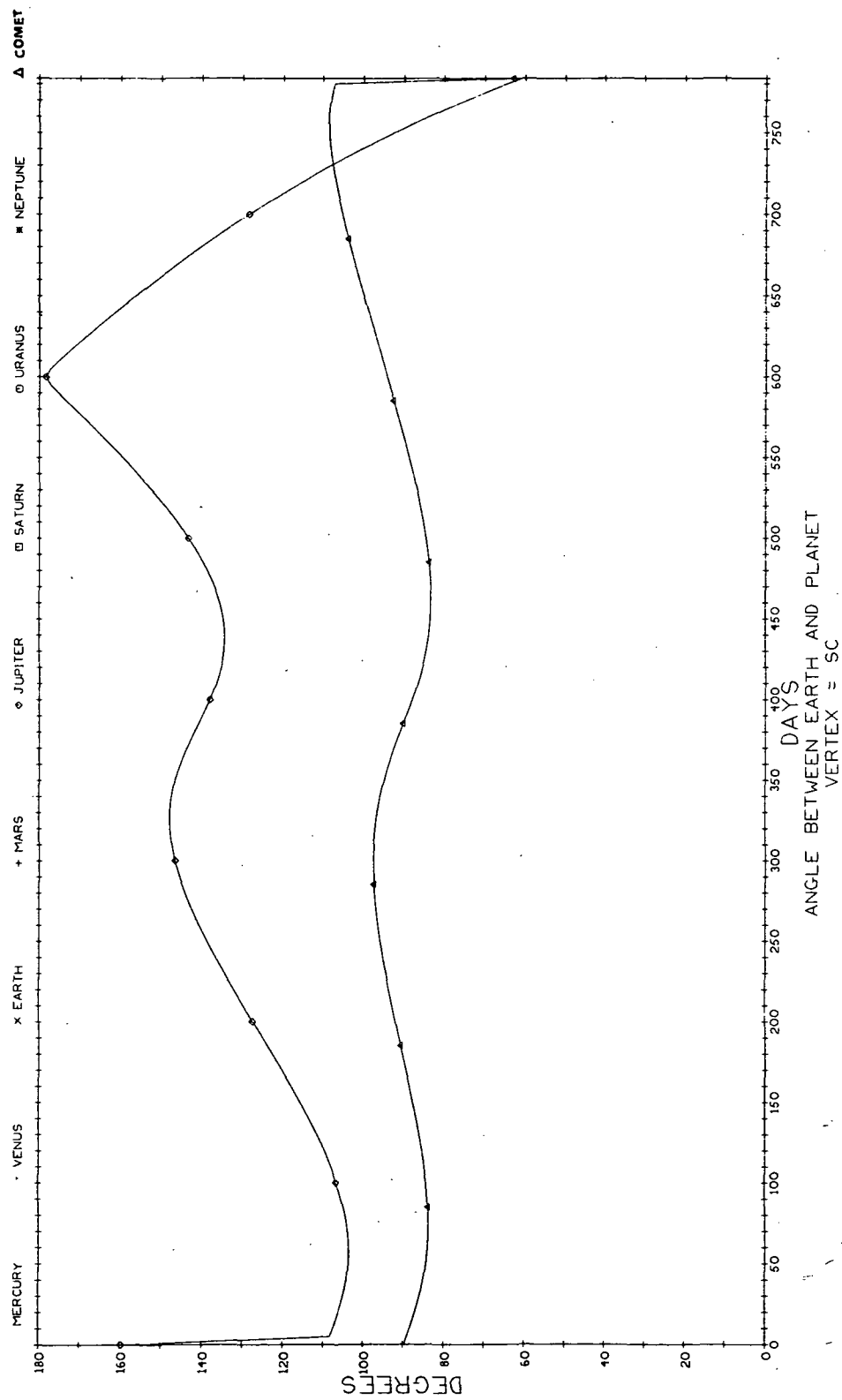


Fig. C-3-4 Earth-Spacecraft-Planet Angles During Jupiter-Comet Interplanetary Leg
of the Tuttle-Giacobini-Kresak Mission

APPENDIX D

800 DAY JUPITER ENTRY MISSION PLOTS

This appendix contains the plots for the 800 Day Jupiter Entry Mission. An explanation of their use is given in Appendix A.

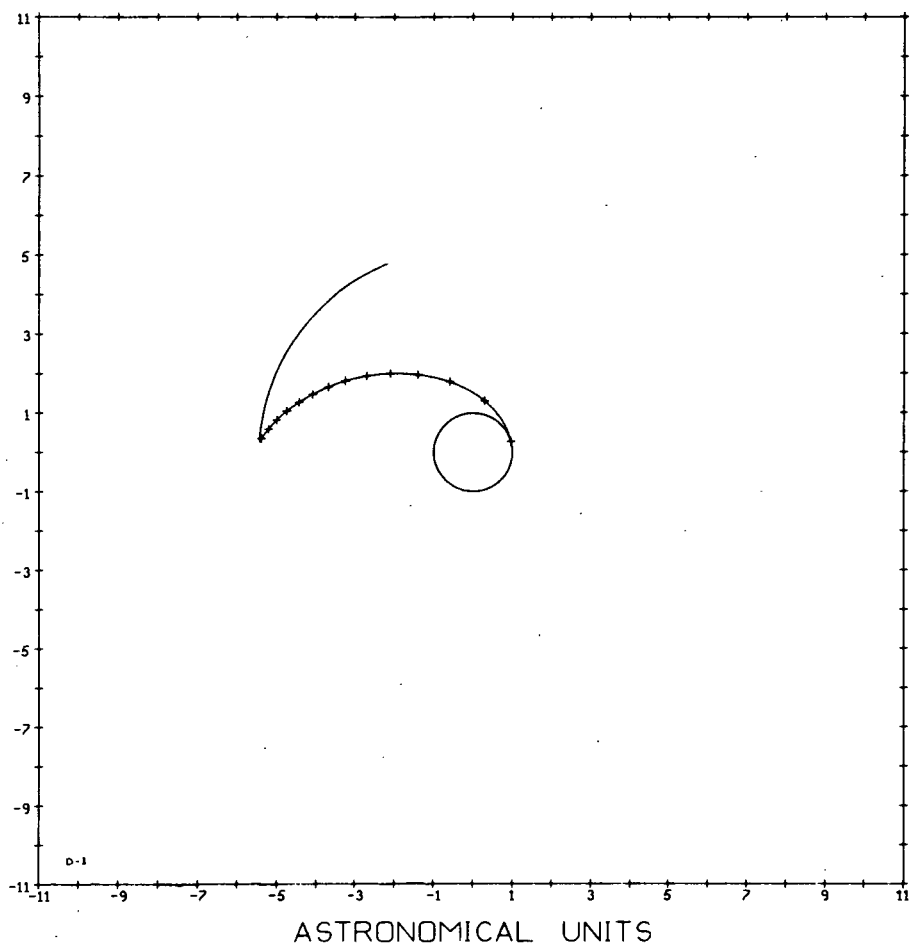


Fig. D-1 Trajectory for the 800 Day Jupiter Mission

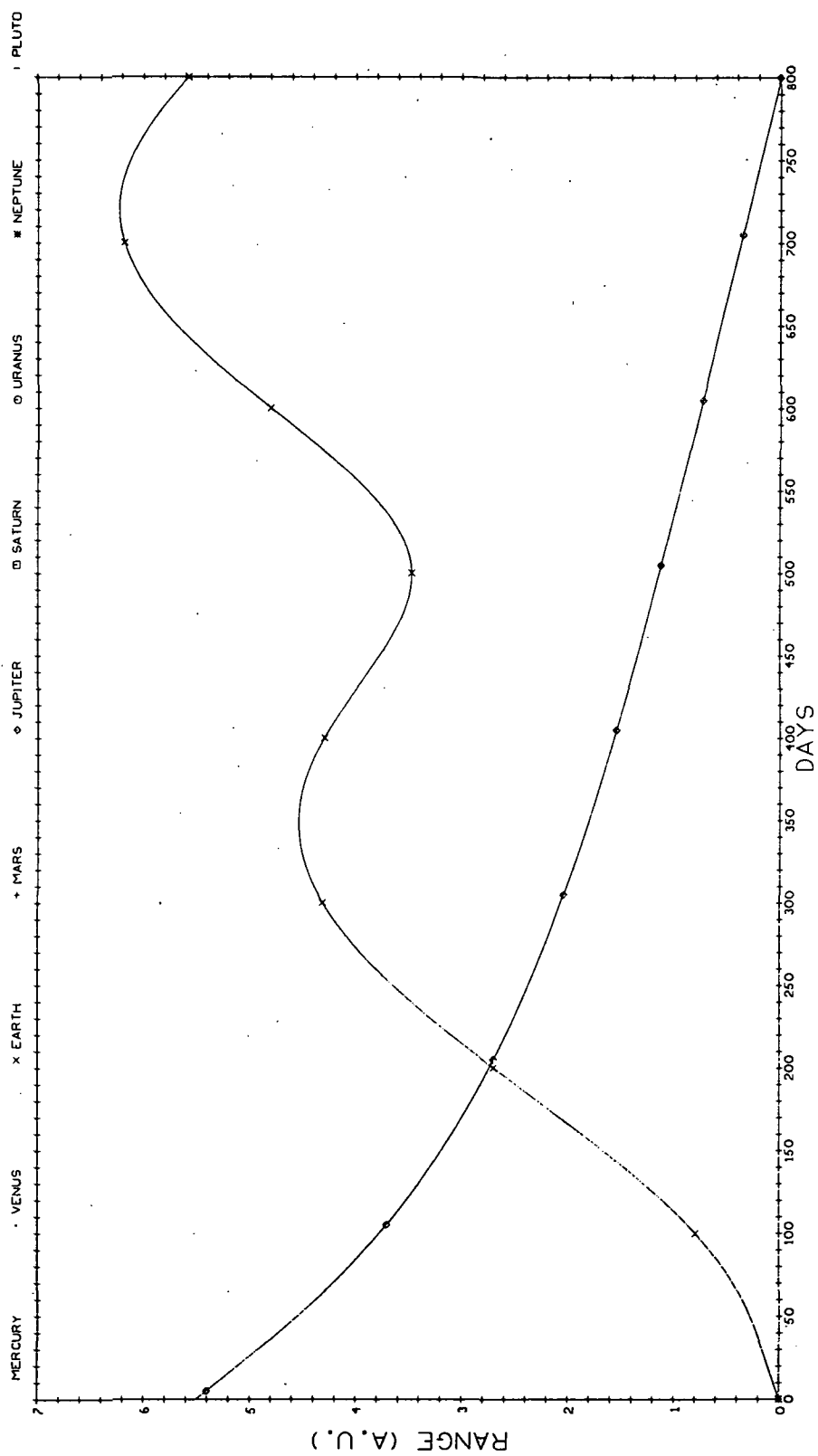


Fig. D-2-1 Ranges to Planets for the Interplanetary (Earth-Jupiter) Leg of the 800 Day Jupiter Mission

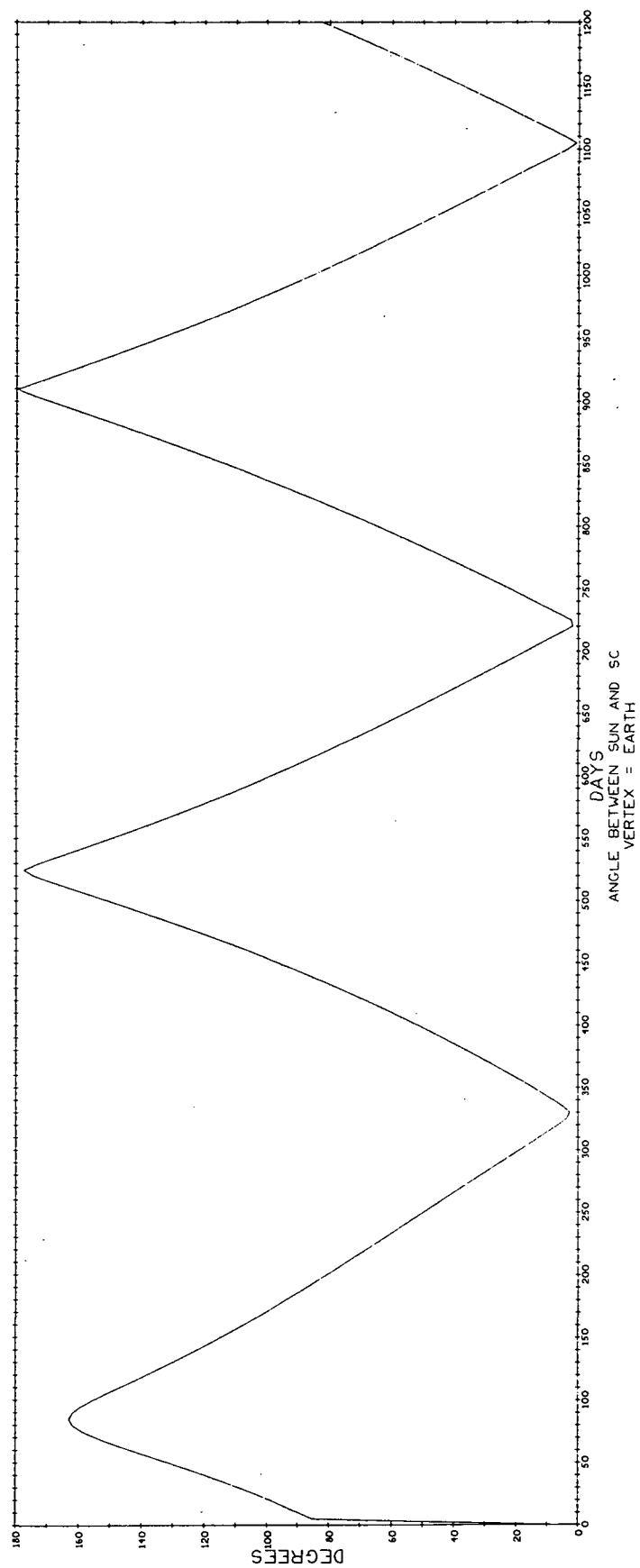


Fig. D-2-2 Spacecraft-Earth-Sun Angles for the Interplanetary (Earth-Jupiter) Leg of the 800 Day Jupiter Mission

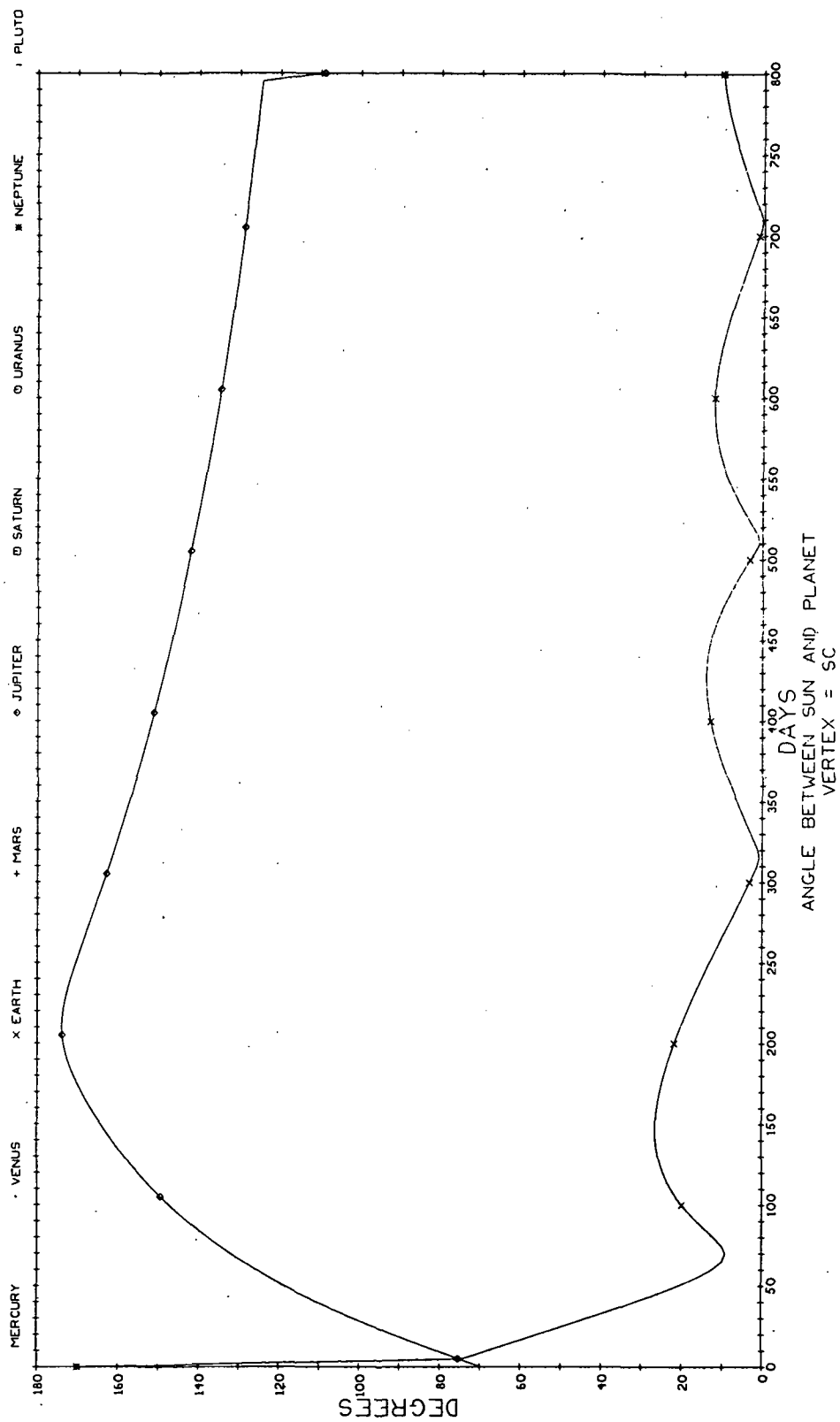


Fig. D-2-3 Sun-Spacecraft-Planet Angles for the Interplanetary (Earth-Jupiter) Leg of the 800 Day Jupiter Mission

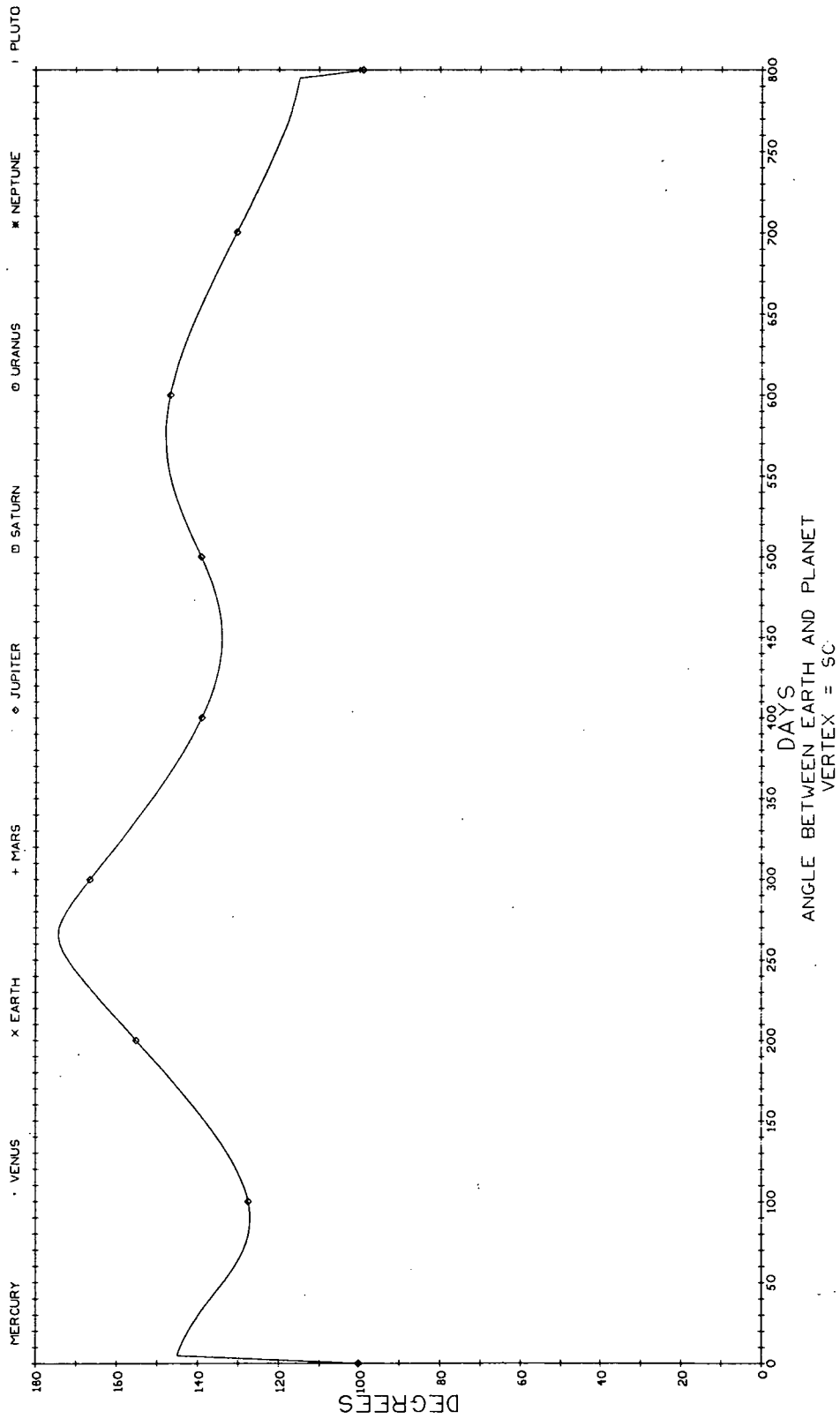


Fig. D-2-4 Earth-Spacecraft-Jupiter Angle for the Interplanetary (Earth-Jupiter) Leg of the 800 Day Jupiter Mission

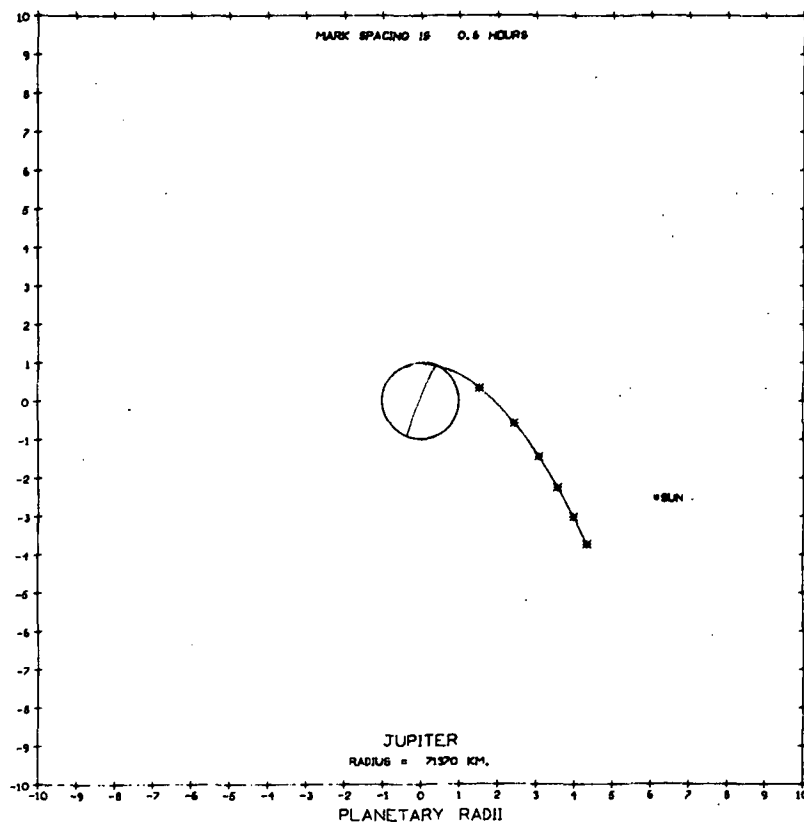


Fig. D-3-1 Trajectory Plan View During Jupiter Passage on the 800 Day Jupiter Mission

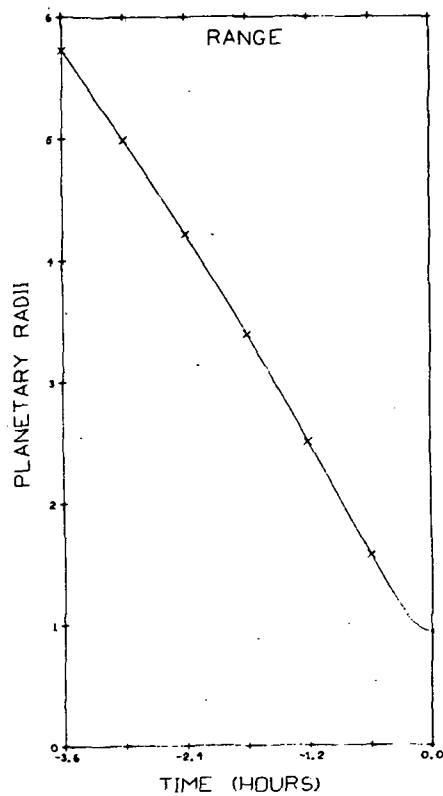


Fig. D-3-2 Range to Planet During Jupiter Passage on the 800 Day Jupiter Mission

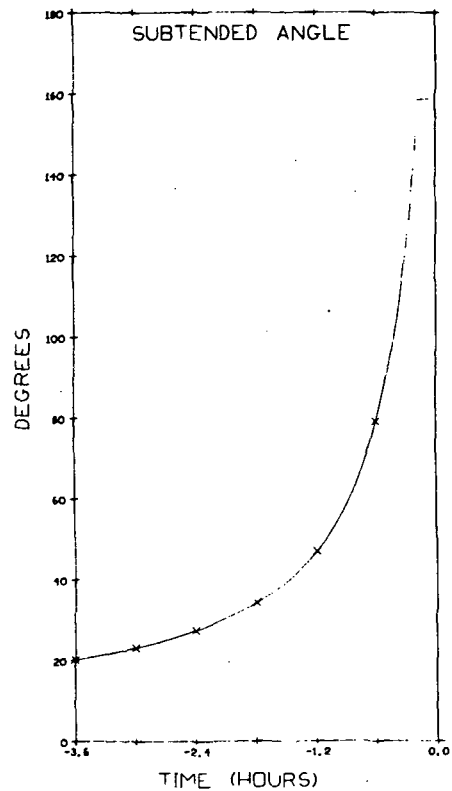


Fig. D-3-3 Angle Subtended by Planetary Limbs During Jupiter Passage on the 800 Day Jupiter Mission

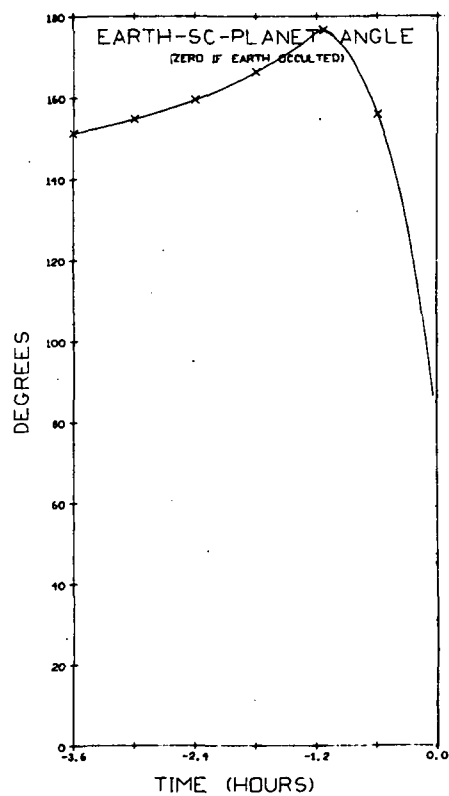


Fig. D-3-4 Earth-Spacecraft-Planet Angle During Jupiter Passage on the 800 Day Jupiter Mission

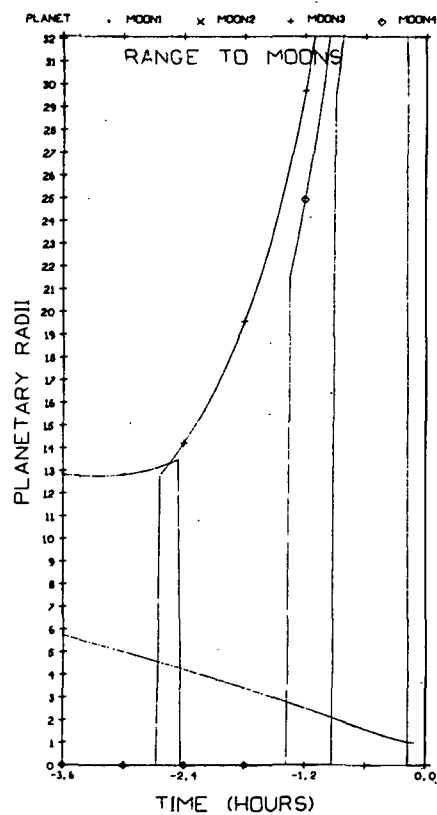


Fig. D-3-5 Range to Principle Moons During Jupiter Passage on the 800 Day Jupiter Mission

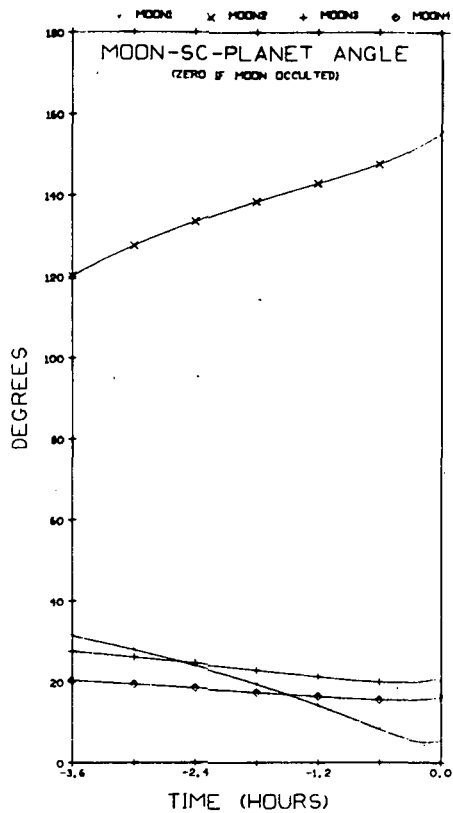


Fig. D-3-6 Moon-Spacecraft-Planet Angle During the Jupiter Passage on the 800 Day Jupiter Mission

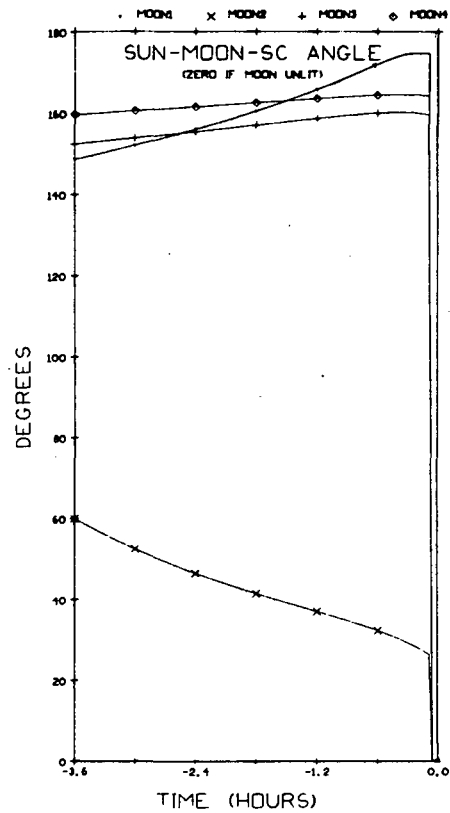


Fig. D-3-7 Sun-Moon-Spacecraft Angle During Jupiter Passage on the 800 Day Jupiter Mission

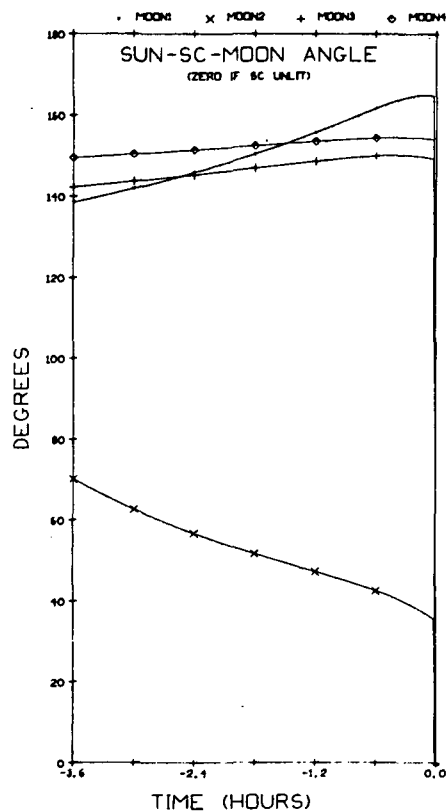


Fig. D-3-8 Sun-Spacecraft-Moon Angle
During Jupiter Passage on
the 800 Day Jupiter Mission

APPENDIX E

1200 DAY JUPITER ENTRY MISSION PLOTS

This appendix contains the plots for the 1200 Day Jupiter Entry Mission. An explanation of their use is given in Appendix A.

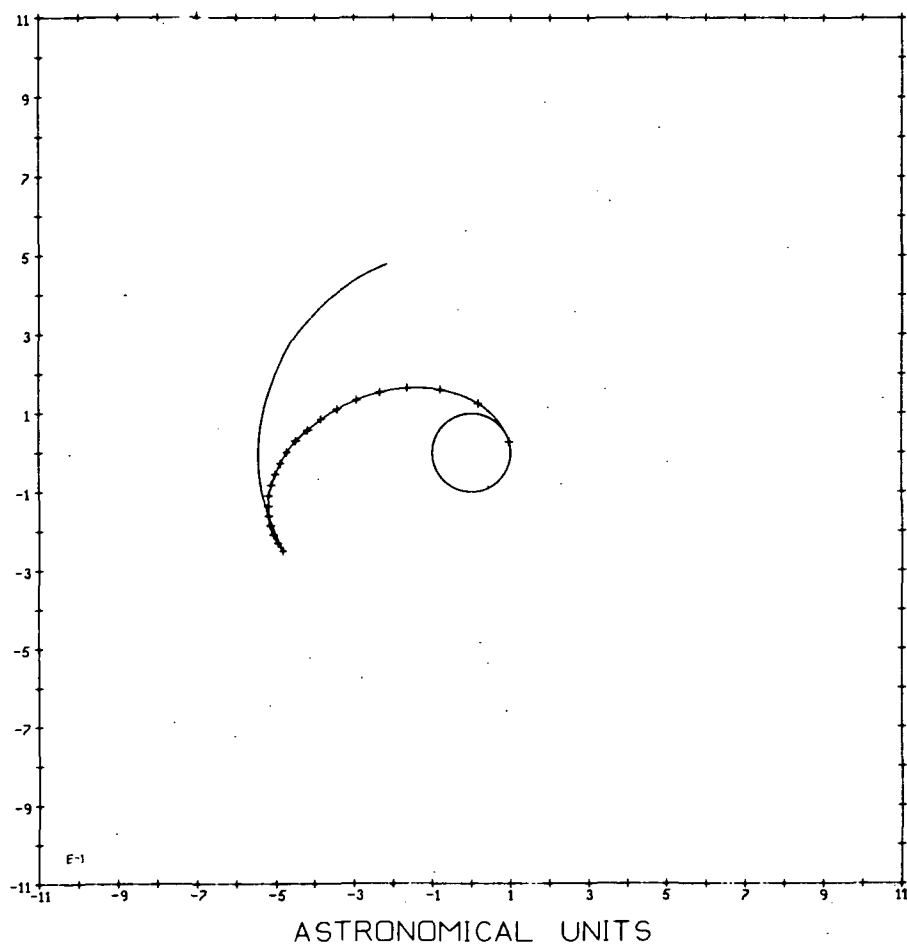


Fig. E-1 Trajectory for the 1200 Day Jupiter Mission

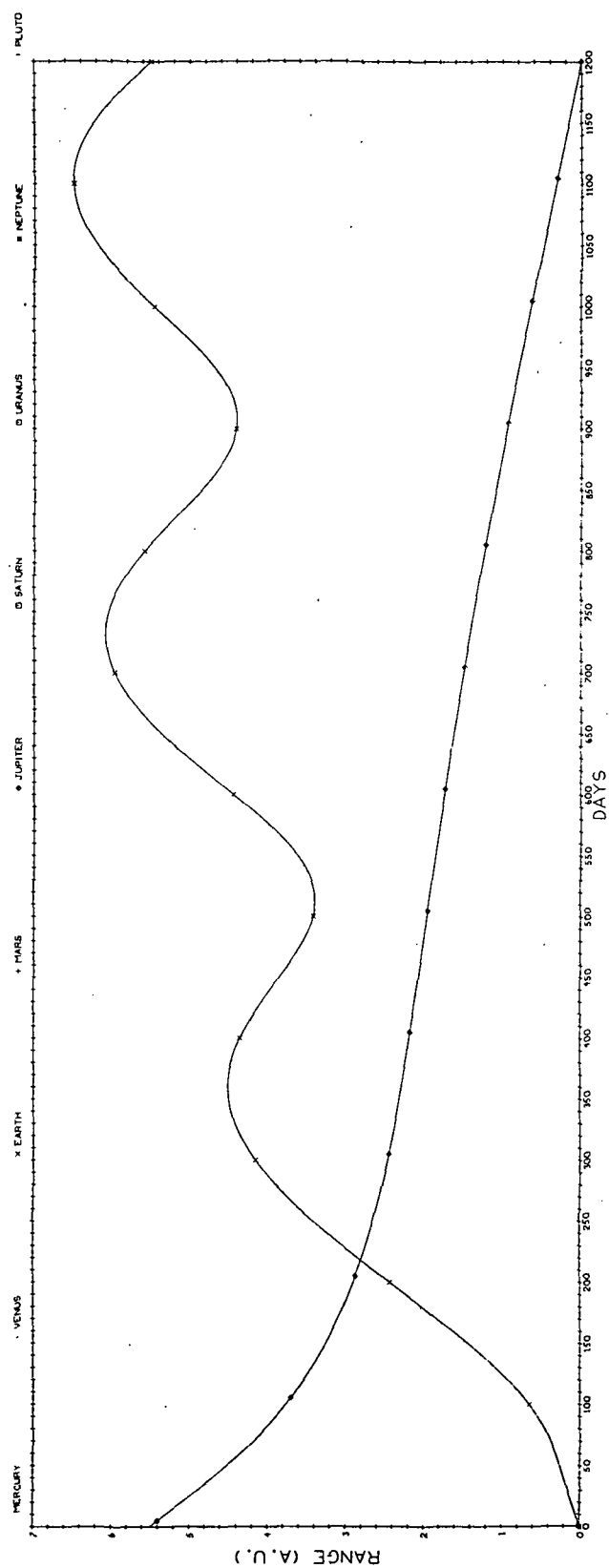


Fig. E-2-1 Ranges to Planets for the Interplanetary (Earth-Jupiter) Leg of the 1200 Day Jupiter Mission

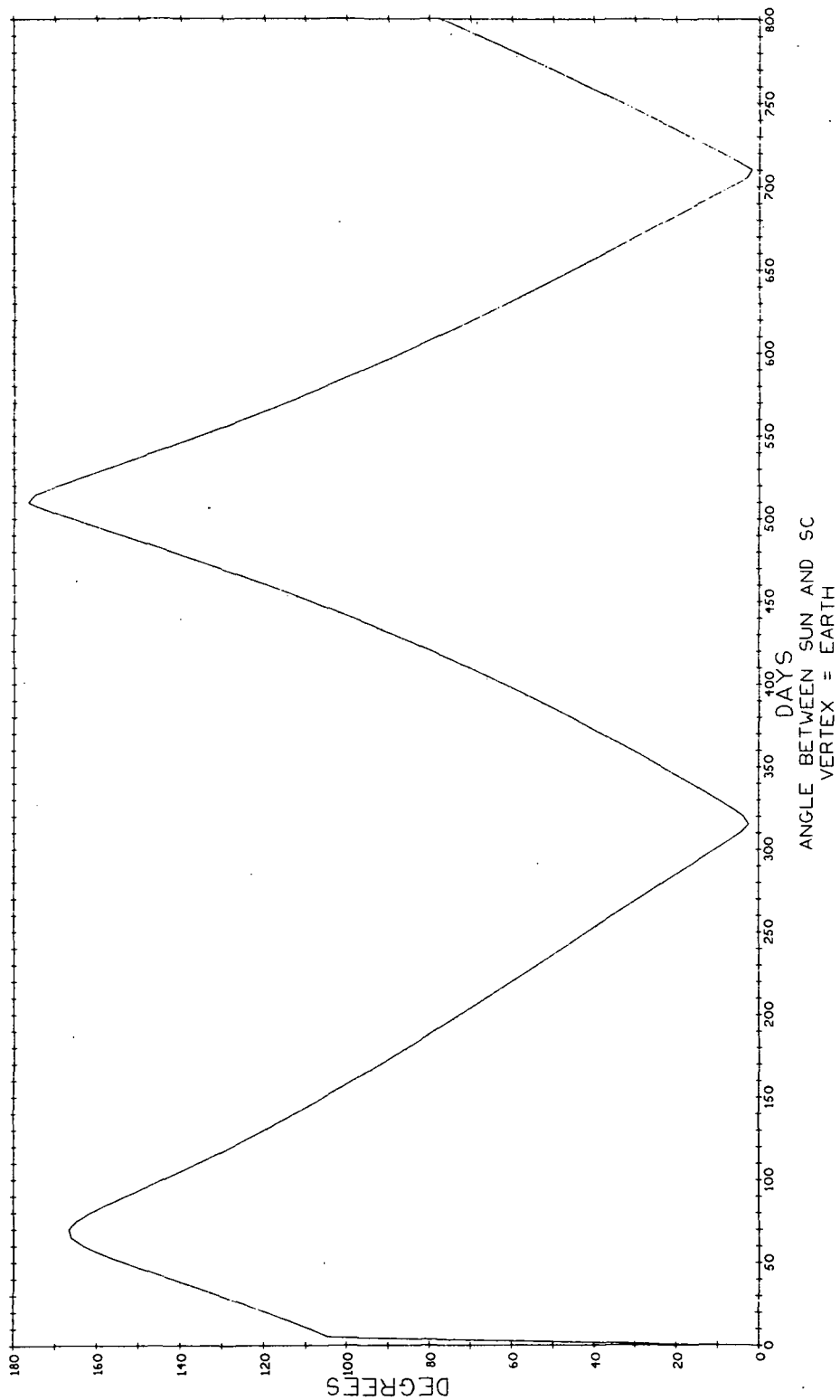


Fig. E-2-2 Spacecraft-Earth-Sun Angle for the Interplanetary (Earth-Jupiter) Leg of the 1200 Day Jupiter Mission

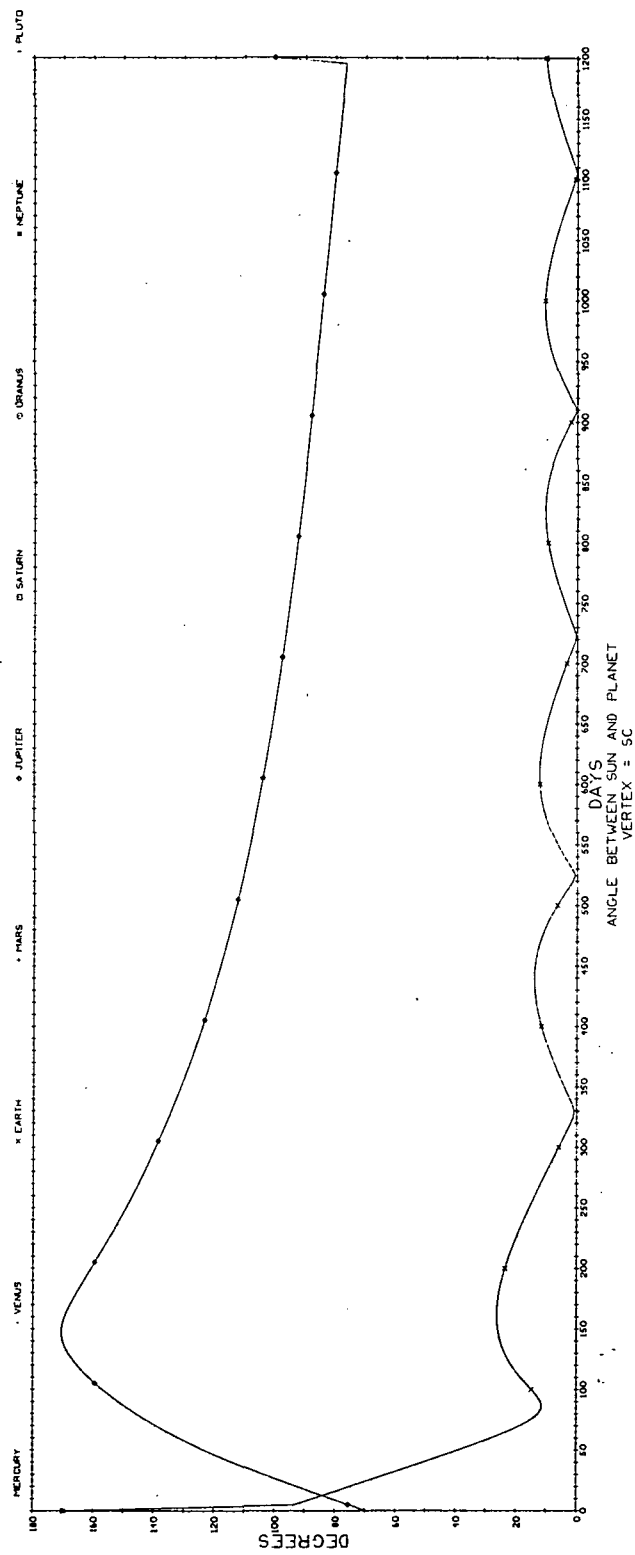


Fig. E-2-3 Sun-Spacecraft-Planet Angles for the Interplanetary (Earth-Jupiter) Leg of the 1200 Day Jupiter Mission

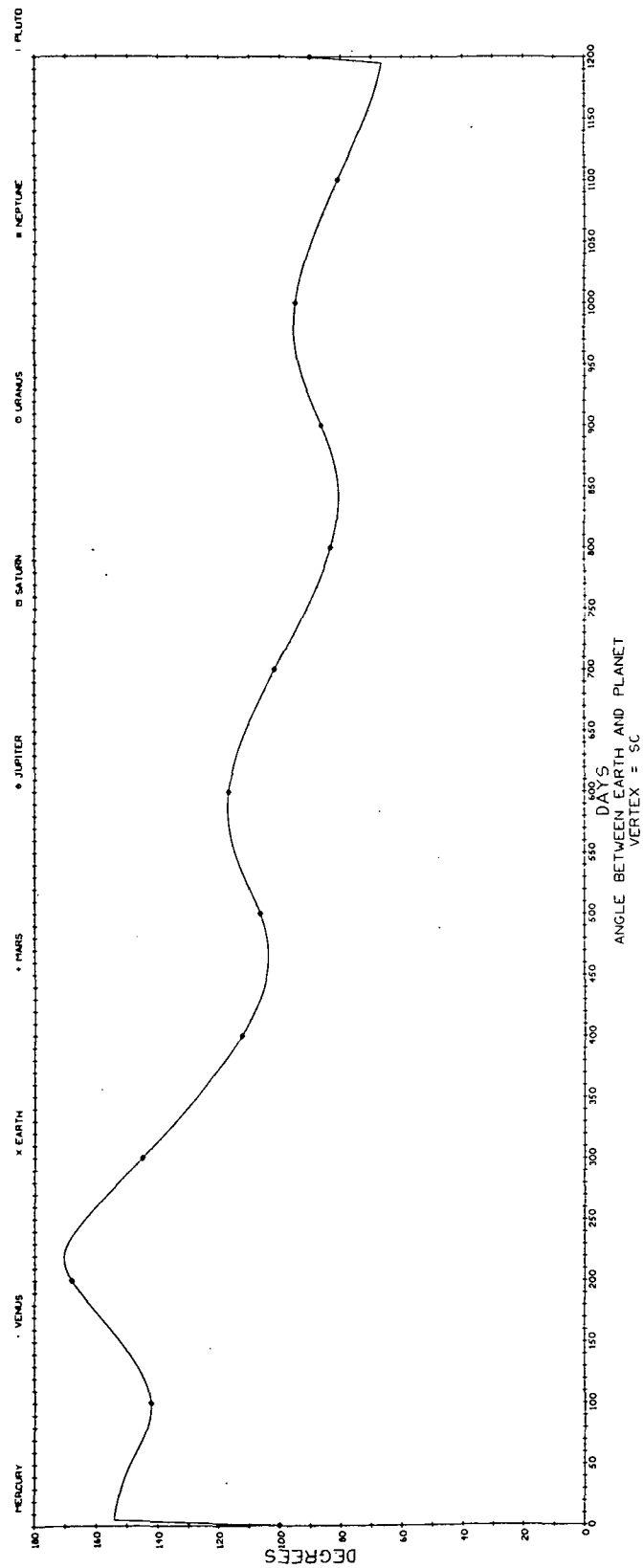


Fig. E - 2-4 Earth-Spacecraft-Planet Angle for the Interplanetary (Earth-Jupiter) Leg of the 1200 Day Jupiter Mission

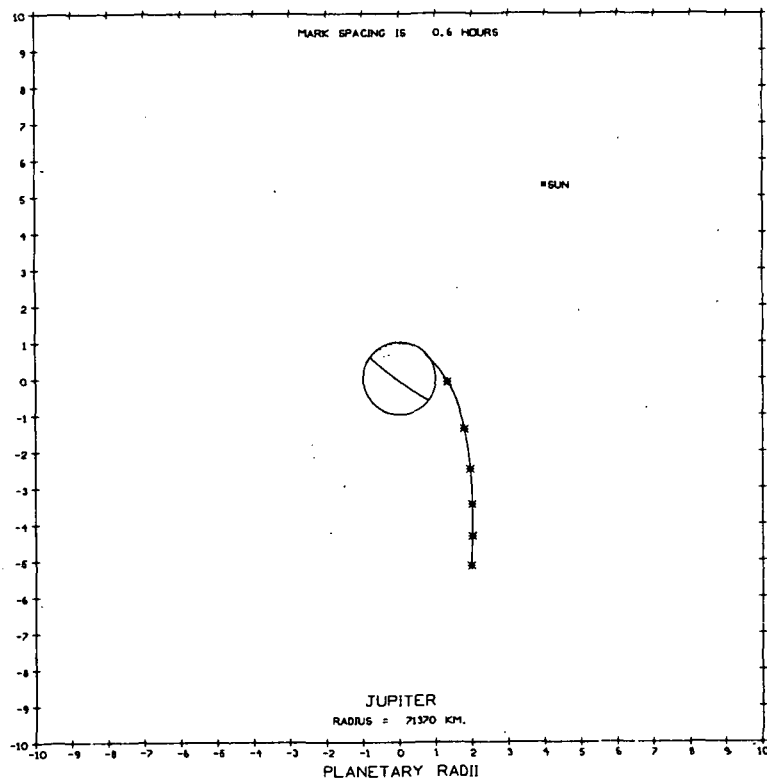


Fig. E-3-1 Trajectory Plan View During Jupiter Approach on the 1200 Day Jupiter Mission

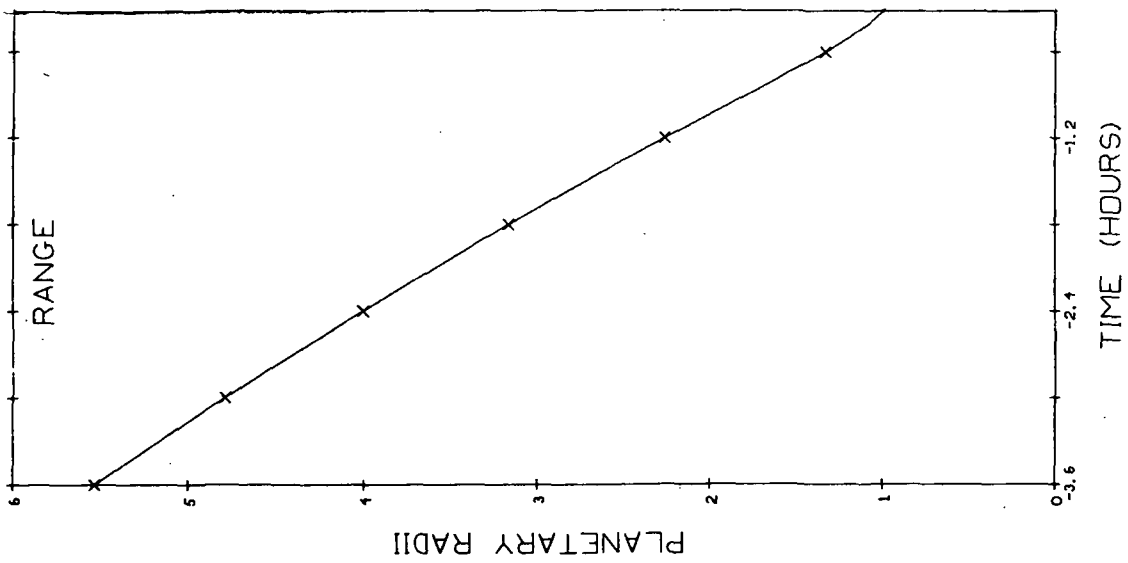


Fig. E-3-2 Range to Planet During Jupiter Approach on the 1200 Day Jupiter

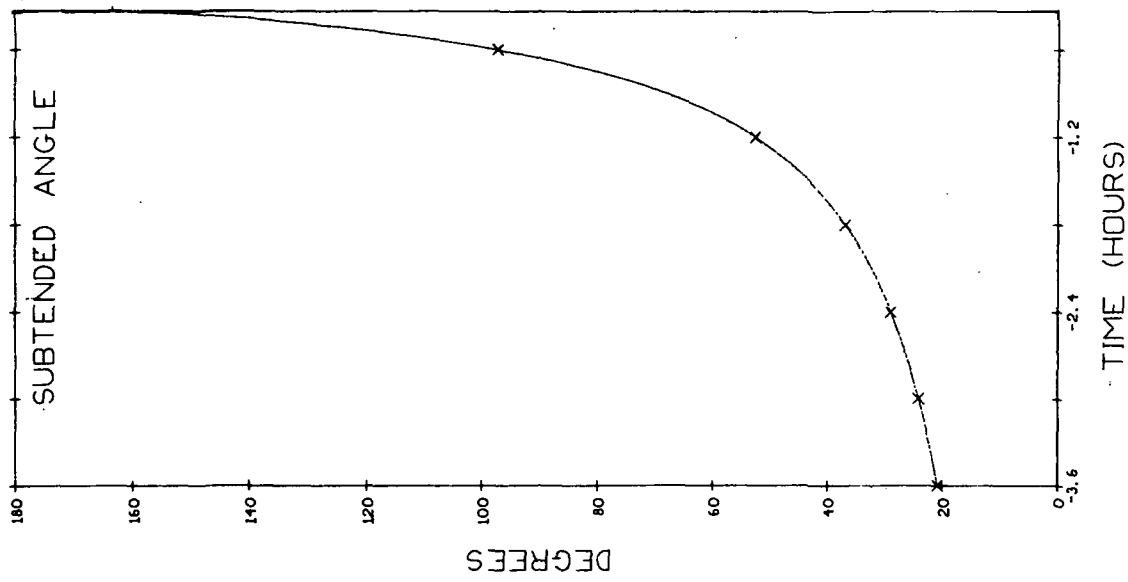


Fig. E-3-3 Angle Subtended by Planetary Limbs During Jupiter Approach on the 1200 Day Jupiter

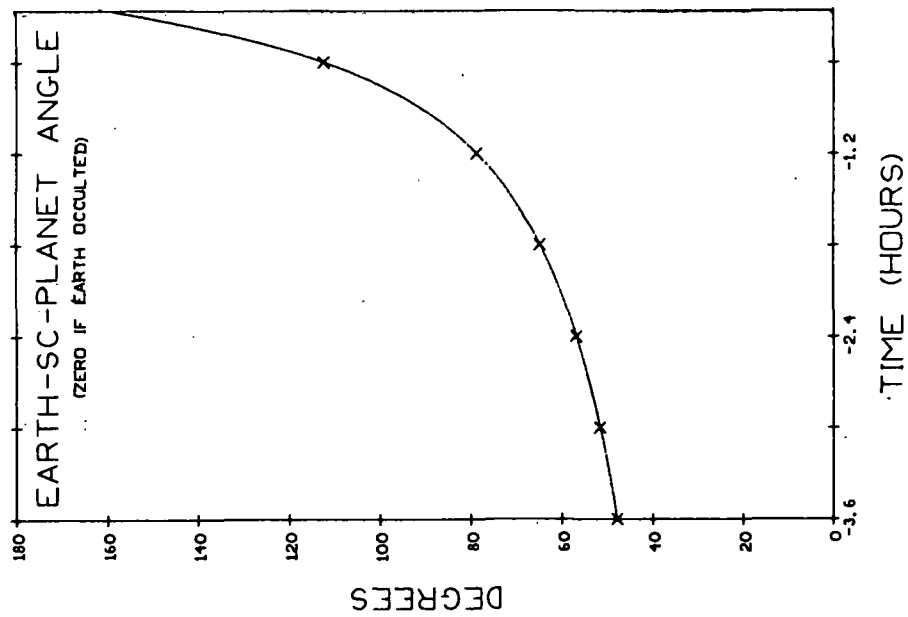


Fig. E-3-4 Earth-Spacecraft-Planet Angle During Jupiter Approach on the 1200 Day Jupiter Mission

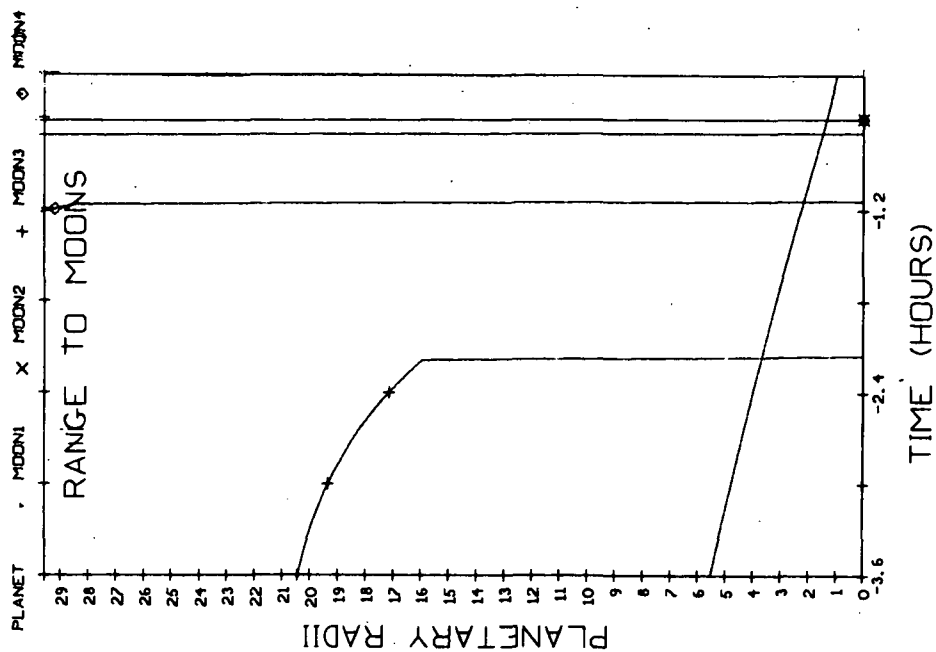


Fig. E-3-5 Ranges to Principle Moons During Jupiter Approach on the 1200 Day Jupiter Mission

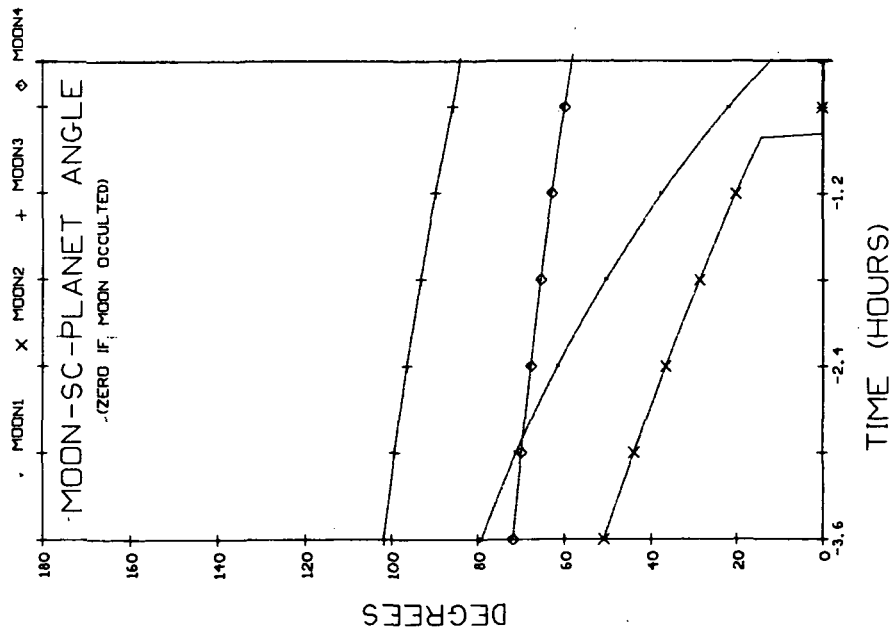


Fig. E-3-6 Moon-Spacecraft-Planet Angle During Jupiter Approach on the 1200 Day Jupiter Mission

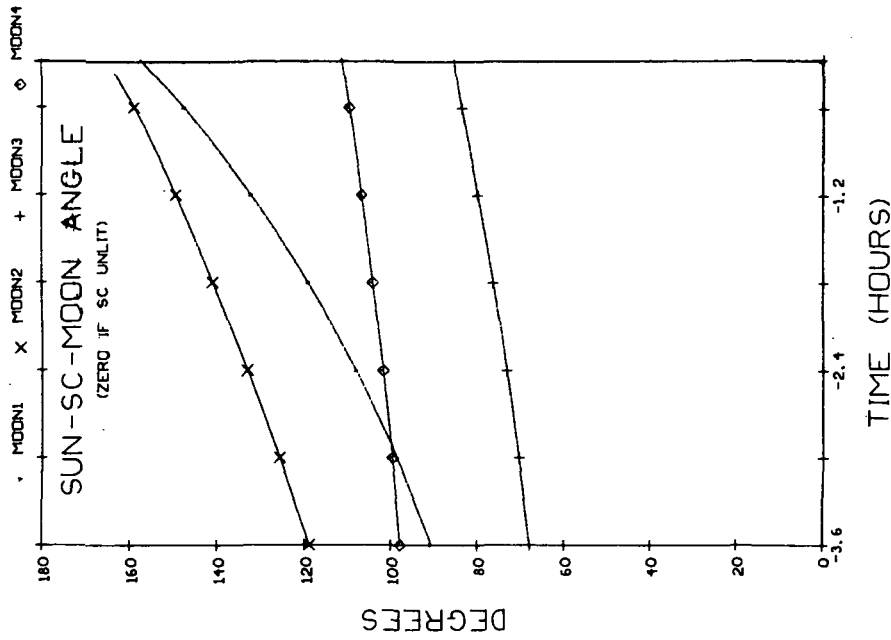


Fig. E-3-7 Sun-Spacecraft-Moon Angle During Jupiter Approach on the 1200 Day Jupiter Mission

APPENDIX F

NEPTUNE GRAND TOUR MISSION PLOTS

This appendix contains the plots for the Neptune Grand Tour Mission. An explanation of their use is given in Appendix A.

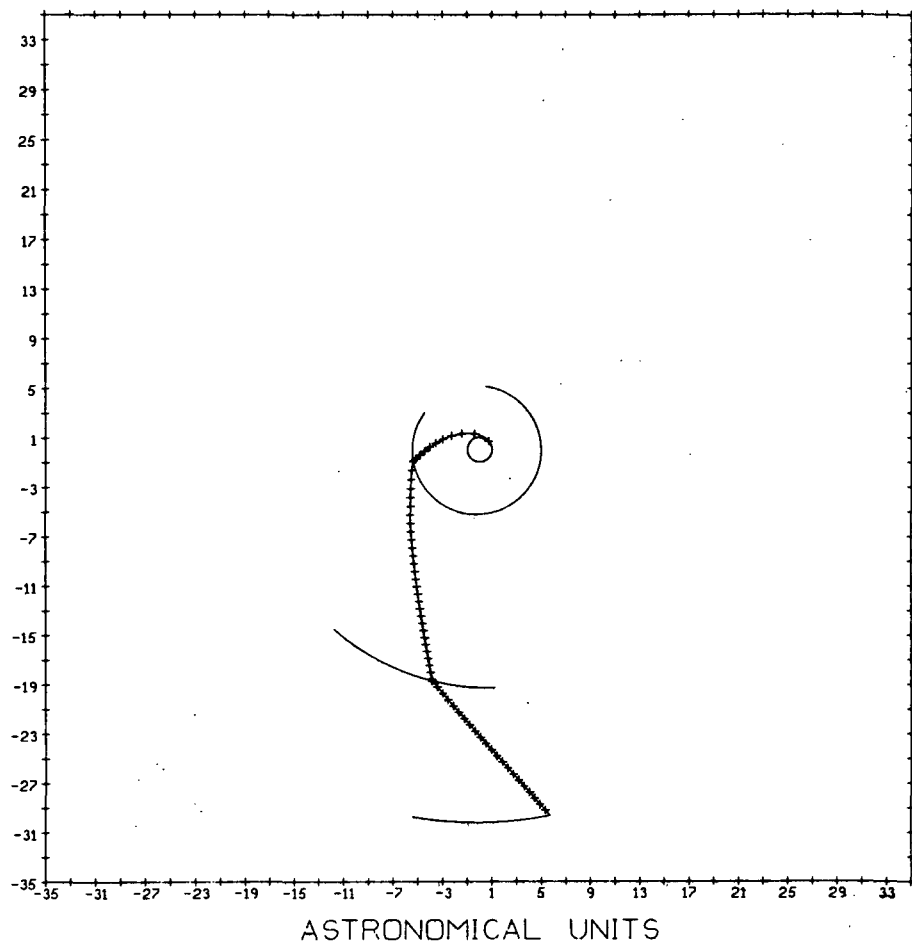


Fig. F-1 Trajectory for Neptune Grand Tour

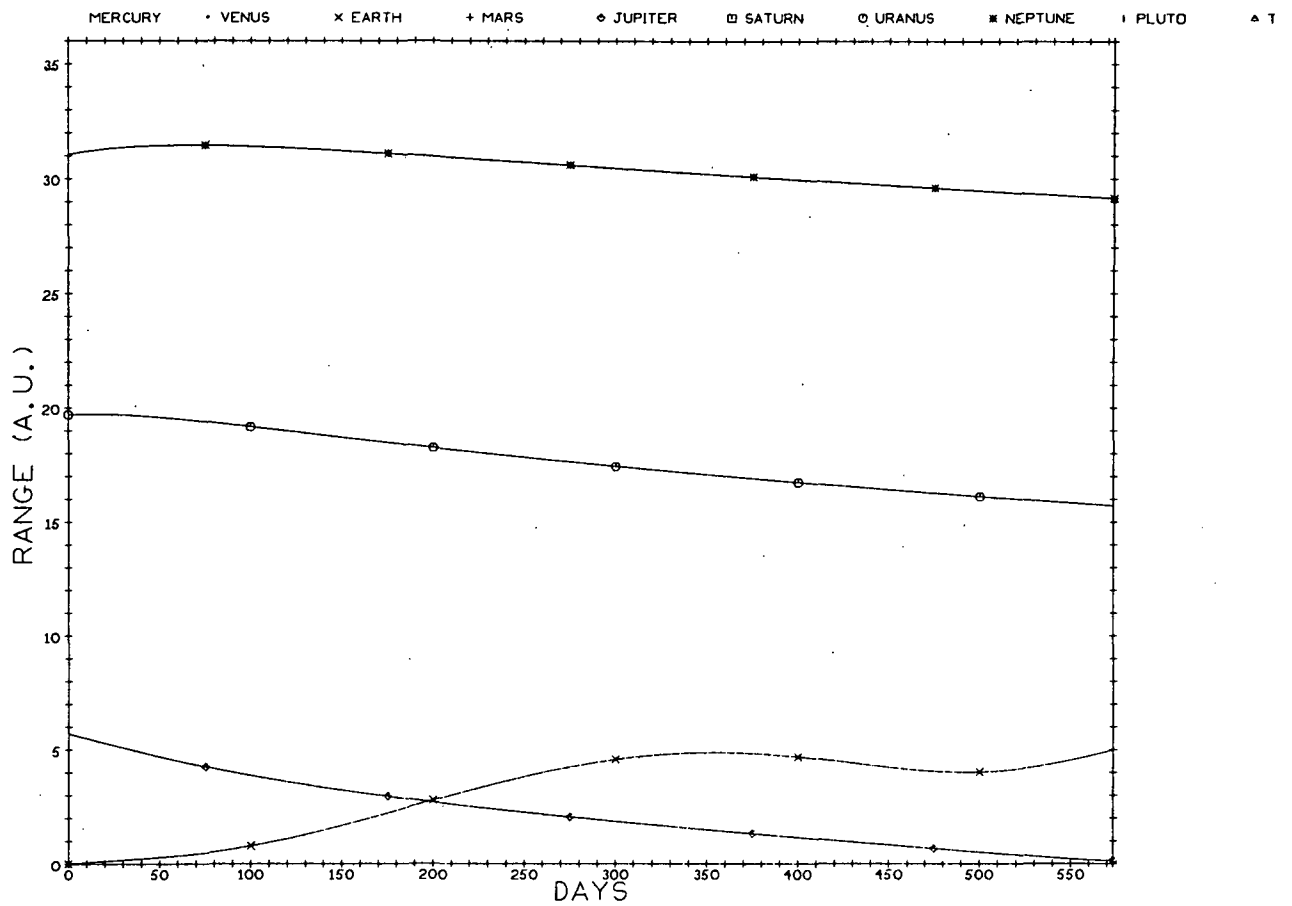


Fig. F-2-1 Ranges to Planets for the Earth-Jupiter Interplanetary Leg of the Neptune Grand Tour

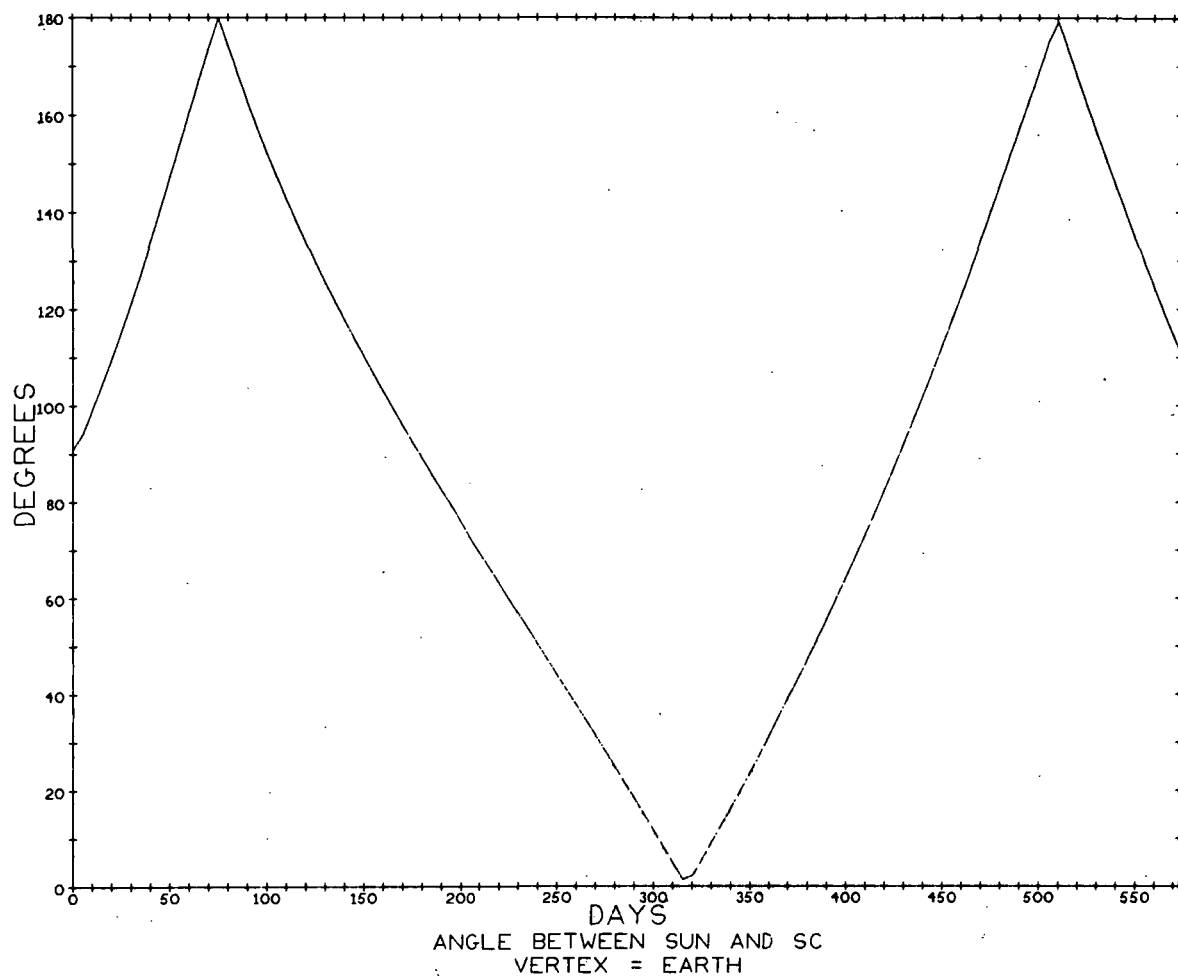


Fig. F-2-2 Spacecraft-Earth-Sun Angle for Earth-Jupiter Interplanetary Leg of Neptune Grand Tour

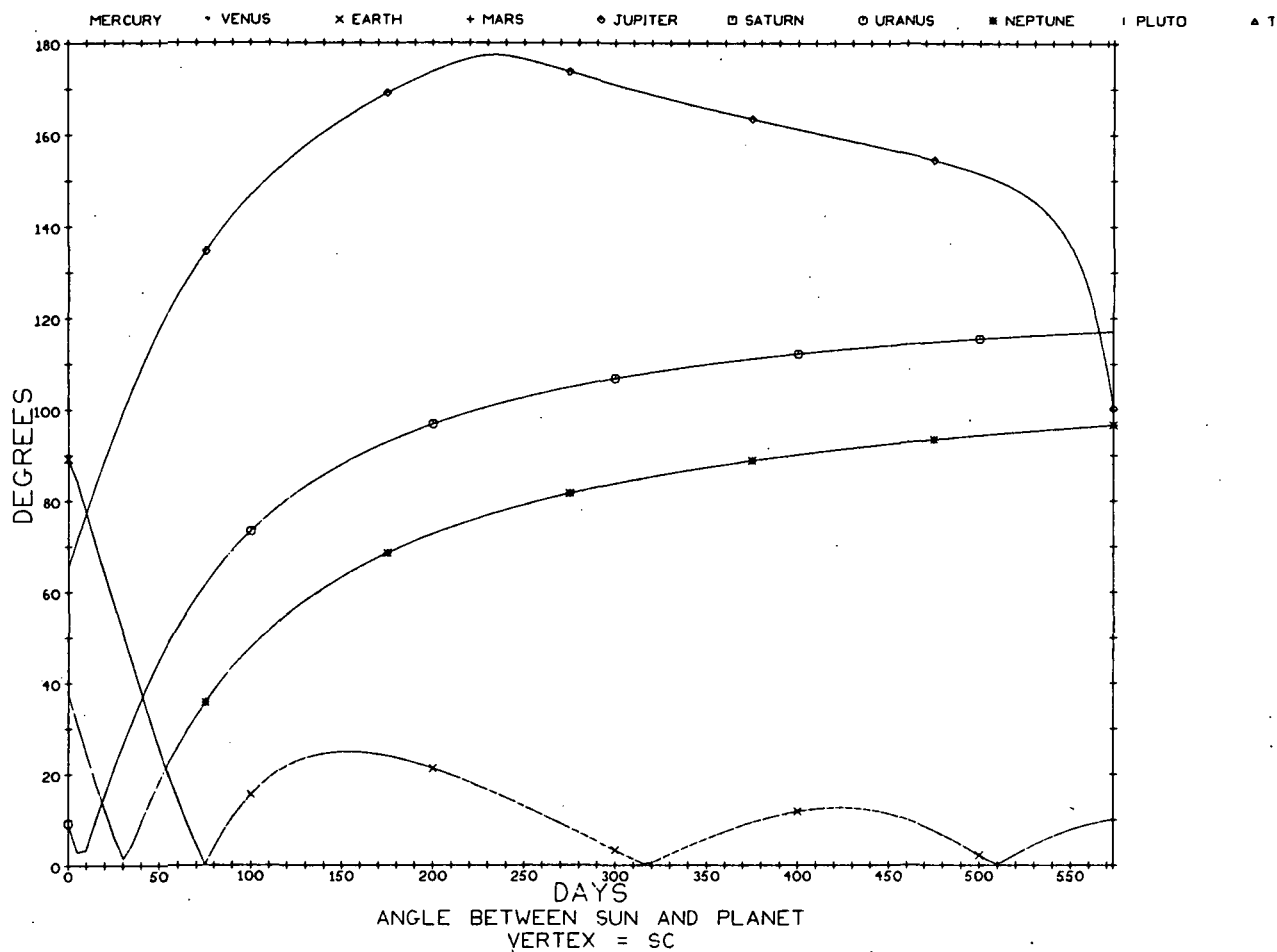


Fig. F-2-3

Sun-Spacecraft-Planet Angles for the Earth-Jupiter
Interplanetary Leg of the Neptune Grand Tour

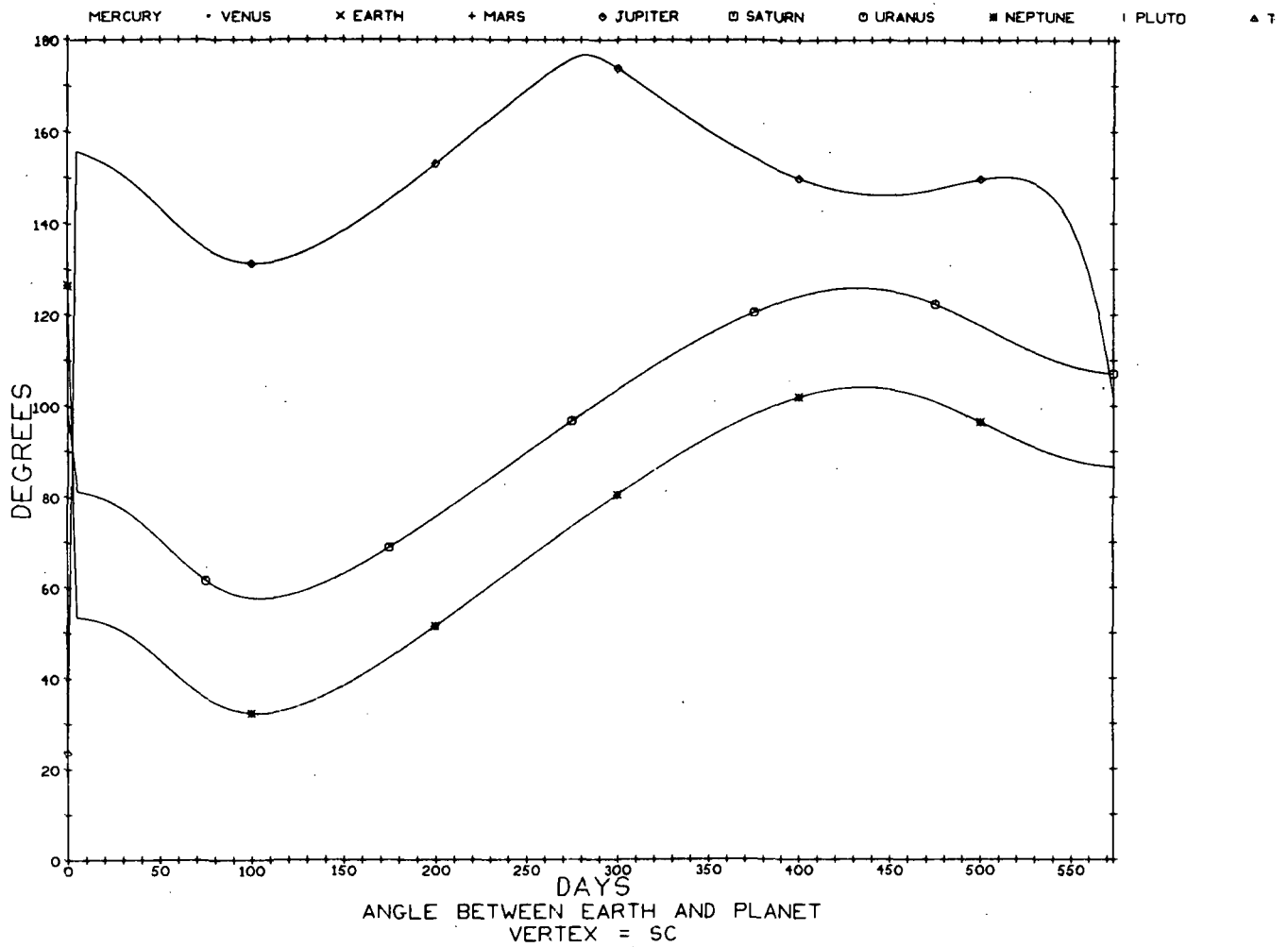


Fig. F-2-4 Earth-Spacecraft-Planet Angles for the Earth-Jupiter Interplanetary Leg of the Neptune Grand Tour



Fig. F-3-1 Range to Planets for Jupiter-Uranus Interplanetary Leg of Neptune Grand Tour

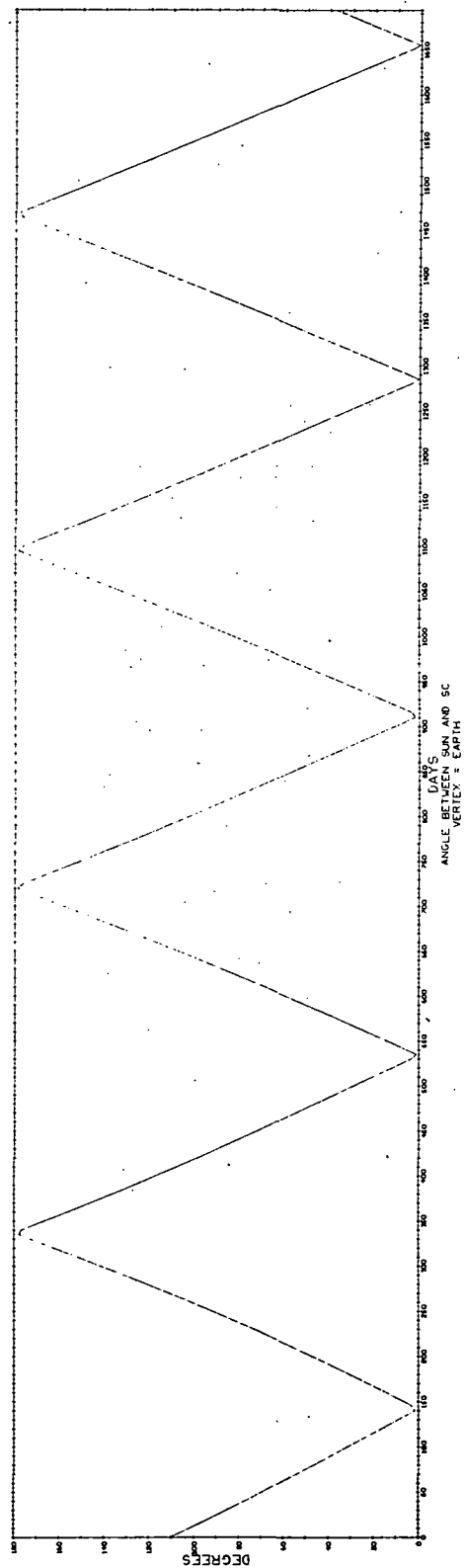


Fig. F-3-2 Spacecraft-Earth-Sun Angle for Jupiter-Uranus Interplanetary Leg of Neptune Grand Tour

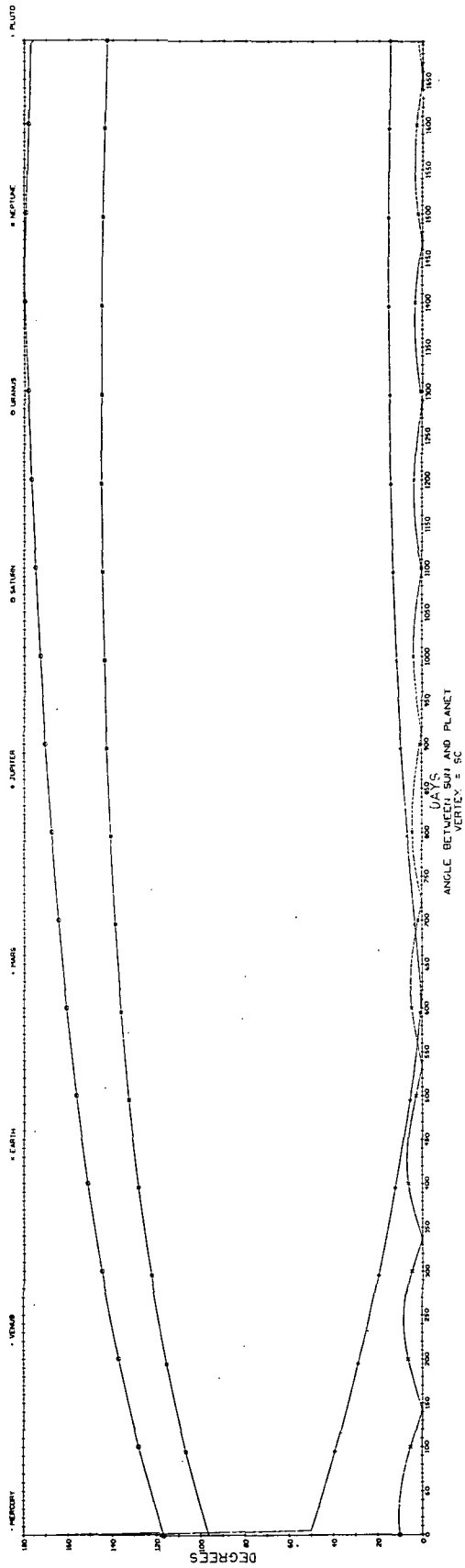


Fig. F-3-3 Sun-Spacecraft-Planet Angles for Jupiter-Uranus Interplanetary Leg of Neptune Grand Tour

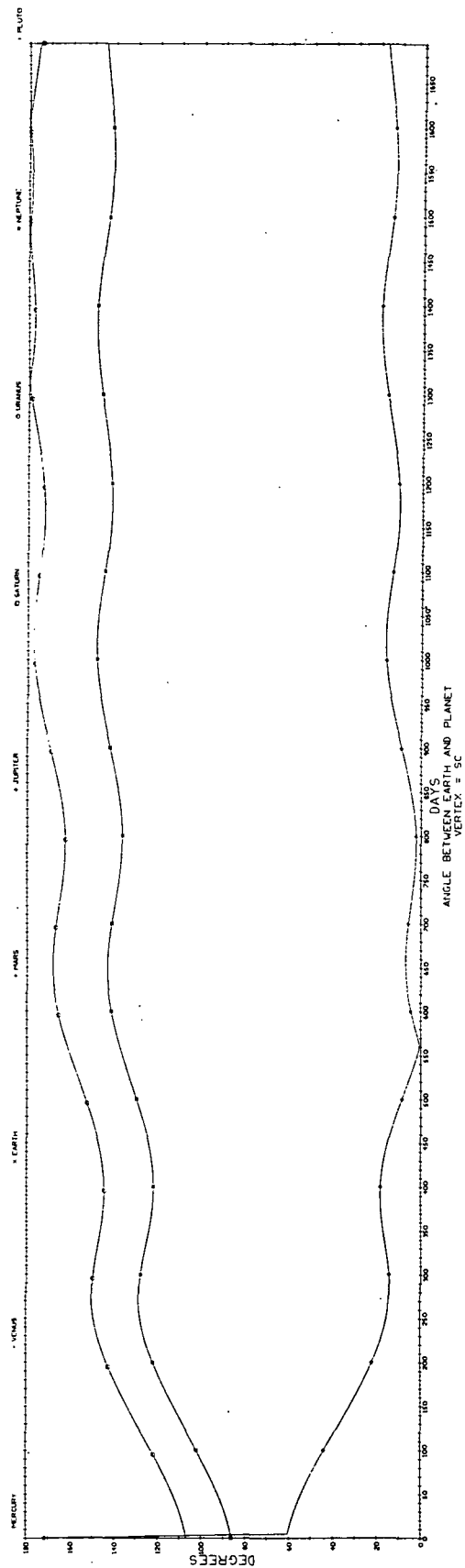


Fig. F-3-4 Earth-Spacecraft-Planet Angles for Jupiter-Uranus Interplanetary Leg of Neptune Grand Tour

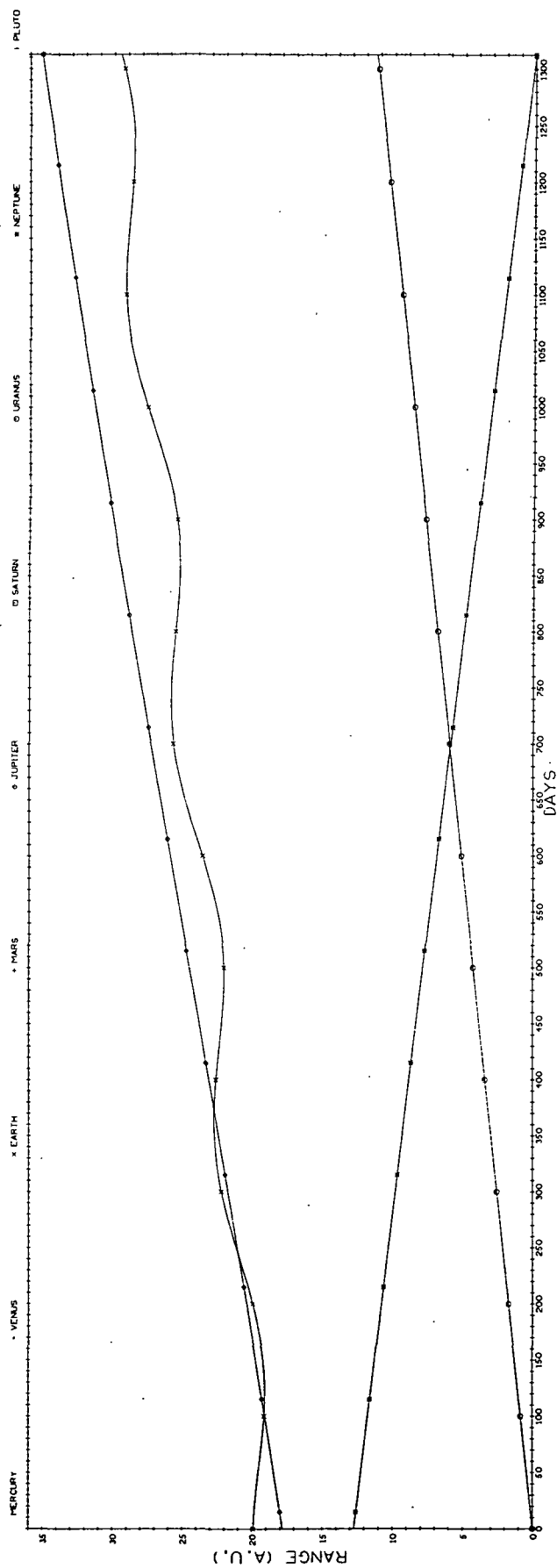


Fig. F-4-1 Ranges to Planets for the Uranus-Neptune Interplanetary Leg of the Neptune Grand Tour

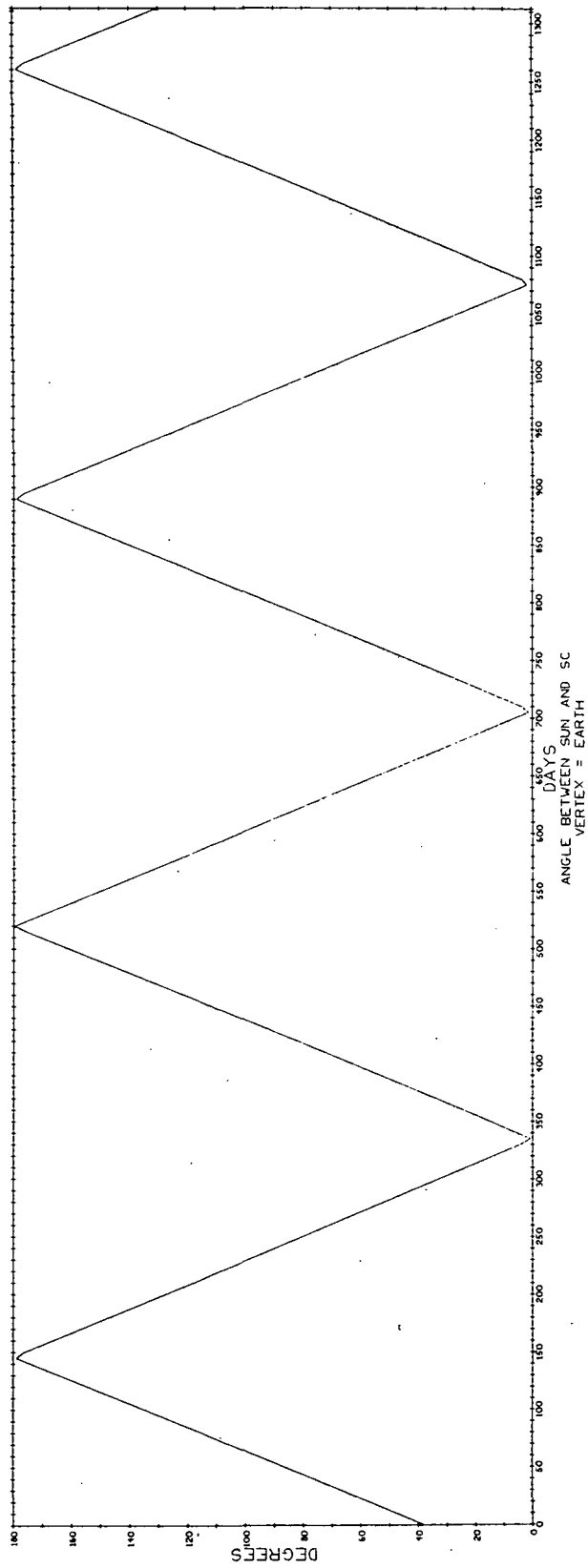


Fig. F-4-2 Spacecraft-Earth-Sun Angle for Uranus-Neptune Interplanetary Leg of Neptune Grand Tour

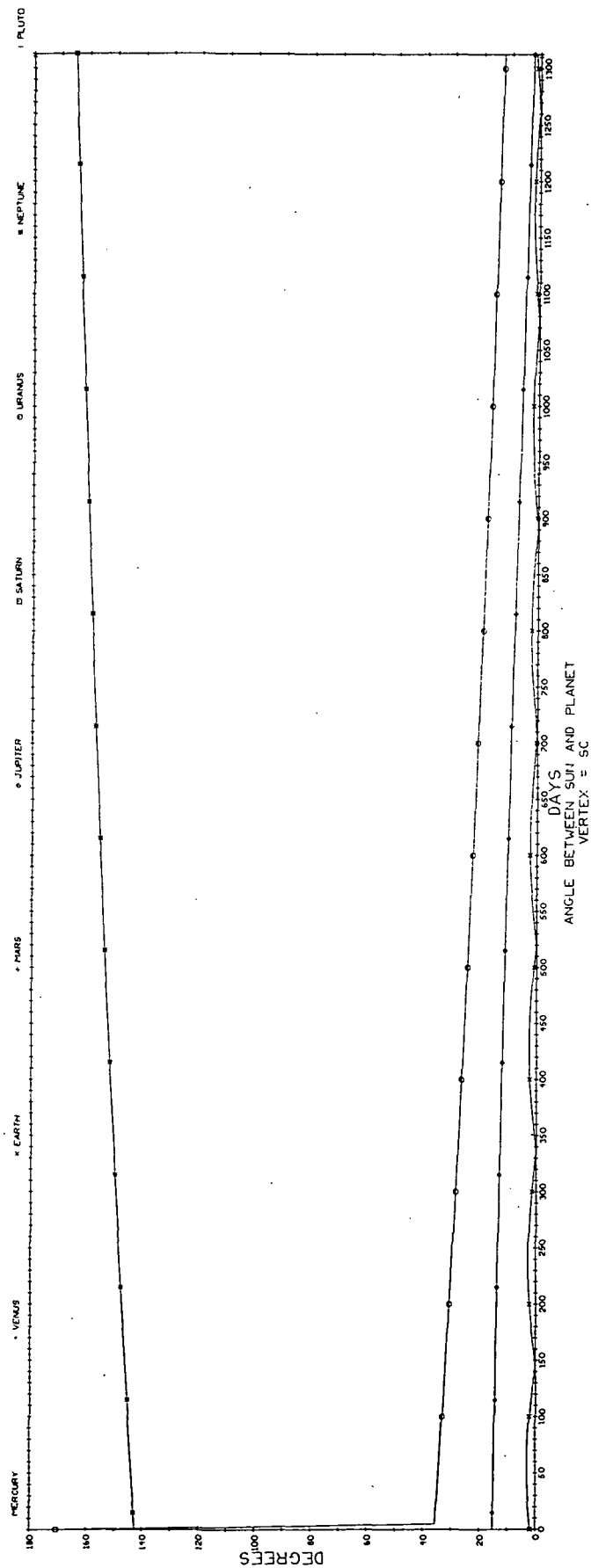


Fig. F-4-3 Sun-Spacecraft-Planet Angles for the Uranus-Neptune Interplanetary Leg of the Neptune Grand Tour

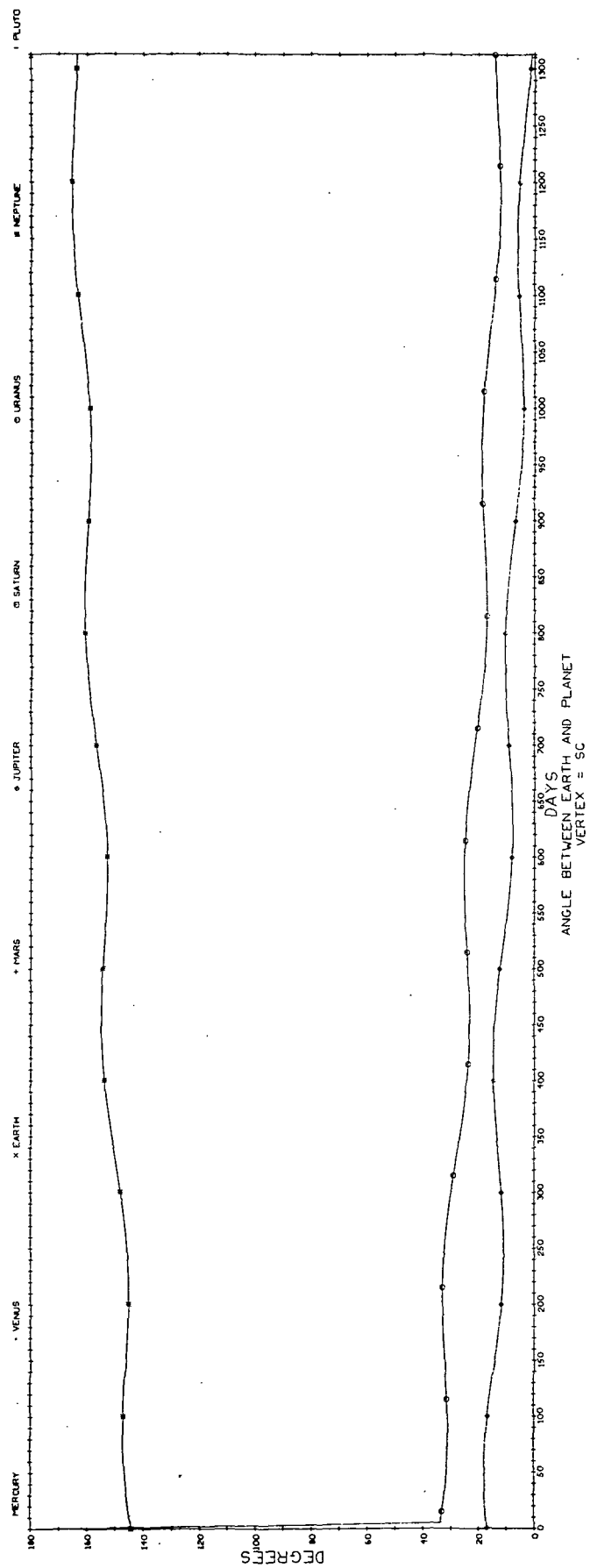


Fig. F-4-4 Earth-Spacecraft-Planet Angle for the Uranus-Neptune Interplanetary Leg of the Neptune Grand Tour

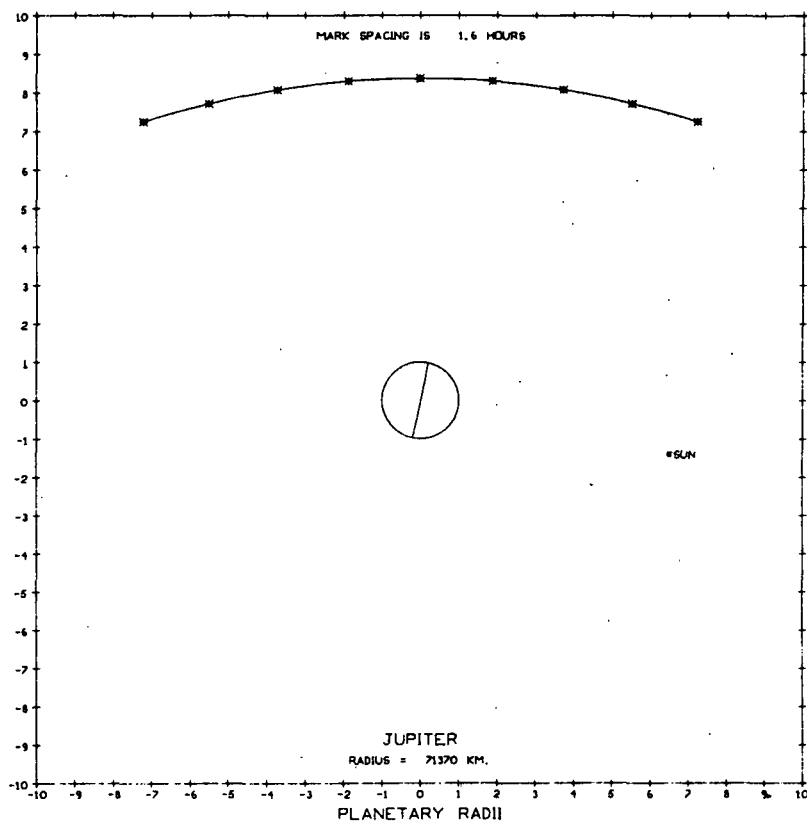


Fig. F-5-1 Trajectory Plan View During Jupiter Passage on the Neptune Grand Tour

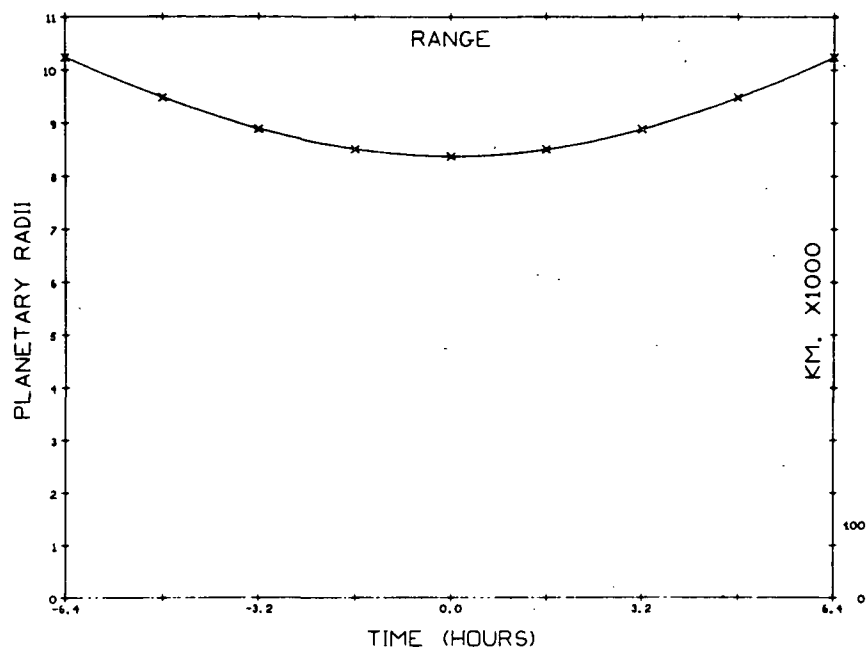


Fig. F-5-2 Range to Planet During Jupiter Passage on the Neptune Grand Tour

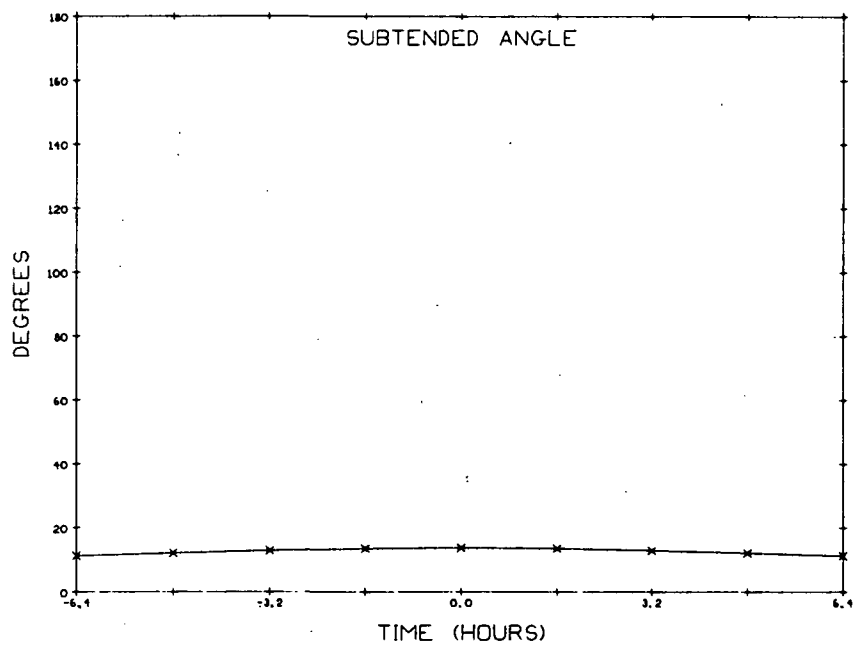


Fig. F-5-3 Angle Subtended by Planetary Limbs During Jupiter Passage on the Neptune Grand Tour

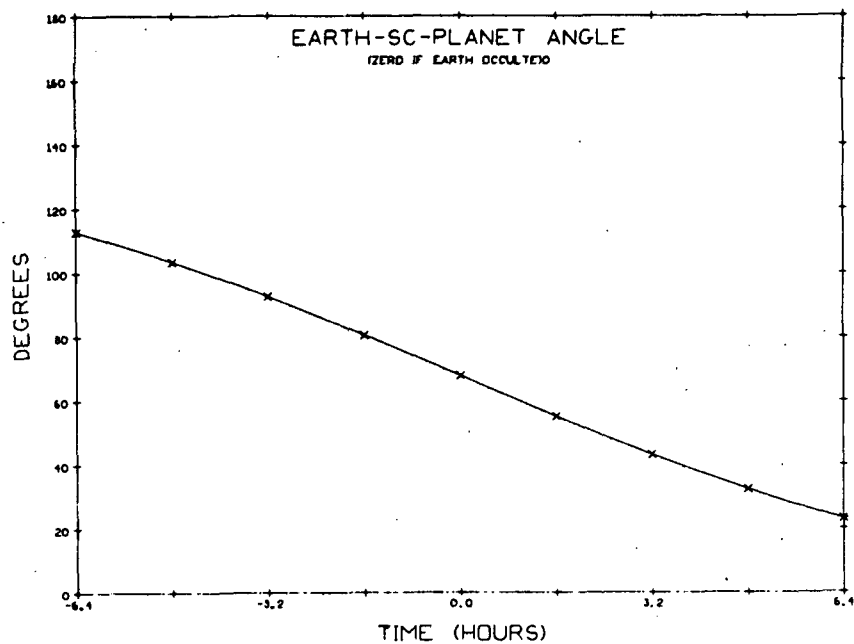


Fig. F-5-4 Earth-Spacecraft-Planet Angle During Jupiter Passage on the Neptune Grand Tour

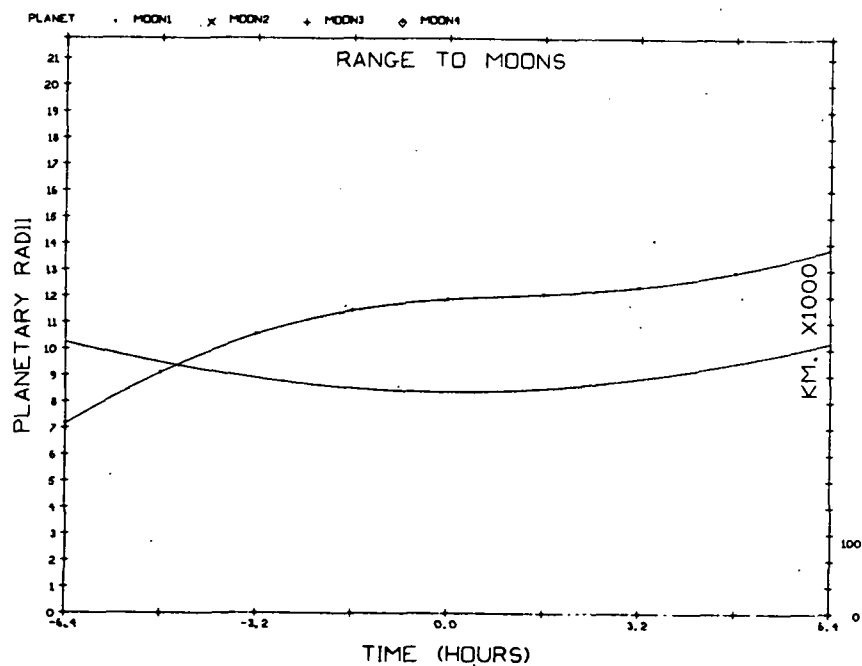


Fig. F-5-5 Range to Principle Moons During Jupiter Passage on the Neptune Grand Tour

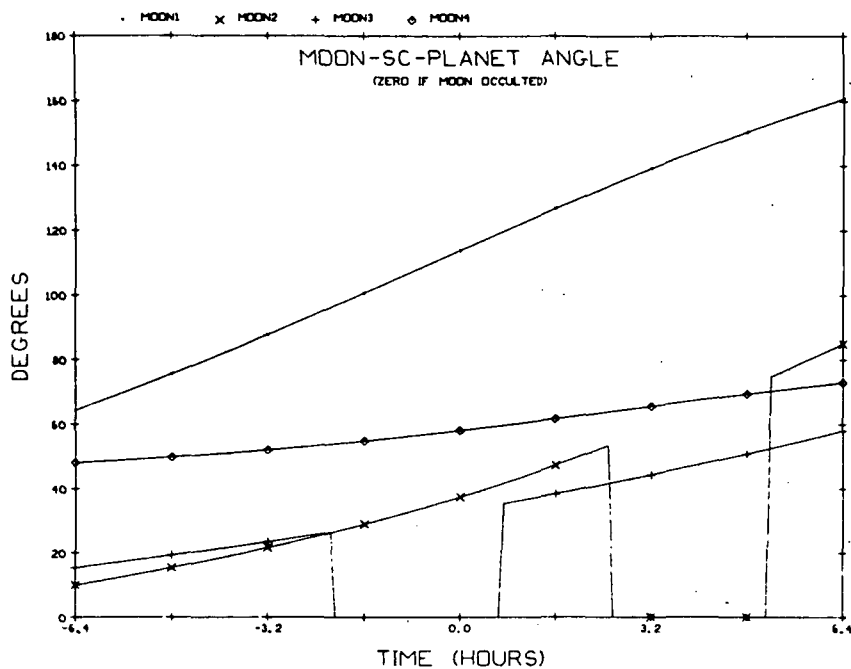


Fig. F-5-6 Moon-Spacecraft-Planet Angle During Jupiter Passage on the Neptune Grand Tour

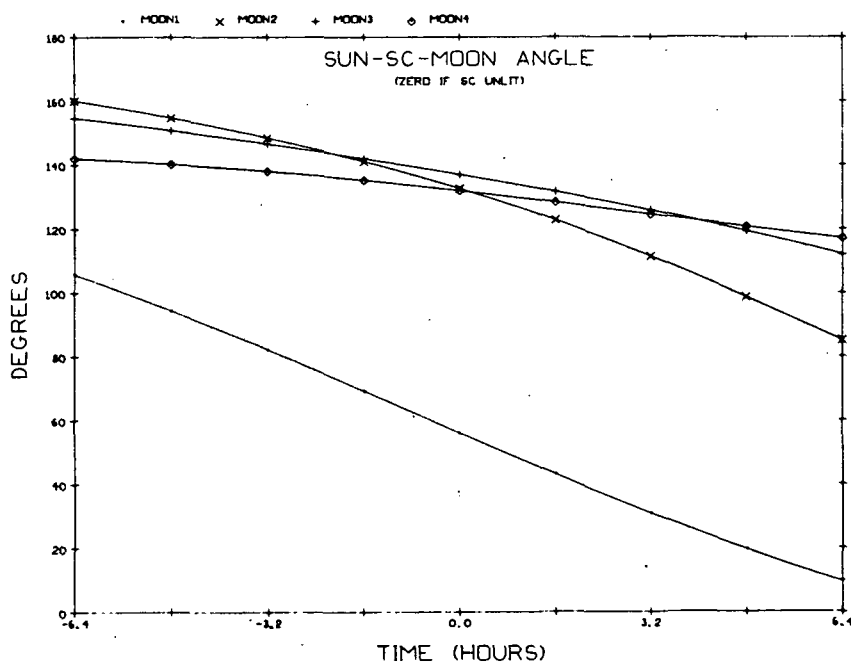


Fig. F-5-7 Sun-Spacecraft-Moon Angle During Jupiter Passage on the Neptune Grand Tour

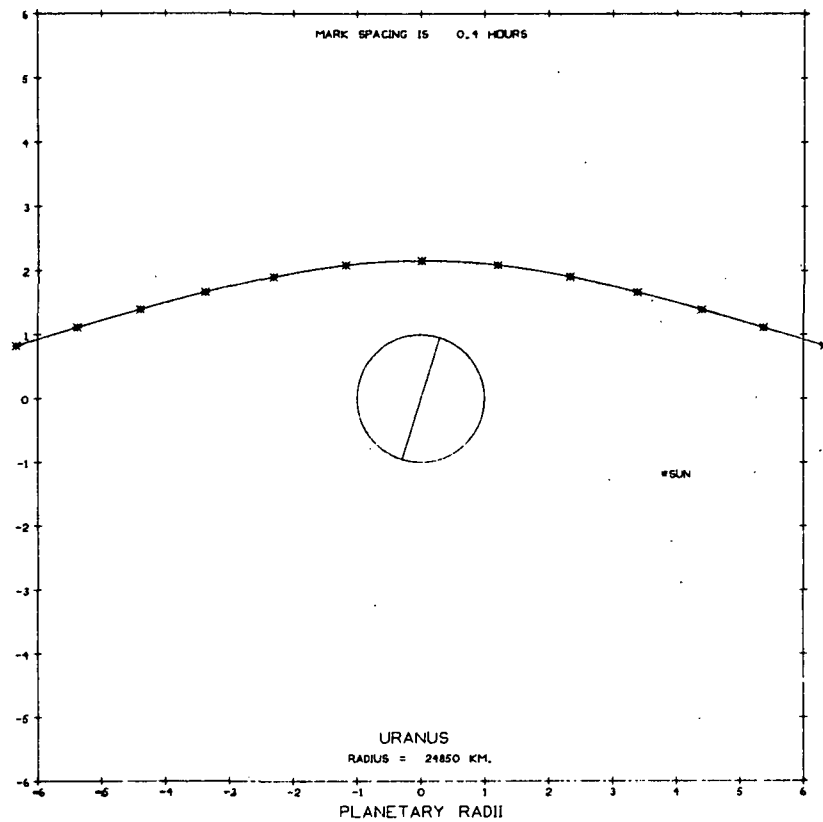


Fig. F-6-1 Trajectory Plan View During
Uranus Passage on the Neptune
Grand Tour (View Beneath Ecliptic)

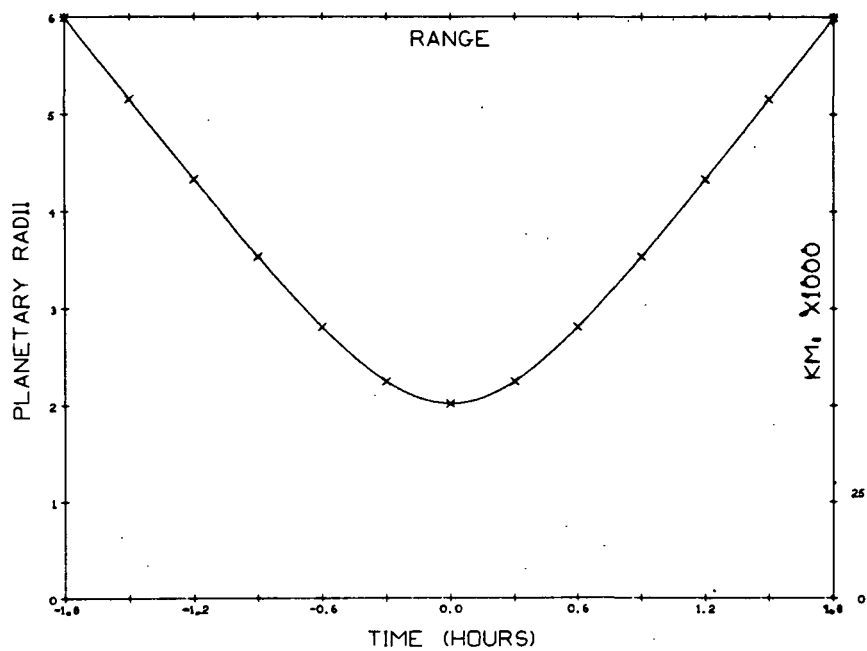


Fig. F-6-2 Range to the Planet During Uranus Passage on the Neptune Grand Tour

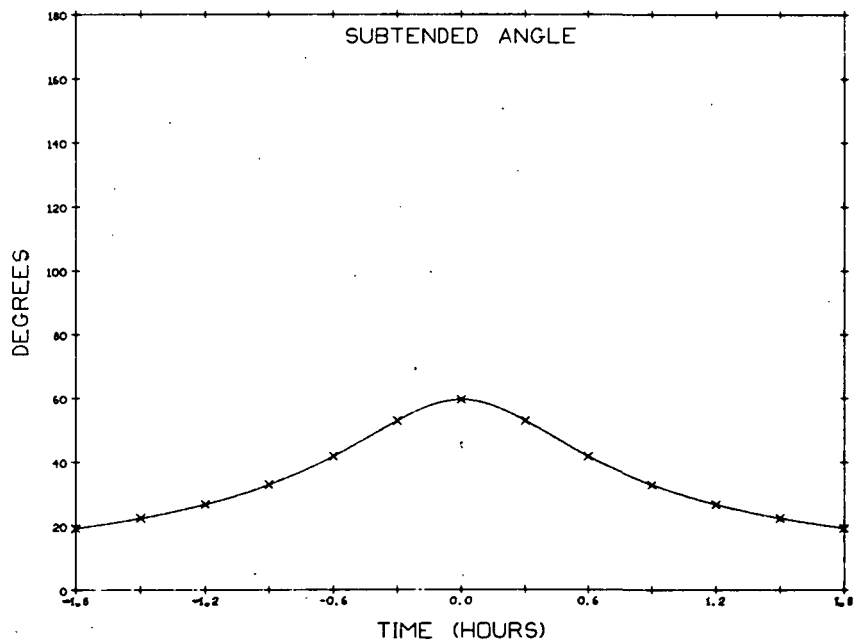


Fig. F-6-3 Angle Subtended by Planetary Limbs During Uranus Passage on the Neptune Grand Tour

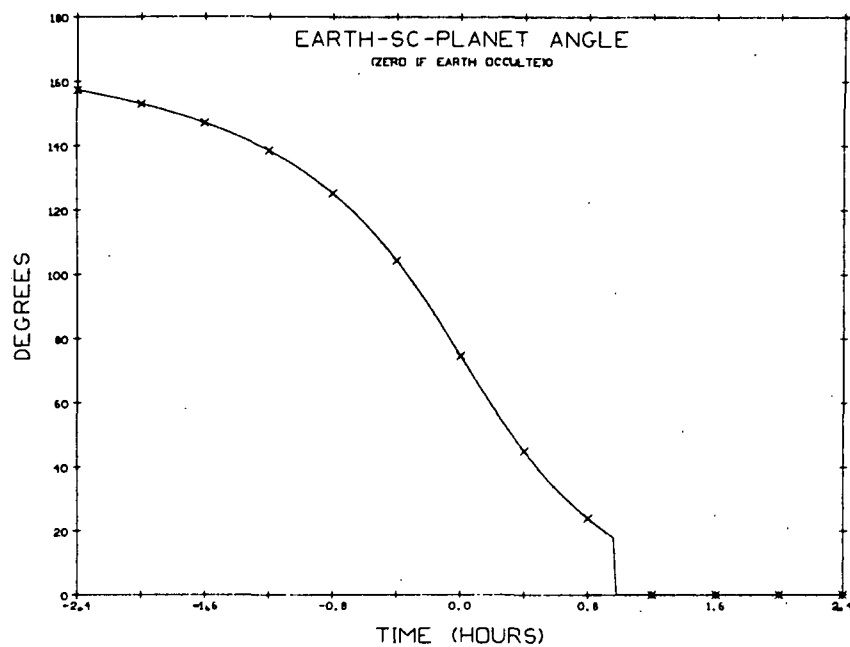


Fig. F-6-4 Earth-Spacecraft-Planet Angle During Uranus Passage on the Neptune Grand Tour

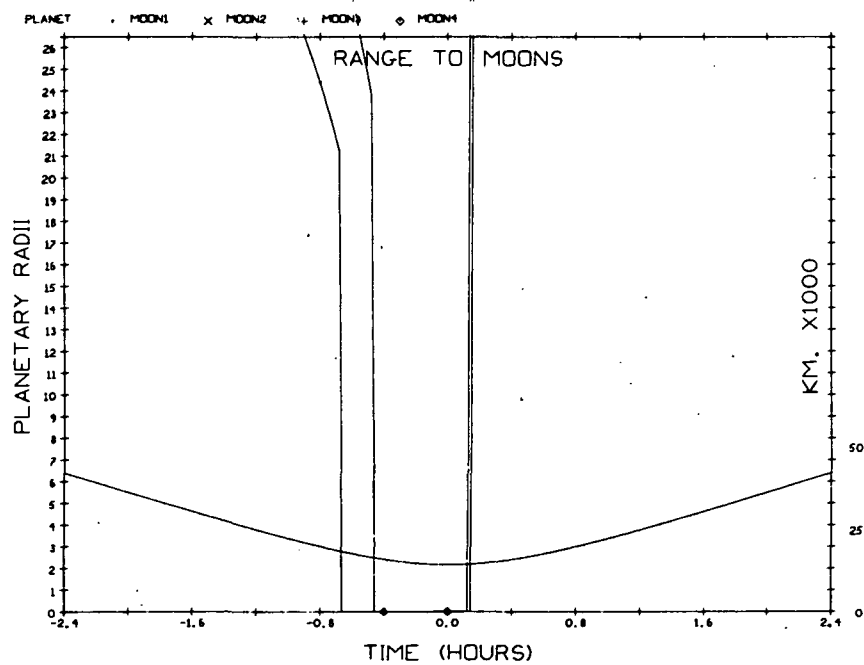


Fig. F-6-5 Range to Principle Moons During Uranus Passage on the Neptune Grand Tour

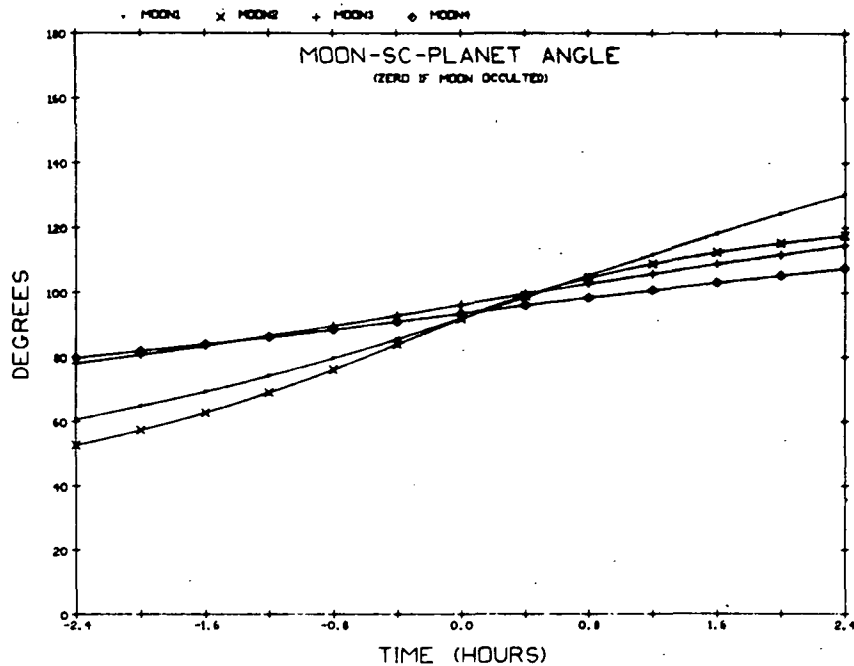


Fig. F-6-6 Moon-Spacecraft-Planet Angle During Uranus Passage on the Neptune Grand Tour

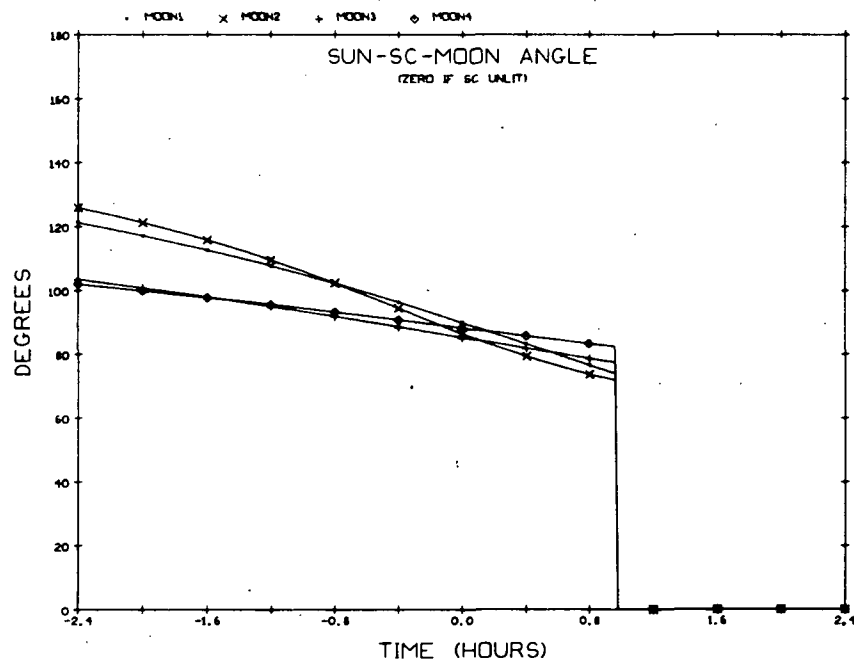


Fig. F-6-7 Sun-Spacecraft-Moon Angle During the Uranus Passage on the Neptune Grand Tour

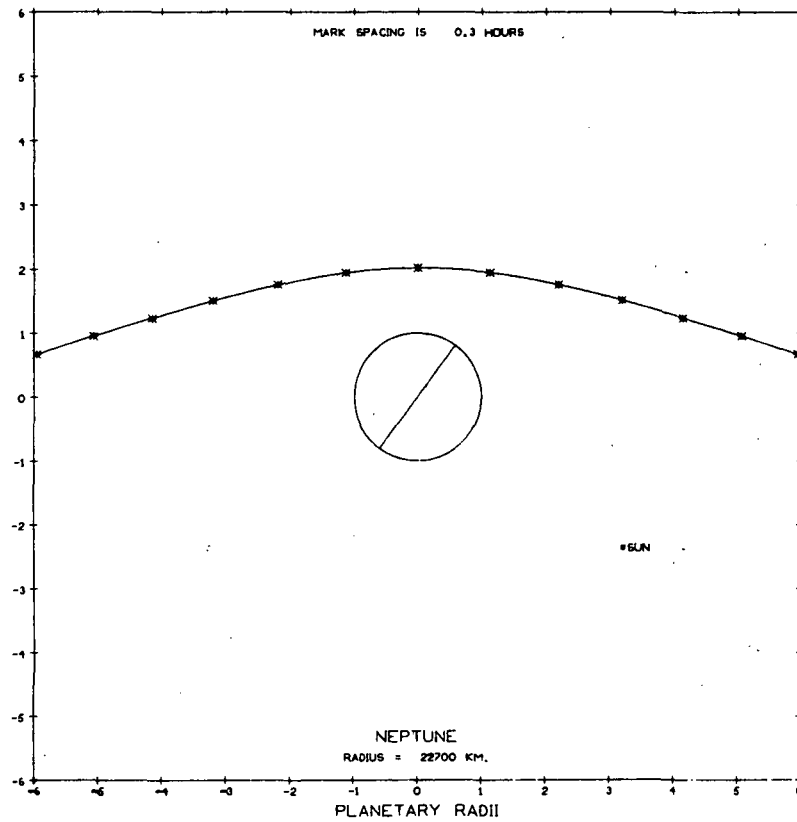


Fig. F-7-1 Trajectory Plan View During Neptune Passage on Neptune Grand Tour

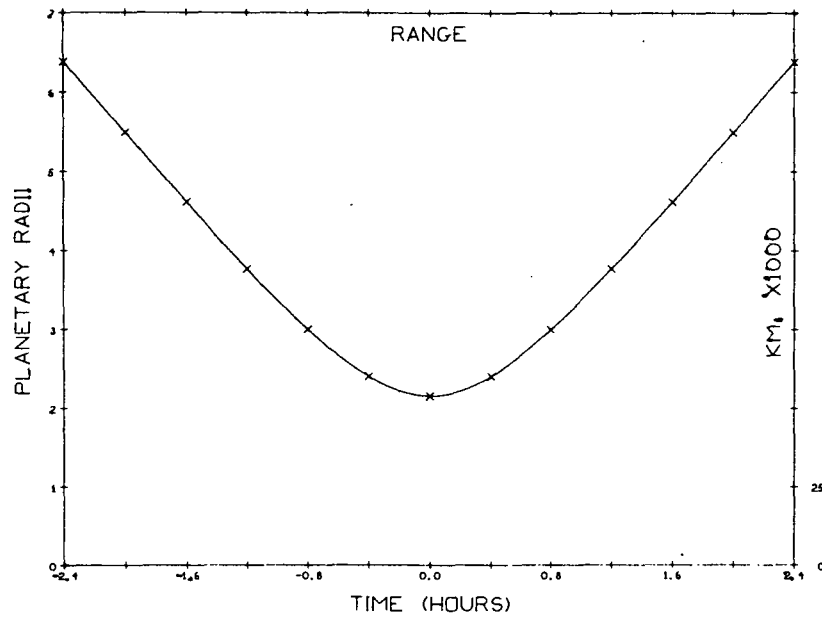


Fig. F-7-2 Range to Planet During Neptune Passage on the Neptune Grand Tour

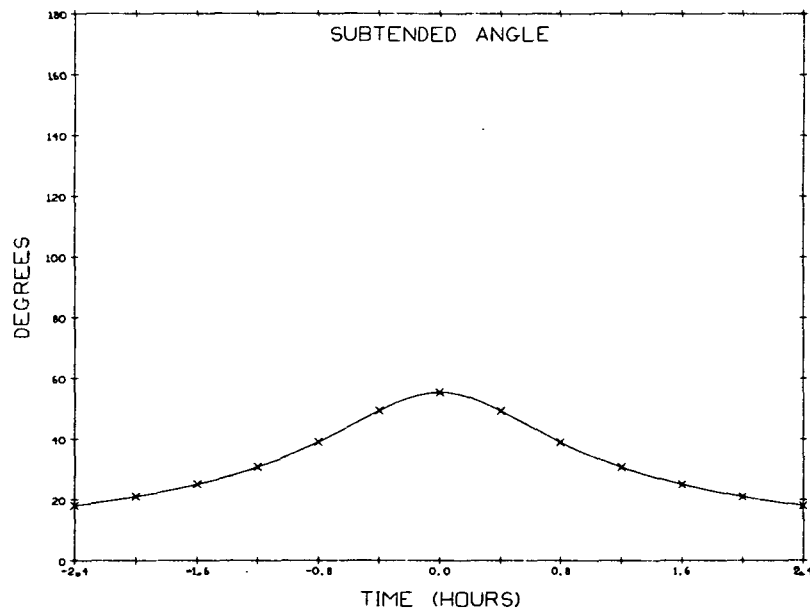


Fig. F-7-3 Angle Subtended by Planetary Limbs During Neptune Passage on the Neptune Grand Tour

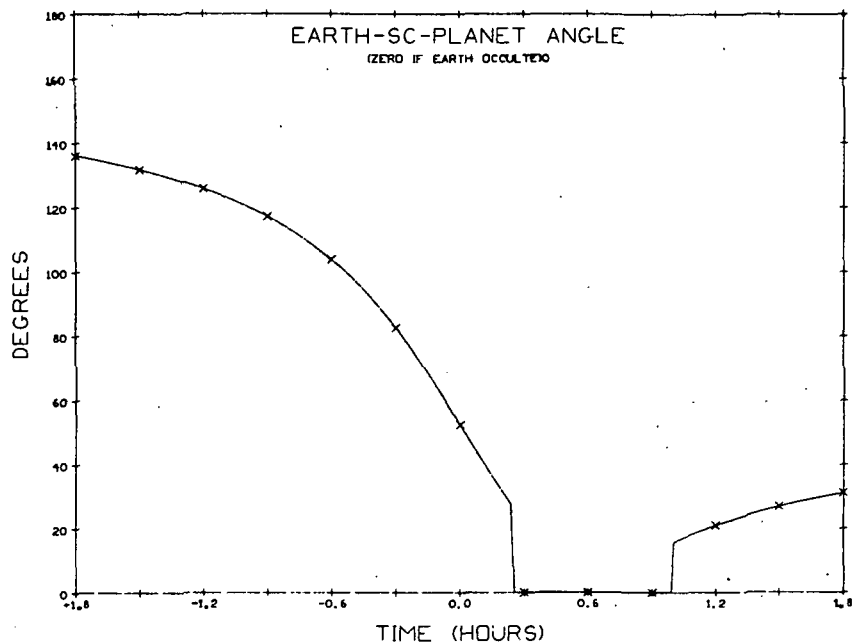


Fig. F-7-4 Earth-Spacecraft-Planet Angle During Neptune Passage on the Neptune Grand Tour

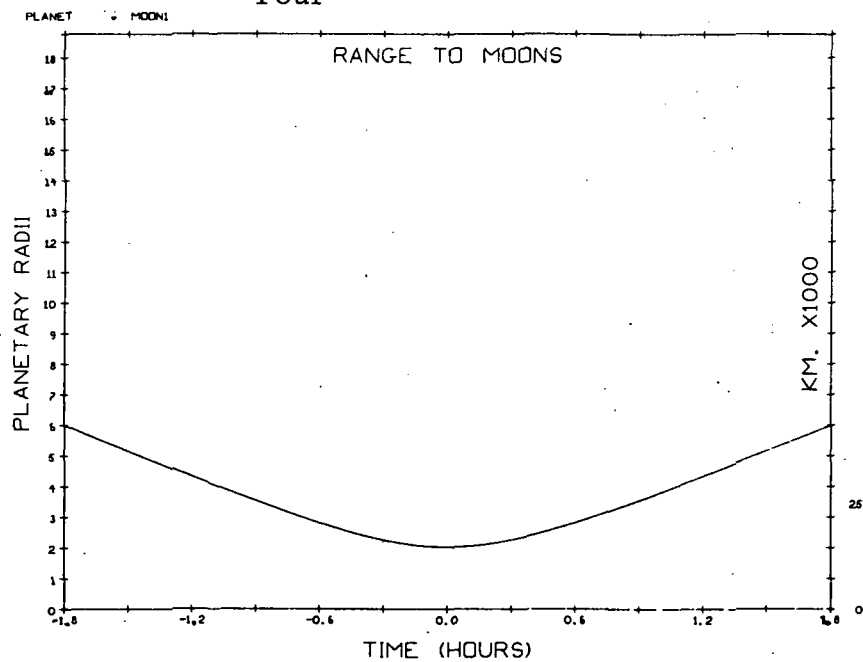


Fig. F-7-5 Range to Principle Moon During Neptune Passage on the Neptune Grand Tour

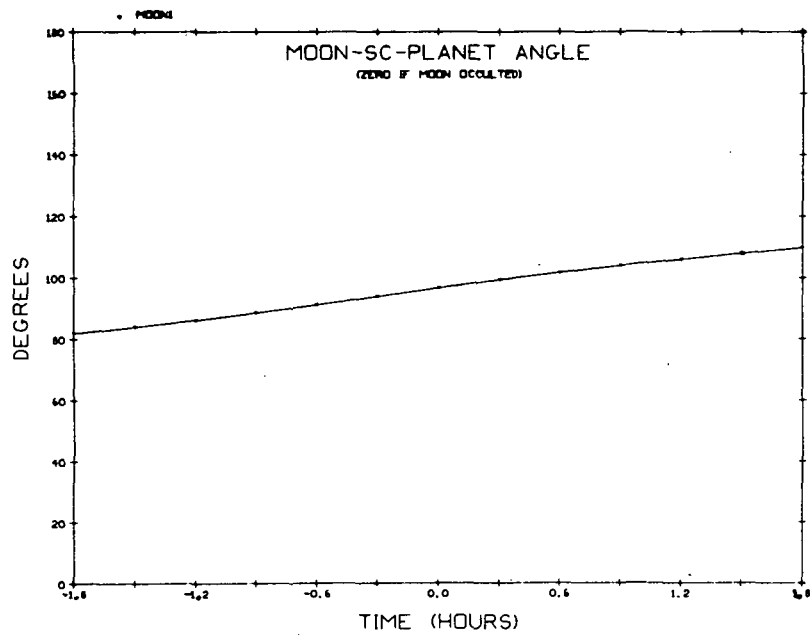


Fig. F-7-6 Moon-Spacecraft-Planet Angle During Neptune Passage on the Neptune Grand Tour

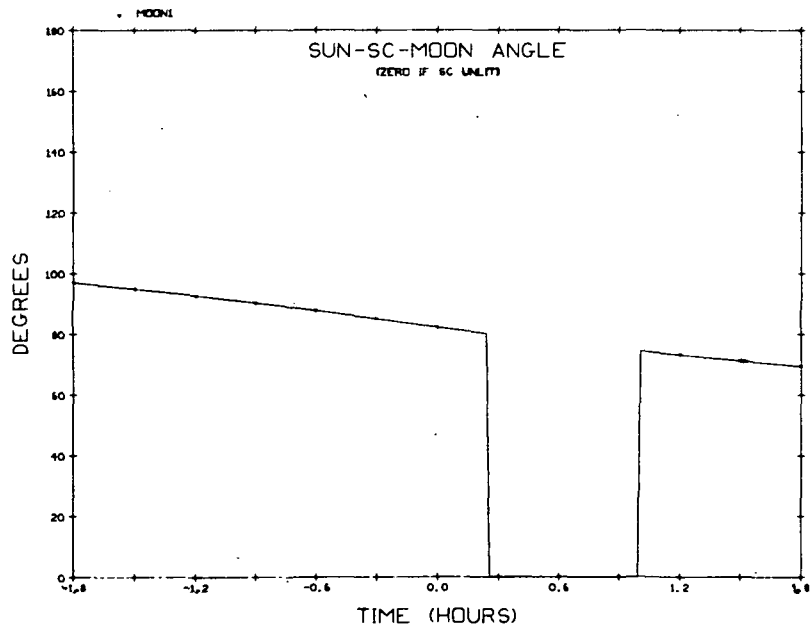


Fig. F-7-7 Sun-Spacecraft-Moon Angle During Neptune Passage on the Neptune Grand Tour

APPENDIX G

PLUTO GRAND TOUR MISSION PLOTS

This appendix contains the plots for the Pluto Grand Tour Mission. An explanation of their use is given in Appendix A.

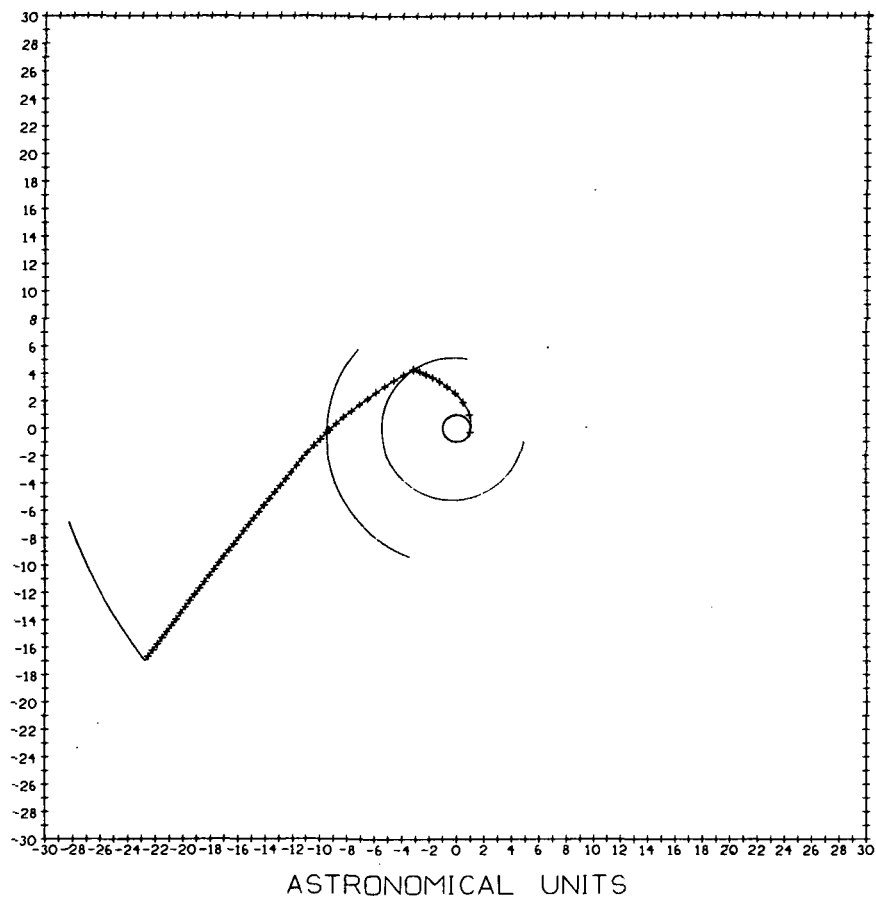


Fig. G-1 Trajectory for Pluto Grand Tour

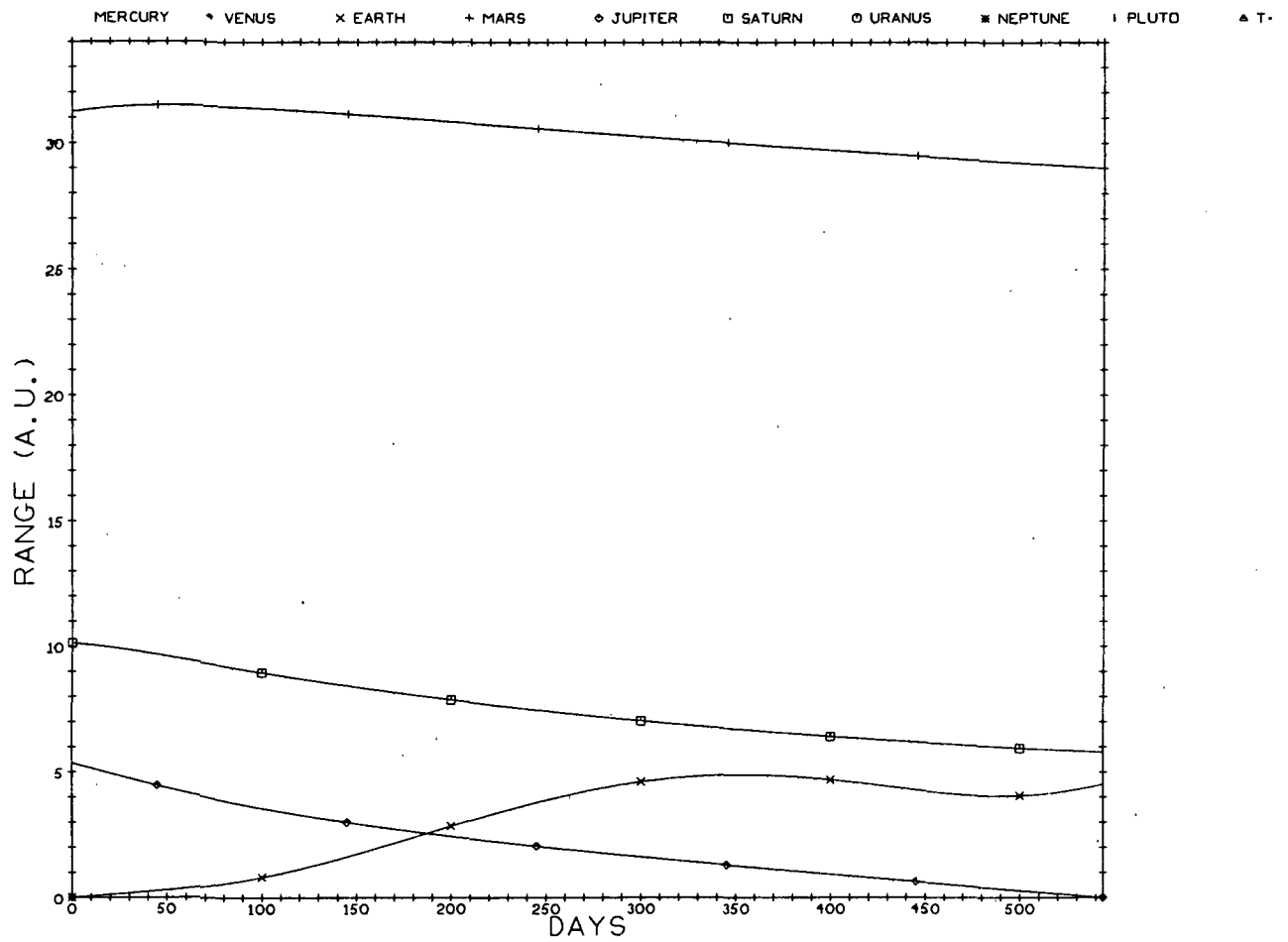


Fig. G-2-1 Ranges to Solar System Planets for Interplanetary (Earth-Jupiter) Leg of the Pluto Grand Tour

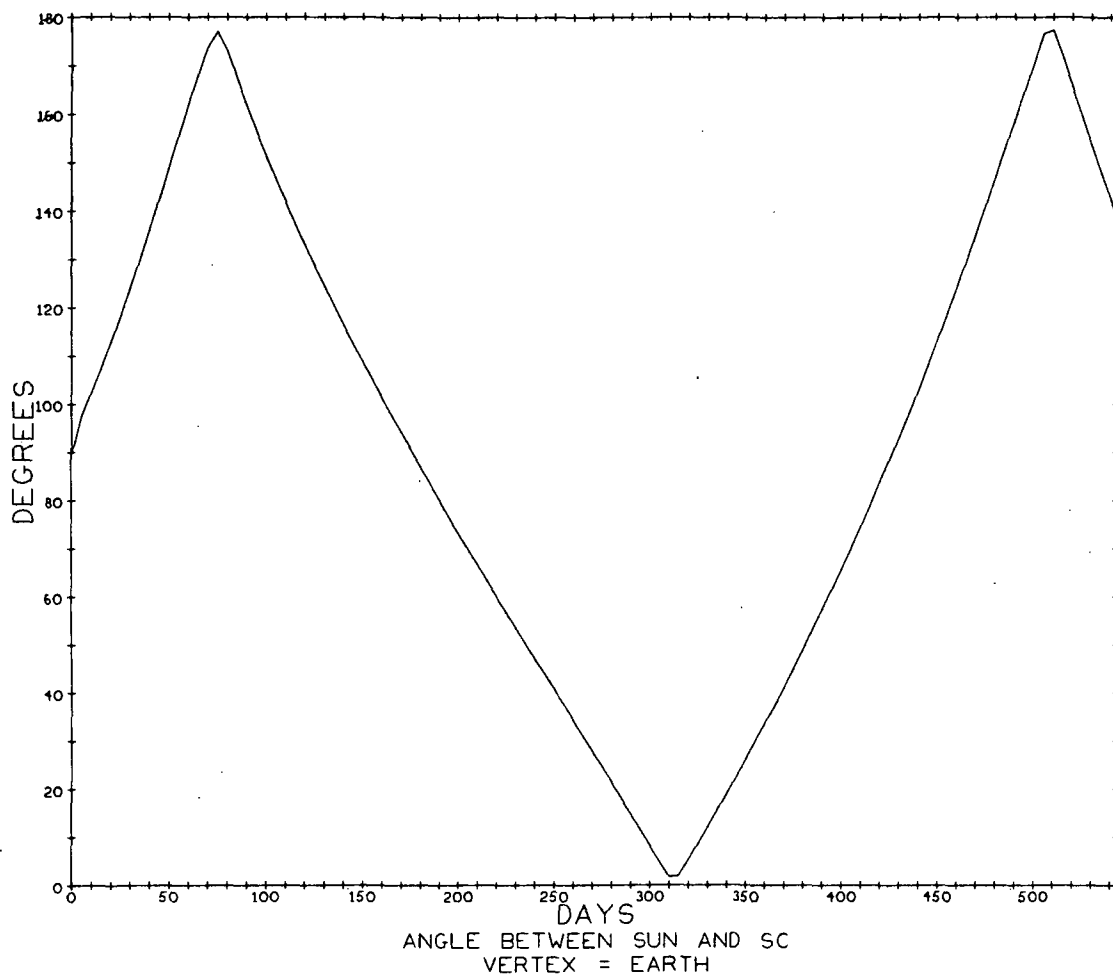


Fig. G-2-2 Spacecraft-Earth-Sun Angle for the Interplanetary (Earth-Jupiter) Leg of the Pluto Grand Tour

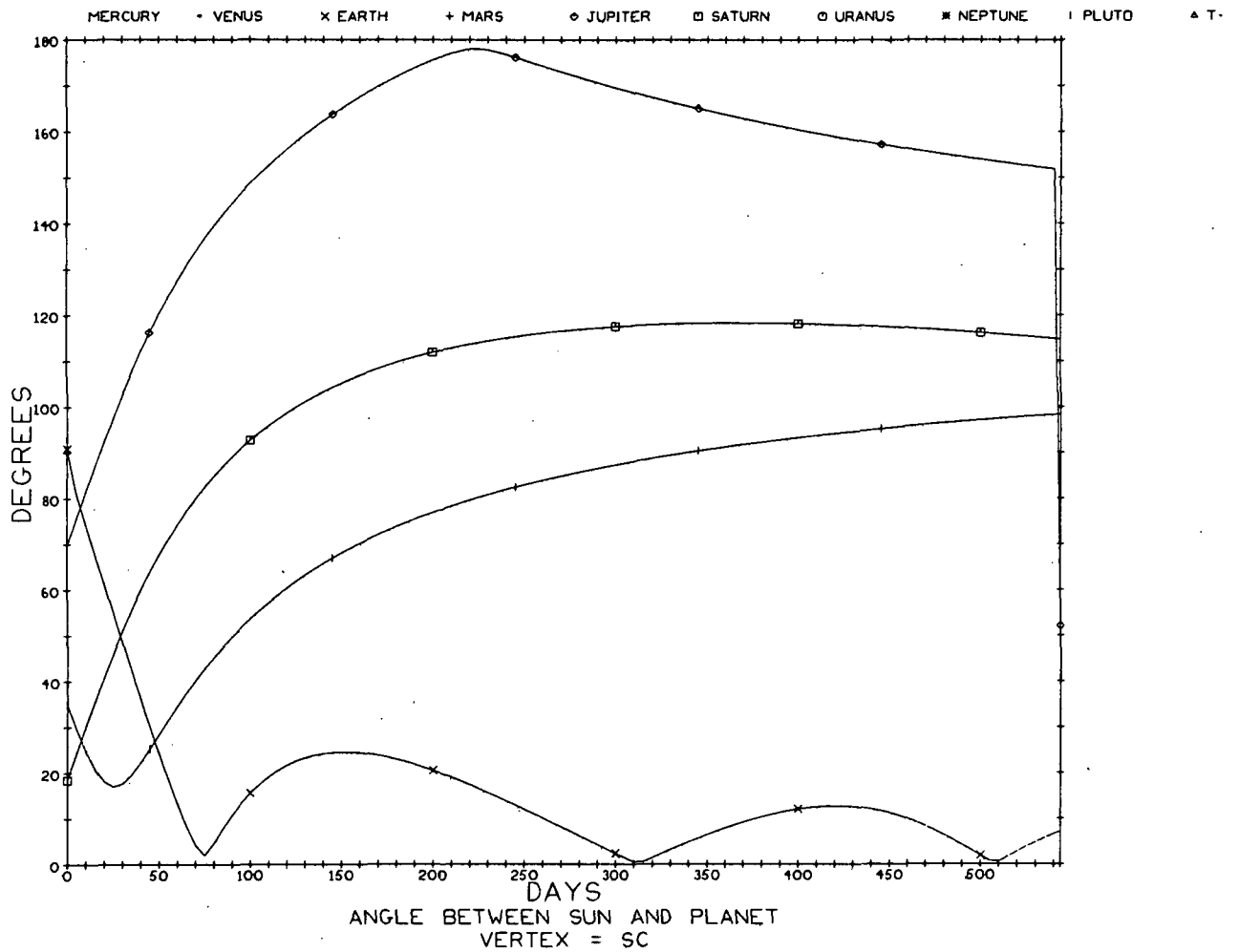


Fig. G-2-3 Sun-Spacecraft-Planet Angle for the Interplanetary (Earth-Jupiter) Leg of the Pluto Grand Tour

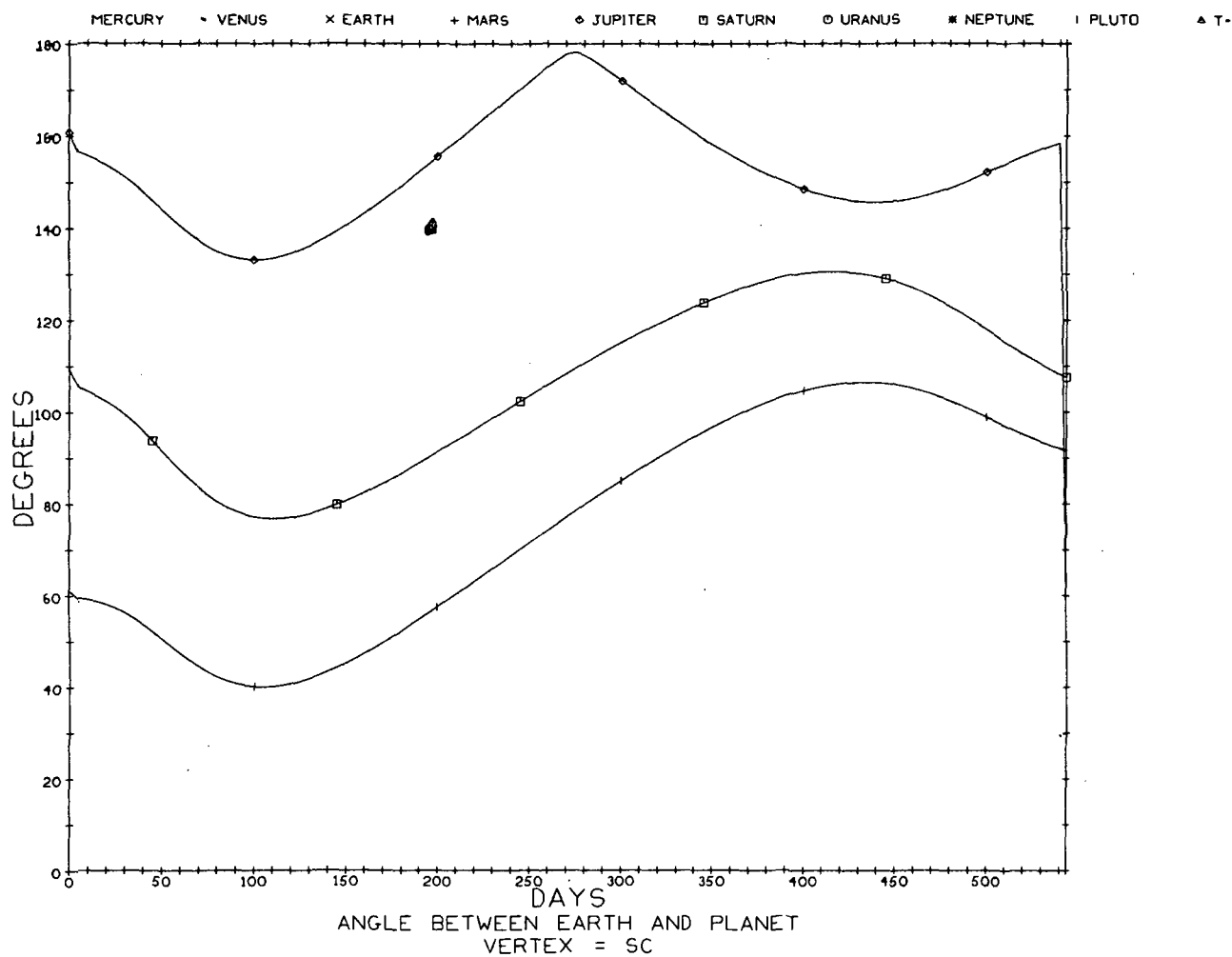


Fig. G-2-4 Earth-Spacecraft-Planet Angles for the Interplanetary (Earth-Jupiter) Leg of the Pluto Grand Tour

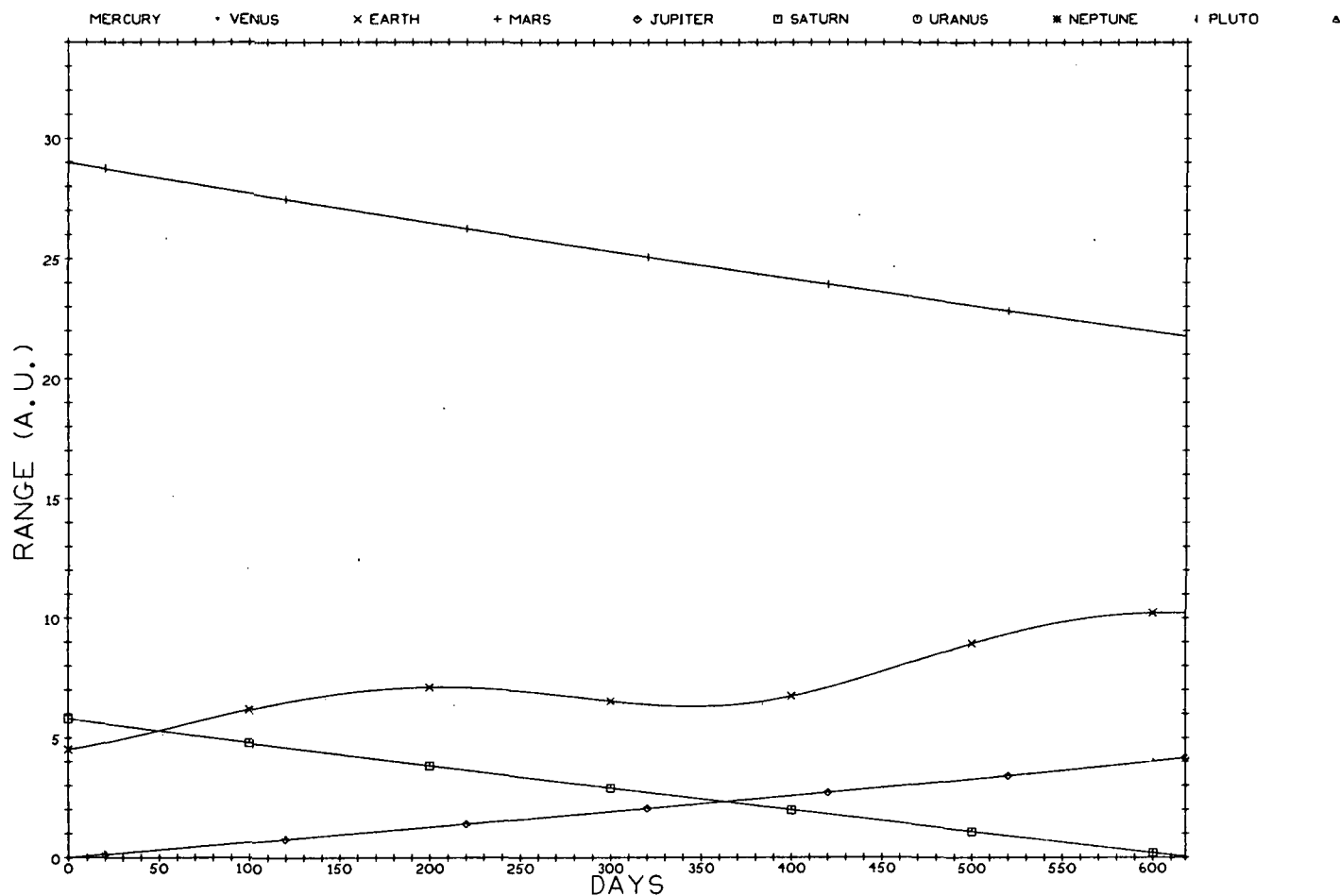


Fig. G-3-1

Ranges to Solar System Planets for the Interplanetary (Jupiter-Saturn) Leg of the Pluto Grand Tour

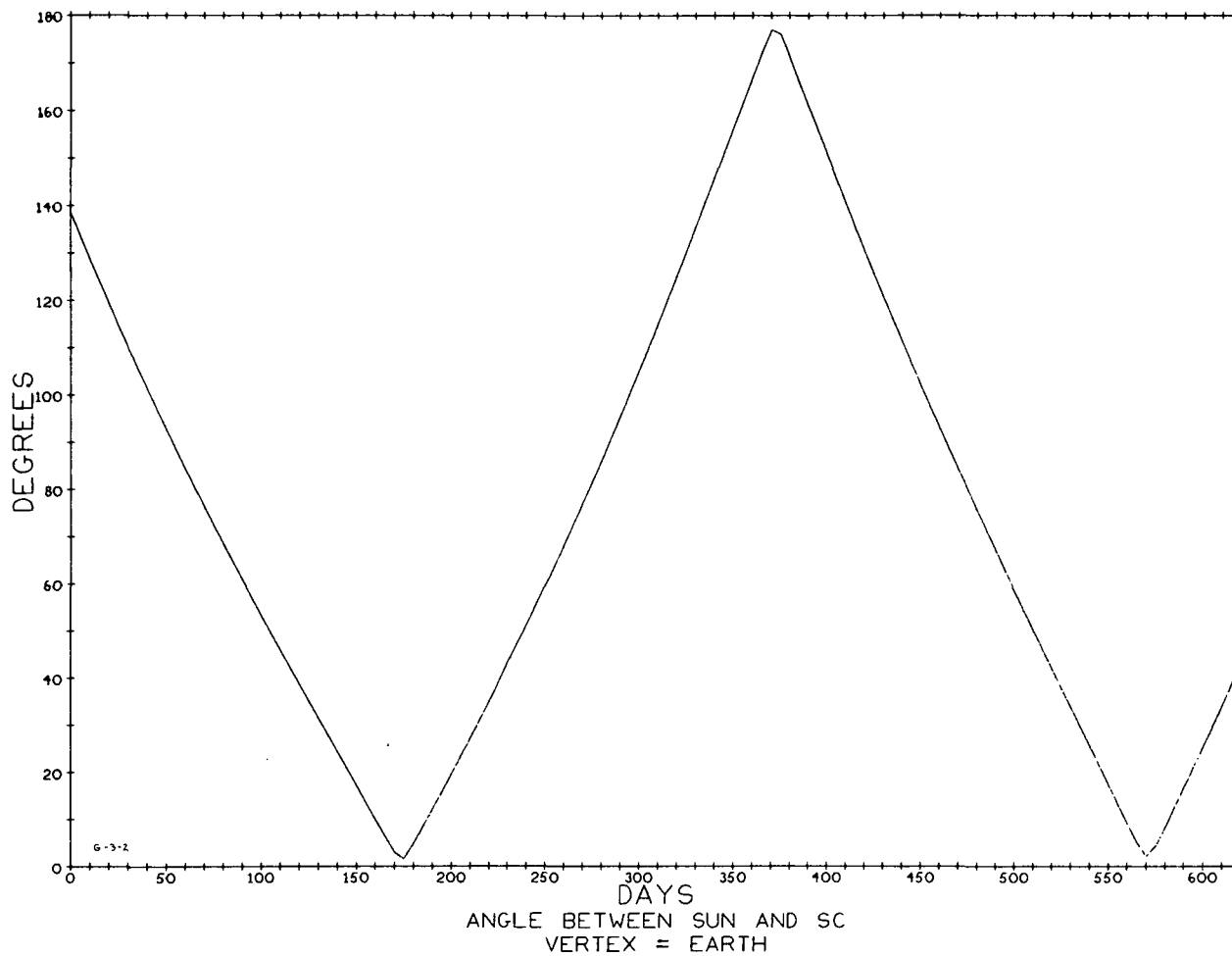


Fig. G-3-2 Spacecraft-Earth-Sun Angle for the Interplanetary (Jupiter-Saturn) Leg of the Pluto Grand Tour

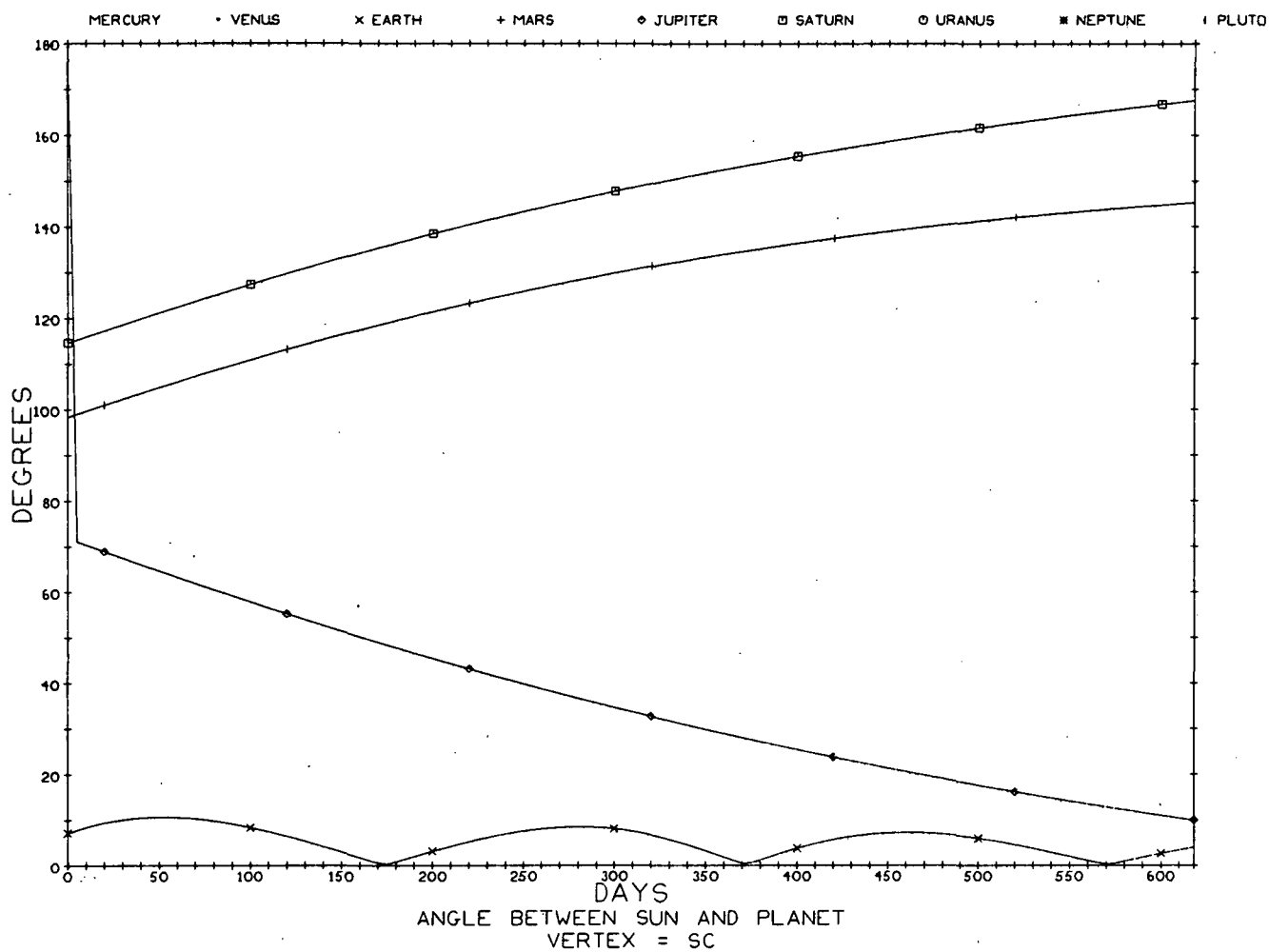


Fig. G-3-3

Sun-Spacecraft-Planet Angles for the Interplanetary
(Jupiter-Saturn) Leg of the Pluto Grand Tour

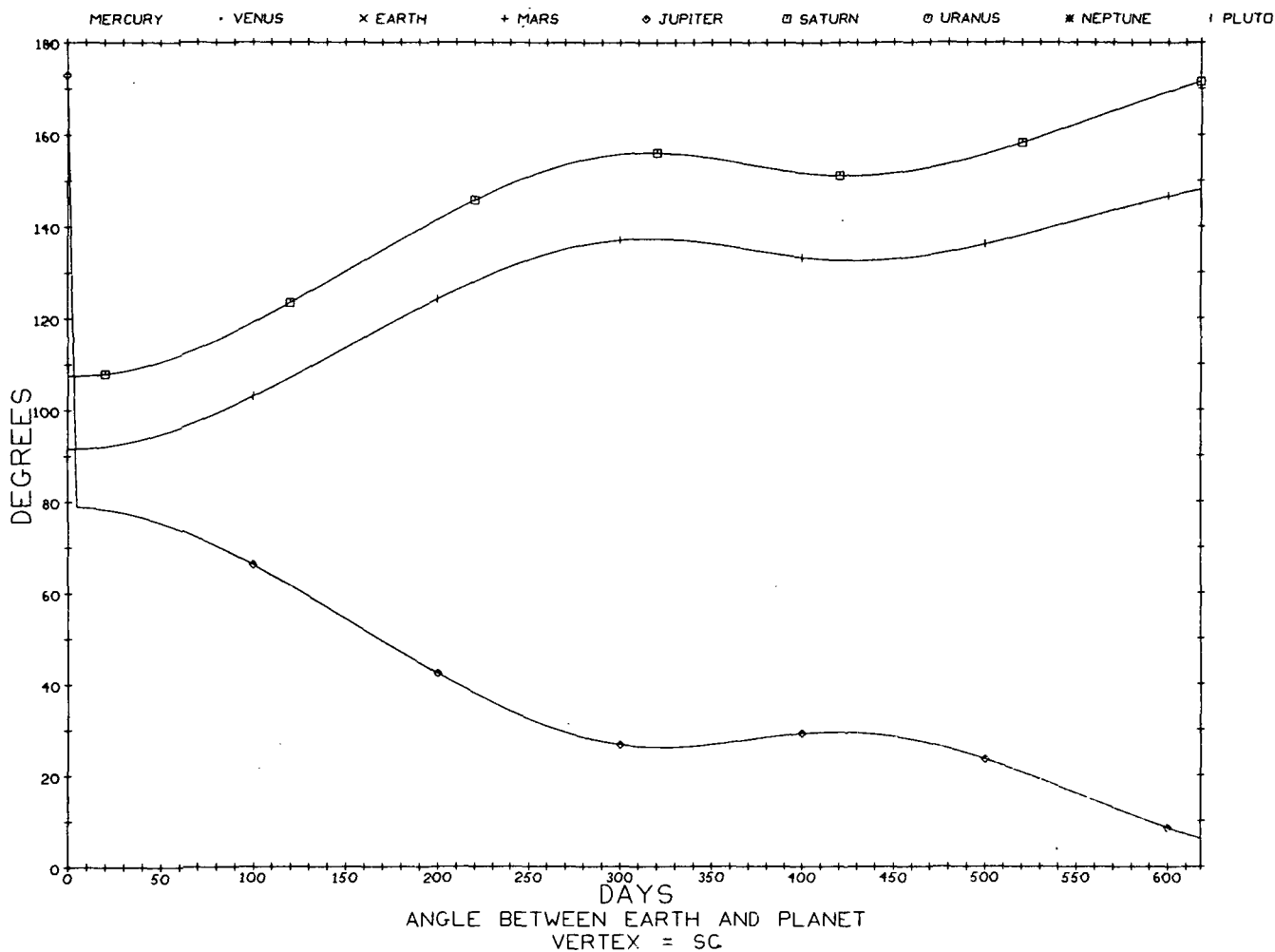


Fig. G-3-4 Earth-Spacecraft-Planet Angles for the Interplanetary (Jupiter-Saturn) Leg of the Pluto Grand Tour

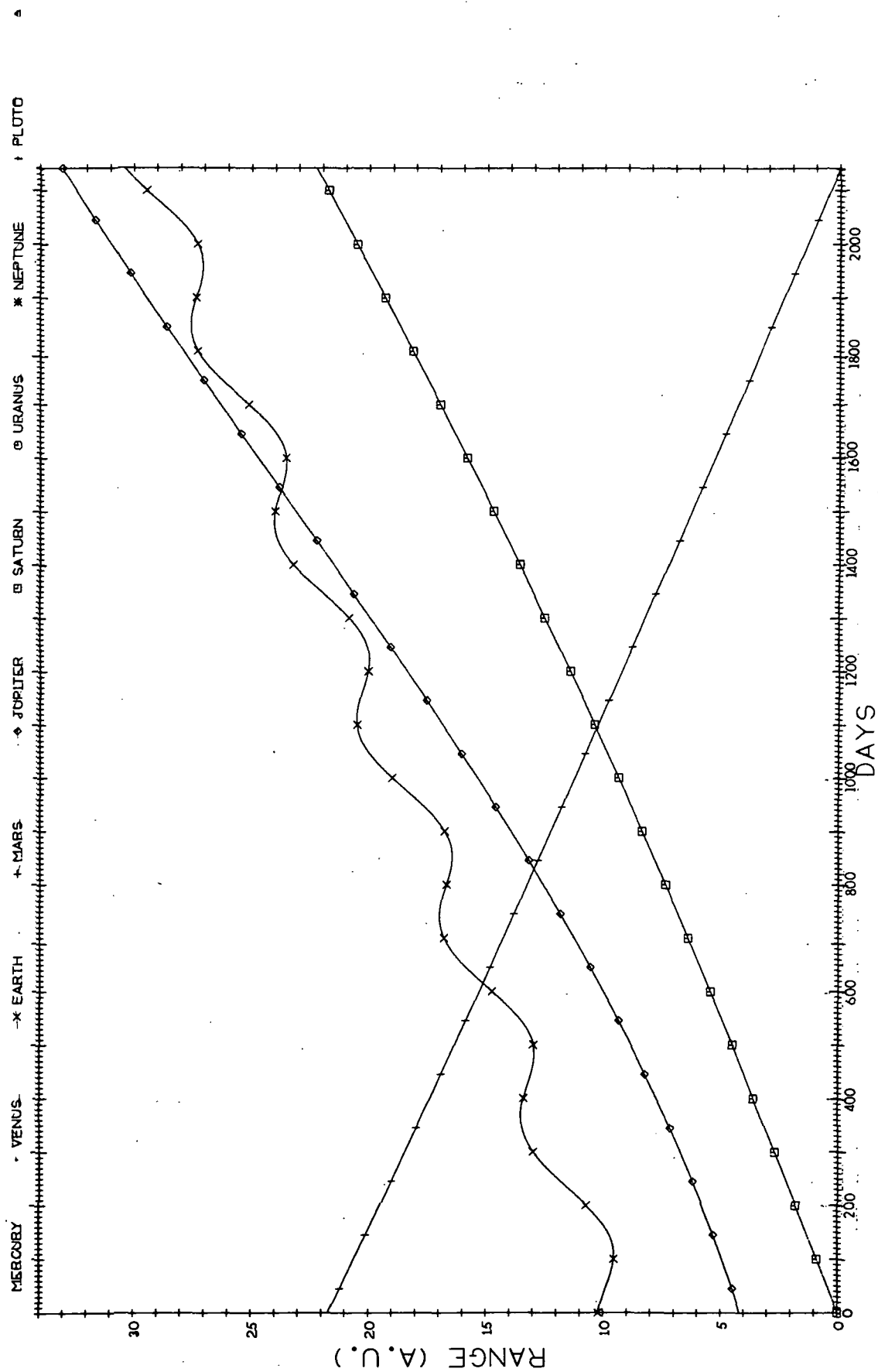


Fig. G-4-1 Ranges to Solar System Planets for Interplanetary (Saturn-Pluto) Leg of the Pluto Grand Tour

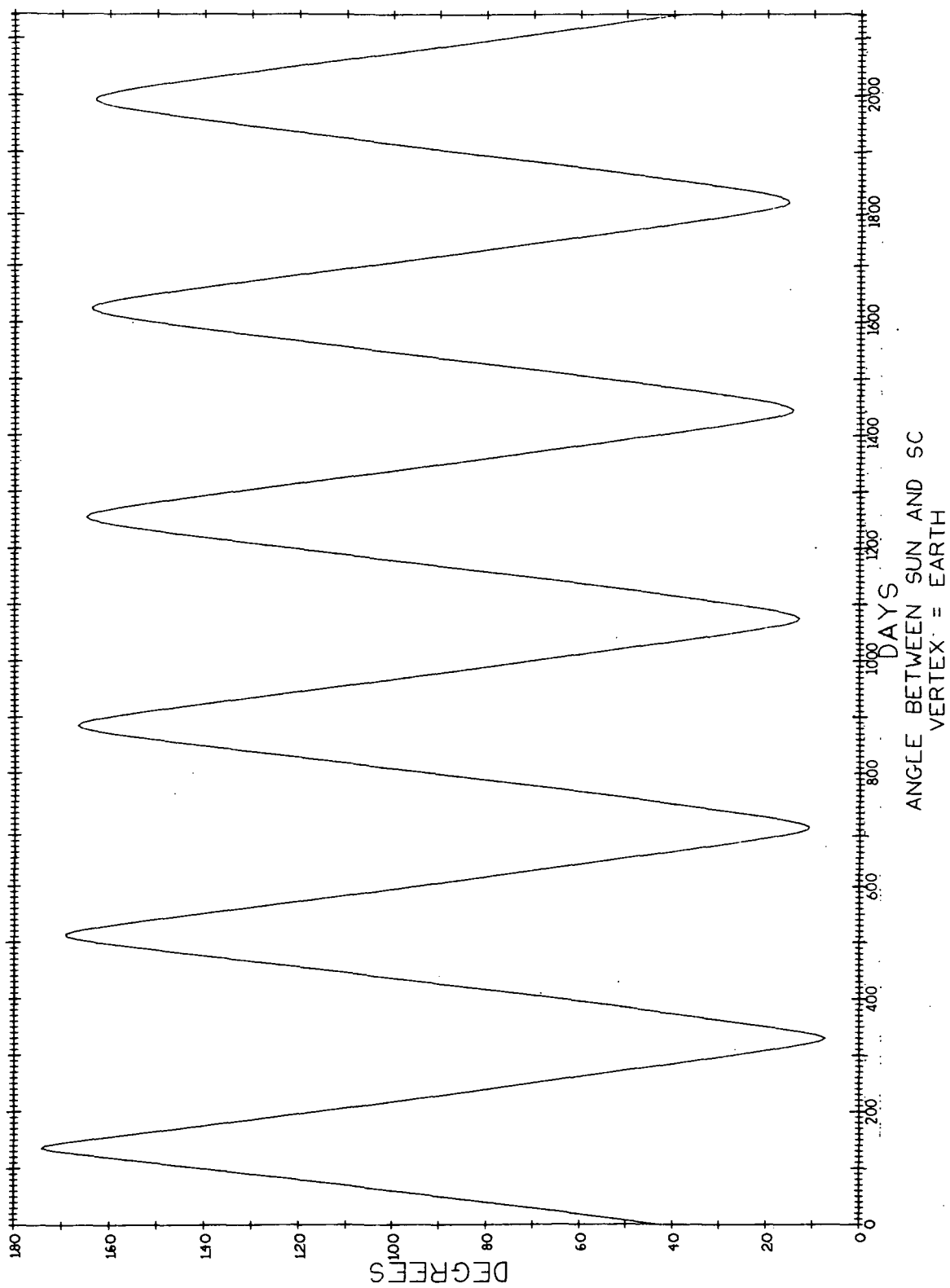


Fig. G-4-2 Spacecraft-Earth-Sun Angle for the Interplanetary (Saturn-Pluto) Leg of the Pluto Grand Tour

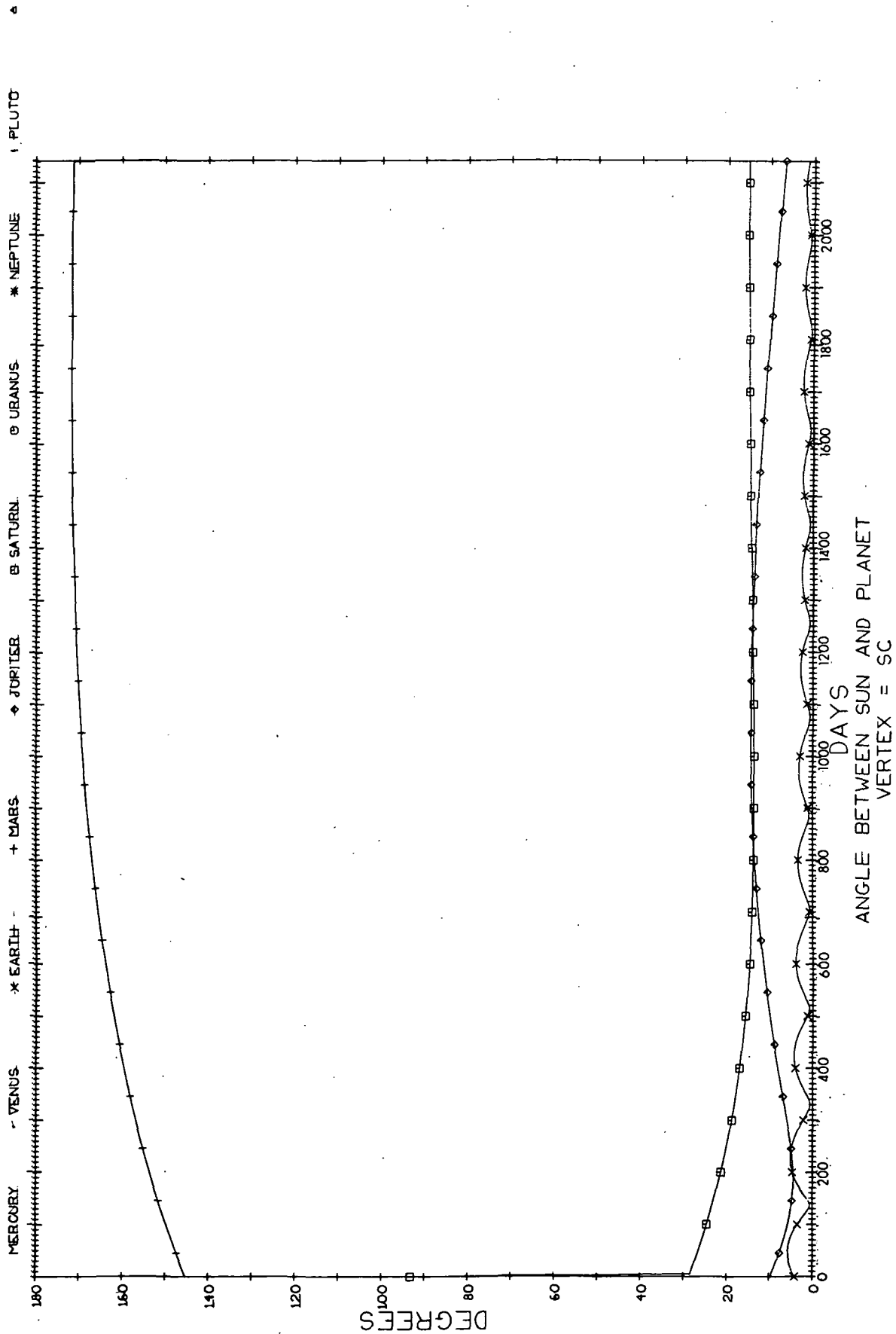


Fig. G-4-3 Sun-Spacecraft-Planet Angles for the Interplanetary (Saturn-Pluto) Leg of the Pluto Grand Tour

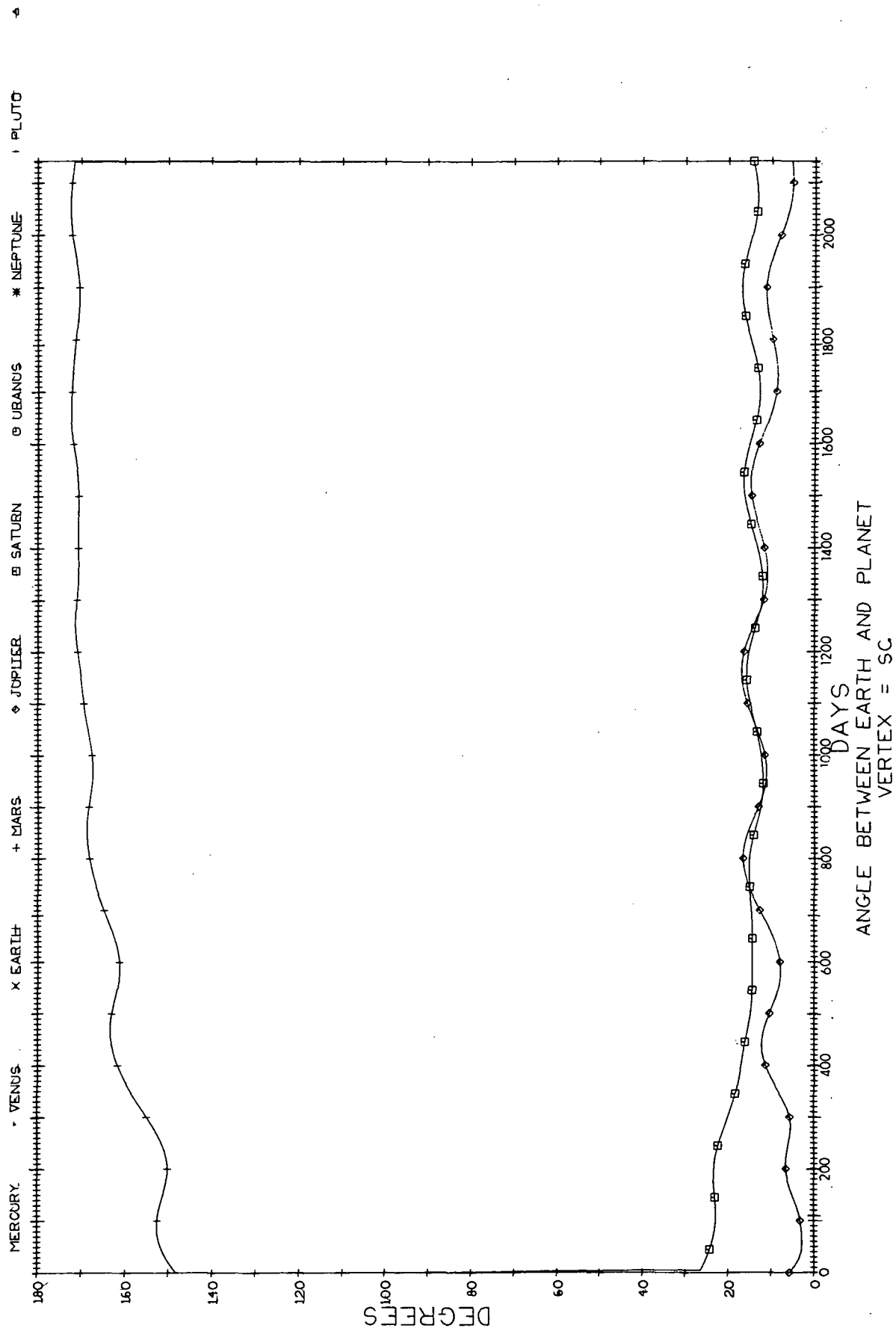


Fig. G-4-4 Sun-Spacecraft-Planet Angles for the Interplanetary (Saturn-Pluto) Leg of the Pluto Grand Tour

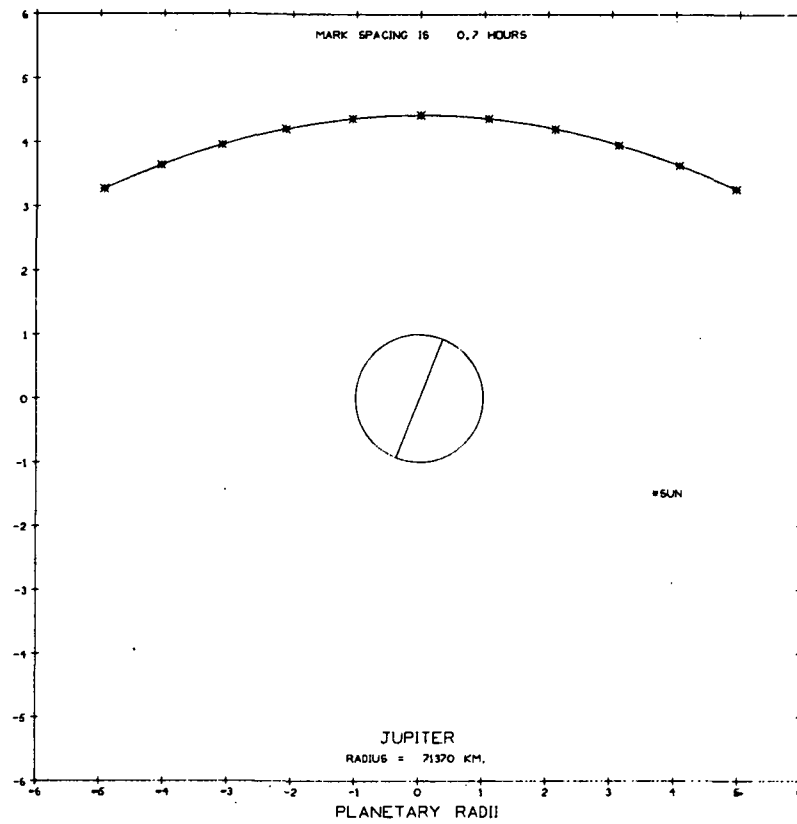


Fig. G-5-1 Trajectory Plan View During Jupiter
Passage on Pluto Grand Tour
12 Radii Field

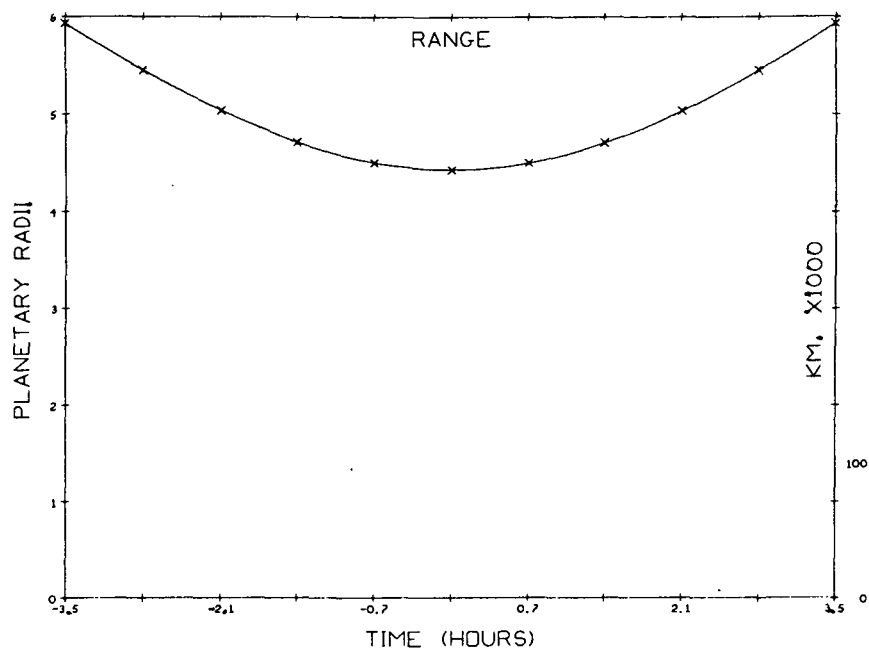


Fig. G-5-2 Range to Planet During Jupiter Passage on Pluto Grand Tour

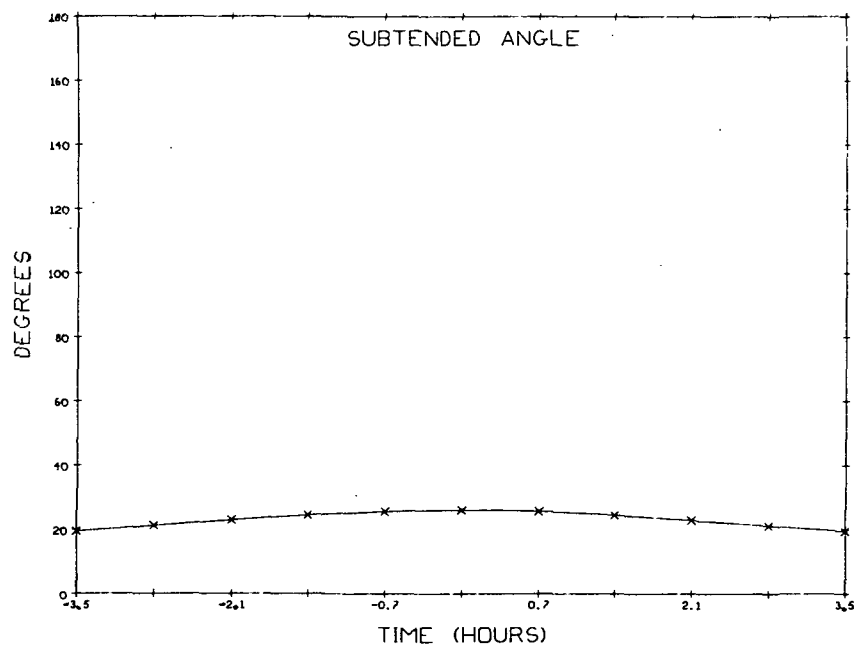


Fig. G-5-3 Angle Subtended by Planetary Limbs During Jupiter Passage on the Pluto Grand Tour

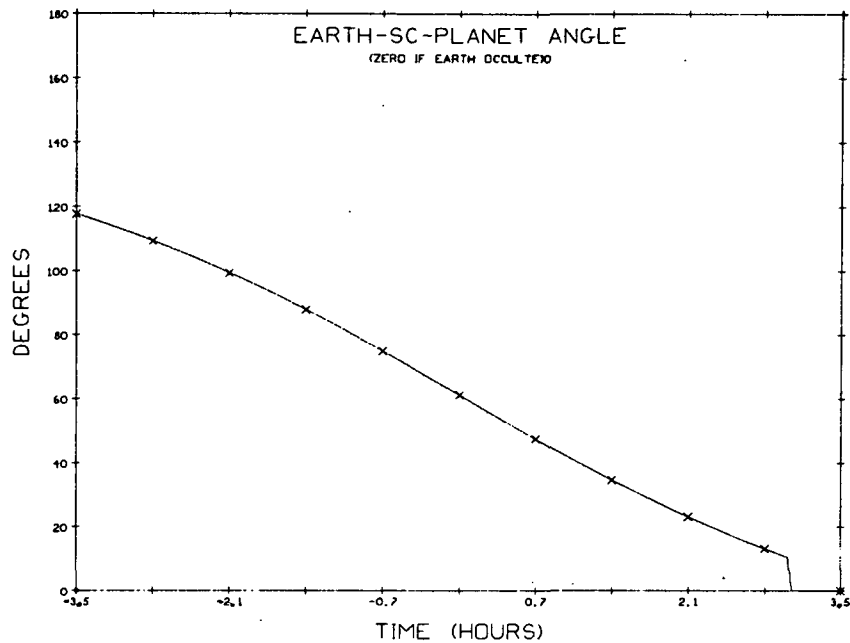


Fig. G-5-4 Earth-Spacecraft-Planet Angle During Jupiter Passage on the Pluto Grand Tour

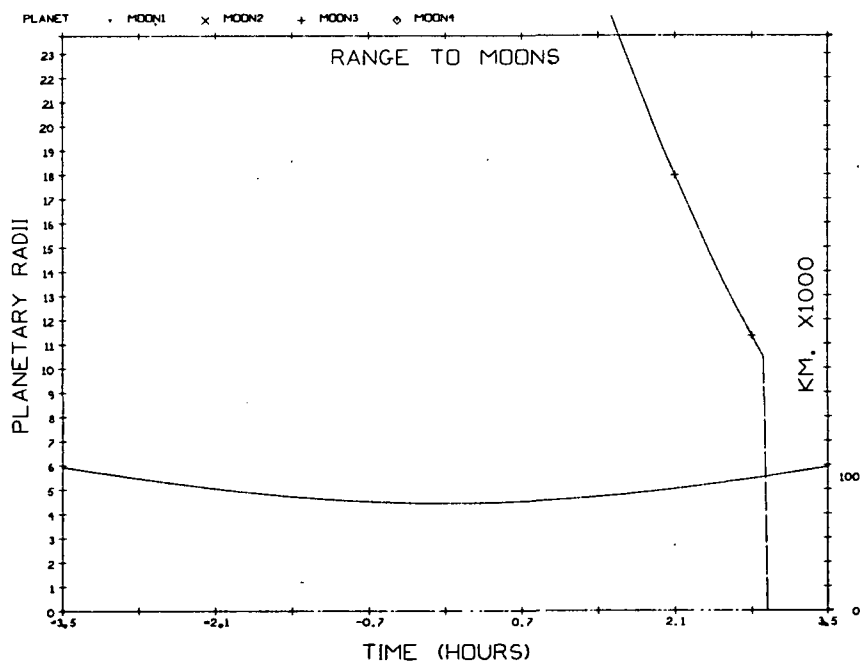


Fig. G-5-5 Range to Principle Moons During Jupiter Passage on the Pluto Grand Tour

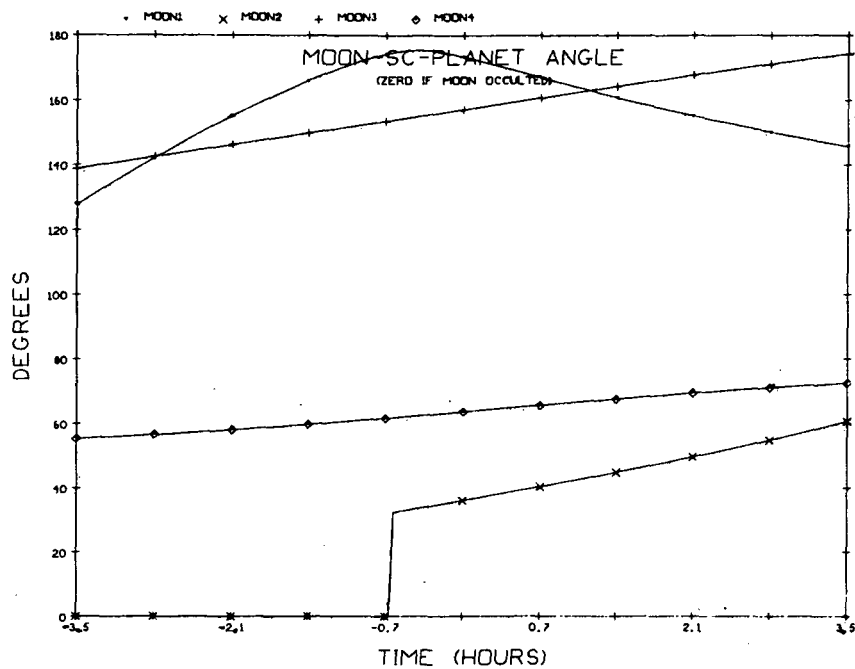


Fig. G-5-6 Moon-Spacecraft-Planet Angle During Jupiter Passage on the Pluto Grand Tour

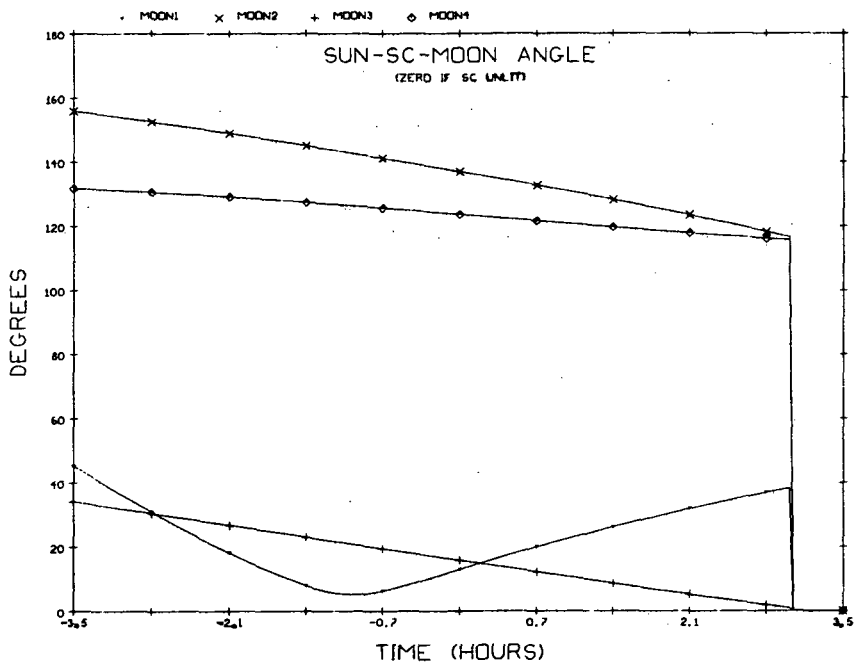


Fig. G-5-7 Sun-Spacecraft-Moon Angle During the Jupiter Passage on the Pluto Grand Tour

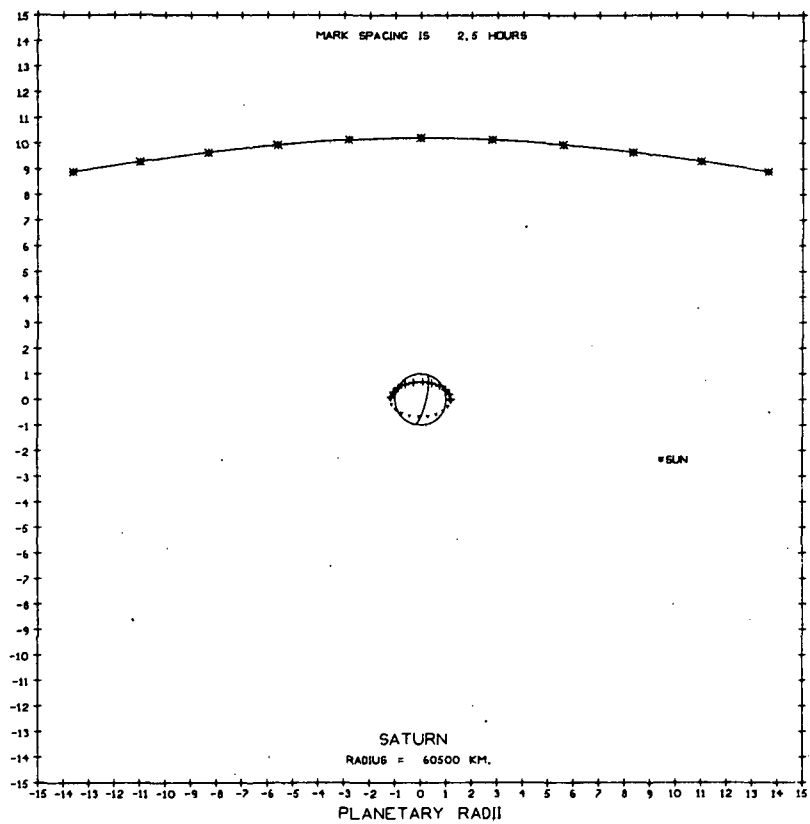


Fig. G-6-1 Trajectory Plan View During Saturn Passage on the Pluto Grand Tour

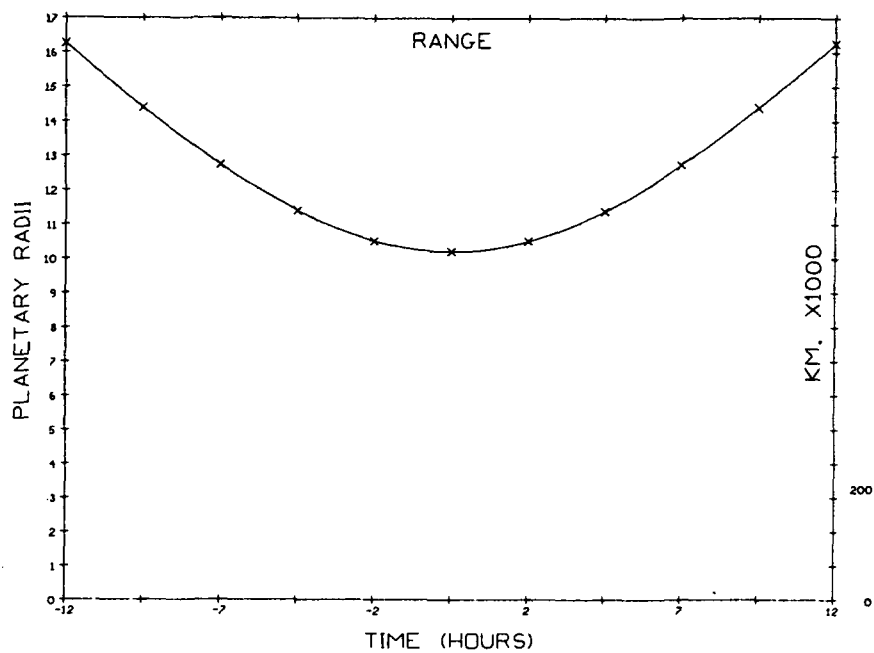


Fig. G-6-2 Range to Planet During Saturn Passage on the Pluto Grand Tour

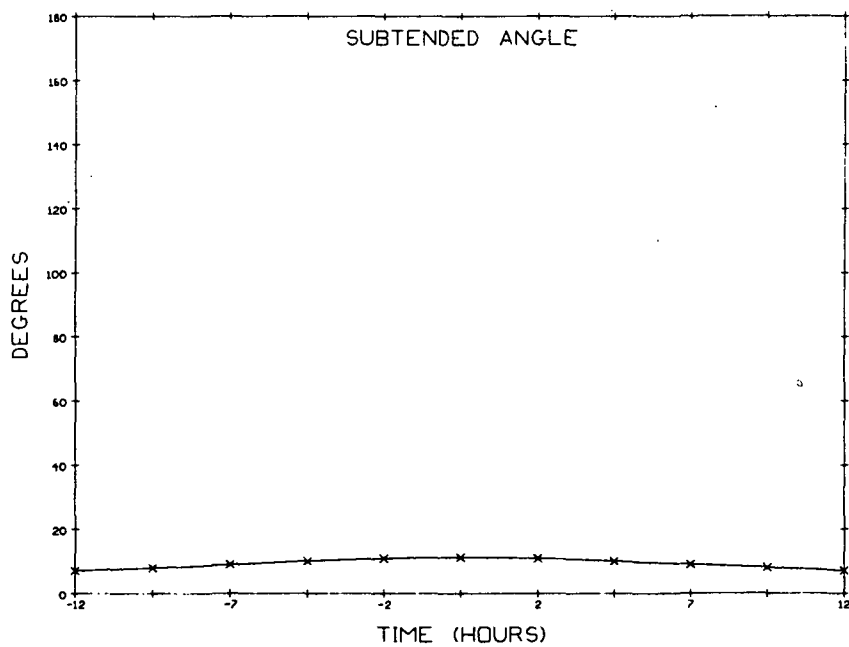


Fig. G-6-3 Angle Subtended by Planetary Limbs During Saturn Passage on the Pluto Grand Tour

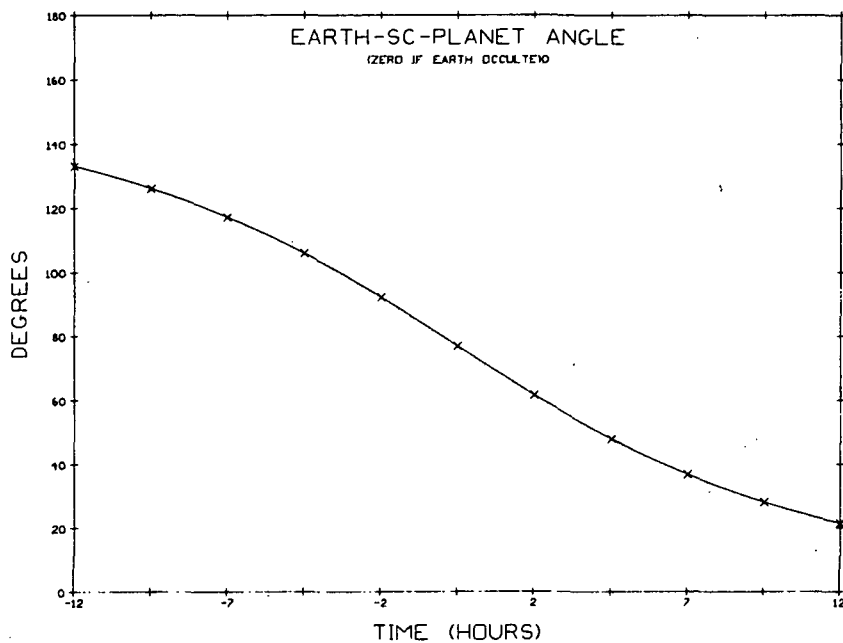


Fig. G-6-4 Earth-Spacecraft-Planet Angle During Saturn Passage on the Pluto Grand Tour

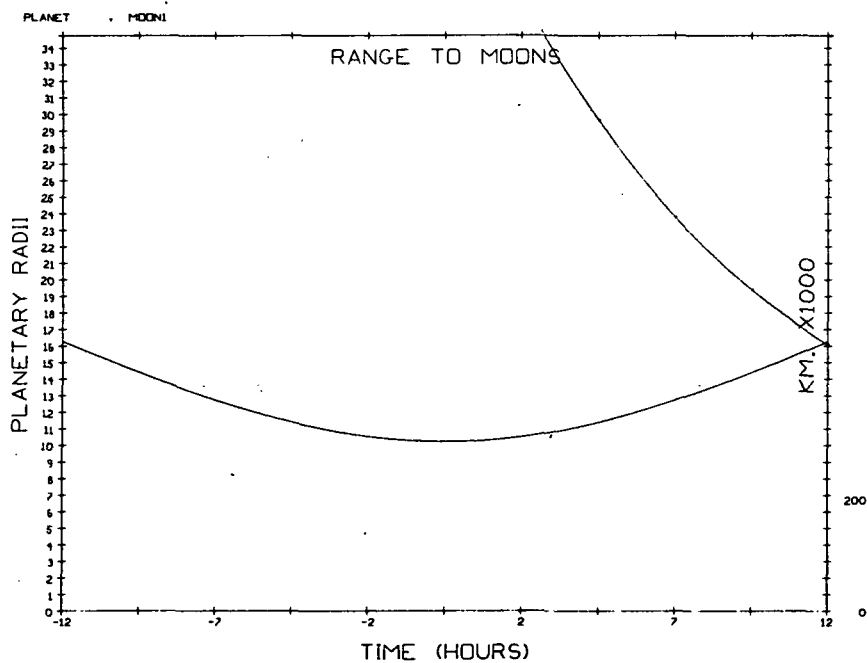


Fig. G-6-5 Ranges to Principle Moon and Planet During Saturn Passage on the Pluto Grand Tour

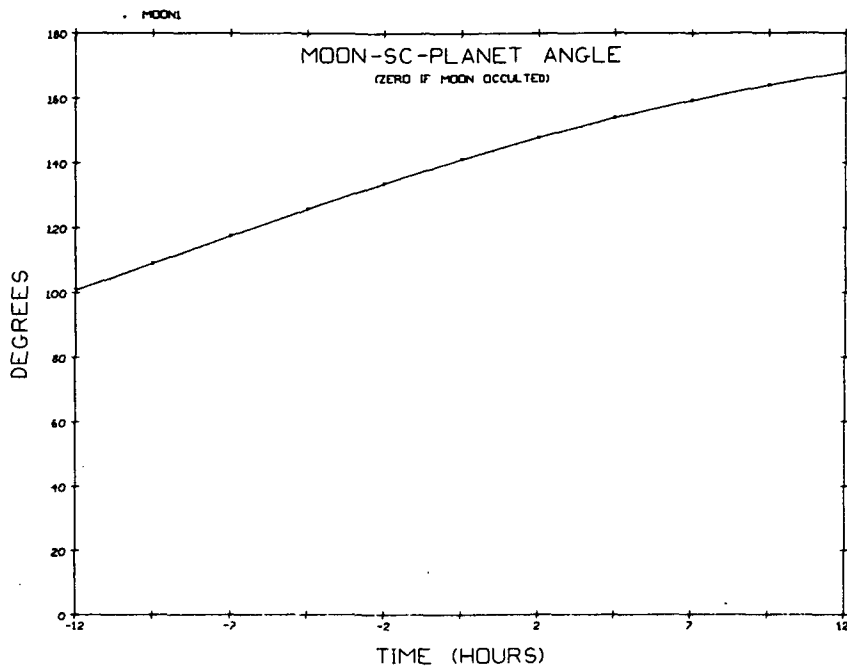


Fig. G-6-6 Moon-Spacecraft-Planet Angle During Saturn Passage on the Pluto Grand Tour

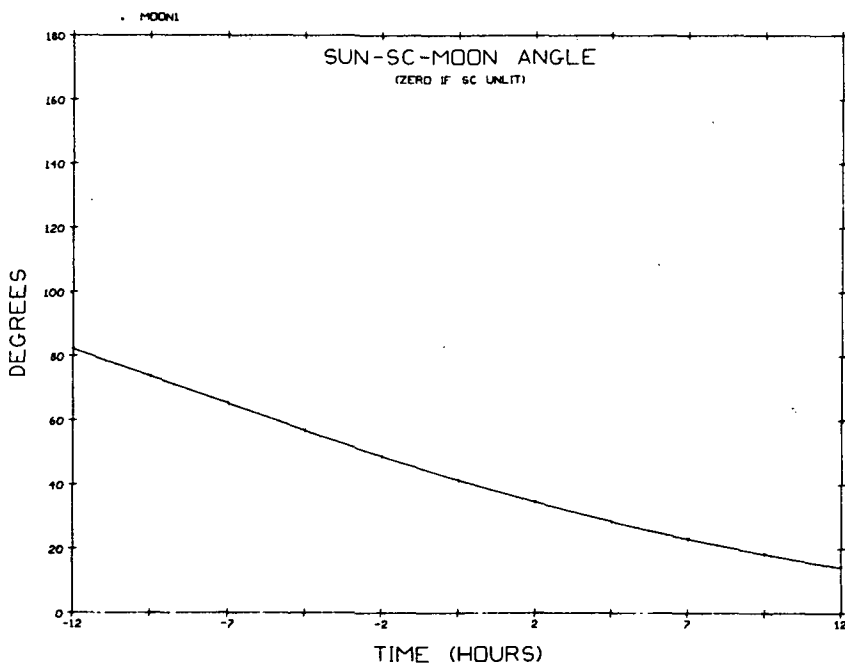


Fig. G-6-7 Sun-Spacecraft-Moon Angle During Saturn Passage on the Pluto Grand Tour

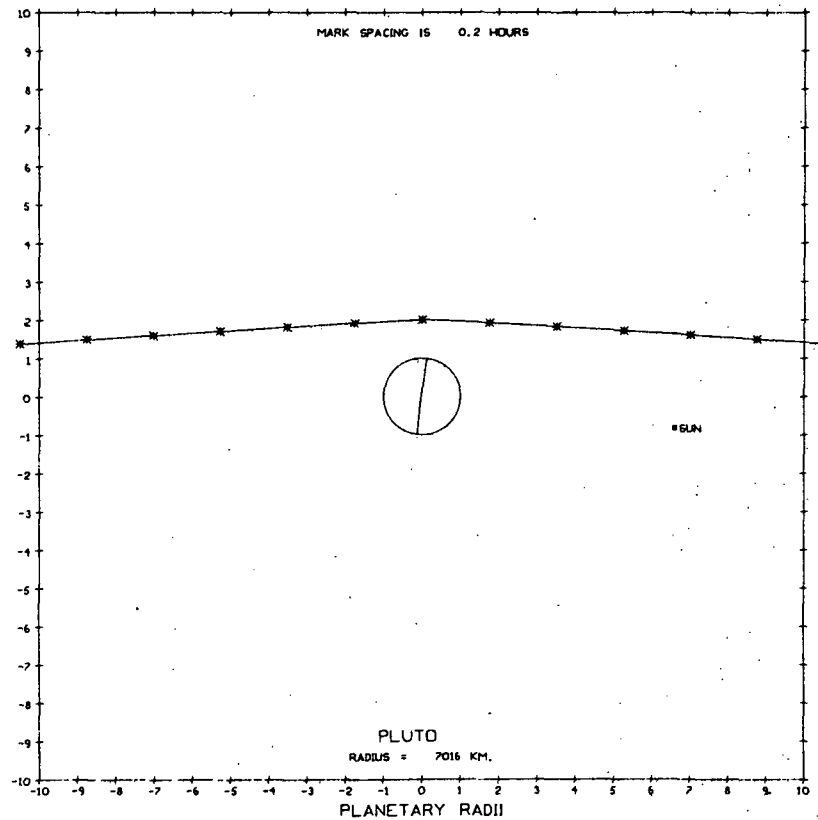


Fig. G-7-1 Trajectory Plan View During Pluto Passage on Pluto Grand Tour

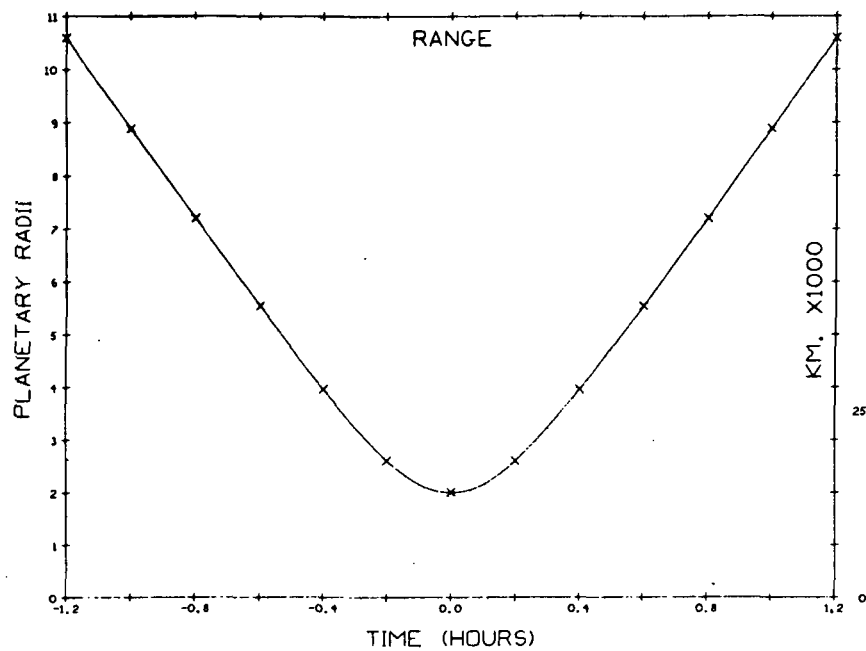


Fig. G-7-2 Range to Planet During Pluto Passage on Pluto Grand Tour

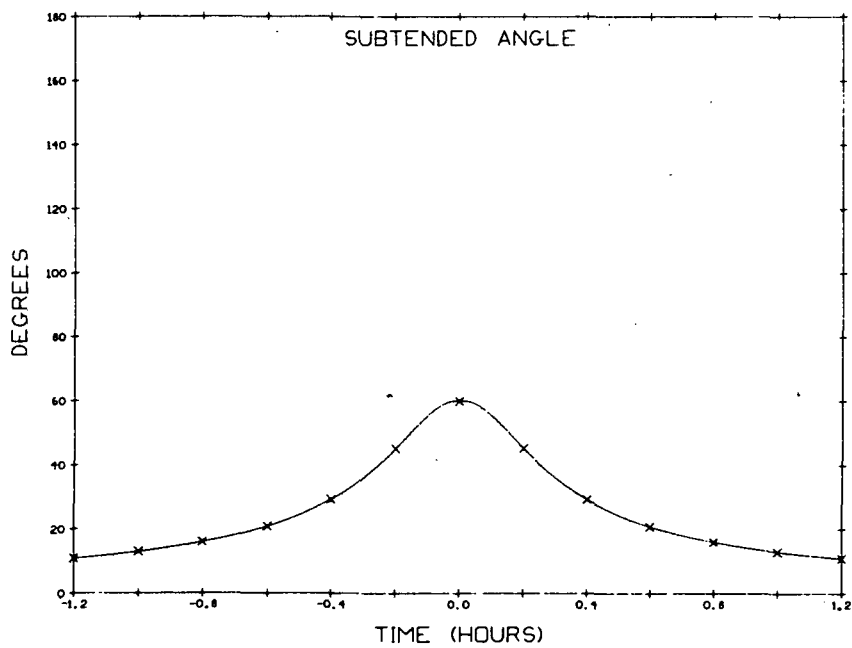


Fig. G-7-3 Angle Subtended by Planetary Limbs During Pluto Passage on Pluto Grand Tour

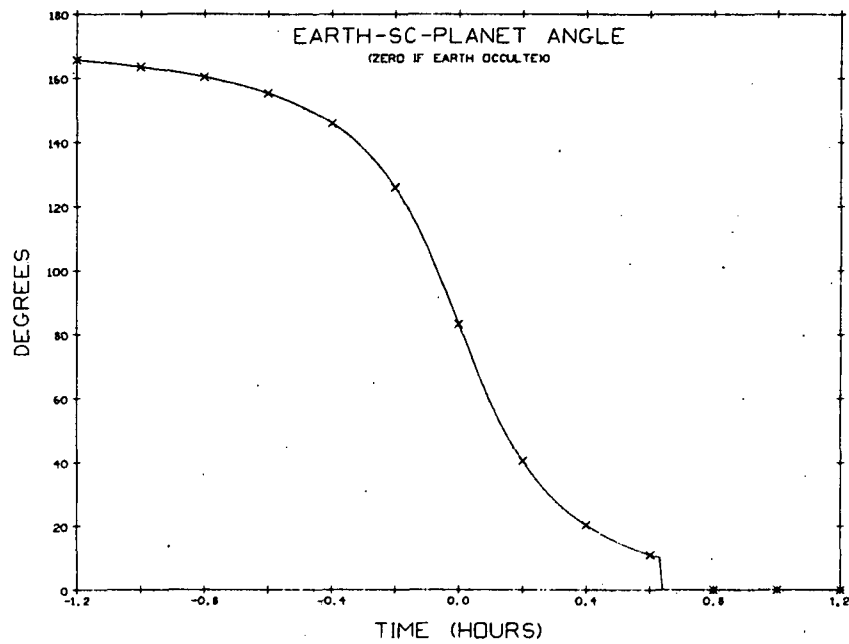


Fig. G-7-4 Earth-Spacecraft-Planet Angle During Pluto Passage on Pluto Grand Tour

APPENDIX H

ONBOARD SENSOR CONSIDERATIONS

In previous phases of these studies the problem of using a scanning photometer as a navigation instrument has been examined. The high thrust mission studies (Vol. II) showed that such a device would encounter adequate signal levels, and would produce a useful level of sighting accuracy when scanning the outer planet limbs. Maximum expected weight, volume, and power consumption estimates were made which included an onboard computer capable of processing sensor data. In the second phase of these studies, concerned with low-thrust missions, a scanning photometer was again analyzed as a navigation sensor in an environment characterized by less favorable spacecraft altitude conditions. The device was found to be less useful for navigation error reduction on these missions because they did not extend beyond Saturn where onboard navigation begins to save fuel. Again weight, volume and power consumption requirements were estimated, this time using smaller, more realistic estimates, and not including onboard computer weight as part of the sensor weight.

The present studies are concerned with missions that provide requirements for onboard navigation which are different than those considered previously. For example, the Jupiter entry missions emphasize the role of the onboard sensor as a limb finding device so that accurate entry angle guidance can be achieved. The comet missions present weak signaled and potentially ill defined navigation objects. Finally, it has been proposed⁴ that the satellites of the outer planets be used as the primary onboard sighting phenomena for outer planet missions instead of planet limb sightings. Sensor problems associated with this technique are examined.

This Appendix examines the potential problems associated with onboard navigation sensors when applied to Jupiter entry and comet missions, and problems related to satellite sensing. Both imaging and

moving field-of-view (scanning) devices are considered. Signal levels expected for each situation are presented followed by discussions of signal to noise ratio and related problems for each type of device.

H.1 SIGNAL LEVELS

Outer planet radiance values were estimated during the earlier grand tour studies and have been listed in Vol. II. Estimates were made for the radiant signal impinging on a detector while a telescopic field of view scanned the given planet. This was done for silicon diode and thermister bolometer detectors. For the present studies it is also required to have estimates of signals received from planetary satellites and short period comets. The cometary nuclei and the planetary satellites are assumed to be viewed from sufficient range to image the entire object on the detector.

H.1.1 Planetary Satellite Magnitudes

The primary mode of usage of the planetary satellites for navigation as proposed in Ref. 4 is to view them against the star background with an image tube. It is useful therefore to know the magnitudes of the satellites as observed from the spacecraft on a particular mission. Using spacecraft trajectory data and satellite ephemerides for the Jupiter Entry and Grand Tour missions the appropriate geometry was computed. Initial magnitudes have been taken from the tabulation in Ref. 13. The phase angle dependence for all satellites was taken to be

$$\left(\frac{2}{1 + \cos \theta} \right)^2$$

which is not perfectly accurate for all satellites but sufficient for magnitude to magnitude comparisons between stars and satellites. The visual magnitude formula used is therefore

$$m = m_0 + 2.5 \log(4R/(1+\cos\theta)^2 R_0)$$

where $R_0 = 1$ if R is expressed in astronomical units. Figures H-1 to 7

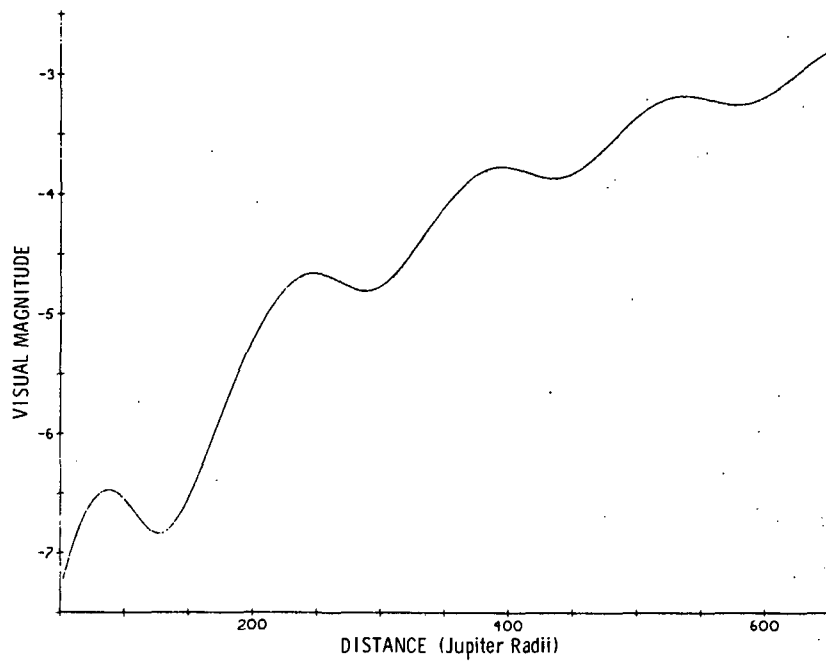


Fig. H-1 Ganymede Magnitude on Jupiter 800 Day Approach

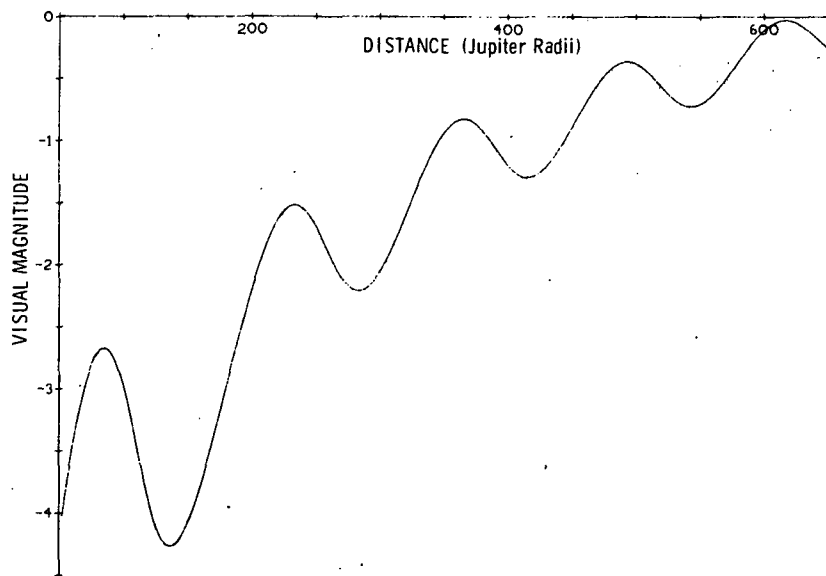


Fig. H-2 Ganymede Magnitude on Jupiter 1200 Day Approach

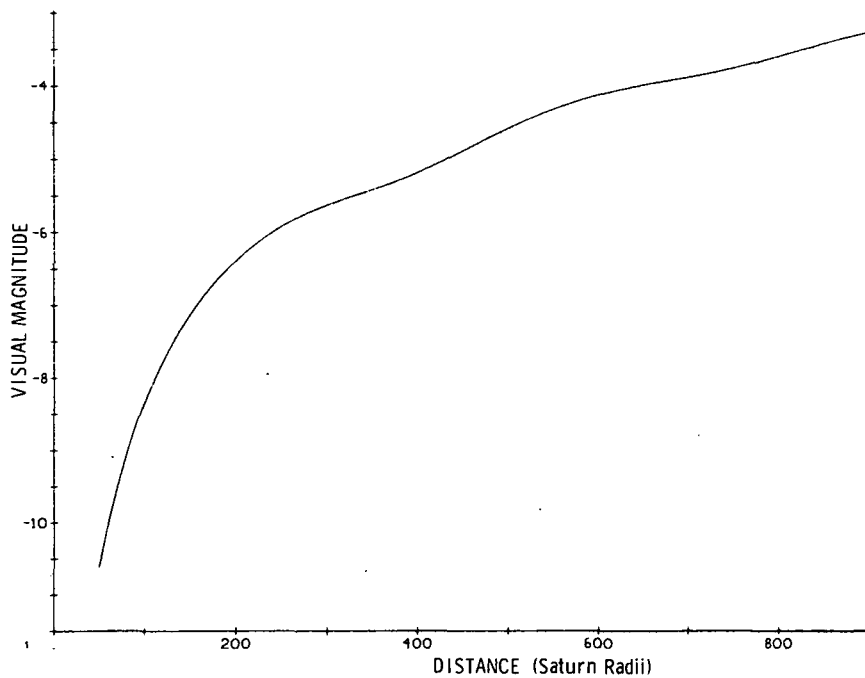


Fig. H-3 Titan Magnitude on Inbound Saturn Passage, Pluto Swingby Mission

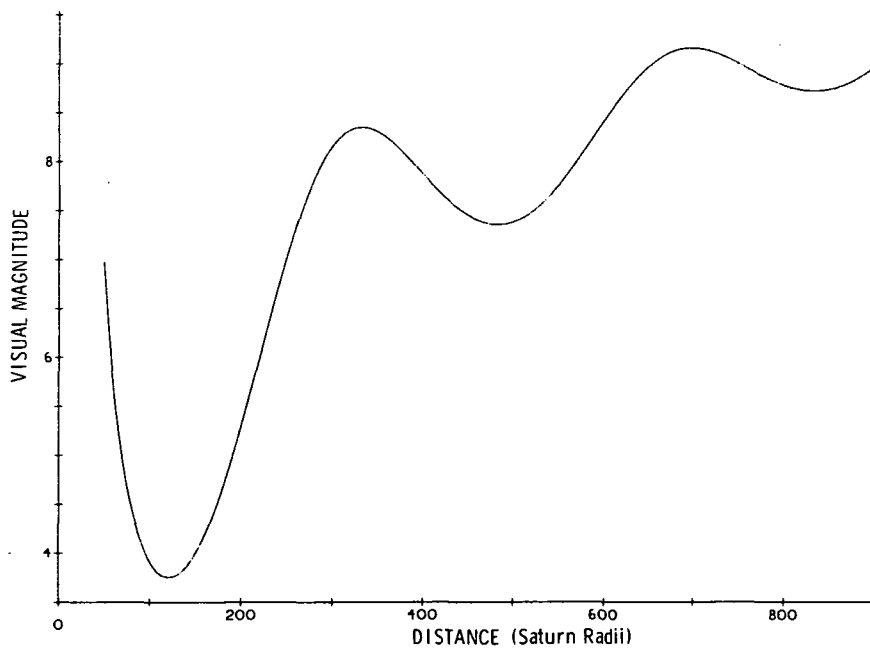


Fig. H-4 Titan Magnitude on Outbound Saturn Passage, Pluto Mission

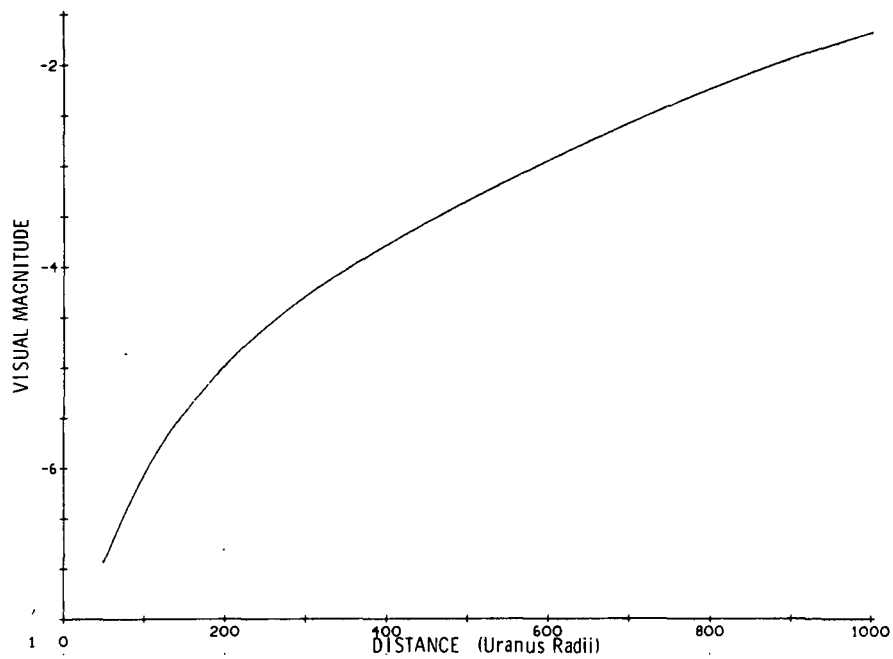


Fig. H-5 Oberon Magnitude on Inbound Uranus Passage, Neptune Mission

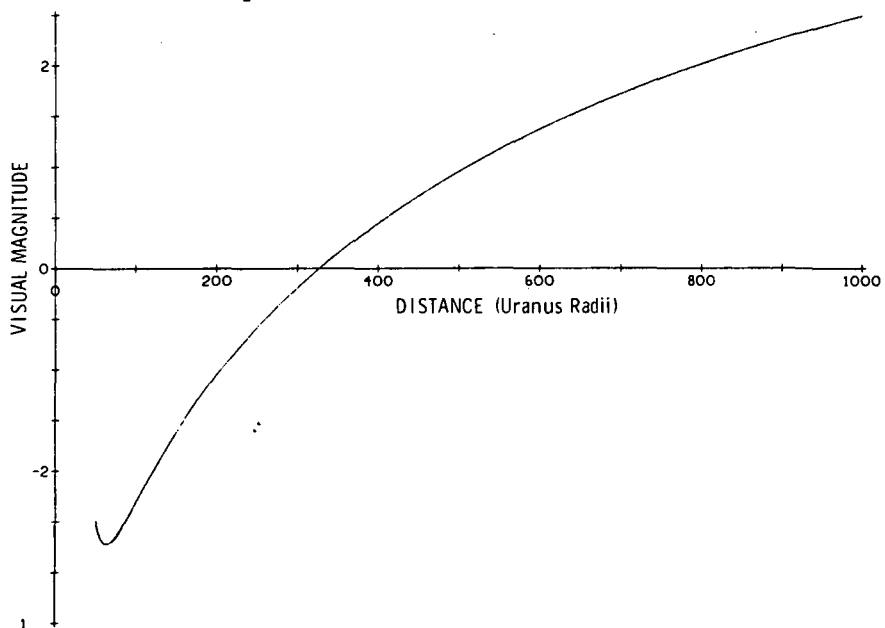


Fig. H-6 Oberon Magnitude on Outbound Uranus Passage, Neptune Mission

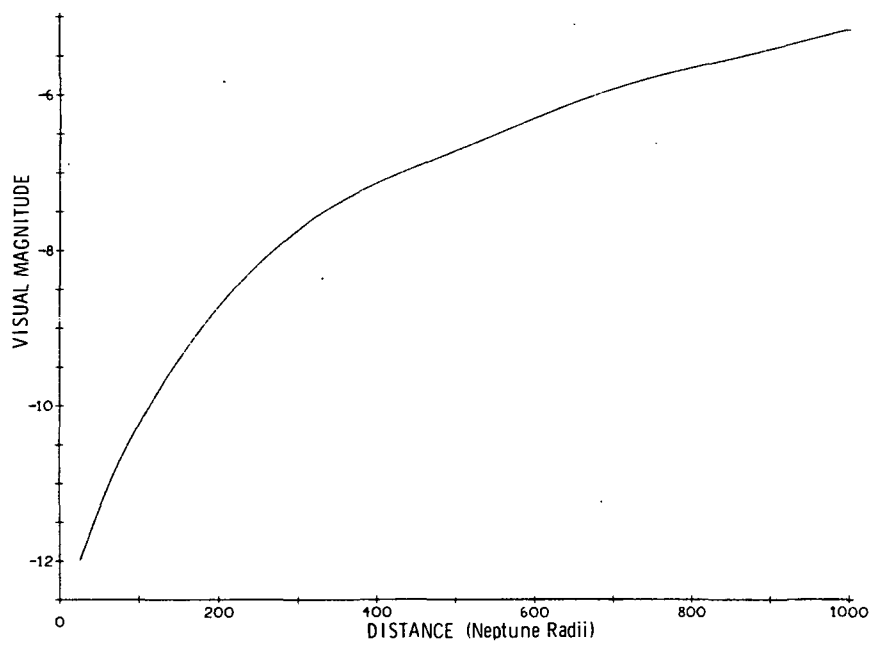


Fig. H-7 Triton Magnitude on Neptune Approach

are the magnitudes of selected satellites versus range to the parent planet. The brighter satellites of Jupiter have been chosen as likely navigation objects. This group includes numbers I, II, III and IV. Satellite V is too close to Jupiter while numbers VIII, IX, X, XI and XII are marginally detectable with reasonable signal integration times. Satellites VI and VII are sufficiently bright and well placed but have less well determined ephemerides. One satellite each has been plotted for Jupiter, Saturn, Uranus and Neptune.

In Figures H-1 and H-2 the magnitude of Jupiter's Ganymede is plotted for the 800 and 1200 day entry missions. The figures show that the brightnesses are more than adequate for these missions. The satellite is about three magnitudes dimmer on the 1200 day mission approach because of the larger phase angle. Titan yields (Figure H-3) a strong signal on the inbound part of the Saturn passage, but on the outbound trajectory (Figure H-4) the satellite is rather dim, never looking brighter than about 4th magnitude. If 6th magnitude were chosen as an acceptable signal level, then only a small portion of the outbound flight could use Titan for TV navigation. Oberon, in Figures H-5 and H-6 is adequately bright although considerably dimmer on the outbound flight. Oberon magnitude does not oscillate because of the near perpendicularity of its orbit to the ecliptic. Finally, Triton of Neptune yields more than enough signal as Figure H-7 shows.

H.1.2 Comet Brightness Levels

Since these missions require knowledge of comet brightness as seen from both Earth and the spacecraft, an effort was made to determine a magnitude formula including comet-sundistance and comet-Earth or comet-spacecraft distance based on recent sighting data. There are a number of aspects of the comet brightness problem that make an exact magnitude calculation impossible. Sightings are made at varying phase angles, and the exact phase-magnitude relationship for a given comet is not known. The sighting conditions vary from sighting to sighting with changing sun placement, background noise levels, and atmospheric transmission. Solar

activity can alter comet brightness. It is difficult to separate nuclear brightness from coma and tail or overall magnitude, and finally the comets change from one perihelion passage to the next so that, even if the magnitude were known exactly at one sighting, it would not necessarily be accurately predictable on the next passage.

The latest sighting information given in the Quarterly Journal of the Royal Astronomical Association^{14,15} was used to establish a distance-magnitude relationship for the two comets chosen for this study. At the chosen rendezvous times which are both roughly two months before perihelion passage, both comets have a sharply defined nucleus.

For Tuttle-Giacobini-Kresak the magnitude reference point was chosen from the Q.J.R.A.A.¹⁴ sighting data showing a stellar appearing condensation of 18th magnitude on Feb. 3, 1962. At this date, which was about 2.5 months before aphelion, the distance to the comet from the sun was $R = 1.6$ A.U. while the comet-Earth distance was $\Delta = 0.6$ A.U. Applying the inverse square brightness relationships and adding E. Roemer's phase angle correction factor gives the T-G-K magnitude as

$$m = 18 + 2.17 \ln (\Delta/0.6) + 2.17 \ln (R/1.6) + 0.03\phi.$$

Here ϕ is the sun-comet-observer angle in degrees. By applying this formula to the geometry of 1989, the magnitude of the comet as seen from Earth around the time of rendezvous can be computed. Figure H-8 shows the nuclear magnitude and the R and Δ to be encountered on the projected mission. Near rendezvous, this comet is only a 21st magnitude object which means it will be difficult to find from Earth observation. At about four months before rendezvous the sun-Earth-comet angle becomes less than 45° as shown on the figure. With sun angles less than 45° seeing conditions are greatly deteriorated, so that four months before rendezvous becomes roughly the earliest this comet could possibly be seen from Earth.

A similar exercise was carried out for the comet Tempel 2. This comet was observed in 1967, and a summary of the observations is listed in the Quarterly Journal of the Royal Astronomical Association¹⁵. Like

Tuttle-Giacobini-Kresak, this comet has a sharply defined nucleus at the projected rendezvous time. The reference magnitude is taken as 19th from the Feb. 12.8, 1967 observation, and with phase angle correction the magnitude formula becomes

$$m = 18 + 2.17 \ln (\Delta/1.19) + 2.17 \ln (R/1.87) + 0.03\phi.$$

Figure H-9 shows the R , Δ , and m related to Earth for the projected 1993 mission to Tempel 2. Tempel 2 is about 2 magnitudes brighter as seen from Earth near rendezvous, but the sighting conditions are poor due to a small sun angle. Earth based observations may be limited to 3 months or more before rendezvous.

If the comet angular subtense is such that all of the image is deposited on the onboard navigation detector, then a useful signal quantity is the irradiance at the telescope aperture. This can be calculated from the inverse square brightness relationship:

$$P = A \cdot \frac{F}{R^2} \cdot \frac{U}{D^2} \cdot \phi$$

where

- A = albedo of the comet nucleus
- F = solar irradiance at Earth
- R = distance of comet from sun in A.U.
- U = comet radius
- D = distance to comet from spacecraft
- ϕ = phase angle factor.

Using a comet albedo of 0.7 (see Chapter 2) and radii of 0.1 and 0.6 km for Tuttle-Giacobini-Kresak and Tempel 2, and a phase angle factor of 1/4 gives the curves shown in Figure H-10. The solar input was assumed to be roughly equivalent to the silicon responsive bandwidth from 0.4 to 1 micron. Over this range the solar input F is about 0.09 watts/cm². If the comets were at the same distance from the sun, the curves would be separated

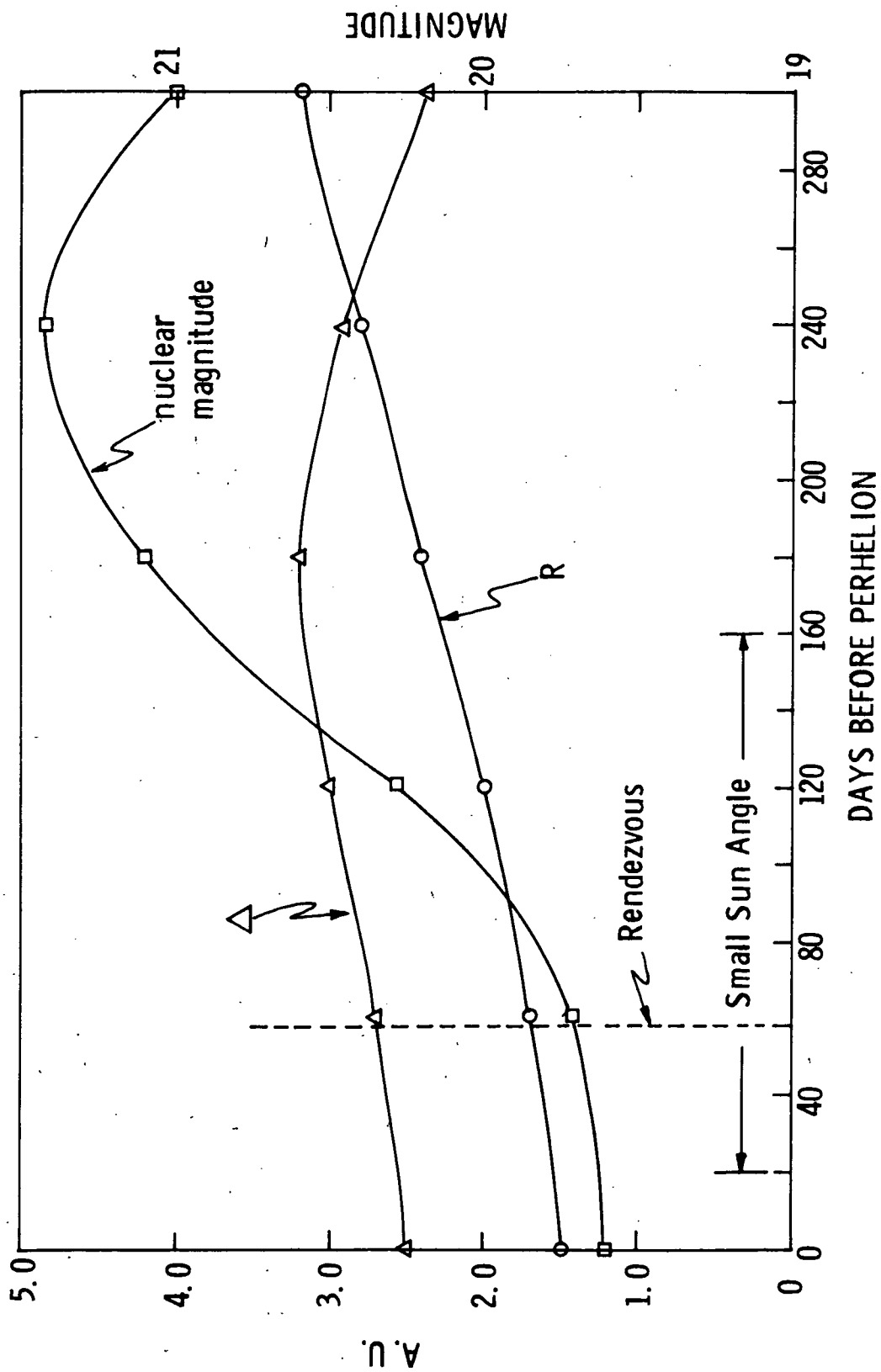


Figure H-8. Magnitude of P/Tuttle-Giacobini-Kresak as Seen From Earth on 1989 Mission.

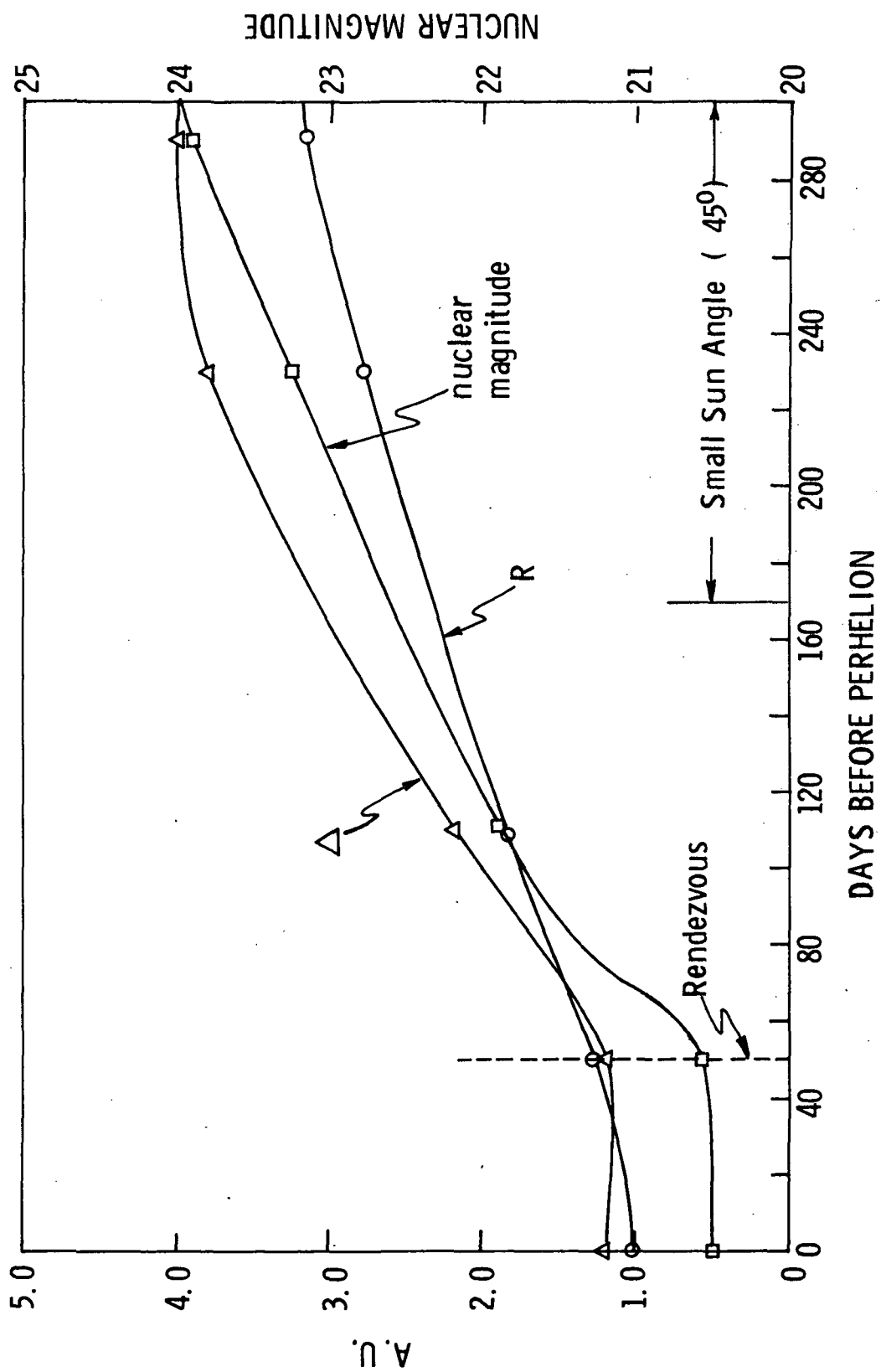


Figure H-9. Magnitude of P/Tempel 2 as Seen From Earth on 1993 Mission.

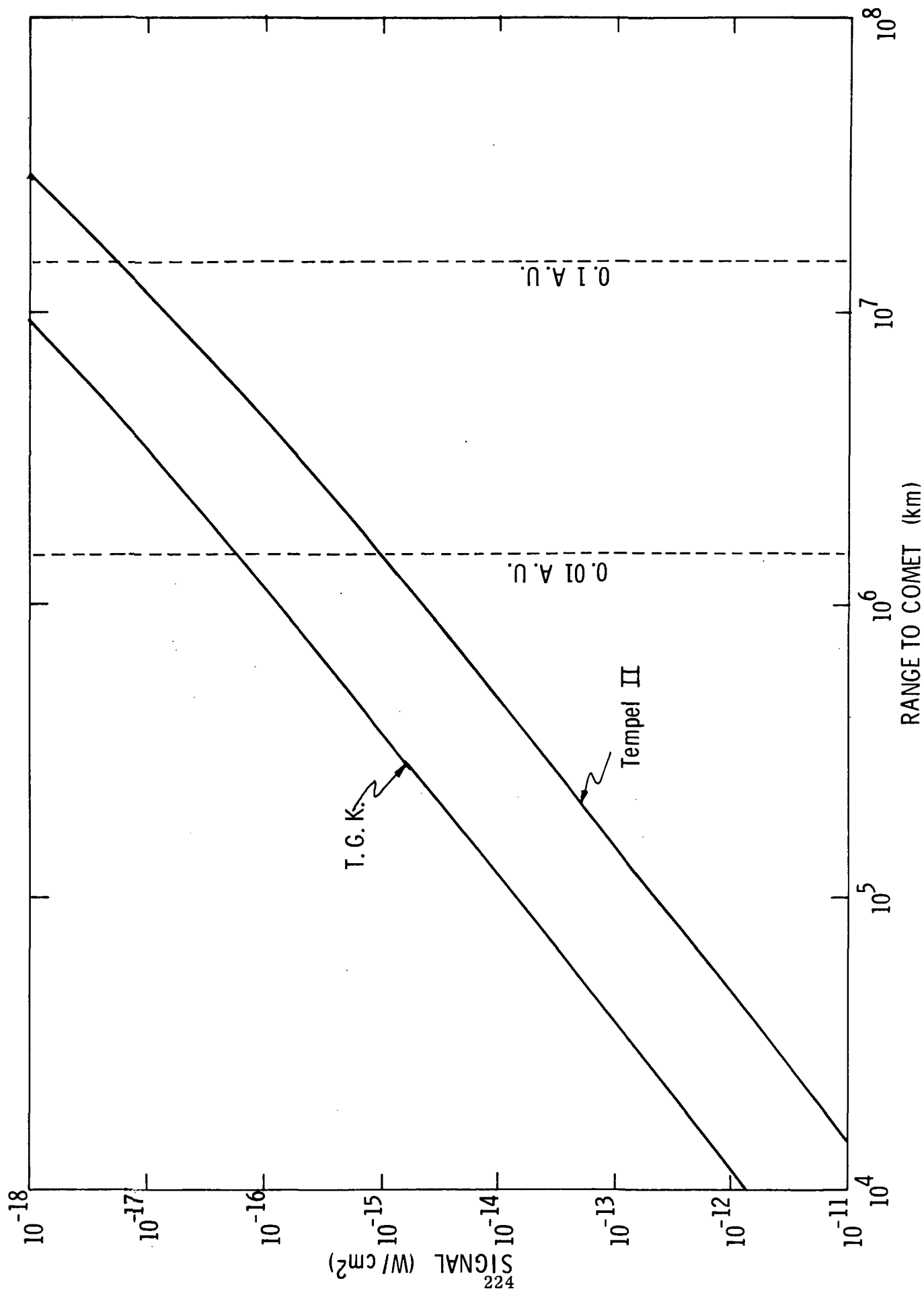


Fig. H-10 Nucleus Power Density vs. Range To Comet

by a factor of 36 or just the ratio of the nuclear areas. However, Tuttle-Giacobini-Kresak is at 1.2 A.U. from the sun at rendezvous whereas Tempel 2 is at about 1.6 A.U. Thus the relative irradiances are different by only a factor of 20.

It is sometimes useful to express these signal levels in terms of visual magnitudes. Using the relationship of Ramsey¹⁶ we have that 5×10^{-12} watts/cm² = -3 visual magnitude. From this the curves of Figure H-11 can be constructed. These curves are useful for comparing the comet signal with the star background.

Although the coma of these comets is expected to be much dimmer (per unit solid angle) than the nucleus, it is important to estimate the coma brightness to see how this signal tends to mask stars that are in the field of view of a TV sensor.

The total magnitude of Tempel 2 on July 4, 1967 (20 days before perihelion) was measured as 11.8 magnitudes, whereas the nuclear magnitude was 14.5. Converting to photometric brightness units one has

$$\frac{B_N}{B_N + B_C} = 2.5^{(11.5 - 14.5)}$$

where B_N is the nuclear brightness and B_C is the brightness of the coma. Solving for the relationship between B_N and B_C gives

$$B_C = 10.5 B_N$$

i.e., the total coma brightness is 10.5 times the nucleus brightness. To see how sharply defined the nucleus would be under these circumstances, one compares adjacent areas of the apparition having equal solid angle substance. Following the suggestion by Wells¹⁷, we assume that brightness falls off as $1/r$ in the coma nucleus. Then total brightness of the coma is

$$B_C = \int_{R_N}^{R_C} B(r) dA$$

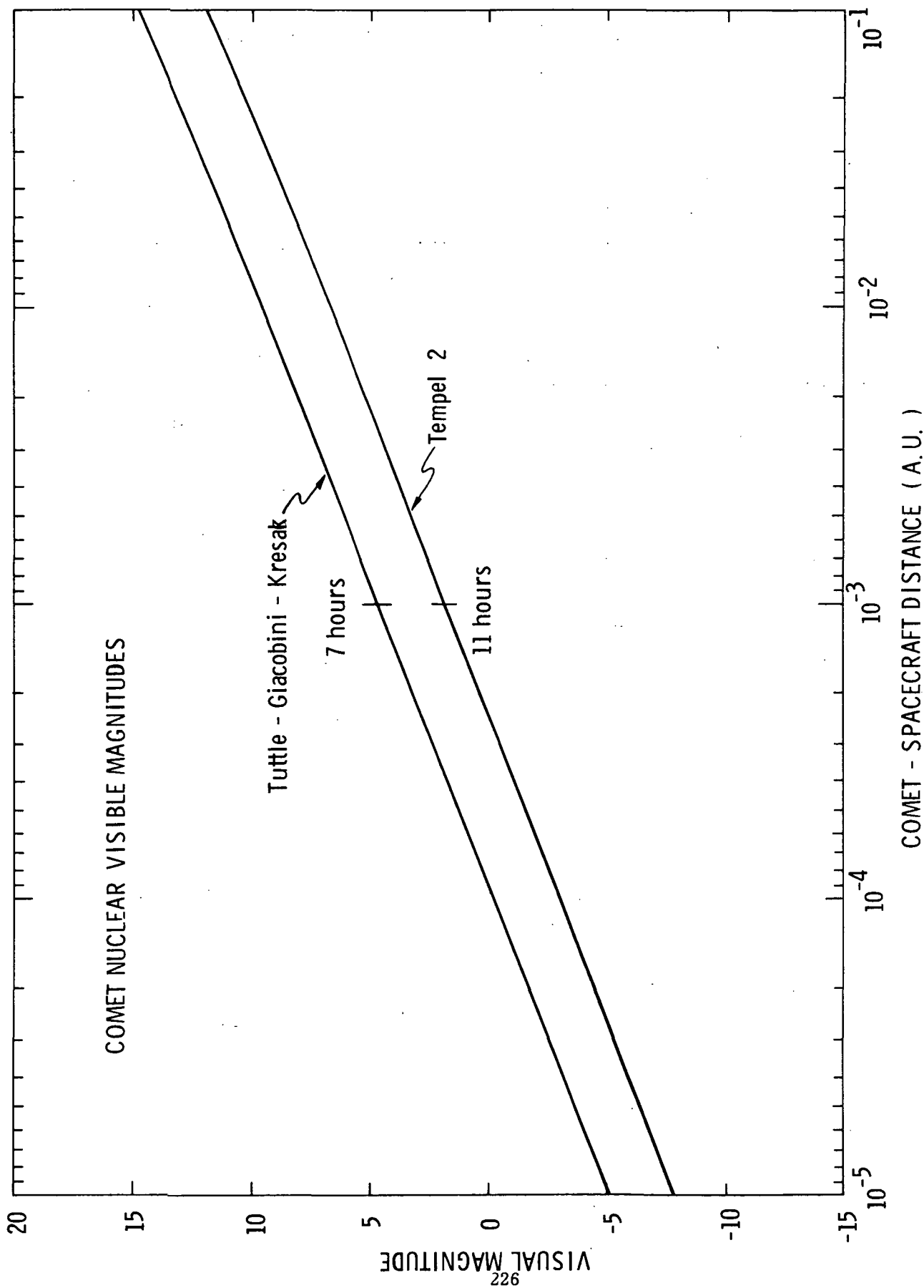


Figure H-11. Comet Visual Magnitudes From Space Craft.

where A is coma area (or solid angular substance). Let B(r) be given by C/r while dA = 2 π rdr then

$$B_c = C \int_{R_N}^{R_c} \frac{2\pi r dr}{r} = 2\pi C \int_{R_N}^{R_c} dr,$$

where R_N and R_c are the nuclear and coma radii. Therefore $C = B_c/2 (R_c - R_N)$. A ring of coma extending from radius R_N to R then has brightness

$$B = \frac{B_c \cdot 2\pi}{(R_c - R_N)} (R - R_N).$$

For a ring of thickness ΔR the brightness is

$$\Delta B = 2\pi \frac{B_c \Delta R}{(R_c - R_N)},$$

and for a fraction of the ring, $\Delta R/2\pi R$,

$$\Delta B' = \frac{B_c (\Delta R)^2}{(R_c - R_N) R} \quad (\text{Eq. H-1})$$

This is the brightness of an area $(\Delta R)^2$ of the coma. The area adjacent to the nucleus at a distance $R \approx \Delta R$ away has brightness

$$\Delta B' = \frac{B_c \Delta R}{(R_c - R_N)}.$$

If we take ΔR to the nuclear radius (R_N), and assume $R_N \ll R_c$ we have simply $\Delta B' = B_c \Delta R/R_c$. If $\Delta R = 0.6$ km as for Tempel 2 and $R_c = 1500$ km (estimate based on Q.J.R.A.A.¹⁵ 1967 data) then

$$\Delta B' = B_r \frac{0.6}{1500} \approx \frac{10 B_N 0.6}{1500} \approx \frac{B_N}{250}.$$

Thus the area adjacent to the nucleus that fills the same solid angle is 250 times dimmer than the nucleus or about 6 magnitudes dimmer.

H.2 PROBLEMS WITH IMAGE TUBES AND SATELLITE SIGHTINGS

The sighting procedure proposed by Duxbury⁴ (1969) would image a planetary satellite against a stellar background, and using the known directions to store within a recognizable pattern would determine the direction to the satellite. A sequence of such sightings would produce a relatively accurate estimate of the direction to the parent planet mass centroid. However, this technique has certain attendant problems as does any other technique. To sight satellites against a star background it is necessary to balance image tube sensitivity, noise level and dynamic range against the signal range of the stars and satellites. The effects of scattered light from the sun and parent planets have to be considered. Finally star distribution factors must be accounted for.

H.2.1 Limiting Stellar Magnitudes

The system proposed by Duxbury would use a star background admitting stars up to 6th or 7th magnitude. Stars at this level would appear to cause no signal problems by themselves given that an image integrating sensor were used with sufficient integration time. For example, Burt and Jolliffe¹⁸ tested various image orthicons and found that a magnesium-oxide target would allow the detection, with a signal-to-noise ratio of three, of 9th magnitude stars. This was done experimentally with a 2.5 second integration time, and a 25 cm² aperture. 9th magnitude is a useful limit for this type of sighting because it is the star catalog limit as well as a sensor limit. Burt and Jolliffe also tested a vidicon having a higher dark current than the image orthicon, and found a limiting magnitude of about 3 which is clearly inadequate for the proposed navigation sighting. The authors estimated that by making several engineering improvements stars of 13th magnitude could be sensed with the magnesium-oxide image orthicon. However, special catalogs would have to be established for the stars whose use was anticipated. Furthermore, the star magnitudes become less certain as the signal-to-noise ratio drops thus increasing the recognition problem.

H.2.2 Star Availability

Johnson¹⁹ has derived a formula for the probability of finding at least n stars in a field of view of solid angle A . For two stars the formula is

$$P = 1 - e^{-A \cdot \rho} (1 + A\rho)$$

where ρ is the average stellar density. This formula is based on a Poisson distribution of stars over the celestial sphere which of course is not the case, however it does give an indication of what one might expect on the average. For a field of view of 9 square degrees the formula yields the following:

<u>Magnitude</u>	<u>Density</u>	<u>Probability of ≥ 2 in Field</u>
6	0.122/sq. deg	0.31
7	0.366/sq. deg	0.84
8	1.22/sq. deg	0.99

Thus on the average, if one wants a high probability of finding two stars or more in the field of view it is necessary to sense stars near 8th magnitude. This figure is confirmed by Stanton²⁰ who has parametrically determined the star magnitude requirement for seeing two stars in various fields of view based on an actual spacecraft trajectory and scan region on the celestial sphere. He finds that stars fainter than those cataloged are required when the field of view becomes smaller than one square degree.

H.2.3 Dynamic Range Problems - Image Spreading

Many of the planetary satellites have visual magnitudes near -1 at the anticipated pickup range. If a satellite of this brightness is imaged against a star background with 9th magnitude stars there will be a 10 magnitude brightness range or a signal strength difference of 10^4 . However, the linear dynamic range of the average image orthicon (for example) is less than several magnitudes. Thus if the 9th magnitude stars are just seen after a sufficient integration time, the satellite image will be severely

saturated and subject to strong image spreading. This would lead to degraded accuracy and possibly a center finding problem. Also stars near the spreading satellite image may be blotted out. For these reasons it is important to pick a tube with maximum dynamic range and to try to minimize the satellite-star brightness differences by proper selection of satellites and measurement positions.

H.2.4 Scattered Light Noise Problems

Serious scattered light problems occur with the satellite imaging technique due to light scattered within the optics from the sun and parent planets. Scattered sunlight is not expected to be a problem on the planetary approach legs of the outer planet missions, however if navigation sightings are to be made after passage, the sun could present a severe problem. It would take extremely good scattered light baffling to prevent the sun from blotting out faint stars.

Another potential scattered light source is the present parent planet which would have roughly the same surface intensity as the satellite, but because of its large substance would potentially contribute a large scattered light signal. For example, Jupiter is about 1000 times brighter than Io. If Jupiter were just outside of the image tube field of view the resulting scattered light signal would be several orders of magnitude down from the Jupiter signal, but 9th magnitude stars would also be dimmer by a factor of 0.5×10^{-6} , thus the Jupiter signal has at least the potential of swamping the weaker star signals. Of course if the planet's image was inside the field of view there would be image spreading problems in addition to the scattered light background problems. Figures H-12, 13, 14, 15, and 16 show typical angular separations between satellite and planet for the considered missions. In the figures, the separation in degrees is plotted against the time in days from the sphere of influence. The endpoints of the curves correspond to spacecraft distances from the planet from 900 to 50 planetary radii. In each figure the dashed line indicates the portion of the flight time that would exclude navigation sightings if a minimum separation criteria of 1.5° were imposed. The curves do not go to zero

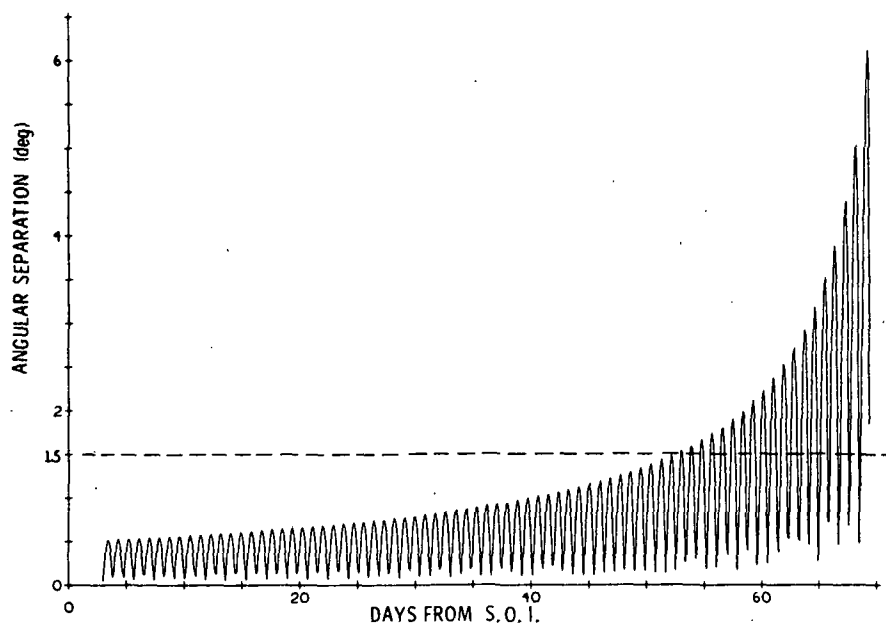


Fig. H-12 Jupiter 800 Day Entry Mission, Angular Separation of I_o

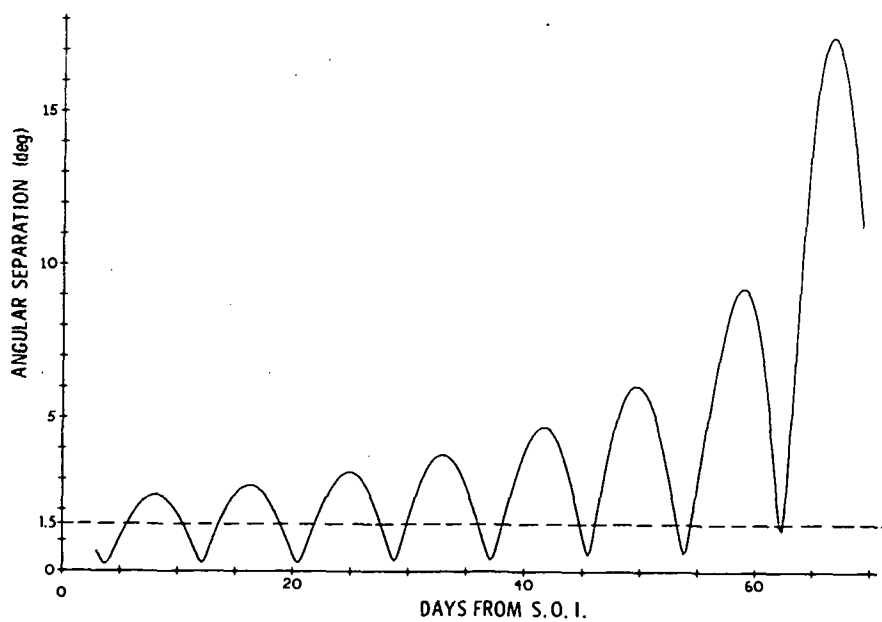


Fig. H-13 Angular Separation of Callisto from Jupiter, Jupiter 800 Day Entry Mission

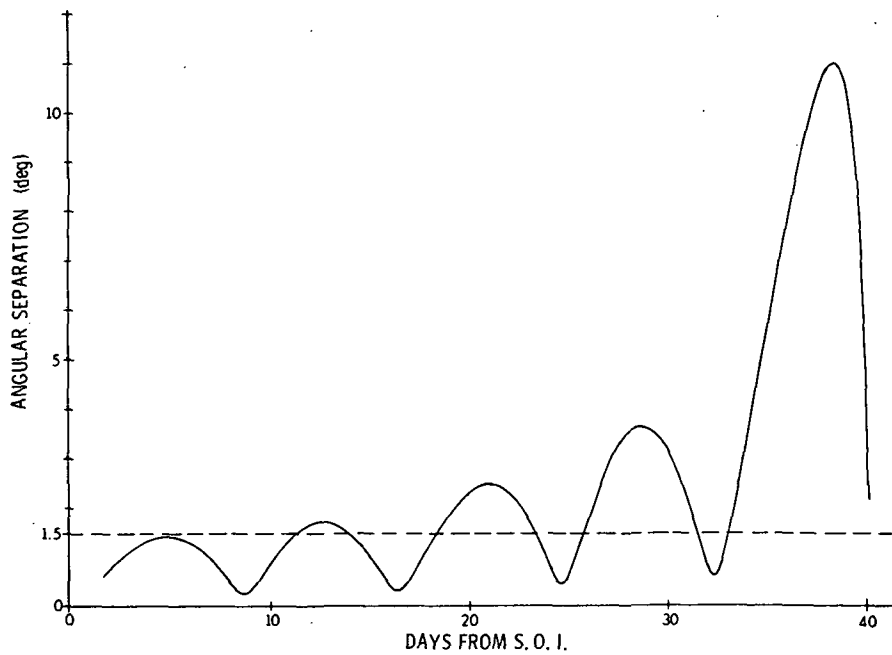


Fig. H-14 Angular Separation of Titan from Saturn,
Jupiter-Saturn-Pluto Swingby Mission

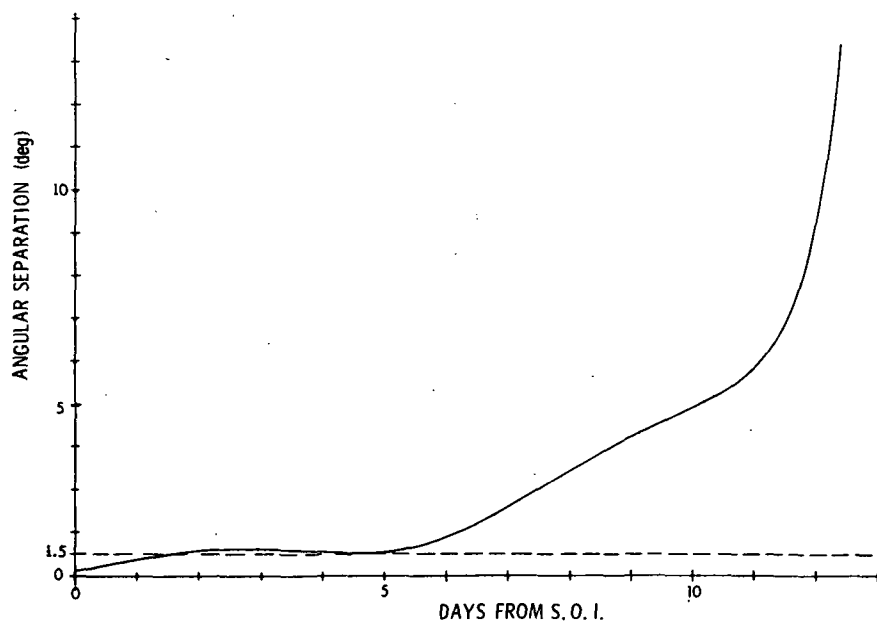


Fig. H-15 Angular Separation of Oberon from Uranus,
Jupiter-Uranus-Neptune Swingby Mission

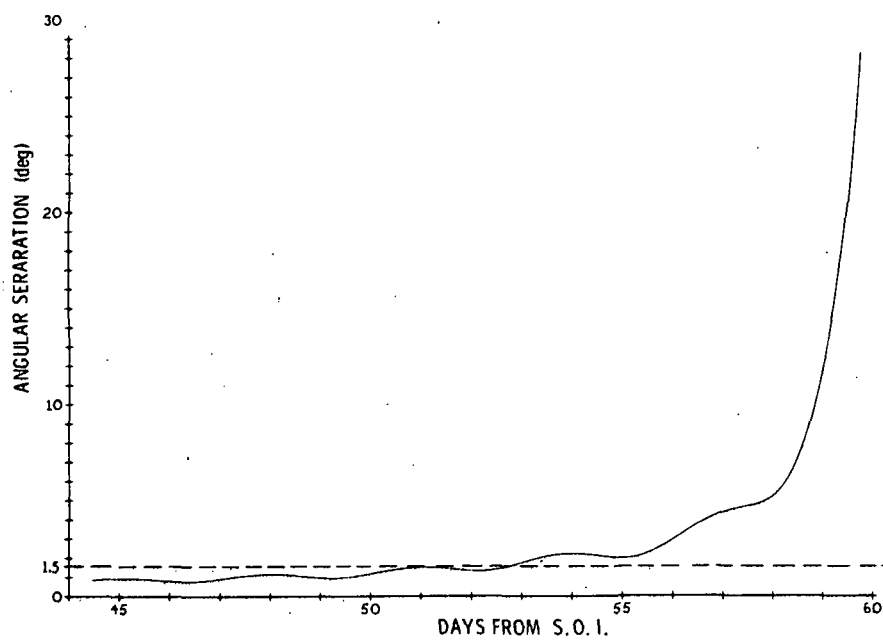


Fig. H-16 Triton-Neptune Angular Separation

because of the finite time step size used in the computer calculations. Figure H-12 shows the separation for Io. With a 1.5° separation requirement this satellite would be usable for about a 15 day interval, however only about half the time within this interval has an associated adequate separation angle. Measurement times would have to be carefully selected with an accuracy of a few hours. Figure H-13 shows the separation on the same mission for the satellite Callisto which is seen to be usable over most of the time from the sphere of influence inward. Similar results are shown in Figures H-14, 15, and 16 for flights passing Saturn, Uranus and Neptune.

Since the satellites are as much as a dozen orders-of-magnitude brighter than stars of 8th magnitude, it may also be necessary to examine the diffraction image in relation to the star brightness.

H.2.5 Image Tube Choices for Satellite Navigation

The image orthicon using a magnesium-oxide target can, as discussed above, detect sufficiently dim stars given a few seconds of integration time. However, the linear dynamic range of this type of tube is typically from two to three orders of magnitude which would be exceeded by an order of magnitude on some of the brighter satellites. Under these conditions there would be severe satellite image blooming, strong scattered light imaging, and possible tube damage. One possible solution to this problem would be to deposit on an area of the tube target, a region of lowered sensitivity on which to image the brighter satellite. For example, if the spacecraft altitude control system and scan platform combination were capable of pointing the sensor to a satellite with an accuracy of say a few arcminutes, then an area of a few arcminutes on a side might have lowered sensitivity to increase the effective dynamic range. A scan beam cue would probably be required to indicate when the less sensitive region was being interrogated.

Silicon diode array vidicons have recently been developed which might offer some advantages over the uniform oxide coating type tube. The use of silicon oxide diodes deposited on a resistive matrix leads to a more rugged tube with a larger linear dynamic range. However, these tubes have been designed for television cameras and not for image storage.

Currently, dark-current levels are of the order of 10 nanoamps which is too high, but this level could be dropped by lowering the operation temperature and by leaving the scan beam filaments turned off during integration. Preamp bandwidth can also be reduced from current 10 MHz values for TV to perhaps 1 KHz which would drop the noise by a factor of 100. Diode leakage rates for the TV tubes are of the order of 10^{-14} amps, and these could be lowered by increasing the matrix resistance.

Self scanned diode arrays are under development, and such devices would combine the advantages of beam-scanned arrays with a virtual elimination of electronic shape distortion. Current developmental versions of the self scanned array have dimensions of 256 x 256 elements,²¹ and arrays of 500 x 500 are considered feasible. An order of magnitude increase in array size would make the self scanned array competitive in resolution with existing tubes.

H.3 COMET NAVIGATION SENSORS

Two instruments are considered as sensor candidates for the onboard navigation function, namely a scanning photometer and a storage-type image tube. The image tube appears to exhibit more appropriate characteristics for these missions, but both devices are operating under severe conditions.

H.3.1 Scanning Photometer Problems

This device would focus the signal passing through a rectangular telescopic aperture on an appropriate detector. A simple and rugged detector might be a silicon diode used in an unbiased photoelectric mode. As the comet was scanned the appropriate signal enhancement would be sensed, and a signal threshold would be used as a locator. Figure H-17 illustrates how P/Tempel 2 with its coma would look to a scanning sensor with a 10 arcsecond by one degree field of view. The curves are based on the coma signal model given in Section H.1.2.

The telescope aperture area is 100 cm^2 . A typical silicon diode detector, with an appropriate low-pass filter applied to the preamplifier, has a noise equivalent power level of about 10^{-13} watts. The signal power

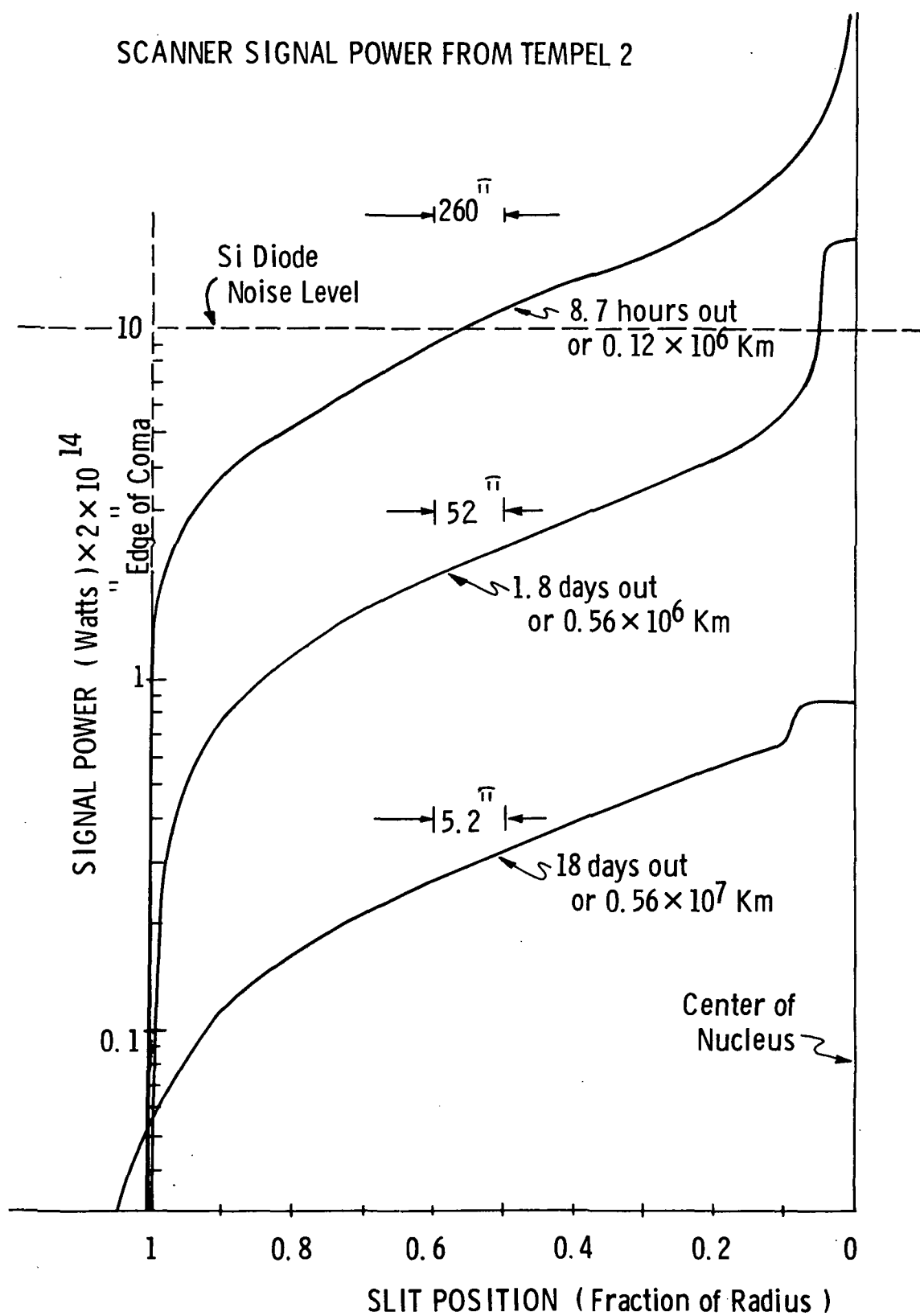


Fig. H-17 Tempel II Scan Signal

curves show that on P/Tempel 2 the signal-to-noise ratio of this device when scanning the nucleus would be near unity at 1.8 days before rendezvous. To achieve a larger signal-to-noise ratio the scanning would have to take place closer in, say for example at 8.7 hours from rendezvous. On the P/Tuttle-Giacobini-Kresak mission, scanning would begin even later because the signal level is down by a factor of twenty. A serious problem of comet recognition is also presented to the scanning device. P/Tuttle-Giacobini-Kresak, at 8.7 hours out from rendezvous is approximately a 4th magnitude object. Furthermore, the ephemeris uncertainty associated with this comet would make its angular direction uncertain to within approximately 2° . The effective scan area would then be four square degrees. Within this area would also be, on the average, a few dozen stars of magnitude 10 or brighter, and unless these stars were accurately placed with respect to the scan position it would be difficult to determine which signal output was due to the comet and which was due to various combinations of star signals. The recognition problem could be diminished by waiting until the apparent magnitude of the nucleus decreases so that it becomes brighter than the average star background, but on the P/Tuttle-Giacobini-Kresak mission this would not occur until the spacecraft was at or inside the coma.

H.3.2 Image Tube Problems

A storage type image tube can integrate the comet signal along with surrounding star signals within the field of view to find the comet direction relative to the star background. The integration period is limited by spacecraft motion within its attitude control cycle. Attitude rates as low as 1 arcsecond/sec have been proposed for recent unmanned probes (Ref. 5), and at this rate up to 10 seconds might be spent integrating the comet signal. Using an image orthicon with a magnesium-oxide target and an integration time of 10 seconds, Burit and Jolliffe¹⁸ were able to detect 10th magnitude stars. At this level P/Tuttle-Giacobini-Kresak could be detected at 2 days before rendezvous and P/Tempel 2 at about 10 days. Of course, lateral charge spreading on the image tube target would degrade the position accuracy of the brighter stars falling inside the field of view.

However, the comet recognition problem could probably be solved by Earth-based analysis of the image tube picture using correlation techniques.

The image tube approach puts a heavy burden on the radio down link because a complete picture can take up to 5 hours to transmit to Earth²². The last navigation measurement would therefore have to be incorporated several hours before rendezvous.

At closer ranges the coma signal could potentially blot out parts of the star background thus degrading navigation accuracy. At 8.7 hours before rendezvous the comet nucleus would subtend less than 5 arcseconds which could serve as an upper limit on the size of the image tube picture elements. The coma, at 8.7 hours from rendezvous would subtend - on P/Tempel 2 - roughly $1/2^\circ$ or perhaps $1/6$ of the field of view. Using Earth telescope sighting data (Ref.15) concerning the relative brightness of the coma and nucleus, and assuming a $1/R$ coma brightness fall-off, the signal from the coma deposited on the picture element adjacent to the nucleus can be calculated. For P/Tempel 2, at 8.7 hours out this value is 0.025 times the nucleus signal, or about 4 magnitudes. The P/Tempel 2 nucleus is approximately a 2nd magnitude object at this time, so the adjacent coma magnitude would be near 6th magnitude.

APPENDIX I

ON PLANET CENTER FINDING

Sightings on planets or planetary satellites are used to determine the direction to the planetary mass centroid. One of the most useful navigation measurements is of the direction to a planet mass centroid in celestial coordinates. Unfortunately, there is no beacon attached to the surface of the outer planets which lies in the direction to the mass centroid, and some means must be found to infer the direction to the centroid from other measurements. There are a number of ways to approach this problem and they generally fit into three categories, namely a) those measurements that infer direction from Earth-based tracking of space probe relative motion; b) measurements of planetary satellite direction; and c) measurements involving the edge or limb of the planetary apparition which assume equality of the optical and mass centroids. Some of the apparent possibilities are:

- 1) to infer the direction (and distance) to the planet by monitoring space-probe motion using Earth-based radio tracking (DSN);
- 2) scanning the planetary limbs with a scanning photometer and inferring the direction to the center by means of independent range information;
- 3) scanning the planetary limbs with a scanning photometer and bisecting the angle between limbs;
- 4) simultaneously scanning light and dark edges of the apparition with separate sensors, one for the light edge and one for the dark edge, and measuring and bisecting the angle between their optical axes;
- 5) finding the optical centroid from electronic sensor constructed images;
- 6) viewing satellite motion against a star field background;
- 7) viewing star occultations and assuming that the apparent angular star rate is sufficiently accurately known;

- 8) view the satellite motion without stars, and with respect to a solar inertial reference;
- 9) track an artificial satellite.

Approach no. 9 is not a serious possibility presently since there are no artificial satellites circling the outer planets while approach no. 7 is probably overly dependent on the randomness of star positions. Approach no. 8 is excessively sensitive to uncertainties in spacecraft range and velocity, and approach 4 features rather cumbersome instrumentation.

The remaining procedures are worthy of further discussion.

I.1 DSN BY ITSELF COMPARED TO DSN WITH A LIMB SENSOR

An idea of the capacity of the DSN to provide planet center direction information can be gained from Figure I.1. The data is plotted from the Jupiter flyby on the J-U-N mission. The uppermost curve is the out-of-plane uncertainty in the direction to the mass centroid of Jupiter. Here out-of-plane means parallel to the spacecraft $\underline{r} \times \underline{y}$ direction in Jupiter coordinates and roughly perpendicular to the ecliptic plane. As the spacecraft moves closer to Jupiter, the angular uncertainty in the centroid direction increases from about 10 arcseconds at 6 days out to 1.5 arcminutes near perigee. Below the DSN only out-of-plane uncertainty is the center direction uncertainty that results from sensing the planet limb but assuming that there is a ± 100 km unfilterable bias error in the planetary radius. Comparison of these curves shows that some reduction of the direction uncertainty can be achieved by a simple limb sighting assuming a 5 arcsecond instrument. However if the radius bias is filterable (for example using DSN range information), the out-of-plane uncertainty can be driven down to below the expected scanning instrument noise level as the flat dashed line shows. The slightly sloping curve for the DSN only, in plane, center direction uncertainty shows that this uncertainty is made small by the DSN only measurements. However, from about 1 day inward, the onboard sensor, using DSN range information can also help to reduce the in-plane center direction uncertainty since the onboard associated uncertainty becomes smaller than that associated with DSN only.

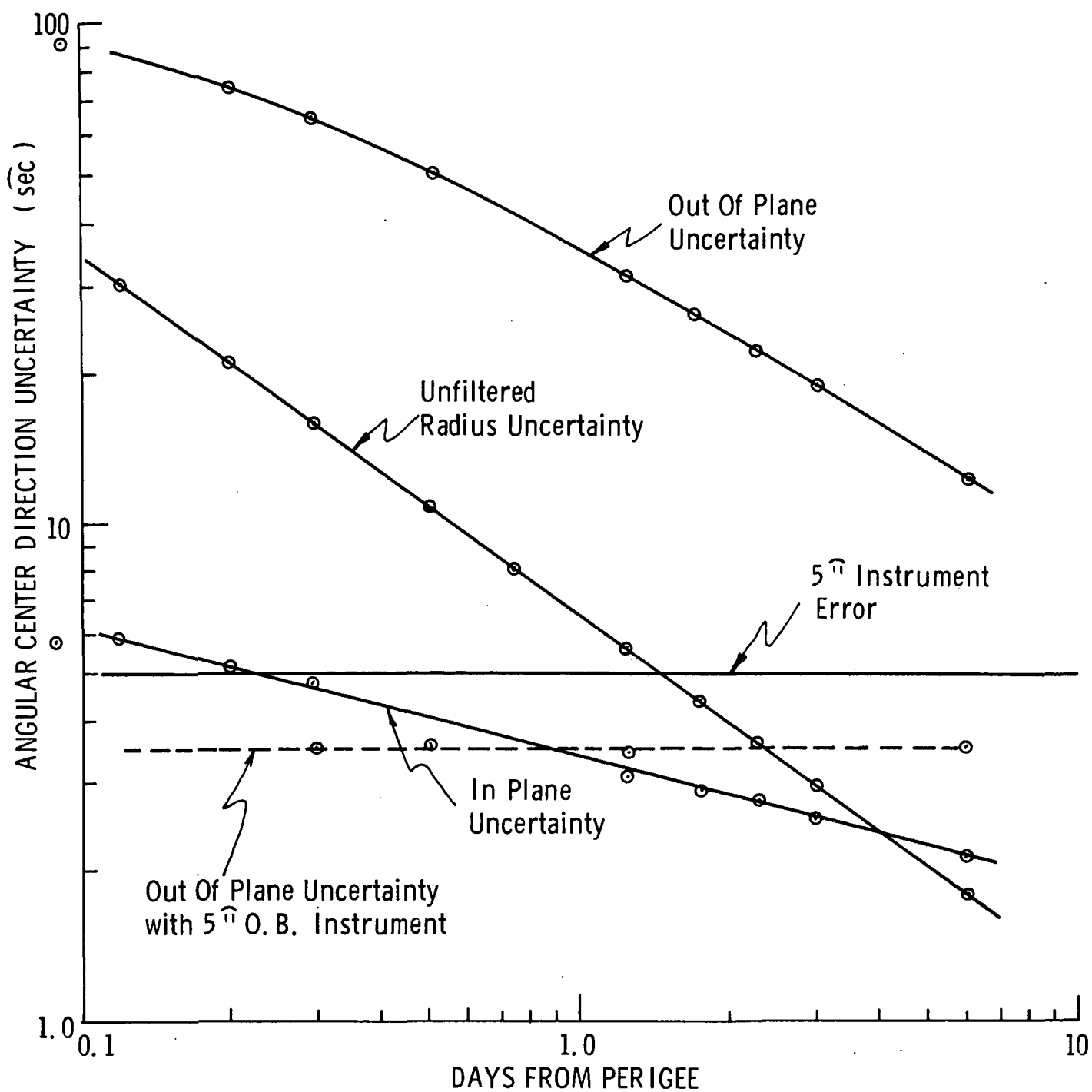


Fig. I-1 Jupiter Center Finding Uncertainties

I.2 BISECTING A TWO-LIMB SCAN

Since the out-of-plane uncertainties are largest, and the onboard system can make its largest contribution to the reduction of this uncertainty, there is some merit in the procedure of bisecting the angle between opposite limbs. A sensor scan can be made perpendicular to the plane of motion since the planetary apparition is generally symmetric about the ecliptic plane. However this technique is fairly restrictive in the scan plane orientation, and the scan field-of-view would not necessarily intersect any chosen stars at all spacecraft positions.

I.3 SIGHTINGS ON THE PLANETARY SATELLITES

Approach no. 5 above involves sightings on the planetary satellites. Although no specific sensor type is required, this type of measurement is usually mentioned in connection with image tube sensors. Imaging of the satellites against a star background allows the satellite motion to be effectively tracked, and the planet gravitational centroid direction to be inferred. This is the approach proposed by Duxbury⁴ and it is estimated to be able to locate planetary centroid direction with an accuracy of the order of 5 arcseconds. Both this technique, and the combination limb scan-DSN technique appear to be capable of good accuracy with relatively simple instrumentation.

I.4 DIRECT PLANETARY IMAGE ANALYSIS

The most direct procedure is to take a picture of the planet and transmit it to Earth for analysis of the centroid direction. This procedure has been tried on the Mariner series³, and was the first attempt at onboard navigation on a planetary, unmanned probe. A stellar reference was obtained through knowledge of the scan platform orientation with respect to the attitude control sensors. However, no attempt was made to provide a highly accurate scan platform to attitude sensor orientation control. Also the TV sensor suffered from moderate electronic and optical distortion. These limitations held the center finding accuracy down to about 0.6 arcminutes at 85 planetary radii away. The accuracy was unimproved from that point inward because the planet filled the $1.1^{\circ} \times 1.4^{\circ}$ field of view.

Because more accurate navigation measurements can be gained closer in with other techniques, and because one encounters planets of various radii, the operating range of this technique for center finding is fairly limited.

APPENDIX J

SIMULATION EQUATIONS

In this appendix the detailed equations used to perform the statistical analysis of the deep space missions under study are given. In the first section the filter equations used at each stage of the simulation are presented in a general form. This includes a description of the square root of the estimation covariance which was utilized in order to reduce the possibility of numerical errors. In the second section the detailed algorithm used to update the square root matrix is briefly described. In the third section the state vector, augmented to include all the "considered" biases is defined; and in the fourth section the manner in which the covariances are affected at a coordinate change is specified. In the fifth section the equations used to obtain the entry angle error are presented. The method of including planet radius in the state estimate is derived in the sixth section. Finally, the equations used in modeling the TV instrument are discussed and presented in the last section.

J.1 FILTER EQUATIONS

In this section the filter equations used to perform the statistical simulations are summarized. The statistical quantities used for the simulation undergo changes during three operations: extrapolation, velocity corrections, and measurement incorporation. In the model used there are unestimated dynamic and measurement parameters. The filter used here is one variation of the "consider mode" with an optimal minimum variance consider filter gain being employed. In order to decrease the possibility of numerical errors, the square root of the error covariance is used in this simulation instead of the covariance itself. The method for updating the error covariance square root matrix at each of the operations is given in this section.

We will begin by stating the needed dynamical and measurement equations. A summary of the standard filter equations follow, and then the square root matrix updates are discussed.

The following quantities will be needed:

\underline{z}	measurement vector (may be a scalar)
\underline{x}	state vector
$\underline{\mu}$	dynamic consider parameters
$\underline{\beta}$	measurement consider parameters
$\underline{\eta}$	measurement white noise

The caret "^^" above a quantity denotes the estimate of that quantity.

Assume a linearization has been made about a nominal trajectory and about nominal measurements, then:

$$\delta \dot{\underline{x}} = A(t) \delta \underline{x} + B(t) \delta \underline{\mu}$$

$$\delta \underline{z} = H(t) \delta \underline{x} + D(t) \delta \underline{\beta} + \underline{\eta}$$

while the estimated quantities satisfy:

$$\delta \dot{\underline{\hat{x}}} = A(t) \delta \underline{\hat{x}}$$

$$\delta \underline{\hat{z}} = H(t) \delta \underline{\hat{x}}$$

where for the considered parameters $\delta \underline{\hat{\mu}} = 0$ and $\delta \underline{\hat{\beta}} = 0$ (see e.g. Ref. 23, pg. 283)

Let the errors in the estimates be:

$$\underline{e} = \delta \underline{\hat{x}} - \delta \underline{x}$$

$$\underline{\gamma} = \delta \underline{\hat{z}} - \delta \underline{z},$$

then:

$$\dot{\underline{e}} = A(t) \underline{e} - B(t) \delta \underline{\mu}$$

$$\underline{\gamma} = H(t) \underline{e} - D(t) \delta \underline{\beta} - \underline{\eta}$$

Between measurements or velocity corrections $\delta \underline{x}$, \underline{e} , $\delta \underline{\mu}$, $\delta \underline{\beta}$ can be propagated using $\Phi(t_2, t_1)$, the state transition matrix for the linearized

state equations, and $\Psi(t_2)$ which is the partial of the state at time t_2 with respect to μ . Thus

$$\delta \underline{x}(t_2) = \Phi(t_2, t_1) \delta \underline{x}(t_1) + \Psi(t_2) \delta \underline{\mu}$$

$$\begin{bmatrix} \underline{e}(t_2) \\ \delta \underline{\mu} \\ \delta \underline{\beta} \end{bmatrix} = \begin{bmatrix} \Phi(t_2, t_1) & -\Psi(t_2) & 0 \\ 0 & I & 0 \\ 0 & 0 & I \end{bmatrix} \begin{bmatrix} \underline{e}(t_1) \\ \delta \underline{\mu} \\ \delta \underline{\beta} \end{bmatrix}$$

At a measurement:

$$\delta \underline{x}_+ = \delta \underline{x}_-$$

$$\delta \hat{\underline{x}}_+ = \delta \hat{\underline{x}}_- + W(\delta \underline{z} - \delta \hat{\underline{z}}_-)$$

$$\begin{bmatrix} \underline{e} \\ \delta \underline{\mu} \\ \delta \underline{\beta} \end{bmatrix}_+ = \left\{ I - \begin{bmatrix} W \\ 0 \\ 0 \end{bmatrix} \begin{bmatrix} H & 0 & -D \end{bmatrix} \right\} \begin{bmatrix} \underline{e} \\ \delta \underline{\mu} \\ \delta \underline{\beta} \end{bmatrix}_- + \begin{bmatrix} W \\ 0 \\ 0 \end{bmatrix} \underline{n}$$

where the subscript + indicates a time immediately after a measurement and - indicates immediately before.

If W is the optimal consider gain in the sense of Volume II, then it is given by:

$$W = [I \quad 0] E \begin{bmatrix} H^T \\ 0 \\ D^T \end{bmatrix} \left\{ (H \quad 0 \quad -D) E \begin{bmatrix} H^T \\ 0 \\ -D^T \end{bmatrix} + R \right\}^{-1}$$

where $R = \underline{\eta} \underline{\eta}^T$ and I is an identity matrix of the dimension of \underline{x} .

For convenience, define

$$\Phi_E(t_2, t_1) = \begin{bmatrix} \Phi(t_2, t_1) & -\Psi(t_2) & 0 \\ 0 & I & 0 \\ 0 & 0 & I \end{bmatrix}$$

$$\Phi_X(t_2, t_1) = \begin{bmatrix} \Phi(t_2, t_1) & \Psi(t_2) & 0 \\ 0 & I & 0 \\ 0 & 0 & I \end{bmatrix}$$

$$K = I - \begin{bmatrix} W \\ 0 \\ 0 \end{bmatrix} [H \quad 0 \quad -D]$$

Extrapolation:

$$E(t_2) = \Phi_E(t_2, t_1) E(t_1) \Phi_E^T(t_2, t_1)$$

$$X(t_2) = \Phi_X(t_2, t_1) X(t_1) \Phi_X^T(t_2, t_1)$$

$$C(t_2) = \Phi_X(t_2, t_1) C(t_1) \Phi_E^T(t_2, t_1)$$

Measurement incorporation:

$$\begin{aligned} E_+ &= K E_- K^T + \begin{bmatrix} W \\ 0 \\ 0 \end{bmatrix} \overline{\eta \eta^T} [W^T, 0, 0] \\ X_+ &= X_- \\ C_+ &= C_- K^T - \begin{bmatrix} W \\ 0 \\ 0 \end{bmatrix} [H \quad 0 \quad -D] E_- K^T \\ &\quad + \begin{bmatrix} W \\ 0 \\ 0 \end{bmatrix} \overline{\eta \eta^T} [W^T \quad 0 \quad 0] \end{aligned}$$

At a midcourse velocity correction

$$\delta \hat{\underline{x}}_+ = (I + MB) \delta \hat{\underline{x}}_-$$

$$\underline{e}_+ = \underline{e}_- + M\underline{\nu}$$

$$\delta \underline{x}_+ = (I + MB) \delta \underline{x}_- + MB\underline{e}_- - M\underline{\nu}^{\#}$$

as in Volume II.

It will be convenient to define an augmented estimation error covariance (E) and a deviation error covariance (X) as follows:

$$E = \overline{\begin{pmatrix} \underline{e} \\ \delta \underline{\mu} \\ \delta \underline{\beta} \end{pmatrix} \begin{pmatrix} \underline{e}^T & \delta \underline{\mu}^T & \delta \underline{\beta}^T \end{pmatrix}}$$

$$X = \overline{\begin{pmatrix} \delta \underline{x} \\ \delta \underline{\mu} \\ \delta \underline{\beta} \end{pmatrix} \begin{pmatrix} \delta \underline{x}^T & \delta \underline{\mu}^T & \delta \underline{\beta}^T \end{pmatrix}}$$

where the overbar indicates that we are taking an ensemble expected value.

The following quantity must also be defined.

$$C(t) = \begin{bmatrix} \overline{\delta \hat{\underline{x}} \underline{e}^T} & \overline{\delta \hat{\underline{x}} \delta \underline{\mu}^T} & \overline{\delta \hat{\underline{x}} \delta \underline{\beta}^T} \\ \overline{\delta \hat{\underline{\mu}} \underline{e}^T} & \overline{\delta \hat{\underline{\mu}} \delta \underline{\mu}^T} & \overline{\delta \hat{\underline{\mu}} \delta \underline{\beta}^T} \\ \overline{\delta \hat{\underline{\beta}} \underline{e}^T} & \overline{\delta \hat{\underline{\beta}} \delta \underline{\mu}^T} & \overline{\delta \hat{\underline{\beta}} \delta \underline{\beta}^T} \end{bmatrix}$$

where the last two rows are all zeros since $\delta \hat{\underline{\mu}} \equiv \delta \hat{\underline{\beta}} \equiv 0$.

The statistical quantities needed for a simulation are E, X and C. They are affected by the following types of updates: extrapolation, measurement incorporation, and velocity correction. A summary follows.

Velocity correction:

$$\begin{aligned}
 E_+ &= E_- + \begin{bmatrix} M \\ 0 \\ 0 \end{bmatrix} \overline{\underline{\nu} \underline{\nu}^T} [M^T \ 0 \ 0] \\
 X_+ &= \left(I + \begin{bmatrix} M \\ 0 \\ 0 \end{bmatrix} [B \ 0 \ 0] \right) (X_- - E_-) \left(I + \begin{bmatrix} M \\ 0 \\ 0 \end{bmatrix} [B \ 0 \ 0]^T \right) \\
 &\quad + \left(I + \begin{bmatrix} M \\ 0 \\ 0 \end{bmatrix} [B \ 0 \ 0] \right) C_- [B \ 0 \ 0]^T \begin{bmatrix} M \\ 0 \\ 0 \end{bmatrix}^T \\
 &\quad + \begin{bmatrix} M \\ 0 \\ 0 \end{bmatrix} [B \ 0 \ 0] C_- \left(I + \begin{bmatrix} M \\ 0 \\ 0 \end{bmatrix} [B \ 0 \ 0]^T \right)^T \\
 &\quad + \begin{bmatrix} M \\ 0 \\ 0 \end{bmatrix} Q^\# [M \ 0 \ 0] + E_-
 \end{aligned}$$

Note that the C matrix does not directly affect the covariance E. The square root of E could thus be processed without needing to be concerned about the dependence of E on C and X.

If a square matrix E is positive semidefinite, one can obtain a matrix S such that $E = SS^T$. The matrix S, which is the square root of the estimation error covariance matrix, can then be updated at the measurement incorporation and the velocity correction using the Gram-Schmidt

orthogonalization procedure discussed in Ref. 24. In this procedure an algorithm is used which give S where

$$SS^T = QQ^T + AA^T \quad J.1.1$$

given Q and A. The resulting S is a lower triangular matrix. Q is any square matrix of the dimension of the augmented state; A need not be square. The algorithm for updating S in this way is detailed in the next section.

Note that the updates for E at a measurement incorporation and at a velocity correction have the form of Eq. J.1.1. At a measurement incorporation let

$$Q = K S$$

$$A = \begin{bmatrix} W \\ 0 \\ 0 \end{bmatrix} \text{SQRT} \left(\overline{\underline{\eta} \underline{\eta}^T} \right)$$

At a velocity correction

$$Q = S$$

$$A = \begin{bmatrix} M \\ 0 \\ 0 \end{bmatrix} \text{SQRT} \left(\overline{\underline{\gamma} \underline{\gamma}^T} \right)$$

Then, Eq. J.1.1 may be used at a measurement time or at a velocity correction to update S.

The S matrix is extrapolated by

$$S(t_2) = \Phi_E(t_2, t_1) S(t_1)$$

At the beginning of a simulation S , $\text{SQRT}(\underline{\eta}\underline{\eta}^T)$, $\text{SQRT}(\underline{\nu}\underline{\nu}^T)$ are calculated. Thereafter only S need be updated at each step using the above procedure.

It does not appear that the X and C matrix can be updated using a square root algorithm because the updates for X at a velocity correction, and of C at any update, cannot be put in the form of Eq. J.1.1. One could use the square root update if one defined the large matrix:

$$\begin{bmatrix} \underline{e} \\ \delta \underline{x} \\ \delta \underline{\mu} \\ \delta \underline{\theta} \end{bmatrix} \quad [\underline{e}^T \quad \delta \underline{x}^T \quad \delta \underline{\mu}^T \quad \delta \underline{\theta}^T]$$

This matrix contains all the information of E , X and C and at each update it has the correct form so that its square root could be updated using the algorithm previously described. In general this matrix is rather large, thus the number of computations needed is quite large compared to updating the smaller matrices E , X and C . Thus in this study X and C were updated using the method given in Vol. II.

J.2 GRAM-SCHMIDT SQUARE ROOT UPDATE

In this section the basic procedure of the Gram Schmidt algorithm is presented. This is a method for finding S where $SS^T = QQ^T + PP^T$ where Q and P are given. This is accomplished by a method of triangularizing a nonsquare matrix by postmultiplying by an orthogonal matrix whose rows are determined using a Gram-Schmidt orthonormalizing procedure on the rows of the original matrix. This method is simple to implement and does not require a great deal of storage in a computer. Let

$$P = [Q \quad B]$$

where Q is of dimension $n \times n$, P is $n \times p$, B is $n \times (p-n)$ and P has rank $k \leq n$. We wish to find a lower triangular $n \times n$ matrix S such that

$$SS^T = PP^T.$$

Let

$$P^T = \begin{bmatrix} Q^T \\ B^T \end{bmatrix} = [\underline{d}_1, \underline{d}_z, \dots, \underline{d}_n]$$

Construct k p -dimensional basis vectors which span the subspace of p -space spanned by the rows of P .

$$\underline{b}_i = \begin{cases} \text{unit}(\underline{d}_i^{(i-1)}) & , \underline{d}_i^{(i-1)} \neq \underline{0} \\ \underline{0} & , \underline{d}_i^{(i-1)} = \underline{0} \end{cases}$$

$$\underline{d}_\ell^{(0)} = \underline{d}_\ell \quad 1 \leq \ell \leq n$$

$$\underline{d}_\ell^{(i)} = \underline{d}_\ell^{(i-1)} - \underline{b}_i^T \underline{d}_\ell^{(i-1)} \underline{b}_i, \quad 1 \leq i < \ell \leq n$$

$$\underline{d}_\ell^{(i)} = \underline{0} \quad , \quad 1 \leq \ell \leq i < n$$

The k nonzero \underline{b} vectors are orthonormal and form a basis for the subspace of $2n$ space spanned by \underline{d}_1 through \underline{d}_n . The S matrix is given by

$$S = \begin{bmatrix} b_1^T d_1 & & & \\ b_1^T d_2 & b_2^T d_2^{(1)} & & \\ \vdots & \vdots & & \\ b_1^T d_n & b_2^T d_n^{(1)} & \dots & b_n^T d_n^{(n-1)} \end{bmatrix}$$

where $n-k$ columns of S are zero.

J.3 STATE DEFINITION

In this section the state vector components will be defined. The vector will be termed the augmented state vector since it will include the unestimated dynamic and measurement biases in addition to the estimated variables and parameters. The square root of the estimation covariance of this augmented state was utilized for the navigational aspects of this study.

Define the augmented state as

$$\delta \underline{y} = \begin{bmatrix} \delta \underline{r} \\ \delta \underline{v} \\ \delta \underline{a} \\ \delta R \\ \delta \mu \\ \delta \underline{\beta} \end{bmatrix}$$

where \underline{r} is the position vector of the spacecraft, \underline{v} is its velocity vector, \underline{a} is the position of the planet (comet) relative to the sun, R is the radius of the planet or comet, μ represents the dynamic unestimated bias, and $\underline{\beta}$ represents the measurement unestimated biases. When TV is used, δR is not applicable and therefore is not included.

During an interplanetary leg \underline{r} is measured with respect to the sun; during a near planet leg, it is measured with respect to the planet.

J.4 COORDINATE TRANSFORMATIONS

When going from a sun-centered to a planet-centered leg or vice versa, the X , C and S (where $SS^T = E$) must be adjusted. The equations for doing this are given in this section.

$$\text{Let } A = \begin{bmatrix} I & 0 & -I & 0 \\ 0 & I & 0 & 0 \\ 0 & 0 & I & 0 \\ 0 & 0 & 0 & I \end{bmatrix}$$

where A is given in terms of 3×3 blocks except for the last row and column which have dimensions equal to the sum of the dimensions of δR , $\delta \mu$, $\delta \underline{\beta}$. Then when going from sun centered to planet centered coordinates:

$$X = A X A^T$$

$$C = A C A^T$$

$$S = A S$$

In addition, if $\delta\mu$ represents the sun gravitational constant for the interplanetary leg and the planet gravitational constant for the near planet leg, the rows and columns corresponding to it in X and C are set to zero. The row of S corresponding to $\delta\mu$ is also set to zero. Then the new $\delta\mu^2$ is inserted on the diagonal of X in the correct position, and its square root is added via a square root update to S.

$$\text{Let } A' = \begin{bmatrix} I & 0 & I & 0 \\ 0 & I & 0 & 0 \\ 0 & 0 & 0 & 0 \\ 0 & 0 & 0 & I \end{bmatrix}$$

Again A' is given in terms of 3×3 blocks except for the last row and column, the dimensions of which are determined in the same way as for the matrix A. When going from planet centered to sun centered coordinates:

$$X = A' X A'^T$$

$$C = A' C A'^T$$

$$S = A' S$$

In addition, the rows and columns of X and C and the rows of S corresponding to δR , $\delta\mu$, and the $\delta\beta$ corresponding to onboard measurement biases (not DSN) must be set to zero. Then the 3×3 ephemeris block of the next planet, the new $\delta\mu^2$ and $\delta\beta \delta\beta^T$ must be placed on the diagonal of X in the appropriate positions and their square roots must be added to the S matrix via the square root update.

J.5 ENTRY ANGLE EQUATIONS

For the Jupiter entry missions it was of particular interest to find the error in entry angle. The equations used are given in this section. Let \underline{r} be the vector from the planet center to the spacecraft, and \underline{v} the spacecraft velocity relative to the planet. The included angle, θ , is given by $\underline{r} \cdot \underline{v} = |\underline{r}| |\underline{v}| \cos \theta$. The entry angle ($\gamma = 90^\circ - \theta$) is then given by

$$\underline{r} \cdot \underline{v} = |\underline{r}| |\underline{v}| \sin \gamma$$

(see Fig. J-1). Taking the variation

$$\begin{aligned} \delta \underline{r} \cdot \underline{v} + \underline{r} \cdot \delta \underline{v} &= \frac{\underline{r} \cdot \delta \underline{r}}{|\underline{r}|} |\underline{v}| \sin \gamma \\ &+ \frac{\underline{v} \cdot \delta \underline{v}}{|\underline{v}|} |\underline{r}| \sin \gamma + |\underline{r}| |\underline{v}| \cos \gamma \delta \gamma \end{aligned}$$

Solving for $\delta \gamma$, one obtains

$$\begin{aligned} \delta \gamma &= \frac{1}{|\underline{r}| \cos \gamma} \left(\frac{\underline{v}}{|\underline{v}|} - \frac{\underline{r}}{|\underline{r}|} \sin \gamma \right) \cdot \delta \underline{r} \\ &+ \frac{1}{|\underline{v}| \cos \gamma} \left(\frac{\underline{r}}{|\underline{r}|} - \frac{\underline{v}}{|\underline{v}|} \sin \gamma \right) \cdot \delta \underline{v} \end{aligned} \quad (\text{J.5.1})$$

If the 6x6 portion of the guidance error covariance, X , is partitioned

$$X = \begin{bmatrix} X_{rr} & X_{rv} \\ X_{vr} & X_{vv} \end{bmatrix}$$

and if the vector coefficients of $\delta \underline{r}$ and $\delta \underline{v}$ in Eq. J.5.1 are denoted \underline{e} and \underline{f} , respectively, then

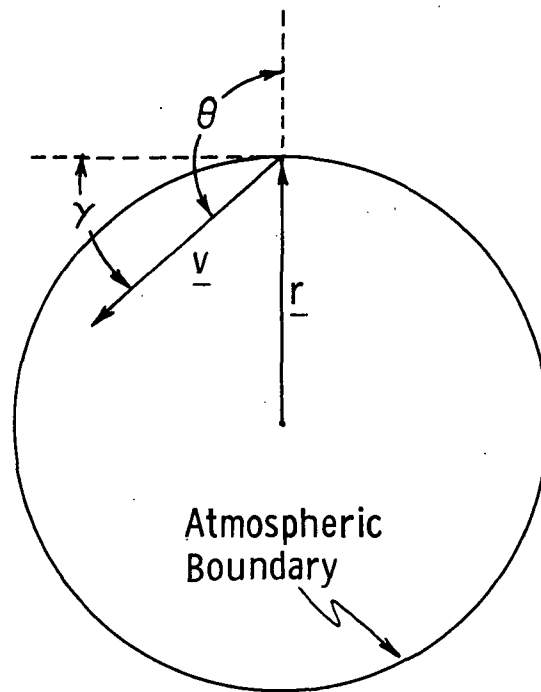


Fig. J-1 Entry Geometry

$$\overline{\delta\gamma^2} = \underline{e}^T X_{rr} \underline{e} + 2 \underline{e}^T X_{rv} \underline{f} + \underline{f}^T X_{vv} \underline{f}$$

A similar expression which involves the estimation error covariance ensues for the error in the estimate of $\delta\gamma$.

J.6 STAR ELEVATION MEASUREMENT WITH PLANET RADIUS

Only star elevation measurements were assumed to be made with the scanning photometer instrument. Planet radius error was adjoined to the state and estimated. This requires a modification of the measurement partial given in Battin.²⁵ This measurement partial is derived in this section.

Let \underline{n} be a unit vector from the spacecraft toward a star, \underline{r} be the vector from planet (or comet) center to spacecraft, z be the radius of the planet (comet), ℓ be a line from spacecraft to the planet limb in the plane of star-planet-spacecraft, A be the angle between ℓ and \underline{n} , γ be the angle between \underline{r} and ℓ . Then

$$\underline{n} \cdot \underline{r} = -r \cos (A + \gamma)$$

Assume only \underline{n} is fixed and take the variation.

$$\begin{aligned} \underline{n} \cdot \delta \underline{r} &= \frac{r}{|\underline{r}|} \cdot \delta \underline{r} \cos (A + \gamma) \\ &+ |\underline{r}| \sin (A + \gamma) (\delta A + \delta \gamma) \end{aligned} \quad (J.6.1)$$

Noting that $\sin \gamma = \frac{z}{|\underline{r}|}$, then

$$\begin{aligned} \cos \gamma \delta \gamma &= -\frac{z}{|\underline{r}|^3} \underline{r} \cdot \delta \underline{r} + \frac{\delta z}{|\underline{r}|} \\ &= -\frac{\sin \gamma}{|\underline{r}|^2} \underline{r} \cdot \delta \underline{r} + \frac{\delta z}{|\underline{r}|} \end{aligned} \quad (J.6.2)$$

Combining Eq. J.6.1 with Eq. J.6.2 and solving for δA produces

$$\delta A = \left(\frac{(|\underline{r}| \underline{n} + \underline{r} \cos(A+\gamma))}{\sin(A+\gamma)} + \tan \gamma \underline{r} \right) \frac{1}{|\underline{r}|^2} \cdot \delta \underline{r} - \frac{\delta z}{\cos \gamma |\underline{r}|}$$

which gives the necessary measurement partial.

J.7 TELEVISION MEASUREMENT EQUATIONS

In this section the measurement equations associated with the TV navigation instrument are presented. The use of this instrument in the simulation was discussed in Sec. 2.3. The source of the values for the instrument errors and some of the problems in using this type of sensor was discussed in Appendix H.

A television (image tube) instrument would be used to measure the direction toward a celestial object such as a satellite or comet nucleus. The expression for the measured image location on the screen (Eq. 1 of Ref. 2) is given by

$$\begin{bmatrix} X_m \\ Y_m \end{bmatrix} = \frac{f}{w} \begin{bmatrix} 1 & 0 & 0 \\ 0 & 1 & 0 \end{bmatrix} (I - E) M \frac{\underline{t}}{|\underline{t}|} + \begin{bmatrix} X_{op} \\ Y_{op} \end{bmatrix} + \begin{bmatrix} X_{em} \\ Y_{em} \end{bmatrix} + \begin{bmatrix} \eta_x \\ \eta_y \end{bmatrix}$$

where f/w is essentially a scaling factor and can be set to one, M is a matrix which rotates the inertial x-y-z coordinate system, $(I - E)$ is a rotation matrix that defines the deviation of the actual TV orientation from the measured orientation. This difference was assumed negligible and thus the matrix was just the identity matrix. \underline{t} is the vector from the spacecraft to the object being sighted, X_{op} , Y_{op} are the components of the optical distortion, X_{em} , Y_{em} are the components of electromagnetic distortion,

η_x, η_y are the components of measurement noise due to pixal and scan line resolution. All of the measurement errors were lumped together into an equivalent white noise and bias, thus the actual measurement equation used had the form

$$\begin{bmatrix} X_m \\ Y_m \end{bmatrix} = \begin{bmatrix} 1 & 0 & 0 \\ 0 & 1 & 0 \end{bmatrix} M \frac{\underline{t}}{|\underline{t}|} + \underline{b} + \underline{\eta}$$

where \underline{b} is the bias term and $\underline{\eta}$ is the white noise term.

It is assumed the groups of stars have been used to calibrate optical distortion and electromagnetic distortion has been calibrated using a reseau grid or clusters of stars.¹ The bias and white noise error components approximate the effect of residual error in electromagnetic and optical distortion and errors in knowledge of the transformation M.

The rotation matrix M was assumed to be given by

$$M = \begin{bmatrix} \text{unit}((\underline{r} \times \underline{v}) \times \underline{t})^T \\ \text{unit}(\underline{t} \times ((\underline{r} \times \underline{v}) \times \underline{t}))^T \\ \text{unit}(\underline{t})^T \end{bmatrix}$$

Taking the variation one obtains the measurement partial

$$= \begin{bmatrix} \delta X_m \\ \delta Y_m \end{bmatrix} = \begin{bmatrix} 1 & 0 & 0 \\ 0 & 1 & 0 \end{bmatrix} M \frac{\delta \underline{t}}{|\underline{t}|} + \underline{b} + \underline{\eta}$$

Making the obvious identifications let

$$\underline{z} = H^T \delta \underline{t} + \underline{b} + \underline{\eta}$$

For the planet centered case, when the TV is being used to sight on a satellite

$$\underline{z} = H^T(-\delta \underline{r} + \delta \underline{a}) + \underline{b} + \underline{\eta}$$

where \underline{r} is the vector from planet to spacecraft and \underline{a} is the vector from planet to satellite.

For the case of sighting on a comet while in sun-centered coordinates a similar equation results, with \underline{r} being identified as the vector from sun to spacecraft and \underline{a} the vector from sun to comet.

Distribution - Internal

R. Battin
P. Bowditch
S. Croopnick
J. Deckert
T. Edelbaum
P. Felleman
D. Fraser (20)
C. Gray
D. Gustafson
D. Hoag
P. Kachmar
A. Klumpp
B. Kriegsman
L. Larson
G. Levine
H. Malchow (3)
E. Muller
G. Ogletree
T. Parr
P. Philliou
P. Pollock
W. Robertson
L. Sackett (3)
N. Sears
W. Tempelman
MIT/CSDL Library (10)
Apollo Library (2)
MIT/CSDL Contract Office

Distribution - External

NASA Headquarters - Washington, D. C. 20546

OART

R/Mr. Oran W. Nicks
RP/Mr. Adelbert O. Tischler
RE/Mr. Frank J. Sullivan
REE/Mr. Charles E. Pontious
REG/Mr. Jules I. Kanter
REI/Mr. Gene A. Vacca
RES/Mr. Charles H. Gould
RET/Mr. Henry L. Anderton
RN/Mr. William H. Woodward
RNT/Mr. James Lazar
RMD/Mr. Richard J. Wisniewski
RR/Dr. Hermann H. Kurzweg
RV/Mr. Milton B. Ames, Jr.
REG/Mr. Theodore S. Michaels

OSSA

S/Dr. John E. Naugle
SS/Dr. Henry J. Smith
SL/Mr. Robert S. Kraemer
SL/Mr. Norri Sirri

OMSF

M/Mr. Dale D. Myers

Ames Research Center - NASA, Moffett Field, California 94035

Mr. C. A. Syvertson, Mail Stop 200-2
Dr. Leonard Roberts, Mail Stop 200-3
Mr. John S. White, Mail Stop 210-3
Mr. Charles F. Hall, Mail Stop 244-8
Mr. Howard F. Matthews, Mail Stop 244-7
Mr. Larry Manning, OART/ACMD

Goddard Space Flight Center - NASA, Greenbelt, Maryland 20771

Mr. Donald P. Hearth, Code 100
Dr. Rydolf A. Stampfl, Code 401
Mr. Robert T. Groves, Code 551
Mr. Kenneth I. Duck, Code 734

Jet Propulsion Laboratory - 4800 Oak Grove Dr., Pasadena, Calif. 91103

Dr. Donald Rea, Mail Stop 180-404
Mr. Peter N. Hauran, Mail Stop 180-302
Dr. R. Rhoads Stephenson, Mail Stop 156-203
Mr. James Long, Mail Stop 180-302
Mr. Tom W. Hamilton, Mail Stop 180-402
Mr. John R. Scull, Mail Stop 198-226
Dr. James F. Jordan, Mail Stop 156-229
Dr. Roger D. Bourke, Mail Stop 126-235
Mr. Robert G. Nagler, Mail Stop 180-703
Mr. Thomas Duxbury, Mail Stop 156-229
Dr. Louis Friedman, Mail Stop 156-229

Langley Research Center - NASA, Langley Station, Hampton, Va. 23365

Mr. William H. Phillips, Mail Stop 152
Mr. George B. Graves, Jr., Mail Stop 476
Mr. Richard C. Dingeldein, Mail Stop 156

Lewis Research Center - NASA, 21000 Brookpark Road, Cleveland, Ohio
44135

Dr. Seymour C. Himmel, Mail Stop 173-303
Mr. Richard J. Wever, Mail Stop 501-302

Marshall Space Flight Center - NASA, Marshall Space Flight Center, Ala.
35812

PD/DIR/Mr. William R. Lucas
S&E-Aero-G/Mr. Clyde D. Baker
S&E-Aero-M/Mr. J. P. Lindberg

Outside Agencies

North American Rockwell
Space Division
12214 Lakewood Boulevard
Downey, California 90241

Mr. Robert Epple, D192-400
Mr. J. R. Eyman, BB77
Mr. E. J. Dazzo, BB57

Mr. George Townsend
North American Rockwell
Suite 143
3322 South Memorial Parkway, S. W.
Huntsville, Alabama 35801

TRW Systems Group
One Space Park
Redondo Beach, California 90278

Mr. H. F. Meissinger, R5/2291
Mr. Robert A. Park, R5/2291

Mr. Brian T. Howard
Director, Space Sciences and
Advanced Manned Missions Division
Bellcomm, Inc.
955 L'Enfant Plaza No. S.W.
Washington, D. C. 20024

Mr. Alan L. Friedlander
IIT Research Institute
10 West 35 Street
Chicago, Illinois 60616

Mr. B. Gentry Lee
Viking Projects Mission Analysis
SSB 8947
Martin Marietta Corp.
P.O. Box 179
Denver, Colorado 80201

Mr. B. Galman
Re-Entry and Environmental Systems Div.
General Electric Co.
3198 Chestnut Street
Philadelphia, Pennsylvania 19101

Mr. D. D. Fields
AVCO Systems Division
201 Lowell Street
Wilmington, Massachusetts 01387